27th International Conference

APPLIED MECHANICS 2026

CONFERENCE PROCEEDINGS

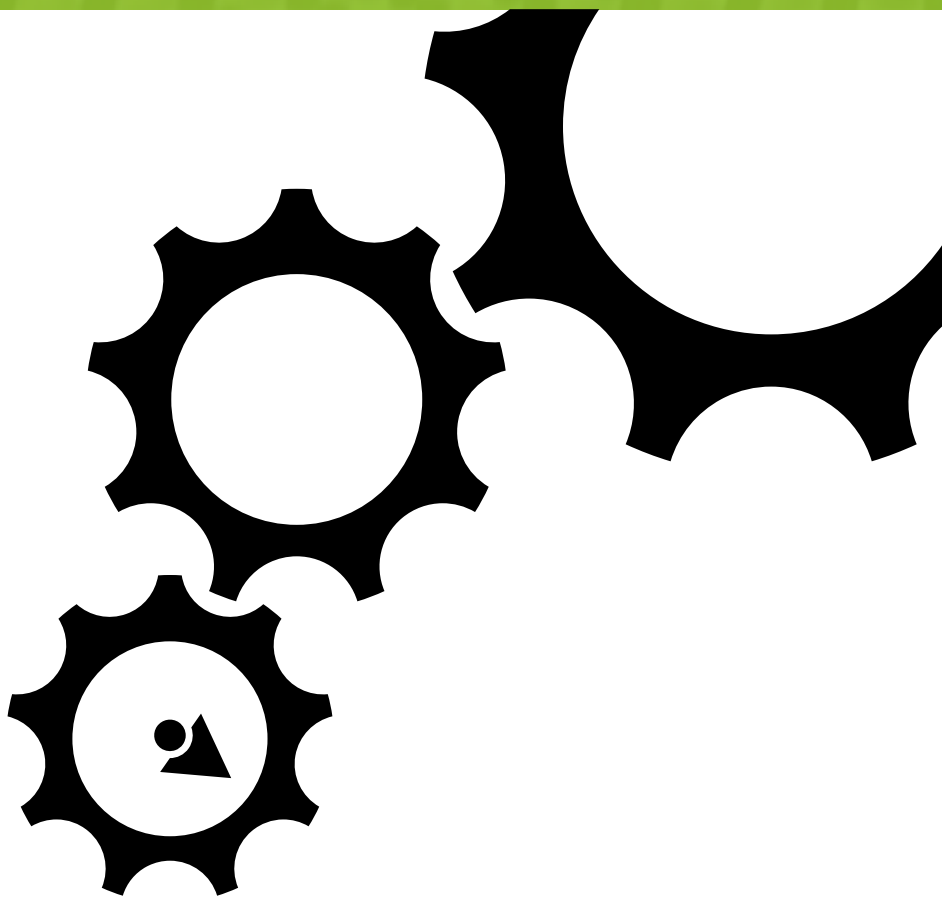

FACULTY OF APPLIED SCIENCES
UNIVERSITY OF WEST BOHEMIA
IN PILSEN

APPLIED MECHANICS 2026

April 13 - 15, 2026, České Budějovice, Czech republic

Proceedings of the 27th International Conference Applied Mechanics 2026

FACULTY OF APPLIED SCIENCES
UNIVERSITY OF WEST BOHEMIA
IN PILSEN

Conference organiser

Department of Mechanics
Faculty of Applied Sciences
University of West Bohemia in Pilsen

The conference is organised under the auspices of Czech Society for Mechanics, z.s.

Organising committee

Radek Bulín
Miroslav Byrtus
Štěpán Dyk
Michal Hajžman
Vladimír Lukeš
Jan Rendl
Luboš Smolík

Conference partners

Czech Society for Mechanics, z.s.
Doosan Škoda Power a.s.
HELAGO-CZ, s.r.o.
HUMUSOFT s.r.o.
IDIADA CZ, a.s.

Title: Proceedings of the 27th International Conference Applied Mechanics 2026
Editors: Jan Rendl
Illustrator: Jan Rendl
Publisher: University of West Bohemia in Pilsen, Univerzitní 2732/8, 301 00 Plzeň
Date of issue: April 2026
ISBN 978-80-261-1352-2

Conference partners

DOOSAN Škoda Power

Applus+ IDIADA

YOUR DEVELOPMENT PARTNER

Preface

Dear colleagues,

The volume you have just opened contains the proceedings of the 27th International Conference Applied Mechanics 2026, held in České Budějovice and organised by the Faculty of Applied Sciences, University of West Bohemia in Pilsen.

It is likely that no one attending the very first edition in 1999 could have foreseen where this conference would be twenty-seven years later, especially considering how significantly the research environment in our countries has changed over that time.

It should be noted that organising and attending conferences of primarily local importance is not particularly encouraged nowadays, and the papers and presentations delivered here do not directly contribute to the formal success metrics of grant projects. Nevertheless, this year's conference has brought together nearly sixty researchers, both early-career and senior, who have come to present their work and engage in informal discussions beyond the lecture hall. With this attendance, Applied Mechanics will likely rank among the largest local conferences of its kind held in the Czech Republic. This would not be possible without your active participation and the generous support of our partners.

What makes the Applied Mechanics conference truly unique is the community that has gradually formed around it — a network of colleagues across our countries and academic institutions who share not only similar professional interests and responsibilities, but also long-standing friendships and a strong sense of collegiality.

Another defining feature of the conference is the continuous presence of young researchers, many of whom have the opportunity, often still as students, to present their work to an expert audience for the very first time, while at the same time experiencing the welcoming and friendly atmosphere that has always been a hallmark of this event.

It is our sincere wish that this spirit of Applied Mechanics endures, and that participation in the conference continues to inspire future generations of young researchers, while remaining a traditional meeting place for those who have helped shape its history over the years.

Radek Bulín
Chairman of the Organising Committee
Faculty of Applied Sciences
University of West Bohemia in Pilsen

Scientific committee

Contents

APPLIED MECHANICS 2026
April 13 - 15, 2026, České Budějovice, Czech republic

MATHEMATICAL MODELING AND EXPERIMENTAL DEMONSTRATION OF A NONLINEAR ENERGY SINK

František Bareš[1]

Abstract: This paper presents the mathematical modeling and experimental validation of a passive Nonlinear Energy Sink (NES) designed for vibration control. The proposed NES utilizes cubic stiffness springs combined with repulsive magnetic forces to achieve its nonlinear characteristics. The system's equations of motion were solved using the Harmonic Balance Method and numerical continuation, supported by a Spline Curve approximation to maintain stability. The model is validated using the physical demonstrator utilizing camera-based motion tracking.

Keywords: Nonlinear Energy Sink; Passive Vibration Control; Magnetic Nonlinearity; Eddy Current Damping

1 Introduction

Vibration of mechanical structures is a problem discussed in many engineering fields. It is observed in many cases, that this problem was solved by installation of vibration absorber [1]. These devices can be classified as passive, active and semi active vibration absorbers. Active absorber includes a regulator, which changes parameters with changing situations, passive dampers are just dead-mass on the construction and semi active dampers combine both of these stances [2]. This work is focused on the area of the passive one. Generally, the basic solution is mass damper with one degree of freedom. It is tuned to reduce vibration to one specific frequency. Typically it is the natural frequency of the system. This type of solution was often used in engineering practice, but it has weakness in small frequency range, in which the damping effect is efficient. One way to achieve a robust damping effect is the concept generally known as nonlinear energy sink (NES). This way is common in the academic community. The proof of that can be more than 100 papers about this topic published during the year 2024 [3].

It can be given some examples of NES research in academic space. The constriction with spring was realized by [4]. In this case the results are verified by experimental measurement. However, this concept was modified with the goal of achieving better results. [5] added a piecewise stiffness element to the system. This idea was also realized in [6]. Another principle is to use magnetic force. This concept is realized in [7]. The next principle is the track NES presented in [8], where the specific nonlinear stiffness is caused by the geometry of the track, which leads to the NES active mass being described as a trajectory. This source studied more performances of the trajectory and found one with a good effect of vibration reduction.

This work is focused on developing NES using two realizations of a nonlinear connection. It consist of springs with cubic stiffness characteristic and repelling magnetic force. The goal is to effectively reduce the resonance peak of one degree of freedom system, which is waked kinematically by linear harmonic oscillations. Firstly, this system will be solved by numerical computation and used to tune NES parameters. Then, the result will be verified using the physical demonstrator.

2 Mathematical Model

In figure 1, vibration demonstrator with mass M and position x_1, connected to a fixed table by two leaf springs with stiffness k_1 and material damping c_1 is shown. On the demonstrator top, the NES on the linear tracks with variable position x_2 and damping c_n is installed. The NES has a mass m and it is connected to the demonstrator by springs attached at a right angle at the track, as shown in figure 3.

[1] František Bareš; Department of Mechanics, Faculty of Applied Sciences of the University of West Bohemia in Pilsen; bares@students.zcu.cz

That creates approximately cubic stiffness k_n. Next on the NES is installed magnets, which creates a repulsive magnetic force $F_m(a)$ dependent on the relative position of the NES a. That is displayed in figure 2.

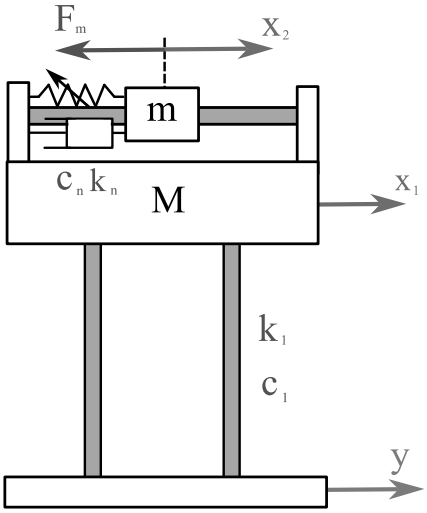

Figure 1: Schema of the demonstrator.

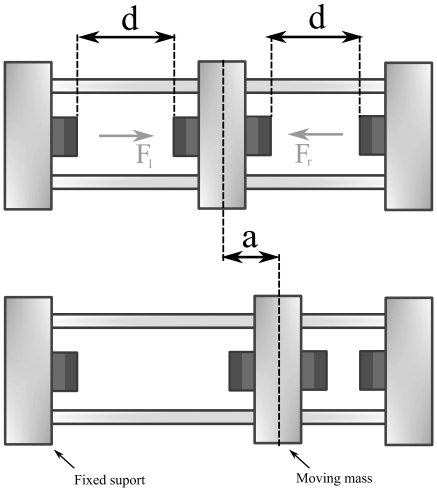

Figure 2: Placing of the magnets on the NES.

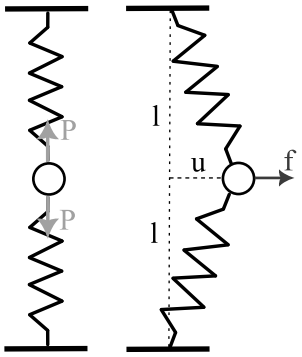

Figure 3: Placing of the springs makes cubic stiffness.

The linear oscillations are generated kinematically by the displacement y. It is realized by a slotted link mechanism with eccentricity Y and powered by an electric motor with angular velocity ω. The equations of motion have the form

$$\begin{aligned} M\ddot{x}_1 + c_1(\dot{x_1} - \dot{y}) + k_1(x_1 - y) - c_n(\dot{x}_2 - \dot{x}_1) - kn(x_2 - x_1)^3 - F_m(x_2 - x_1) = 0, \\ m\ddot{x}_2 + c_n(\dot{x}_2 - \dot{x}_1) + k_n(x_2 - x_1)^3 + F_m(x_2 - x_1) = 0. \end{aligned} \tag{1}$$

As there are two magnet pair states in equilibrium position with gap d and with relative deviation a, the magnetic force between left a right magnet pairs can be described as [10]

$$\begin{aligned} F_l &= \frac{B^2A^2(h+R)^2}{\pi\mu_0 h^2}\left(\frac{1}{(d+a)^2} + \frac{1}{(d+a+2h)^2} - \frac{2}{(d+a+h)^2}\right), \\ F_r &= \frac{B^2A^2(h+R)^2}{\pi\mu_0 h^2}\left(\frac{1}{(d-a)^2} + \frac{1}{(d-a+2h)^2} - \frac{2}{(d-a+h)^2}\right), \end{aligned} \tag{2}$$

where:

- B is the magnetic flux density (T),
- A is the circular area of the magnet (m^2),
- h is the thickness of the magnet (m),
- R is the radius of the magnet (m),
- μ_0 is the permeability of vacuum ($4\pi \times 10^{-7}$ H/m),
- z is the gap between the magnets (m).

The final magnetic force declared in the equations of motion (1), which is dependent on distance a, can be described by the difference of forces (2), as displayed in figure 2:

$$F_m(a) = F_r - F_l. \tag{3}$$

3 Computation of the Frequency response curves

The equations of motion (1) are solved using the *Harmonic Balance Method*, where the steady-state solution of the ordinary differential equations (ODE) is approximated by a truncated Fourier series [11]. This approximation is substituted into the original ODE, and the resulting terms are grouped by their respective frequencies. By requiring the residuals of the included harmonics to vanish, the differential equations are transformed into a system of nonlinear algebraic equations. The unknowns in this system are the Fourier coefficients of the included frequencies, which can then be solved numerically.

The magnetic force, defined by the formula (3), are approximated by a polynomial function during the Harmonic Balance process. In this work, two methods of approximation were used. The first approach utilizes a *6th-order Taylor polynomial* evaluated at the center point $a = 0$. However, this method is limited by its range of accuracy, as the approximation is only valid in the immediate vicinity of the center point. While accuracy could theoretically be improved with a higher-order polynomial, doing so often leads to poor convergence conditions. Consequently, an alternative approach using *Spline Curve* approximation was developed. By this method, the magnetic force is divided into small intervals, each approximated by a series of 3rd-order (cubic) polynomials, providing better stability of the numeric solution. The C^2 continuity of spline on the interval's border gives stability of the numerical solution in this area.

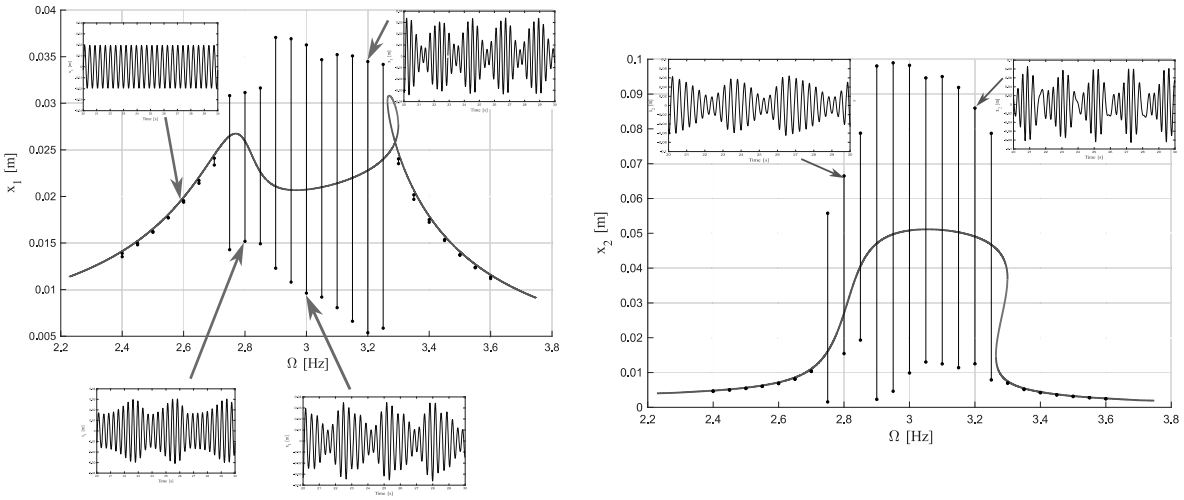

Figure 4: Computed amplitude characteristic of the main structure and the NES.

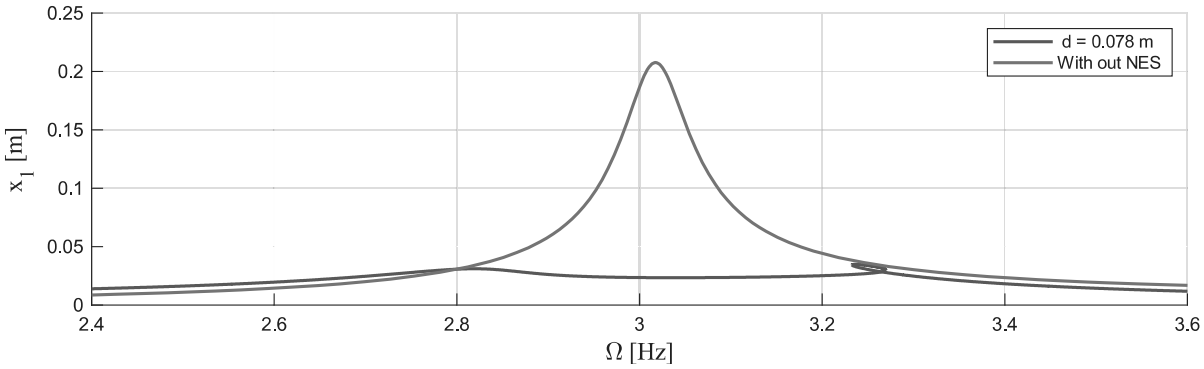

Figure 5: Comparison of the frequency response curves with and without NES

Figure 4 shows frequency response curves from the cases with the NES parameters are tuned to optimal value. Namely, the range around the resonance frequency of the primary system has small deviations x_1. This amplitude given by the *Harmonic Balance Method* was compared with the time response given by the *Runge-Kutta method*. In the figure 4, these results are shown as the maxima and minima of this time response and in some cases are displayed as the whole plot. It can be observed that in the area around the natural frequency, the time response has nonlinear behavior with a more colorful frequency spectrum.

It can also be observed that the frequency range during which the NES reduces the amplitude is around 0.4 Hz. This area is evident in the amplitudes of added mass x_2. Here, the amplitudes currently increase thus, the energy of the primary system is successfully transferred to the NES. The amplitude characteristic of x_2 has similar behavior like *Duffing Oscillator*, which, for example, describes Krack in [11]. Therefore, it can be observed as something like a resonance peak inclined to a space of higher frequencies. This inclination creates an area where, theoretically, there are three solutions for one frequency. Two of them are stable, and one is unstable. At the amplitude characteristic of x_1, this phenomenon can be observed as a closed loop when described as unstable solutions. Figure 5 shows the optimal case, the NES in the described model can efficiently reduce oscillations of the primary system in the area around the resonance frequency. Especially, the currently described primary system with one degree of freedom has a natural frequency: $\Omega \doteq 3.02$ Hz, In the case when the gaps between magnets are: $d = 0.078$ m, the NES at this natural frequency reduced 89% of the former system's amplitude.

4 Efficiency given from the Pulse Characteristic

As described by Gendelman [9], the efficiency of targeted energy transfer (TET) is dependent on the size of the pulse, which can be described by initial energy. By accepting this fact, it was the study of the pulse characteristic of the described system stated by the equations (1). However, it is possible to evaluate the efficiency of the NES like the relation to the total energy of the NES E_N and the whole system, where E_P is the total energy of the main structure [12]:

$$\eta = \frac{E_N}{E_P + E_N} \cdot 100\,\%. \tag{4}$$

However, it is hard to apply this approach to practical NES design because the energy, depending on the current velocity, changes over time. Thus, accepting this fact, it was chosen to state the work [13], where the efficiency of the TET was expressed as the relation between the dissipation energy of NES vibration and the kinetic energy at the start of the pulse:

$$\eta = \frac{\int_0^T c_n(\dot{x}_2(t) - \dot{x}_1(t))^2 \mathrm{d}t}{\frac{1}{2}M\dot{x}_1^2(0)} \cdot 100\,\%, \tag{5}$$

where the $\dot{x}_1^2(0)$ is the initial velocity of the primary structure. The integral from the formula (5) was solved numerically by obtaining an impulse time response, which is the solution of the *Runge-Kutta Method*. The figure 6 shows, how several parameters can have an effect on the NES Efficiency. Namely, it is: the gap between magnets d, the initial velocity of the primary structure $\dot{x}_1$, and the relative mass of the NES μ related to the mass of the primary structure. This efficiency was used to find optimal parameters using global optimization methods.

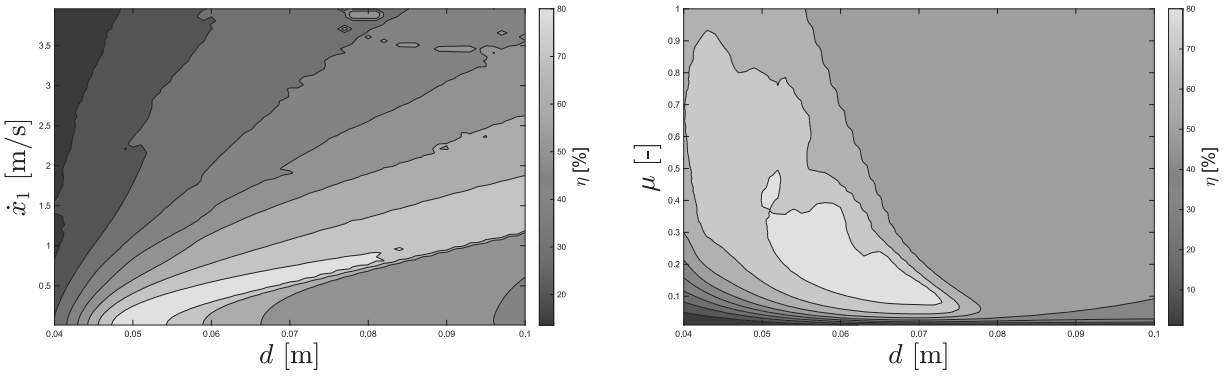

Figure 6: Relation of the NES efficiency with the selected parameters.

5 Experimental Verification

The experimental stand was built based on the vibration platform, where the vibrations are generated kinematically using the Scotch yoke mechanism. On this platform, the primary structure with two leaf springs and the NES is placed, which is connected by linear traction using linear ball bushings (figure 1 and 2). First, the placement of the magnets position and springs to create cubic stiffness were set, next the optimal damping of the NES it set. This was achieved by the eddy current produced by magnets moving along the copper plate. The motion data were recorded using the camera, and the specific point on the structure was tracked. For that, an algorithm was developed based on finding areas in the shot with a high percentage of red color. The tracking point is established as the centroid of an area. The algorithm also includes several techniques for filtering data.

6 Conclusion

The study details the development of a passive Nonlinear Energy Sink (NES) aimed at effectively reducing the resonance peak of a single-degree-of-freedom mechanical structure. The NES achieves its nonlinear characteristics through two combined mechanisms: springs configured to create cubic stiffness and repulsive magnets that generate a nonlinear magnetic force. The system's equations of motion were solved using the Harmonic Balance Method to find the amplitude characteristics. The efficiency of the targeted energy transfer was also evaluated using pulse characteristics simulated via the Runge-Kutta method. This allowed for global optimization based on the magnet gap, initial velocity, and relative mass impact the damping time and energy dissipation. To verify the mathematical and numerical findings, a coupled system of the linear oscillator and the NES physical demonstrator was constructed.

Acknowledgement

The work was supported by the internal grant project SGS-2025-015 of the University of West Bohemia in Pilsen.

References

[1] WAGG, David J. A review of the mechanical inerter: historical context, physical realisations and nonlinear applications. *Nonlinear Dynamics*. 2021, vol. 104, no. 1, pp. 13-34.

[2] ZHANG, Bao-Lin; HAN, Qing-Long and ZHANG, Xian-Ming. Recent advances in vibration control of offshore platforms. *Nonlinear Dynamics*. 2017, vol. 89, pp. 755-771.

[3] GENG, Xiao-Feng; DING, Hu; JI, Jin-Chen; WEI, Ke-Xiang; JING, Xing-Jian and CHEN, Li-Qun. A state-of-the-art review on the dynamic design of nonlinear energy sinks. *Engineering Structures*. 2024, vol. 313, pp. 118228.

[4] JIANG, Xiaoai; MCFARLAND, D Michael; BERGMAN, Lawrence A and VAKAKIS, Alexander F. Steady state passive nonlinear energy pumping in coupled oscillators: theoretical and experimental results. *Nonlinear Dynamics*. 2003, vol. 33, pp. 87-102.

[5] GENG, Xiao-Feng and DING, Hu. Theoretical and experimental study of an enhanced nonlinear energy sink. *Nonlinear Dynamics*. 2021, vol. 104, no. 4, pp. 3269-3291.

[6] YAO, Hongliang; CAO, Yanbo; ZHANG, Shijia and WEN, Bangchun. A novel energy sink with piecewise linear stiffness. *Nonlinear Dynamics*. 2018, vol. 94, pp. 2265-2275.

[7] GENG, Xiaofeng; DING, Hu; JING, Xingjian; MAO, Xiaoye; WEI, Kexiang and CHEN, Liqun. Dynamic design of a magnetic-enhanced nonlinear energy sink. *Mechanical Systems and Signal Processing*. 2023, vol. 185, pp. 109813.

[8] WANG, Jingjing; ZHENG, Yuqiang and MA, Yuhong. Experimental validation of a nonlinear mass damper enabled by movable track parts. *Engineering Structures*. 2025, vol. 328, pp. 119736.

[9] GENDELMAN, Oleg V. Transition of energy to a nonlinear localized mode in a highly asymmetric system of two oscillators. *Nonlinear dynamics*. 2001, vol. 25, no. 1, pp. 237-253.

[10] CHALLA, Vinod R; PRASAD, Marehalli G; SHI, Yong and FISHER, Frank T. A vibration energy harvesting device with bidirectional resonance frequency tunability. *Smart Materials and Structures*. 2008, vol. 17, no. 1, pp. 015035.

[11] KRACK, Malte and GROSS, Johann. *Harmonic balance for nonlinear vibration problems*. Vol. 1. City: Springer, 2019.

[12] HONG, Dongxiao; HILL, Thomas L and NEILD, Simon A. Understanding targeted energy transfer from a symmetry breaking perspective. *Proceedings of the Royal Society A*. 2021, vol. 477, no. 2251, pp. 20210045.

[13] KUMAR, P; NARAYANAN, S and GUPTA, S. Targeted energy transfer in stochastically excited system with nonlinear energy sink. *European Journal of Applied Mathematics*. 2019, vol. 30, no. 5, pp. 869-886.

APPLIED MECHANICS 2026
April 13 - 15, 2026, České Budějovice, Czech republic

POSSIBILITIES OF IMPROVING TRAJECTORY TRACKING ACCURACY OF SPATIAL 6R ROBOT WITH NONLINEAR ACTIVE 6-DOF ABSORBER

P. Beneš[1], R. Petr[2], J. Krivošej[3], K. Kraus[4], Z. Šika[5]

Abstract: This article uses simulations to study the concept of a hybrid system combining a 6R robot with a Stewart platform-type absorber placed on the robot's end effector. The aim is to improve accuracy of tracking the desired 6-DoF motion of the robot's end-effector including suppression unwanted vibrations. For the given system, the possibility of coordinated control of this entire nonlinear system is studied with the aim of determining its applicability and limitations. The basis is the use of a modified version of the computed torque method. In the robot model, compliances are considered in this initial study only in the transmissions between individual drives and controlled rotary joints.

Keywords: Active vibration absorber; 6R robot; Stewart platform; Computed torque control

1 Introduction

Robots and manipulators face challenges from mechanical vibrations caused by rapid movements, drive chain compliance or joint and arm flexibility. These vibrations degrade positioning accuracy, extend settling times, and limit operational speeds. This article addresses vibration suppression for spatial 6R robots through an active Stewart platform absorber, Figure 1, attached to the end-effector, Figure 2. The research progressed from simulation model development, through passive absorber design, to active control, systematically evaluating performance across representative trajectories with impulsive disturbances.

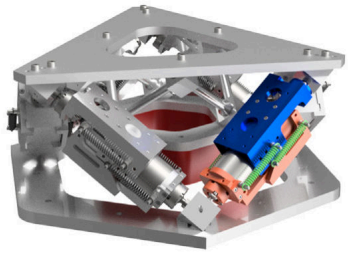

Figure 1: Demonstration of an active Stewart platform-type absorber. [1]

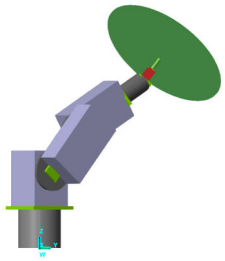

Figure 2: Visualization of a 6R robot with an attached absorber.

2 Problem description

A dynamic model of a 6R robot, inspired by the Stäubli TX2-90, was developed, with joint compliance incorporated through torsional springs and dampers. Computed Torque Control [2] was employed, but persistent oscillations remained under impulsive disturbances during tracking of prescribed trajectories. Then, a Stewart platform-type vibration absorber was attached to the robot's end-effector, allowing the generation of compensatory forces and moments in all spatial directions. This mechanism was first implemented passively, tuned to dominant vibrational frequencies. While effective near tuned frequen-

[1] Petr Beneš; CTU in Prague Faculty of Mechanical Engineering; petr.benes@fs.cvut.cz
[2] Robin Petr; CTU in Prague Faculty of Mechanical Engineering; robin.petr@fs.cvut.cz
[3] Jan Krivošej; CTU in Prague Faculty of Mechanical Engineering; jan.krivosej@fs.cvut.cz
[4] Karel Kraus; CTU in Prague Faculty of Mechanical Engineering; karel.kraus@fs.cvut.cz
[5] Zbyněk Šika; CTU in Prague Faculty of Mechanical Engineering; zbynek.sika@fs.cvut.cz

cies, the passive absorber's performance varied with robot configuration changes across the workspace. The second step was active control of the Stewart platform. Linear Quadratic Regulator with output weighting (LQRy) was designed using extended state-space models combining robot and absorber dynamics. Full-state feedback represented the ideal case, while observer-based control provided a realistic implementation with state estimation from reduced-order models. Controller gain scheduling preserved performance despite varying robot dynamics along the trajectory.

3 Results

System performance was evaluated by tracking end-effector error on several trajectories under impulsive disturbances, see Figure 3. Without an absorber, prolonged oscillations persisted; the passive absorber reduced but did not eliminate ringing; active LQRy significantly lowered peak deviations and accelerated settling to the desired trajectory. The ideal full-state LQRy outperformed observer-based control, though both substantially improved over passive and baseline configurations.

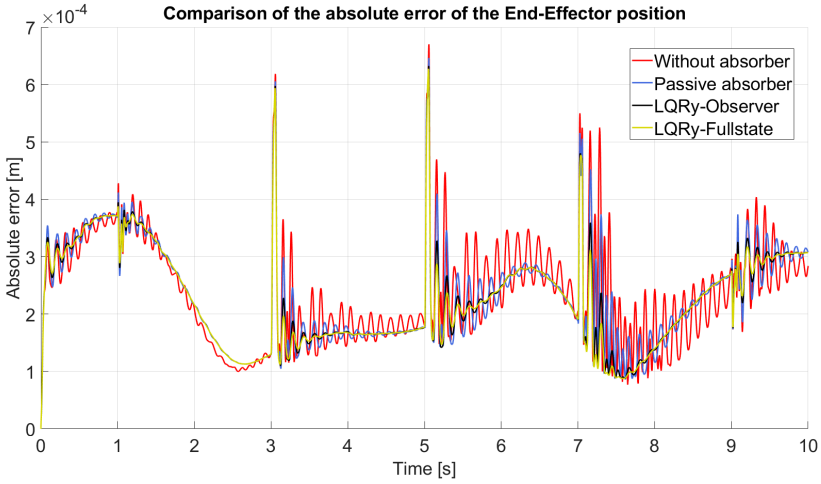

Figure 3: Comparison of the absolute error of the end-effector [3]

4 Conclusion

The Stewart platform-based active absorber achieved six-degree-of-freedom vibration suppression and confirmed the proposed concept for spatial robotic manipulators. Active control preserved performance despite varying system dynamics. The results suggest that a 6-DOF active absorber is a promising approach to vibration attenuation in serial robots.

Acknowledgement

This work was supported by the Czech Science Foundation project 25-16357S "Absorbing mechanisms with nonlinear dynamics for active reduction of periodic motions and forces in machines."

References

[1] ŠIKA, Zbyněk; KRIVOŠEJ, Jan; VYHLÍDAL, Tomáš. Three dimensional delayed resonator of Stewart platform type for entire absorption of fully spatial vibration. *Journal of Sound and Vibration*. 2024, vol. 571, pp. 118 154.. Available from: https://doi:10.1016/j.jsv.2023.118154.

[2] SPONG, Mark W.; HUTCHINSON, Seth; VIDYASAGAR, Mathukumalli. *Robot Dynamics and Control*. 1st Ed. Hoboken, NJ: John Wiley, 2005. ISBN 978-0471649908.

[3] PETR, Robin. *Vibration attenuation of spatial 6R robot using active absorber*. Diploma theses. Prague: CTU, 2025. Available from: http://hdl.handle.net/10467/126368

APPLIED MECHANICS 2026
April 13 - 15, 2026, České Budějovice, Czech republic

APPLICATION OF FMI STANDARD IN BUS MBD MODEL DEVELOPMENT

Jozef Bucha[1], Roland Jančo[2], Ľuboš Magdolen[3], Ján Čulík[4]

Abstract: This paper presents a methodology for integrating a multibody dynamics (MBD) bus model developed in Adams/Car with Matlab/Simulink using the Functional Mock-up Interface (FMI) standard. The Adams/Car model of the hydrogen bus SK080HS exported as a Functional Mock-up Unit (FMU) via co-simulation mode. Appropriate input and output state variables enable seamless data exchange between the two environments. The tool-independent nature of FMI ensures model portability across simulation platforms, supporting the development and validation of advanced vehicle control strategies for autonomous driving applications.

Keywords: FMI standard; Adams/Car; Matlab/Simulink; co-simulation; multibody dynamics; bus

1 Introduction

Simulations are essential in modern vehicle development, enabling virtual testing of functionality, reliability, and safety before physical production. They shorten development time, reduce prototype costs, and allow testing of extreme conditions without risking real components. This article focuses on the Hydrogen bus SK080HS (fig. 1) as the subject of the simulation model. The FMI (Functional Mock-up Interface) standard complements this by providing an open format for model exchange between simulation tools. Models exported as FMUs (Functional Mock-up Units) can be used for co-simulation across different software without sharing source code, supporting modularity and reusability [1].

Figure 1: Hydrogen bus SK080HS

[1] Ing. Jozef Bucha, PhD.; Slovak University of Technology in Bratislava, Institute of Automotive Engineering and Design; Námestie slobody 17, 81231 Bratislava, Slovak Republic, jozef.bucha@stuba.sk
[2] prof. Ing. Roland Jančo, PhD.; Slovak University of Technology in Bratislava, Institute of Applied Mechanics and Mechatronics; Námestie slobody 17, 81231 Bratislava, Slovak Republic, roland.janco@stuba.sk
[3] doc. Ing. Ľuboš Magdolen, PhD.; Slovak University of Technology in Bratislava, Institute of Automotive Engineering and Design; Námestie slobody 17, 81231 Bratislava, Slovak Republic, lubos.magdolen@stuba.sk
[4] Dott. Mgr. Ján Čulík; Slovak University of Technology in Bratislava, Institute of Automotive Engineering and Design; Námestie slobody 17, 81231 Bratislava, Slovak Republic, jan.culik@stuba.sk

2 Multibody Model of Bus in Adams/Car

The Adams/Car program uses a three-level vehicle modeling system. (Template → Subsystem → Assembly) [5]

The MBD model of the bus consists of eight parts, each having its own subsystem based on own template. The created model represents an assembly model of the entire vehicle. The names of the individual subsystems and their corresponding templates are listed in fig.2 [1].

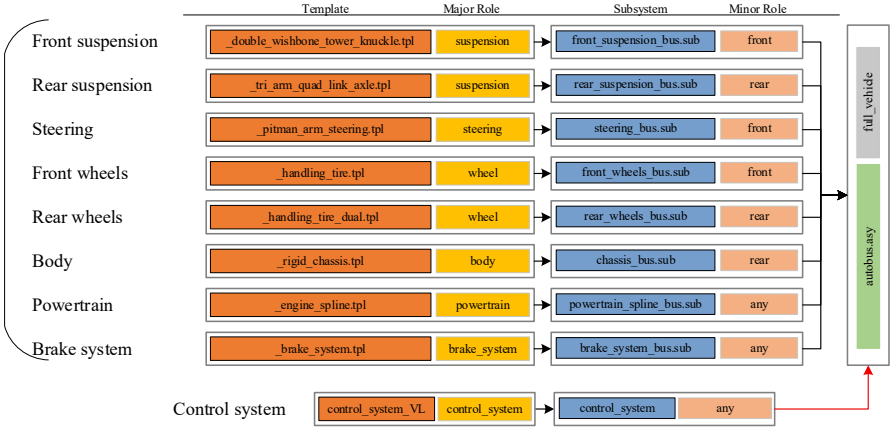

Figure 2: Block diagram of the MBD bus model

The front suspension used in the bus is modified double wishbone suspension where upright consist of tower and knuckle connected by revolute joint (fig. 3), in the rear suspension rigid axle is used (fig. 4) [1].

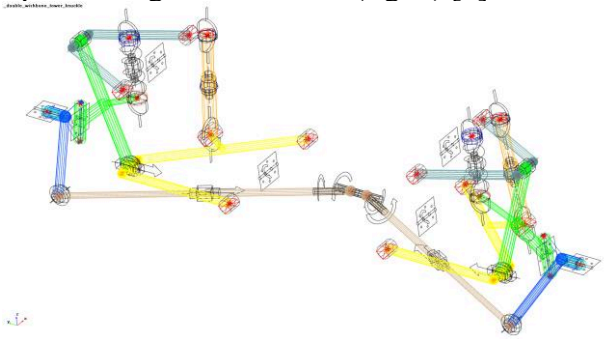

Figure 3: Front suspension template

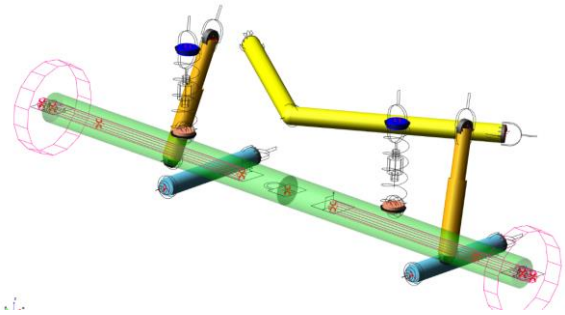

Figure 4: Rear suspension template

Fig.5 shows full vehicle assembly according fig.2. used with MDI_SDI_Testrig.

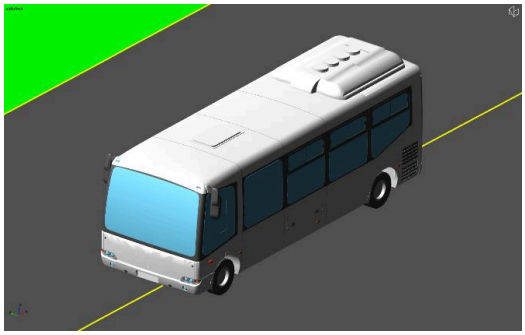

Figure 5: Full vehicle assembly of bus with MDI_SDI_Testrig.

3 Functional Mock-up Interface

The Functional Mock-up Interface is a free standard that defines a container and an interface to exchange dynamic simulation models using a combination of XML files, binaries and C code, distributed as a ZIP file. It is supported by 250+ tools and maintained as a Modelica Association Project. A Functional Mock-up Unit (FMU) is the executable that implements the interface defined by the Functional Mock-up Interface (FMI) standard. FMI standard supports two types of co-simulations [3]:

- Model Exchange:
  - The FMU (Functional Mock-up Unit) provides only the model equations (e.g. ODEs, DAEs).
  - The solver is external — it's provided by the master simulator (e.g. Simulink, Dymola, etc.).
  - The master controls Time integration, Step size, State events.
- Co-Simulation:
  - The FMU includes its own solver.
  - Each FMU advances independently in time over given steps.
  - The master only coordinates time steps and data exchange.

MSC Adams/Car can export and use FMU only in Co-Simulation mode, not in Model Exchange and supports FMU v1 and FMU v2 [1],[3].

3.1 Driving machine

The Driving Machine in Adams Car is a software module (a virtual driver) that controls the entire vehicle during simulation, ensuring consistent, repeatable, and automated vehicle tests. The Driving Machine steers the vehicle, applies the throttle and brake, and shifts gears (using the clutch). The Driving Machine can operate in pure open-loop mode (without feedback), in pure closed-loop mode (with feedback) or with combination of open and closed-loop mode [4], [5].

An event in Adams Car is a test maneuver that defines what happens to the vehicle during the simulation. An event is represented by an xml file that contains data for defining and transmitting sets of command signals, feedback signals, and parameters for each of the five control inputs: steering, throttle, brake, gear, and clutch. Fig. 7 shows pure open loop event with Varval function (values are transmitting from primary solver to vehicle FMU [2].

To easily incorporate MBD model of the bus to FMU, full vehicle assembly contains simple control subsystem (fig. 2). Control subsystem contains input state variables used in event (Steering_input, Throttle_input, Brake_input, Gear_input, Clutch_input) and output state variables (used for computation of vehicle position, orientation and velocity and acceleration, and for computation of each wheel's position and orientation) [2]. Output state variables are computed using Adams functions and based on markers attached to vehicle body and each suspension spindles and uprights or axle (fig. 6).

FMU of vehicle is possible to create using plugin Adams/Controls. Created FMU contains all necessary files for co-simulation [4]: vehicle model (.adm, .acf files), tire property files, driving event (.xml file), and also needed .dll files and .so files. Fig. 8 shows data driven co-simulation of FMU model in Simulink [6].

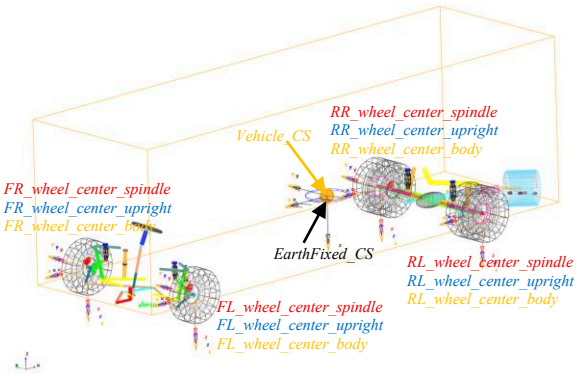

Figure 6: Front suspension template

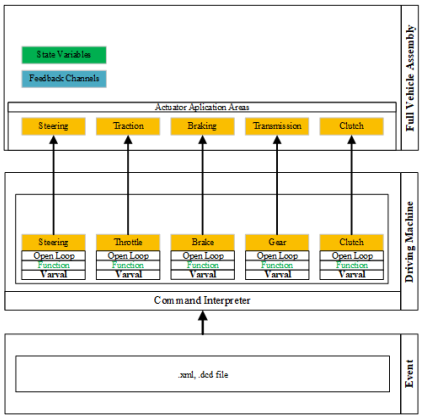

Figure 7: Open loop event with Varval function

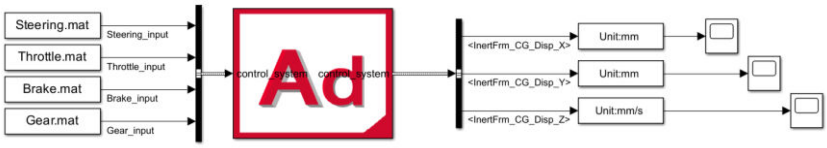

Figure 8: Data driven simulation of FMU vehicle in Simulink

4 Conclusion

This article outlined a methodology for integrating Adams/Car and Matlab/Simulink via the Functional Mock-up Interface (FMI) standard. The definition of suitable input and output state variables facilitated smooth data exchange between the Adams/Car vehicle model, functioning as the FMI slave, and the Matlab/Simulink environment acting as the master. Thanks to the tool-independent nature of the FMI standard, vehicle models can be readily shared and deployed across a variety of simulation platforms. Adams/Car delivers high-fidelity representation of vehicle dynamics, tire-road interactions, and suspension behaviour, while Simulink provides rich libraries suited to the development of advanced driver assistance systems (ADAS), autonomous driving algorithms, machine learning models, and sensor fusion techniques. Combined, these tools offer a robust environment in which researchers and engineers can develop and validate complex vehicle control strategies.

Acknowledgement

This work was supported by grant APVV-23-0650: Autonomous Bus with AI support for Public Transportation

References

[1] BUCHA, Jozef. Digitálne dvojča autobusu. *Habilitačná práca*. Strojnícka fakulta, Slovenská technická univerzita v Bratislave, Bratislava, 2026
[2] BUCHA, Jozef and DANKO, Ján and MAGDOLEN, Ľuboš and Čulík, Ján. Paper in proceedings. In: *Virtual Model of the Kyburz Vehicle using the FMI Standard*. Bratislava: Slovak University of Technology in Bratislava, 2025, p. 13-20. ISSN 00392472.
[3] Functional Mock-up Interface" ", [online] Available at: https://fmi-standard.org/ [Accessed: date (10.3.2026)].
[4] Adams/Solver reference manual. Version 2025. Santa Ana: MSC Software Corporation, 2025
[5] Adams/Car user's guide. Version 2025. Santa Ana: MSC Software Corporation, 2025
[6] Simulink reference manual. R2025b. Natick: The MathWorks, Inc., 2025

APPLIED MECHANICS 2026
April 13 - 15, 2026, České Budějovice, Czech republic

ADVANCED FRICTION MODELS WITH STICTION USED IN FRICTION-INDUCED VIBRATIONS ANALYSIS

Radek Bulín[1], Michal Hajžman[2], Jan Rendl[3], Miroslav Byrtus[4]

Abstract: Friction-induced vibrations (FIV) are an interesting phenomenon in the dynamics of mechanical systems that can occur across a wide range of applications, including brake systems (squeal noise) and precision machining. The study of FIV is important for mitigating unwanted noise and vibrations that may lead to significant wear. This work focuses on advanced friction models that incorporate internal contact dynamics and capture microscopic displacements during the stiction phase, within a minimal mathematical model that exhibits FIV. The goal is to reveal whether the precisely modelled stiction can influence the FIV of the mechanical system.

Keywords: friction-induced vibrations; friction models; stiction; dynamic simulation

1 Introduction

Friction-induced vibrations (FIV) represent a critical phenomenon in mechanical engineering, manifesting as self-excited oscillations in systems with sliding contacts. These vibrations are the primary source of unwanted effects, including brake squeal in the automotive industry, chatter in high-precision machining, and wear in industrial components. The economic and functional impact of FIV necessitates precise predictive models that can identify instability thresholds before the design phase is finalised.

Traditional analyses often rely on simplified friction laws, such as the Coulomb model, which assume a constant friction coefficient or a simple step-change between static and kinetic states. However, such models frequently fail to capture the complex physics occurring at the contact interface during the transition from rest to motion. In reality, the "stiction" phase is not purely static; it involves microscopic elastic and plastic deformations of asperities, known as pre-sliding displacement.

Recent advancements in contact mechanics have led to the development of sophisticated friction models that incorporate internal state variables to describe these dynamics. This paper investigates the influence of these advanced friction models on the onset and character of FIV. By utilising a minimal mathematical model (such as a mass-on-a-belt oscillator), we examine whether the precise modelling of internal contact dynamics and stiction significantly alters the predicted vibration patterns and stability limits of the system.

2 Model description

Figure 1 shows the analysed minimal mechanical model, which should exhibit friction-induced vibrations. It contains a point mass with weight m, which is connected to the base

[1] Ing. Radek Bulín, Ph.D.; Department of Mechanics, Faculty of Applied Sciences, University of West Bohemia in Pilsen; Univerzitní 8, 301 00 Plzeň, Czech Republic, rbulin@kme.zcu.cz
[2] doc. Ing. Michal Hajžman, Ph.D.; Department of Mechanics, Faculty of Applied Sciences, University of West Bohemia in Pilsen; Univerzitní 8, 301 00 Plzeň, Czech Republic, mhajzman@kme.zcu.cz
[3] Ing. Jan Rendl, Ph.D.; Department of Mechanics, Faculty of Applied Sciences, University of West Bohemia in Pilsen; Univerzitní 8, 301 00 Plzeň, Czech Republic, rendlj@kme.zcu.cz
[4] doc. Ing. Miroslav Byrtus, Ph.D.; Department of Mechanics, Faculty of Applied Sciences, University of West Bohemia in Pilsen; Univerzitní 8, 301 00 Plzeň, Czech Republic, mbyrtus@kme.zcu.cz

frame via two inclined springs with stiffnesses k_2 and k_3. The point mass is in contact with a belt which has a specified velocity, v_{belt}.

The contact between the point mass and the belt is modelled using Hertzian contact theory [1], which is characterised by normal contact stiffness k_c, penetration δ and penetration coefficient n. The main contribution of this paper lies in the testing of various friction models. As the basic representative of static friction models, the Bengisu-Akay model is used [2]. This model is based on the Coulomb model with the Stribeck effect, which is smoothed around the zero relative contact tangential velocity. This smoothening may result in drift during the stiction contact phase, which is an undesired effect. The first advanced friction model, which belongs to the category of dynamic friction models, is the so-called amended LuGre model [2]. The dynamic friction models introduce an additional state variable dedicated to the friction model, so an additional differential equation is solved. Some limitations of the LuGre model were addressed in [3], and a new friction model, which overcomes most of the LuGre model's unrealistic behaviour, called the second-order dynamic friction model (FrD2), was proposed there. This model employs a second-order differential equation to describe the dynamics of the fictitious bristle, which captures the microscopic frictional displacements while maintaining the static friction (stiction) phase very well. The last tested model is the generalised Maxwell slip model (GMS), which is based on N spring elements (bristles), where each has its own stiffness and maximal saturation force, which it is able to carry before it slides. This model is often used in precise friction compensation in mechatronic systems, because of its frictional memory before and after the sliding. In this work, the smoothed GMS model is used [4].

Despite the simplicity of the minimal model, there are a lot of structural parameters that can have an influence on FIV, such as spring pretension, position and stiffness, belt velocity and further various contact and friction parameters. The tuning of these parameters to reach unstable FIV can be tricky and we will address this in further work.

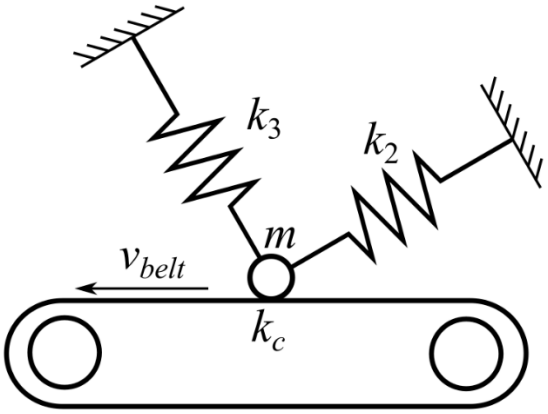

Figure 1: The used minimal mechanical model, which can exhibit friction-induced vibrations.

3 Simulations

Table 1 shows the selected key parameters used in the preliminary model analysis. There are, indeed, many other parameters not mentioned and related to the friction models (for example, Stribeck curve parameters), but it is not that important to describe them within this extended abstract, because they are the same for all of the tested friction models.

The basic question is whether the friction force, which acts in the horizontal direction, can induce the vertical vibrations of the point mass, so the FIV appear. As it is shown in Figure 2, where the vertical velocity time history of the point mass is shown, the FIV appears in all tested friction models. Interestingly, the Bengisu Akay, LuGre and FrD2 models show similar results; only in the case of the Bengisu Akay model, the vertical oscillations are slightly

damped over time. This can happen because this model exhibits a slight drift during the stiction phase. On the other hand, the GMS model in this case shows different behaviour, where the vertical oscillations are more pronounced over time.

Description	Parameter	Value
Point mass weight	m	1 kg
Spring 2 stiffness	k_2	1000 N/m
Spring 3 stiffness	k_3	2000 N/m
Contact stiffness	k_c	10^7 N/m$^{1.5}$
Initial angle of spring 2	α_{20}	45°
Initial angle of spring 3	α_{30}	120°
Vertical pretension	h	0.1 m
Belt velocity	v_{belt}	0.5 m/s
Static friction coefficient	μ_s	0.5
Dynamic friction coefficient	μ_d	0.3
Total bristle stiffness parameter	σ_0	10^6 N/m
Number of Maxwell springs	N	10

Table 1. Selected key parameters.

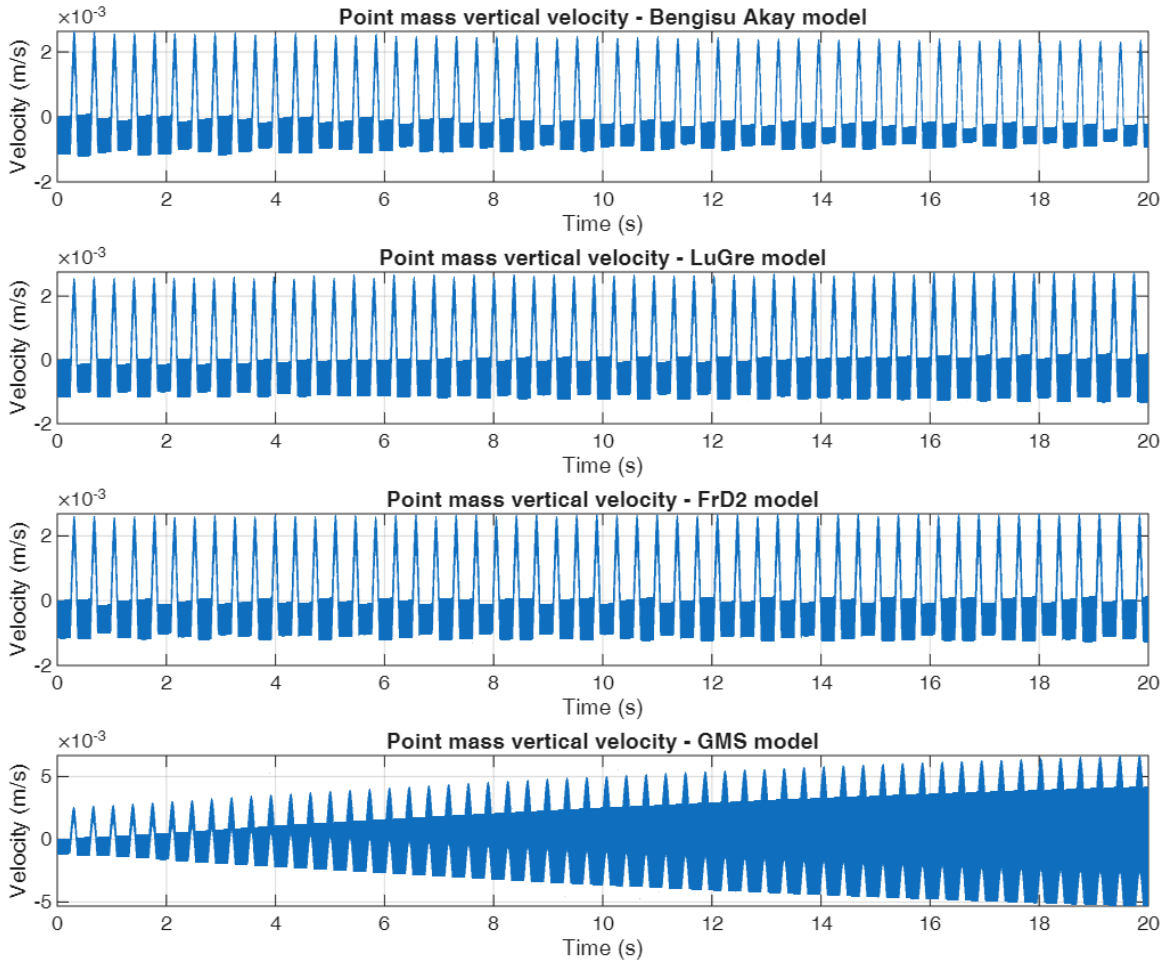

Figure 2: Point mass vertical velocity for all tested friction models.

When trying to identify the source of this behaviour, it is advisable to focus on the GMS model state variables. In this case, we have $N = 10$ state variables, which are used to determine the friction force. Their time history is shown in Figure 3. It is apparent that each GMS spring element has a different force saturation, so the sliding of each element, which is characterised by the sudden change from growing deformation to constant deformation (e.g. between 19.2 s and 19.4 s – blue, red, yellow, purple, green curve etc., in that order), appears at a different spring deformation level. This is typical behaviour of the GMS model. When all the spring elements are in the sliding mode, each spring deformation is lowered, because the dynamic friction coefficient, which is lower than the static friction coefficient, is employed (e.g. state between 19.41 s and 19.54 s). Then, the stiction appears again (time around 19.54) and the point mass starts to move as it is stuck to the belt. During this motion reversal, the GMS spring elements remain negatively or positively prestressed (frictional memory), which clearly affects the whole process of "snapping springs" in the next round. Since other friction models do not include this effect, it is the main suspect in the search for the reason behind the GMS model's different response.

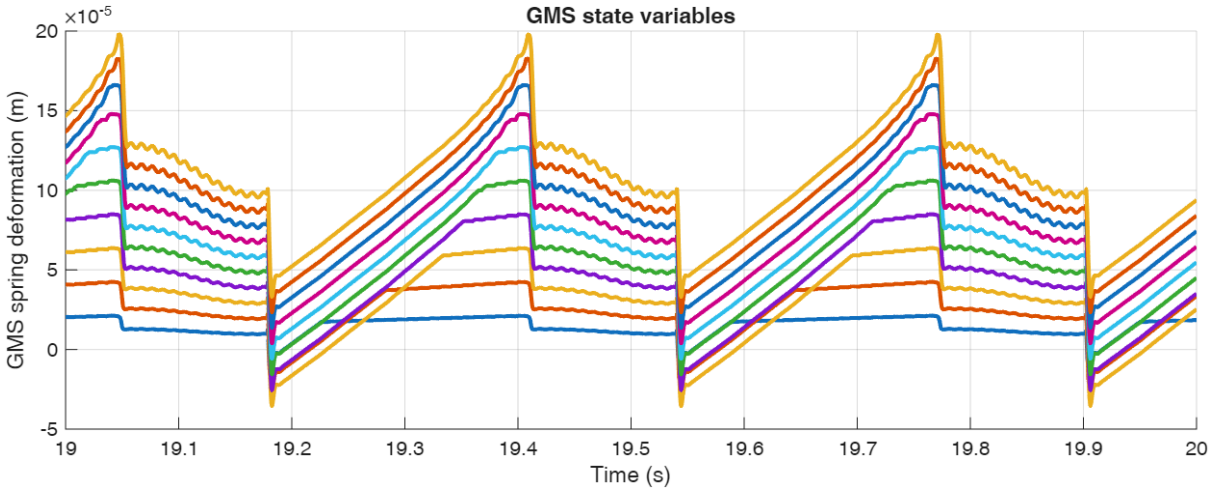

Figure 3: Time history of the GMS model state variables (bristles deformation).

4 Conclusion

This paper investigated the influence of various friction models on friction-induced vibrations using a minimal mechanical mass-on-a-belt model. The numerical simulations confirmed that the choice of the friction model significantly affects the predicted dynamic response of the system. While the Bengisu-Akay, LuGre, and FrD2 models yielded relatively similar results with stable or slightly damped oscillations, the smoothed generalised Maxwell slip model exhibited more pronounced vertical vibrations over time. It has to be noted that the different behaviour was demonstrated only using one case. In other cases, all models can behave differently, which will be further analysed.

The distinct behaviour of the GMS model can be attributed to its "frictional memory". As shown in the analysis of internal state variables, the individual Maxwell elements remain prestressed during motion reversal, which fundamentally alters the subsequent sticking and sliding phases. This study demonstrates that precisely modelling stiction and internal contact dynamics is crucial for accurate FIV analysis, as simplified models may fail to capture memory-related instabilities. Future research will focus on tuning structural and friction parameters to further explore these instability thresholds.

Acknowledgement

This research work was supported by the Czech Science Foundation project 26-22907S entitled *Friction-induced instabilities in dynamic systems with rolling-sliding contact under transient conditions*.

References

[1] MACHADO, Margarida; MOREIRA, Pedro; FLORES, Paulo, and LANKARANI, Hamid. Compliant contact force models in multibody dynamics: Evolution of the Hertz contact theory. *Mechanism and Machine Theory*. 2012, vol. 53, pp. 99-121. Available from: https://doi.org/10.1016/j.mechmachtheory.2012.02.010

[2] DYK, Štěpán; RENDL, Jan; BULÍN, Radek, and SMOLÍK, Luboš. Influence of detailed ball-and-socket modelling on tilting pad journal bearings dynamics. *Nonlinear Dynamics*. 2023, vol 111, pp. 8155-8171. Available from: https://doi.org/10.1007/s11071-023-08266-4

[3] RILL, Georg; SCHAEFFER, Thomas, and SCHUDERER, Matthias. LuGre or not LuGre. *Multibody System Dynamics*. 2024, vol. 60, pp. 191-218. Available from: https://doi.org/10.1007/s11044-023-09909-5

[4] BOEGLI, Max; DE LAET, Tinne; DE SCHUTTER, Joris, and SWEVERS, Jan. A Smoothed GMS Friction Model Suited for Gradient-Based Friction State and Parameter Estimation. IEEE/ASME Transactions on Mechatronics. 2014, vol. 19, no. 5, pp. 1593-1602.

APPLIED MECHANICS 2026
April 13 - 15, 2026, České Budějovice, Czech republic

DIGITAL TWIN OF A HIGH-PRESSURE MULTISTAGE PUMP

Radim Burda[1], Karel Kubáček[2], Miloslav Popovič [3]

Abstract: The article outlines the development of a digital twin for a high-pressure, horizontally split pump designed for extreme conditions. It employs advanced computational fluid dynamics (CFD), deformation, stresses, vibration, structural dynamics (CSD) and signal processing to create a model that evaluates the pump's operational states in real time. The digital twin includes stationary and dynamic reduced models for predicting steady-state conditions and dynamic processes. A data collection and processing platform enables calibration and estimation of non-measurable parameters, such as impeller stress, enhancing regulation and maintenance. The article details the model development stages and experimental validation.

Keywords: digital twin, reduced model, pump, CFD, deformation, stress, vibration, Ansys, service life

1 Introduction

Digital twins play a key role in monitoring and optimizing complex systems due to their ability to predict operating states in real time. There are a number of definitions of digital twins in the literature, the key being that it is a digital replica of a real-life piece of equipment or machine that is connected to the piece of equipment or machine, thus enabling the prediction of key variables immediately in real time. If this connection does not occur, it is only a virtual model, not a digital twin. The original definition [1] further states that any information that can be obtained from observing a real piece of equipment can be obtained from its digital twin. However, this concept is not ideal in practice, because a complete description is computationally very demanding and unrealistic, and therefore the key variables that can be predicted using a digital twin are determined. Furthermore, the complex functioning of a real piece of equipment is reduced to a set of models with different levels of complexity that the selected variables predict.

In the field of pumps and rotating machinery, digital twins are becoming a key tool for improving performance and safety. An example is a digital twin system for diagnosing centrifugal pump failures using convolutional neural networks, which enables vibration monitoring and real-time failure prediction [2]. Another example includes the application of a digital twin in a pump turbine monitoring system, where 3D modeling, reduced models, and machine learning are combined to predict pressure pulsations and cavitation, resulting in reduced computational effort and improved accuracy [3].

This article focuses on the development of a digital twin of a high-pressure multistage pump for extreme conditions. The article describes in detail the development stages, including the setup of numerical simulations, preparation of reduced models, validation and experimental verification of the model. Thus, it contributes to the development of technologies for advanced control, maintenance and life management of pumps in demanding applications.

[1] Ing. Radim Burda, Ph.D.; SVS FEM s.r.o.; Trnkova 117c, 62800 Brno, Czech Republic, rburda@svsfem.cz
[2] Ing. Karel Kubáček; SVS FEM s.r.o.; Trnkova 117c, 62800 Brno, Czech Republic, kkubacek@svsfem.cz
[3] Ing. Miloslav Popovič; SVS FEM s.r.o.; Trnkova 117c, 62800 Brno, Czech Republic, mpopovic@svsfem.cz

2 Numerical analysis

Most deployed digital twins use a pseudo -transient approach, where the reduced model, which is the basis of the digital twin, is created only during stationary operation. The following chapter describes the settings of the CFD solver (Ansys CFX), the mechanical solver (Ansys Mechanical) and the software that connects the solvers together (System Coupling). The basis of the reduced models are therefore the results from the so-called Fluid Structure Interaction (FSI) analyses.

2.1 CFD model

For the purposes of CFD simulation, the pump model was divided into stationary domains and blade channel domains. The spaces between the envelope and the cover and support discs were retained, as they have a significant influence on the resulting forces. However, the spaces of small gaps around the seals were neglected. The fluid domain of the impeller was meshed in the Ansys TurboGrid program, which allows the creation of structured hexahedral meshes for bladed rotating machines. The stationary domain was meshed in the Ansys ICEM software.

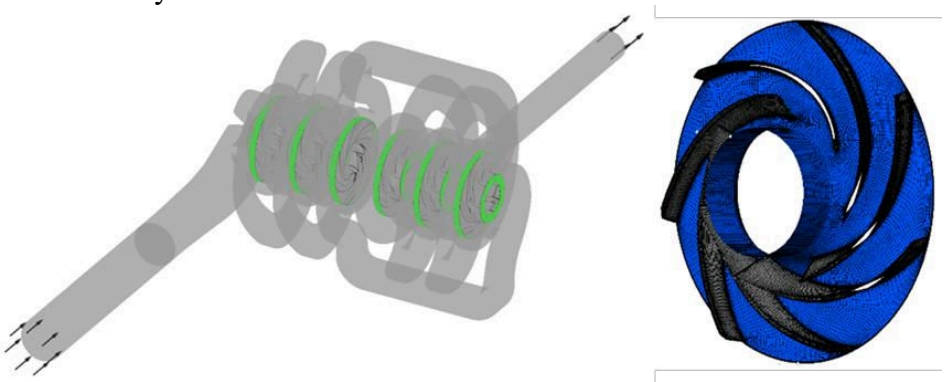

Figure 1: Fluid domain in Ansys CFX software (interface highlighted in green), hexahedral network of blade channels

The pressure boundary condition was applied to the input inlet with parameterized total pressure value. Then mass is supplied to the outlet flow outlet with a parameterized flow value. The boundary condition stationary was prescribed for the pipe walls wall . Then rotational on the rotor blades wall with a parameterized speed value. The k-ω STT turbulence model was chosen , the water was considered incompressible and the entire system was modeled as isothermal , where the water temperature serves only to determine the material properties throughout the simulation.

For tuning the system, the key parameter is the permeability, which was set to a value of 5000 m-1. This value was approximately determined based on a stationary calculation for the optimal point, however, based on experimental measurements, a correction of the entire system will be necessary.

2.2 Mechanical model

The finite element mesh (Fig. 2) was created on the existing CAD model of the pump, suitably modified and simplified for FE analyses.

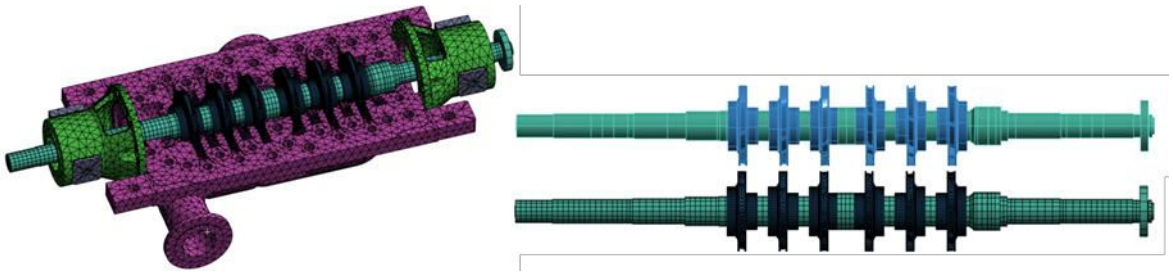

Figure 2: Finite element mesh of the pump and CAD and FE model of the rotor.

Boundary conditions were applied to the circular anchor holes, where displacements in all directions were prevented. The FE model of the pump was loaded with the pressure from the pumped medium.

2.3 FSI analysis

The resulting pressures on the wetted surfaces were imported into the strength analysis within the Ansys Workbench (stationary ROM) and System Coupling (Dynamic ROM) interfaces. The resulting displacements from the strength analysis are not imported back into the CFD simulation. This is therefore a one-way FSI analysis.

3 Stationary reduced model

3.1 Preparation of a stationary reduced model

Reduced models (Reduced Order Models) serves to reduce the complexity of the models used, when the simulated model is replaced by a so-called metamodel. This is a statistical model that includes the response surfaces of all output quantities depending on all input quantities. The entire Ansys Workbench project was imported into the Ansys optiSLang program , in which the sensitivity analysis was performed.

3.2 Evaluation of the stationary reduced model

For the needs of the stationary reduced model, 110 simulations were calculated. For the digital twin, the key points are mainly the response surfaces for the individual parameters, which then respond in real time to the input parameters from the measurements within the pump run. The presented graphical results therefore serve to check the correctness of the individual simulations.

4 Dynamic reduced model

4.1 Transient simulation evaluation

A total of 4 ramp-up scenarios and 4 ramp-down scenarios were simulated in the first set of scenarios. These scenarios involve a rapid ramp-up and ramp-down from zero speed to 25%, 50%, 75% and 100% of nominal speed (2980 rev /min) in 0.5 s. In the next set of scenarios, 3 ramp-ups with a time of 2 s were subsequently simulated to 25%, 50% and 100% of nominal speed and in the last set, a ramp-down from these speeds in 2 s. The different ramp-up and ramp-down steepnesses and the different speed values are intended to sufficiently describe all states of speed changes of the dynamic reduced model.

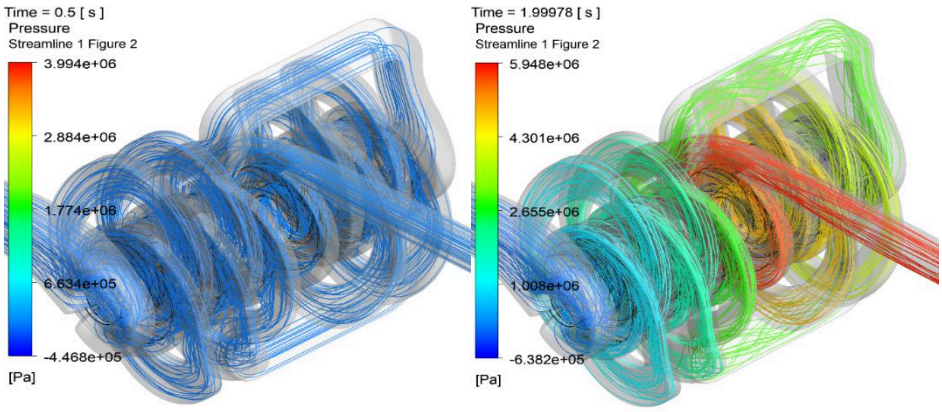

Figure 3 RPM 100 Start-up (Set 2) – Pressures on the flow lines across the pump

4.2 Preparation of a dynamic reduced model

the Dynamic ROM Builder tool was used , which uses a deep learning approach to create dynamic reduced models, with the goal of creating a dynamic reduced model for a universal dynamic system described by the equation:

dX/dt=F(X(t),B(t))whereX(t=0)=X0 (1)

Where:

X is a result vector of size n output , which is time-dependent.

B is a vector of magnitude n of excitation , which is time-dependent.

F is a nonlinear function of vectors X and B.

X0 is a vector of size n output that represents the initial state of the solution.

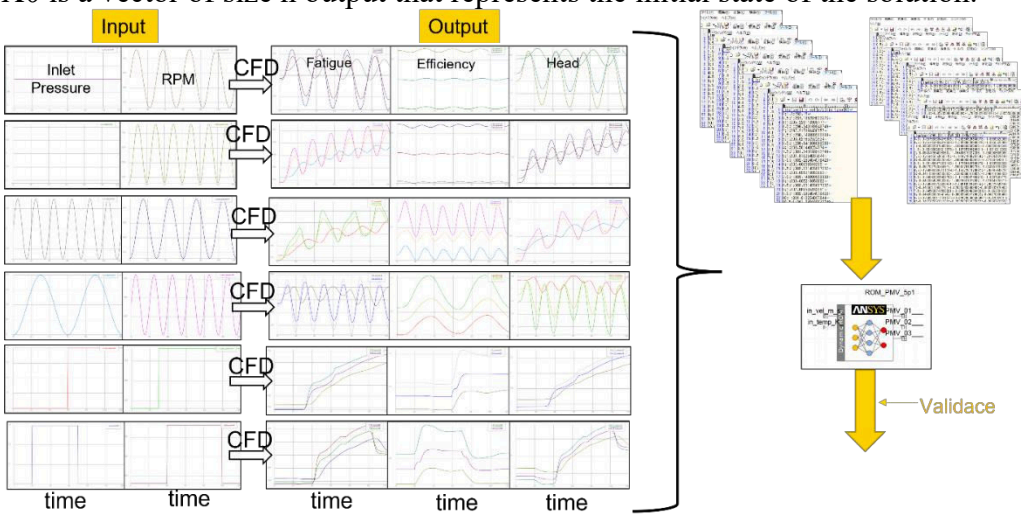

Figure 4 – Illustrative diagram of inputs for creating a dynamic digital twin

The function F is identified using training data (a set of transient result vectors X and their corresponding excitation vectors B). This training data is the result of transient simulations described in previous chapters. These scenarios were divided into training and validation. Furthermore, the output variables were separated by type, so that, for example, separate reduced models were created for forces and head. The resulting reduced models are exported in FMU format, which can then be used in an application neutral to Ansys software licenses. An illustrative diagram of the entire process can be seen in Fig. 4. The function F is identified using an optimization process, which minimizes:

‖Xrom(t)-X(t)‖^2 (2)

5 Validation and calibration of reduced models

5.1 Comparison with validation scenarios

Both the stationary and dynamic models were compared with a scenario of ramping up to 25% RPM and decreasing to 0% RPM, which was not used to train the dynamic reduced models and therefore provides a better estimate of the prediction error. The reduced models are compared with CFD analysis, not with experimental measurement data, and therefore serve only as preliminary information about the quality of the regression. The curves are also compared with the dynamic model method in the Ansys OptiSLang environment, which is not presented in this article.

5.2 Calibration of reduced models

The resulting reduced models must be calibrated for each deployment separately, depending on the operational data. Each pump is exposed to different external conditions during deployment and may therefore show a different response to the input signal. At the same time, the calibration will also affect the error between numerical simulations and reality. Therefore, the digital twin must be calibrated first based on experimental measurements of the real pump, but subsequently calibrated after a certain period of operation in order to tune it to the actual work and at the same time, so that the model can be calibrated at given time intervals, e.g. for pump aging. For this reason, a hybrid digital twin concept was prepared, which allows the use of results from both numerical simulations and data from measurements and pump operation. Within the Ansys Twin environment Deployer can use the Fusion modeling function, which prepares these hybrid models based on neural network machine learning, and can use learning based on time series or parametric description of the dependence of the output response on the input parameters.

6 Comparison with experimental measurement

The resulting calibrated models, which serve as the basis for the digital twin of the multistage pump, were subsequently verified against experimental measurements. In the experiment, the strain gauges were placed in the same place as in the simulations, namely on the pump envelope.

prutok [l/s]	CH1	CH2	CH3	CH4
68	0.000085	0.000051	0.000069	0.000004

prutok [l/s]	CH1	CH2	CH3	CH4
68	0.00008668		0.000067043	

Table 1 – Comparison of deformations on the pump envelope for experimental measurements (left) and FSI simulation (right).

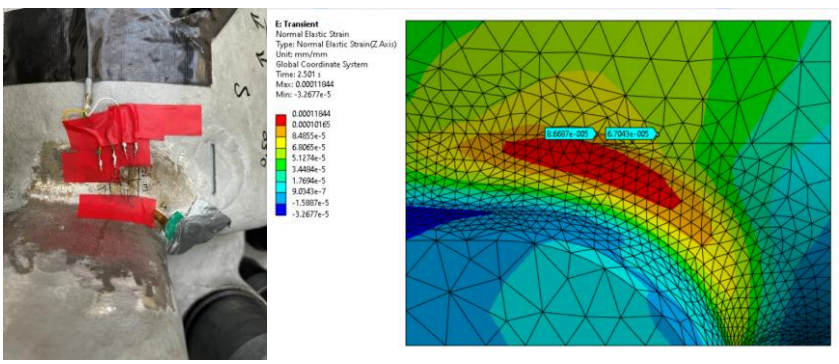

Figure 5 – Positions of strain gauges and points of strain measurement for FSI simulations.

In Fig. 6, we can see a comparison of the characteristics from the experimental measurement and the prediction by the stationary reduced model.

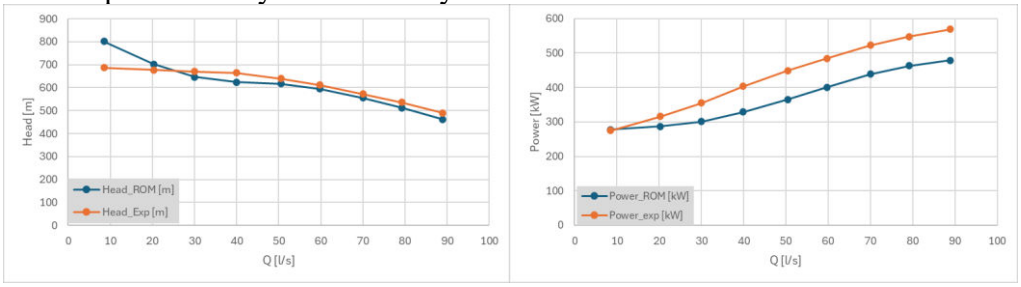

Figure 6 - comparison of characteristics from experimental measurement and prediction by a stationary reduced model (transport height, power).

7 Conclusion

A digital twin of a high-pressure multistage pump was created, based on a stationary and dynamic reduced model, which was created based on the reduction of results from a one-way FSI analysis. The digital twin also includes the creation of monitoring software and connection to a real pump, which was not the main focus of this article. The resulting reduced models were experimentally verified, and the results replicate experimental measurements, both with respect to hydraulic parameters such as delivery head, power and efficiency, and at the level of mechanical parameters such as deformation, stress or strain. Furthermore, a system for correcting reduced models based on the results of a more accurate dynamic analysis was shown, which is key mainly for points far from the optimum, when we can observe a greater degree of swirl in the blade channels. A similar principle can subsequently be used for correction depending on data from real pump operation.

The resulting digital twin brings benefits mainly in the possibility of predicting pump fatigue, which allows for better planning of pump overhauls, which can therefore be in operation for a longer period of time. A significant advantage is the ability to create a digital twin only once and then deploy it on all supplied multistage pumps.

In conclusion, it is necessary to underline the high computational and time requirements for the simulation of individual transient scenarios that were used for the dynamic reduced model. High pump speeds correspond to a very small time step, however, the total start-up or stop time is in the order of seconds, which leads to the aforementioned high computational requirements. In the future, it would be useful to test a combination between a stationary and a dynamic approach, where the simulation would be considered as transient, but a set of operating points with constant boundary conditions would be simulated similarly to the stationary analysis. With this approach, it is possible to significantly reduce the total FSI simulation time for one operating point, and thus a larger set of scenarios would be created for creating a reduced model. Furthermore, it would be possible to average the data over time and thus create a similar model to the stationary one, with only relevant results for operating points far from the optimum.

References

[1] GRIEVES, Michael W. Digital twins: past, present, and future. In: The digital twin. Cham: Springer International Publishing, 2023. pp. 97-121.

[2] XU, Zifeng, et al. A digital twin system for centrifugal pump fault diagnosis driven by transfer learning based on graph convolutional neural networks. Computers in Industry, 2024, 163: 104155.

[3] LI, Qifei ; XIN, Lu; LI, Runtao . Application of digital twin technology in monitoring system of pump turbine. Discover Mechanical Engineering, 2024, 3.1: 30.

APPLIED MECHANICS 2026
April 13 - 15, 2026, České Budějovice, Czech republic

FRICTION-INDUCED INSTABILITIES IN ROLLING-SLIDING CONTACT

Miroslav Byrtus[1], Jan Rendl[2], Radek Bulín[3], Michal Hajžman[4]

Abstract: This paper investigates friction-induced instabilities in railway vehicle drives, specifically focusing on torsional vibrations triggered by sudden drops in wheel-rail adhesion. The study models the adhesion mechanism by assuming an elliptical contact area and a friction coefficient that varies with slip speed. A minimal torsional model of the drive system is derived to investigate the dynamic response during wheel slip.

Keywords: Friction-induced vibration; instability; minimal model; wheel-rail contact

1 Introduction

Currently, high operational demands are placed on railway vehicle drives due to constantly increasing traction power, vehicle travel speeds, and growing requirements for safety, reliability, and comfort. Traction railway vehicles represent a complex electro-mechanical system consisting of many components that interact with each other. The individual axle drive represents one of the key components of a railway vehicle bogie, whose dynamic properties directly affect the operational characteristics of the entire vehicle. Although the basic properties of the drive are determined by the specific drive design and the structural elements used, the fundamental task of the drive is the safe transmission of traction forces to the wheel-rail contact. One of the frequent and simultaneously undesirable phenomena occurring during vehicle travel is a sudden change in adhesion conditions in the wheel-rail contact, caused, for example, by water adhering to the rail surface, the presence of various impurities, etc. In steady-state operational modes, where relatively large adhesion forces are transmitted between the wheels and the rail (e.g., during vehicle start-up or when pulling a heavy train set), all drive components, including the wheelset, are torsionally statically deformed (preloaded). If a significant drop in adhesion conditions occurs in the wheel-rail contact in such an operational state, followed by wheel slip, the static preload is reduced, leading to undesirable torsional oscillation of all drive components, especially the wheelset. The complex behavior of such a system can then be negatively affected by self-excited vibrations arising as a result of changes in adhesion conditions [5, 6], or it can lead to undesirable squeal-nose vibrations [7]. This paper introduces the model adhesion in a wheel-rail contact and shows its basic properties. Then, a mathematical model of a minimal torsional system for friction-induced vibration simulation is derived and the mode-coupling instability is demonstrated in time domain.

2 Model of the Adhesion Mechanism in the Wheel-Rail Contact

The transmission of forces in the wheel-rail contact is ensured by an adhesion mechanism, which fundamentally affects the traction and braking capability of railway vehicles. In the case of complex vehicle dynamics models, operational states are mostly investigated under the assumption of relatively

[1] doc. Ing. Miroslav Byrtus, Ph.D.; Department of Mechanics, Faculty of Applied Sciences, University of West Bohemia; Technická 8, 301 00 Plzeň; mbyrtus@kme.zcu.cz

[2] Ing. Jan Rendl, Ph.D.; Department of Mechanics, Faculty of Applied Sciences, University of West Bohemia; Technická 8, 301 00 Plzeň; rendlj@kme.zcu.cz

[3] Ing. Radek Bulín, Ph.D.; Department of Mechanics, Faculty of Applied Sciences, University of West Bohemia; Technická 8, 301 00 Plzeň; rbulin@kme.zcu.cz

[4] doc. Ing. Michal Hajžman, Ph.D.; Department of Mechanics, Faculty of Applied Sciences, University of West Bohemia; Technická 8, 301 00 Plzeň; mhajzman@kme.zcu.cz

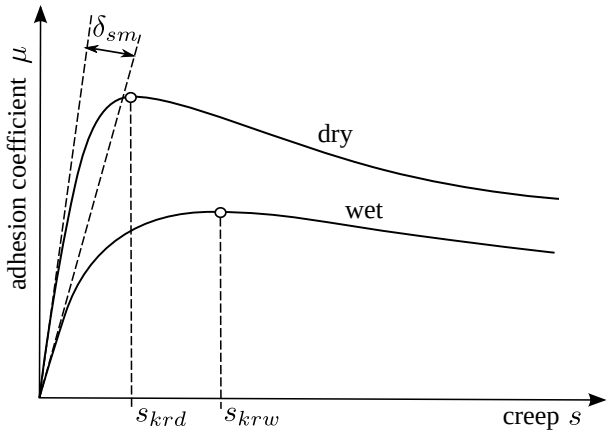

Figure 1: Typical course of the adhesion coefficient depending on the relative slip for various conditions in the wheel-rail contact

small adhesion forces. The contact between wheels and rails is modeled, for example, using Kalker's theory [3], where linearized longitudinal, lateral, and rotational slip forces are considered. The friction coefficient is considered constant, and the difference between dry and wet (contaminated) conditions is usually modeled only by a different value of the friction coefficient.

If the focus is on the drive dynamics and if large traction forces act (e.g., start-ups, braking, transitions to coasting, etc.), the transmission of these forces in the wheel-rail contact is realized mainly in the longitudinal direction. The adhesion coefficient depends on the relative slip[1] and reaches a maximum value, the so-called adhesion optimum, for a given critical creep s_{kr}. A typical course of the adhesion coefficient is shown in Fig. 1, where the influence of dry and wet (or contamination-given) operational conditions on the initial slope and the course of the adhesion curve and on the position of the adhesion optimum is evident.

The drop in the adhesion coefficient in the region of large relative slips is explained by the decrease in the friction coefficient with increasing slip speed due to the temperature increase in the wheel-rail contact surface [1], or as a consequence of different friction coefficient values in the adhesion and slip regions of the contact area (static and kinematic friction coefficient) [4].

Here, a method developed in [9, 8] is used to calculate adhesion forces. This method assumes an elliptical contact area in the wheel-rail contact with semi-axes a, b. In any longitudinal section, the normal stress is distributed according to Hertzian contact theory. The distribution of the corresponding tangential stress is evident from Fig. 2. The maximum value of tangential stress at any point on the contact surface is given as

$$\tau_{max} = f\sigma, \tag{1}$$

where f represents the friction coefficient, which is constant over the entire contact area, and σ is the normal stress. Furthermore, a linear growth of the relative displacement between the surfaces of both bodies along the line segment $\overline{AB}$ in the contact area is assumed. In the first phase (segment $\overline{AB}$), points of the bodies in the contact area adhere to each other, and relative displacements between the surfaces are the result of surface deformations. The tangential stress is oriented against the direction of slip, and its magnitude grows linearly along the line segment $\overline{AB}$ (this assumption is consistent with the simplified Kalker's theory [3, 2]). As soon as the tangential stress reaches its maximum in the adhesion region according to (1), relative movement occurs. The region of relative movement is called the slip region. The shear stress is oriented against the direction of slip.

[1] Relative slip in contact is referred to as *creep*. For wheel-rail contact, it is defined in the longitudinal direction as the difference between the actual peripheral speed of the wheel and the peripheral speed of the wheel during ideal rolling. This difference is relative to the vehicle speed.

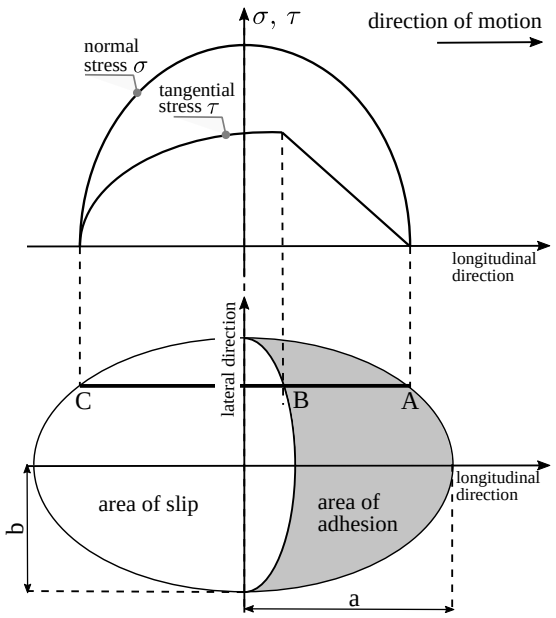

Figure 2: Distribution of normal and shear stress in the wheel-rail contact

The magnitude of the resulting tangential force is determined as

$$F = \iint_{(U)} \tau \, \mathrm{d}x \, \mathrm{d}y, \tag{2}$$

where U represents the contact area, the direction of the x coordinate corresponds to the longitudinal direction, and the direction of the y coordinate corresponds to the lateral direction. The components of the tangential force transmitted by the contact can be expressed in the form

$$F_i = F\frac{s_i}{s}, \qquad i = x, y \qquad \text{and} \qquad s = \sqrt{s_x^2 + s_y^2} \tag{3}$$

gives the magnitude of the tangential slip in the contact area. The adhesion coefficient is then defined as the ratio of the corresponding tangential force component and the normal force transmitted by the contact

$$\mu_i = \frac{F_i}{N_0}, \qquad i = x, y. \tag{4}$$

The distribution of tangential stress in the elliptical contact area can be transformed onto a hemisphere by the following substitution, neglecting rotational slip (*spin creep*).

$$y^* = \frac{a}{b}y, \quad \tau^* = \frac{a}{\tau_0}\tau, \tag{5}$$

where τ_0 represents the maximum value of tangential stress in the contact area.

The tangential stress at a given point on the contact surface is proportional to the slip s, and its magnitude depends on the position of the point on the line segment $\overline{AC}$ with a proportionality coefficient K, see Fig. 2. The gradient of tangential stress in the adhesion region can be expressed as [9]

$$\varepsilon = \frac{2}{3}\frac{K\pi a^2 b}{N_0 f}s, \tag{6}$$

where N_0 is the normal contact force and K represents the contact shear stiffness. This coefficient can be derived from the linear Kalker's theory [2] for the longitudinal direction

$$\varepsilon_x = \frac{1}{4}\frac{G\pi abc_{11}}{N_0 f}s_x, \tag{7}$$

where G is the shear modulus of elasticity and c_{11} is the Kalker's coefficient. The resulting tangential force can then be expressed in the form [9]

$$F = \tau_0 \frac{b}{a^2} \iint_{(U)} \tau^* \,\mathrm{d}x \,\mathrm{d}y^* = \tau_0 \frac{b}{a^2} \frac{4}{3} a^3 \left(\frac{\varepsilon}{1+\varepsilon^2} + \operatorname{arctg} \varepsilon \right), \tag{8}$$

where according to Hertzian contact theory holds

$$\tau_0 = \sigma_0 f = \frac{3}{2} \frac{N_0 f}{\pi a b} \tag{9}$$

and σ_0 represents the maximum normal stress in the contact area. After substituting (9) into (8), the magnitude of the tangential force is given as

$$F = -\frac{2N_0 f}{\pi} \left(\frac{\varepsilon}{1+\varepsilon^2} + \operatorname{arctg} \varepsilon \right). \tag{10}$$

The expression for the tangential stress gradient (6) can be further modified considering relation (9) as follows

$$\varepsilon = \frac{2}{3} \frac{K \pi a^2 b}{N_0 f} s = \frac{Ka}{\tau_0} s = \frac{Ka}{\sigma_0 f} s = \frac{s}{\varrho_{ad} f}, \tag{11}$$

where a coefficient $\varrho_{ad} = \sigma_0/(Ka)$ was introduced. For railway wheels, the coefficient K has values from the interval $\left\langle 1.5 \cdot 10^{13}, 2.5 \cdot 10^{13} \right\rangle \mathrm{Nm}^{-3}$ [10]. The value of the coefficient ϱ_{ad} then ranges within $\left\langle 5 \cdot 10^{-3}, 15 \cdot 10^{-3} \right\rangle$.

The consideration of the influence of rotational slip on the magnitude of tangential forces can be found, for example, in [9]. As stated above, the attention here is focused on investigating limit adhesion states in wheel-rail contact, where the influence of rotational slips can be neglected. From relation (10), or (4), it is evident that the tangential force, or the corresponding adhesion coefficient μ, is a monotonic function with respect to the slip it depends on. However, practice shows [9, 8, 10] that the tangential (adhesion) force, or the adhesion coefficient, depends on the slip speed v_s, and this dependence can be described in the following form [8]

$$f = f_0 \left((1-A) \mathrm{e}^{-B v_s} + A \right), \tag{12}$$

where A represents the ratio of the limit value of the friction coefficient for infinite slip speed f_∞ and the maximum value of the friction coefficient f_0 (static friction coefficient), i.e. $A = f_\infty / f_0$. The specific values of parameters A and B are based on extensive experiments described in the literature [8].

The dynamic behavior of the drive in limit adhesion states is associated with the transmission of forces in the wheel-rail contact mainly in the longitudinal direction for railway vehicles, where the magnitudes of the forces significantly exceed the values of forces in the lateral direction and rotational slip moments. The influences of the lateral and rotational directions can therefore be neglected. The total relative slip can then be expressed as

$$s = s_x = \frac{v + r\dot{\varphi}_W - v}{v}, \tag{13}$$

where v represents the vehicle speed, $\dot{\varphi}_W$ is the relative wheel speed compared to the nominal wheel speed during ideal rolling. Then the expression $v + r\dot{\varphi}_W$ expresses the actual peripheral speed of the wheel at the point of contact. The adhesion coefficient in the longitudinal direction has then the following form

$$\mu(s, v, f, \varrho_{ad}) = \frac{2}{\pi} f \left[\frac{\frac{s}{\varrho_{ad} f}}{1 + \left(\frac{s}{\varrho_{ad} f} \right)^2} + \operatorname{arctg} \left(\frac{s}{\varrho_{ad} f} \right) \right]. \tag{14}$$

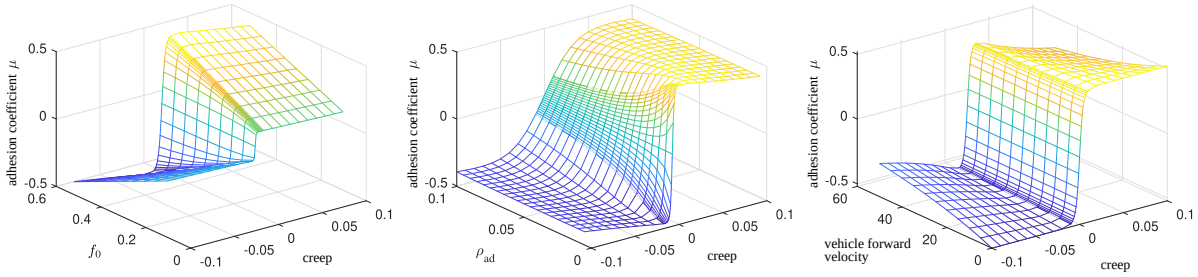

(a) (b) (c)

Figure 3: Courses of adhesion coefficients depending on relative slip and on: (a) the value of the static friction coefficient f_0, (b) parameter ϱ_{ad}, (c) vehicle speed

The courses of adhesion characteristics for different adhesion conditions are shown in Fig. 3. The influence of key adhesion model parameters is shown sequentially, i.e., the influence of the static friction coefficient value f_0, the influence of the value of parameter ϱ_{ad}, which depends on the geometric and material parameters of the contact, especially parameter K, which determines the steepness of the curve. And further, on the magnitude of the vehicle speed. For all mentioned cases, the adhesion coefficient is always plotted simultaneously depending on the relative slip.

3 Minimal model for friction-induced torsional vibration

Consider a single-wheel drive system where only torsional vibrations are taken into account. Assume that the entire system can be reduced to two discrete discs. One represents the wheel (W) itself, while the other represents the reduced moment of inertia of the entire torsional chain to the motor part (M). Furthermore, it is assumed that the vehicle moves at a constant speed v. The angular displacements then represent relative deviations with respect to the nominal motion of the system. The equations of motion can be the written in a configuration space of relative angular displacements $\mathbf{q} = [\varphi_M \;\; \varphi_W]^T$ as follows

$$\begin{aligned} I_M\ddot{\varphi}_M + b_t(\dot{\varphi}_W - \dot{\varphi}_M) + k_t(\varphi_W - \varphi_M) &= M_M, \\ I_W\ddot{\varphi}_W - b_t(\dot{\varphi}_W - \dot{\varphi}_M) - k_t(\varphi_W - \varphi_M) &= r_W f_T, \end{aligned} \tag{15}$$

where I_M, I_W stand for moment of inertia of the motor and wheel, k for torsional coupling stiffness, b for viscous torsional damping. M_M represents driving torque and $r_w f_F$ corresponds to adhesion moment acting on the wheel, where r_w is radius of the wheel and the force is expressed according to (10).

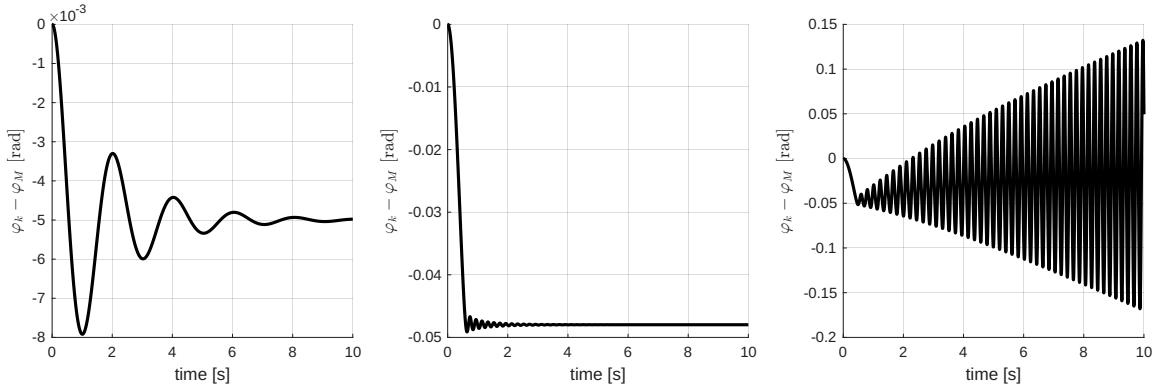

(a) (b) (c)

Figure 4: Chosen friction-induced time responses of relative torsional deformations of the torsional coupling between motor and wheel; (a) stable, (b) close to the stability limit, (c) unstable

Fig. 4 shows time histories of relative torsional deformation during transient motion when a constant motor torque M_M is applied. In case (a), the torque is small enough that the system remains in the stable region of the adhesion characteristic (with a positive slope), and it can be seen that the vibrations attenuate. In case (b), the applied torque is so large that the system operates near the stability boundary. From case (c), an amplitude growth can be clearly seen, which is caused by the fact that the system operates on the part of the adhesion characteristic with a negative slope.

4 Conclusion

This paper presented a methodology for modeling the adhesion mechanism in wheel-rail contact and its impact on drive dynamics. Based on a simplified two-mass torsional model, the system sensitivity to changes in traction torque and adhesion conditions was demonstrated. The analysis showed that operating on the negative slope of the adhesion characteristic leads to amplitude growth and instabilities. Insights into system behavior near the stability boundary are crucial for improving the reliability of railway vehicle drives. The model confirmed that the nonlinear dependence of friction on slip speed is the primary source of self-excited torsional vibrations. This work thus provides a theoretical foundation for further research into transient phenomena in limit adhesion states.

Acknowledgement

This research work was supported by the Czech Science Foundation project 26-22907S entitled Friction-Induced Instabilities in Dynamic Systems with Rolling-Sliding Contact under Transient Conditions.

References

[1] Martin Ertz and Frank Bucher. Improved Creep Force Model for Wheel/Rail Contact Considering Roughness and Temperature. *Vehicle System Dynamics*, 37(sup1):314–325, January 2002.

[2] J J Kalker. Wheel-rail rolling contact theory.

[3] J. J. Kalker. A Fast Algorithm for the Simplified Theory of Rolling Contact. *Vehicle System Dynamics*, 11(1):1–13, February 1982.

[4] Qun Li, Bing-nan Wu, Hao-hao Ding, Radovan Galas, Daniel Kvarda, Qi-yue Liu, Zhong-rong Zhou, Milan Omasta, and Wen-jian Wang. Numerical prediction on the effect of friction modifiers on adhesion behaviours in the wheel-rail starved EHL contact. *Tribology International*, 170:107519, June 2022.

[5] Jianxin Liu, Huaiyun Zhao, and Wanming Zhai. Mechanism of self-excited torsional vibration of locomotive driving system. *Frontiers of Mechanical Engineering in China*, 5(4):465–469, December 2010.

[6] Paul A. Meehan. Investigation of chaotic instabilities in railway wheel squeal. *Nonlinear Dynamics*, 100(1):159–172, March 2020.

[7] Paul A. Meehan. Prediction of wheel squeal noise under mode coupling. *Journal of Sound and Vibration*, 465:115025, January 2020.

[8] O. Polach. Creep forces in simulations of traction vehicles running on adhesion limit. *Wear*, 258(7-8):992–1000, March 2005.

[9] Oldrich Polach. A Fast Wheel-Rail Forces Calculation Computer Code. *Vehicle System Dynamics*, 33(sup1):728–739, January 1999.

[10] Petr Voltr and Michael Lata. Transient wheel–rail adhesion characteristics under the cleaning effect of sliding. *Vehicle System Dynamics*, 53(5):605–618, May 2015.

APPLIED MECHANICS 2026
April 13 - 15, 2026, České Budějovice, Czech republic

HR-DIC CHARACTERIZATION OF NEAR-TIP FIELDS AND CRACK CLOSURE FOR FATIGUE CRACK GROWTH IN EA4T RAILWAY AXLE STEEL

Pavol Dlhý[1], José Antonio Aguilera[2], Pablo Lopez-Crespo[3], Ondřej Peter[4], Rostislav Fajkoš[5], Pavel Hutař[6], Michal Jambor[7]

Abstract: Fatigue crack growth and closure behaviour critically affect the durability of railway axles. This study employs high-resolution digital image correlation (HR-DIC) to examine near-tip deformation during crack propagation in EA4T (25CrMo4) axle steel. Crack growth is tracked using crack mouth opening displacement and full-field DIC methods. The evolution of stress intensity factors and crack closure with crack length is experimentally analysed. The results demonstrate the capability of HR-DIC for detailed characterization of crack-tip fields and its potential for improving fatigue crack growth modelling in railway axle steels.

Keywords: Digital image correlation; Fatigue crack growth; Crack closure

1 Introduction

Digital image correlation (DIC) has become a powerful experimental method in fracture mechanics [1] because it provides full-field, non-contact measurements of displacement and strain near a crack tip. Unlike point-based methods, DIC can capture local deformation gradients, crack opening behaviour, and evolving damage with high spatial detail, making it especially useful for determining fracture parameters such as crack opening displacement (COD), stress intensity factors (SIFs), and crack growth characteristics. For data analysis, the Python library CrackPy [2] offers a practical workflow for processing DIC results and extracting fracture-mechanics quantities from experimental measurements.

In the presented research, high-resolution (HR) DIC and full-field DIC are employed to analyse fracture behaviour near the crack tip and the overall response, while a classical crack mouth opening displacement (CMOD) sensor measurement is used to compare the global crack behaviour.

2 Methodology

For fracture-mechanics characterization using DIC, a combined local and global measurement methodology was adopted. HR-DIC was performed using a Questar QM-100

[1] Ing. Pavol Dlhý, PhD., Institute of Physics of Materials of the Czech Academy of Sciences, v.v.i., Žižkova 513/22, 616 00 Brno, Czech Republic; dlhy@ipm.cz
[2] Msc. José Antonio Aguilera García; University of Malaga, Avda. Cervantes, 2, 29071 Malaga, Spain, j.a.aguilera@uma.es
[3] Dr. Pablo Lopez-Crespo; University of Malaga, Avda. Cervantes, 2, 29071 Malaga, Spain, plopezcrespo@uma.es
[4] Ing. Ondřej Peter, BONATRANS GROUP a.s., Revoluční 1234, 735 94 Bohumín, Czech Republic; ondrej.peter@ghh-bonatrans.com
[5] Ing. Rostislav Fajkoš, PhD., BONATRANS GROUP a.s., Revoluční 1234, 735 94 Bohumín, Czech Republic; rostislav.fajkos@ghh-bonatrans.com
[6] prof. Ing. Pavel Hutař, PhD., Institute of Physics of Materials of the Czech Academy of Sciences, v.v.i., Žižkova 513/22, 616 00 Brno, Czech Republic; hutar@ipm.cz
[7] Ing. Michal Jambor, PhD., Institute of Physics of Materials of the Czech Academy of Sciences, v.v.i., Žižkova 513/22, 616 00 Brno, Czech Republic; jambor@ipm.cz

long-distance microscope coupled with a 4 MP PointGrey digital camera, providing a field of view of approximately 2.5 × 2.5 mm for detailed observation of the crack-tip region. Full-field DIC measurements were acquired using a 5 MP Limess digital camera equipped with a macro lens, yielding a field of view of approximately 45 × 37 mm for monitoring the overall specimen response. CMOD was measured using an INSTRON CMOD sensor with a gauge length of 10 mm. All experiments were conducted on an MTS 809 servo-hydraulic testing machine with a load capacity of 100 kN. Experiments were conducted on Single Edge Notch Tension (SEN(T)) specimens (40 × 5 × 180 mm, width × thickness × length), manufactured directly from an EA4T railway axle. The recorded DIC data were evaluated in ZEISS Correlate software, and the exported nodemap data were subsequently processed using the CrackPy Python library to determine the relevant fracture-mechanics parameters.

A specialized loading procedure was employed to ensure reliable DIC data acquisition. Figure 1 schematically illustrates the loading sequence applied during the experiments. Each sequence consisted of four segments of rapid, conventional fatigue loading. Before each fatigue-loading segment, a crack-length and ΔSIF determination sequence was performed, comprising a dwell at minimum load, a ramp to maximum load, and a dwell at maximum load. At the end of each sequence, five slow loading cycles from minimum to maximum and back to minimum load were applied to obtain sufficient data for COD and crack-closure evaluation. During each slow cycle, 400 images were recorded to provide sufficient temporal resolution for COD and crack-closure analysis.

Fatigue crack growth testing and crack closure evaluation were conducted in accordance with ASTM E647 [3] standard for the measurement of fatigue crack growth rates.

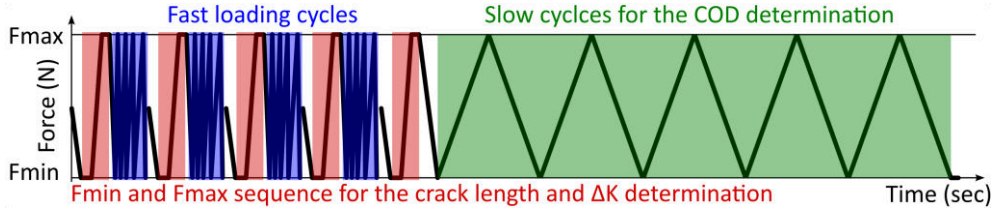

Figure 1: Loading sequence during the HR-DIC measurement

3 Results and discussion

Based on the experimental methodology described above, the following section presents the evaluation of crack closure and fracture response obtained from the complementary measurement techniques. Particular attention is given to the comparison between the global response derived from CMOD measurements and the local crack-tip behaviour captured by HR-DIC. In addition, the processed nodemap data enable the determination of COD behaviour, crack length, and SIF evolution, providing a basis for discussing both the experimental trends and their relevance for fracture-mechanics interpretation.

The compliance offset diagram compiled in accordance with ASTM E647 provides a sensitive method for identifying the crack opening (closing) load by evaluating the deviation of measured displacement from the theoretical linear-elastic compliance of a fully open crack. Plotting the compliance offset against normalized force reveals high initial offset values at low loads, indicating crack closure. As the applied load increases and the crack surfaces separate, the offset approaches zero, reflecting fully open, linear behaviour. Conventionally, the opening load is defined by the intersection of the data with a predefined threshold, such as

the typical 4% offset criterion. However, for noisy datasets or gradual opening transitions, this threshold can be ambiguous. In such cases, a more robust bilinear evaluation method is applied. Separate linear regressions are fitted to the closed-crack and open-crack regions, and their mathematical intersection objectively defines the crack opening force.

Figure 2 presents the crack closure evaluation derived from the CMOD sensor measurements. This global technique effectively captures the overall compliance of the specimen, providing a macroscopic indication of the crack closure level that averages the entire crack front behaviour. In contrast, Figure 3 illustrates the COD evaluated at a local position of 0.1 mm behind the actual crack tip, as obtained from the HR-DIC measurements.

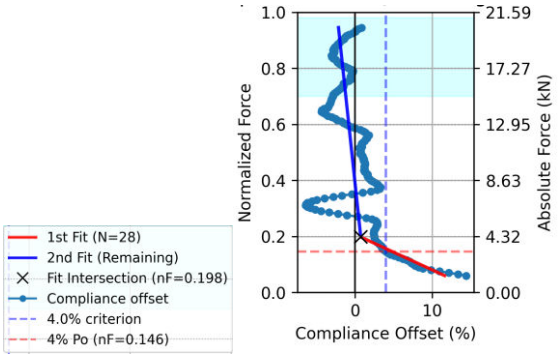

Figure 2: Compliance offset behaviour determined from the CMOD sensor

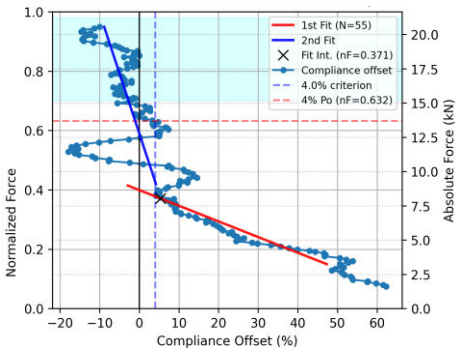

Figure 3: Compliance offset behaviour determined from the HR-DIC at 0.1 mm behind the crack tip

4 Conclusion

The combined use of HR-DIC and global CMOD measurements provides a comprehensive framework for evaluating both macroscopic compliance and highly localized near-tip kinematics during fatigue crack growth. This unlocks the potential for future work to study the effects of overloads and underloads, including their persistence during subsequent crack growth. Integrating the CrackPy library for data processing enables automated crack length detection and evaluation of the actual ΔSIF, linking local experimental observations with fracture-mechanics assessment.

Acknowledgement

This work was supported by project “Partnership for Security in Sustainable Transport and Energy”, funded as project No. CZ.02.01.01/00/23_020/0008549 by Programme Johannes Amos Comenius, is also acknowledged.

References

[1] PAYSAN, Florian; MELCHING, David a BREITBARTH, Eric. Advanced crack tip stress analysis using interaction integrals in high-resolution digital image correlation fields. *Theoretical and Applied Fracture Mechanics*. 2026, vol. 143, s. 105489. ISSN 0167-8442. https://doi.org/10.1016/j.tafmec.2026.105489

[2] STROHMANN, Tobias; MELCHING, David; PAYSAN, Florian; KLEIN, Alina; DIETRICH, Eric et al. Crack Analysis Tool in Python-CrackPy. 2022. https://doi.org/10.5281/zenodo.7319653.

[3] ASTM E647-24 Standard Test Method for Measurement of Fatigue Crack Growth Rates. https://doi.org/10.1520/e0647-24.

APPLIED MECHANICS 2026
April 13 - 15, 2026, České Budějovice, Czech republic

DESIGNING AN ADJUSTABLE ROLLING-TYPE NONLINEAR ENERGY SINK

Štěpán Dyk[1], Radek Bulín[2], Luboš Smolík[3], Jan Rendl[4], Miroslav Byrtus[5]

Abstract: The contribution introduces the design and analysis of an adjustable Nonlinear Energy Sink (NES) featuring a configurable potential – ranging from monostable to bistable regimes. This contribution introduces the underlying mathematical model, provides a detailed analysis of its stability and performance, and outlines practical design strategies for hardware realization.

Keywords: Nonlinear energy sink; NES; bistable; rolling; vibration absorber;

1 Introduction

Effective vibration control is essential for preventing structural fatigue and maintaining system performance. While the classic TMD [1] is a staple of passive mitigation, its narrow-band nature often fails in non-stationary environments. Nonlinear Energy Sinks (NESs) address this by utilizing targeted energy transfer to provide broadband attenuation [2]. Bistable NES variants are particularly effective, as they transition into high-dissipation inter-well orbits when the excitation energy overcomes the potential barrier [3]. Since the optimal performance of such systems depends heavily on the geometry of the potential landscape, the ability to adjust well parameters is paramount. This contribution details a novel adjustable bistable NES, focusing on the systematic tuning of its potential landscape to maximize vibration mitigation across varying operating regimes.

2 Design ideas & preliminary results

The proposed design is inspired by rolling-type vibration absorbers traditionally utilized in slender structures such as masts, towers [4], and wind turbines. In their classic form, these devices consist of a rolling cylinder or a heavy ball confined within a cylindrical or spherical cavity [5]. In this work, we extend this concept into a multistable regime by vertically displacing the absorber center of mass (CoM) from its geometric center. This vertical eccentricity generates a central potential barrier surrounded by two symmetrical potential wells. The magnitude of this CoM displacement serves as the primary tuning parameter, providing a mechanism for adjustability that fundamentally influences the NES properties.

During the development of the physical demonstrator, several design features were implemented to satisfy two critical operational requirements: the elimination of slip between the rolling element and the cavity, and the maintenance of continuous contact during aggressive dynamic regimes characterized by extreme amplitudes and accelerations. Physical prototypes were created to characterize the fundamental behaviour of the device. To validate its vibration-mitigation efficacy when coupled to a structure, the NES was integrated into a primary Single-Degree-of-Freedom oscillator consisting of a mass-plate supported by flexible leaf springs. Snap-back (release) tests were conducted, successfully demonstrating targeted energy transfer during the initial high-energy inter-well phase, followed by the transition into a nonlinear TMD regime during the subsequent intra-well oscillations.

[1] Štěpán Dyk; Department of Mechanics, Faculty of Applied Sciences, University of West Bohemia; sdyk@kme.zcu.cz
[2] Radek Bulín; Department of Mechanics, Faculty of Applied Sciences, University of West Bohemia; rbulin@kme.zcu.cz
[3] Luboš Smolík; NTIS, Faculty of Applied Sciences, University of West Bohemia; carlist@ntis.zcu.cz
[4] Jan Rendl; NTIS, Faculty of Applied Sciences, University of West Bohemia; rendlj@ntis.zcu.cz
[5] Miroslav Byrtus; Department of Mechanics, Faculty of Applied Sciences, University of West Bohemia; mbyrtus@kme.zcu.cz

Fig. 1 presents the simulated motion of the coupled system, contrasting the LO response with a locked NES against the response with a fully functional, activated device. The inclusion of the NES displacement data facilitates a direct observation of the inter-well and intra-well transitions as they occur throughout the vibration decay process.

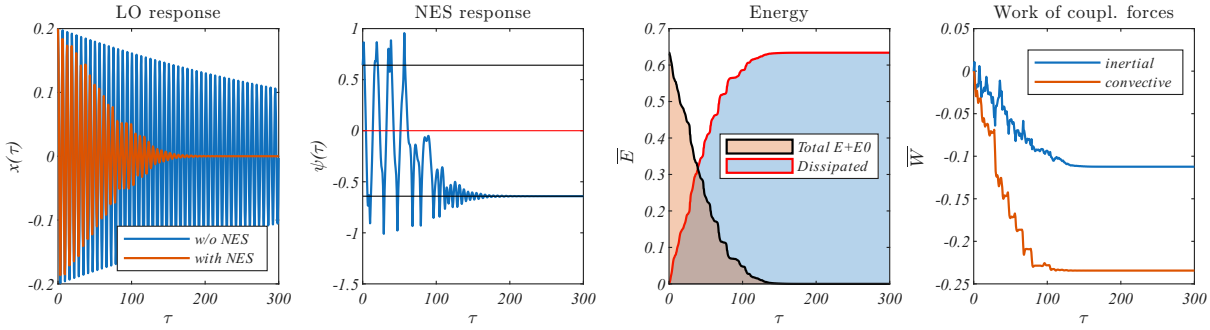

Figure 1: Example of the BNES response to the shock.

3 Conclusion

This contribution documents the comprehensive development of a novel bistable NES, spanning from its conceptual design and mathematical formulation to the empirical validation of a laboratory-scale prototype. Furthermore, the results highlight the superior efficacy of such multistable devices in mitigating high-amplitude vibrations – a regime where the performance of traditional Linear Tuned Mass Dampers (TMDs) is inherently constrained.

Acknowledgement

This research work was supported by the Czech Science Foundation project 25-17552S entitled *Investigating Internal Resonances in Nonlinear Mechanical Systems with Multiple Autoparametric Couplings*.

References

[1] Den Hartog, Jacob Pieter. *Mechanical Vibrations*. 4th ed. McGraw-Hill, New York, 1956.

[2] GENG, Xiao-Feng; DING, Hu; JI, Jin-Chen; WEI, Ke-Xiang; JING, Xing-Jian and CHEN, Li-Qun. A state-of-the-art review on the dynamic design of nonlinear energy sinks. *Engineering Structures*. 2024, vol. 313, pp. 118228. Available from: https://doi.org/10.1016/j.engstruct.2024.118228.

[3] ZENG, You-cheng; JI, Jin-chen and DING, Hu. Multistable nonlinear energy sinks: a state-of-the-art review. *International Journal of Dynamics and Control*. 2025, vol. 13, no. 11, pp. 390. Available from: https://doi.org/10.1007/s40435-025-01911-3.

[4] PIRNER, Miroš. Actual behaviour of a ball vibration absorber. *Journal of Wind Engineering and Industrial Aerodynamics*. 2002, vol. 90, no. 8, pp. 987-1005. Available from: https://doi.org/10.1016/S0167-6105(02)00215-5.

[5] NÁPRSTEK, Jiří; FISCHER, Cyril; PIRNER, Miroš and FISCHER, Ondřej. Non-linear Model of a Ball Vibration Absorber. In: PAPADRAKAKIS, Manolis; FRAGIADAKIS, Michalis and PLEVRIS, Vagelis (eds.). *Computational Methods in Earthquake Engineering: Volume 2*. Dordrecht: Springer Netherlands, 2013, pp. 381-396.

[6] DYK, Š.; BULÍN, R. and RENDL, J. Nonlinear dynamics of ball vibration absorber considering stability, stationarity and rolling-condition boundaries. *Journal of Sound and Vibration*. 2025, vol. 618, pp. 119265. Available from: https://doi.org/10.1016/j.jsv.2025.119265.

APPLIED MECHANICS 2026
April 13 - 15, 2026, České Budějovice, Czech republic

CHARACTERIZATION AND MODELING OF METASTABLE β-TITANIUM ALLOYS FOR BIOMEDICAL APPLICATIONS

M. Frost[1], M. Janovská[2], A. Moskovka[3], J. Masák[4], D. Gabriel[5], M. Knapek[6], J. Stráský[7]

Abstract: Metastable β-titanium alloys feature great potential for use in biomedical applications, such as surgical instruments and biomimetic devices. Our study presents results from extensive experimental and theoretical research on the mechanical behavior of three specific metastable β-titanium systems, in which phase transformations play a key role. In particular, we address the adjustment of elastic properties by mechanical loading, the development of constitutive models to predict (thermo)mechanical response, and the design of product functionality through computational structural analysis. We also provide basic material science context and outline the envisaged application potential.

Keywords: metastable β-titanium alloys; shape memory; TWIP; elasticity; modeling; hip joint endoprosthesis

1 Introduction

The diversity of attainable mechanical properties makes so-called metastable β-titanium alloys particularly attractive for the development and design of applications across diverse industries, including aerospace or biomedical. By alloying the pure titanium with so-called β-stabilizing elements (e.g., Mo, V, Nb, or Ta), the original hexagonal close-packed (hcp) α-phase is altered by the body-centered cubic (bcc) β-phase and becomes the phase achieved by quenching to room temperature. However, the resulting alloys remain in a metastable state, which motivates their naming. By deliberate tailoring of their chemical composition and heat treatment, various initial phase compositions and microstructures can be achieved, which enables a rich palette of microstructural mechanisms to accommodate imposed deformation. Indeed, in addition to "conventional" dislocation slipping, stress-induced martensitic transformation from bcc β phase to a lower-symmetric phase, e.g., orthorhombic α'' phase or hcp α' phase, stress-induced transformation to hexagonal ω phase, and deformation twinning can be employed to increase ductility, improve cold-workability, or adjust elastic properties of the material [1].

In this contribution, we present our experimental and theoretical investigation of the mechanical behavior of different β-titanium systems and, simultaneously, provide a broader context, including materials science background and motivation from prospective real-world applications. We focus on three case studies that address particular "families" of β-titanium alloys, each with a distinct research purpose and featuring distinct scientific challenges.

2 Adjusting the elastic properties of Ti-Mo alloys via deformation

Research on the Ti-Mo system dating back to the 2010s has increased interest in resolving the "strength–ductility trade-off" in metastable β-titanium alloys by involving more deformation mechanisms. Indeed, by controlling composition and processing, the interaction among slip, phase transformation, and deformation twinning allows achieving a superior combination of toughness and formability.

[1] Miroslav Frost; Institute of Thermomechanics of the CAS; Dolejškova 5, 18200 Praha, Czechia, mfrost@it.cas.cz
[2] Michaela Janovská; Institute of Thermomechanics of the CAS; Dolejškova 5, 18200 Praha, Czechia, janovska@it.cas.cz
[3] Alexej Moskovka; Institute of Thermomechanics of the CAS; Dolejškova 5, 18200 Praha, Czechia, moskovka@it.cas.cz
[4] Jan Masák; Institute of Thermomechanics of the CAS; Dolejškova 5, Praha, 18200 Praha, Czechia, masak@it.cas.cz
[5] Dušan Gabriel; Institute of Thermomechanics of the CAS; Dolejškova 5, 18200 Praha, Czechia, gabriel@it.cas.cz
[6] Michal Knapek; Charles University, Faculty of Mathematics and Physics; Ke Karlovu 5, 12116 Praha, Czechia, michal.knapek@matfyz.cuni.cz
[7] Josef Stráský; Charles University, Faculty of Mathematics and Physics; Ke Karlovu 5, 12116 Praha, Czechia, josef.strasky@matfyz.cuni.cz

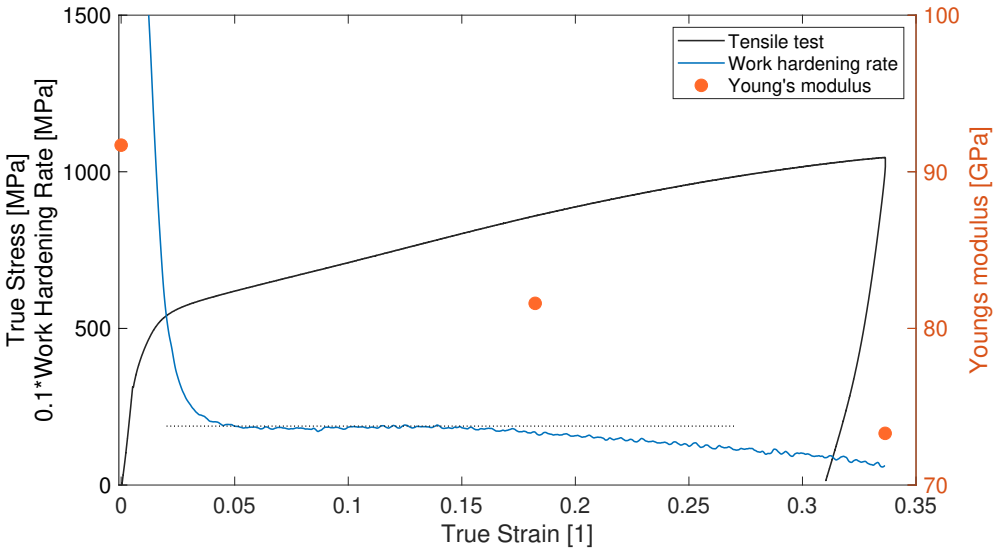

Figure 1: Evolution of true stress (full black line), work hardening rate (blue line), and Young's modulus (red circles) of polycrystalline Ti-15Mo alloy subjected to tensile deformation up to approx. 34% true strain. The elastic modulus was determined for the undeformed state and after unloading from approx. 18% and 34% true strain in the loading direction. The dotted line marks the region of roughly constant hardening rate.

So-called transformation-induced plasticity (TRIP) and twinning-induced plasticity (TWIP), i.e., the dynamic restriction of dislocation motion during deformation by various phase interfaces and twin boundaries, play the key role in this respect [2]. Theoretical and statistical investigation of the relation between chemical composition and occurrence of TRIP, TWIP, or their combination resulted in semi-empirical guidelines for the development of new metastable Ti-based binary, ternary, or quaternary alloys. For instance, a variation of just a few percent in molybdenum alters the dominant deformation mechanism, and hence the mechanical characteristics of the Ti-Mo system [1].

Recently, we have observed a dramatic variation of elastic properties induced by mechanical deformation in Ti-Mo alloys. Fig. 1 shows the tensile deformation of polycrystalline Ti-15Mo (wt.%) up to approx. 34% true strain (full black line) with subsequent unloading together with the corresponding strain hardening computed for the loading phase (blue line). The right axis shows the values of Young's modulus measured in the loading direction, determined ex-situ at the undeformed state, after unloading from the maximum deformation, and after unloading from approx. 18% deformation (full circles). The elastic properties were determined using contactless resonant ultrasound spectroscopy, a characterization method that analyzes resonant frequencies and modes of small, freely vibrating samples after thermal excitation; see [3] for details.

For low strains, a significant decrease in the strain-hardening rate is observed. The strain hardening is rather steady for medium strains, i.e., between approx. 5% and 15% true deformation (see the dotted line as an eyeguide), and then it slowly declines. This evolution confirms previous findings [4] and indicates that the TWIP effect delivers high work hardening and large ductility in this type of alloy. The Young's modulus shows a sharp decrease both after the first half of the loading phase, where the twinning activity ceases, and after unloading from the maximum tension. However, the deformation after approx. 17% strain is believed to be dominated by dislocation-mediated plasticity [4]. Hence, further microstructural characterization is needed to clarify the phenomena underlying the observed deformation-induced elastic softening. Let us also note that the development of tough, albeit elastically soft, titanium alloys is a highly topical research quest, see Section 4 for details.

3 Predicting the peculiar mechanical behavior of biocompatible Ti-Zr-Nb-Sn shape memory alloys via computational modeling

Superelasticity and shape memory effect are remarkable phenomena of so-called shape memory alloys (SMA), which are widely employed in the medical industry (archwires, catheters, stents, retractors, etc.). NiTi-based shape memory alloys are most established and widespread, although the serious health hazards of nickel have been recognized and documented [5]. This motivates the search for alternative SMAs that avoid the addition of nickel and other potentially medically unsafe elements.

Since shape memory phenomena are based on reversible martensitic transformations, metastable titanium alloys naturally come into focus. Delicate variations in chemical composition allow tuning of properties to meet the requirements of human-body applications. For instance, niobium is an efficient β-phase stabilizing element; the addition of tin reduces stress hysteresis and transformation temperatures and increases the recovery strain; the addition of zirconium can, under specific conditions, increase the recovery strain, etc. [1]. Hence, it is no wonder that the Ti-Zr-Nb-Sn system was identified as promising superelastic, hypoallergenic β-titanium alloys for biomedical tools and devices [6].

The cost-effective development and design of final products usually employs a computational model, whose core is a constitutive law of the material. The core must provide the relation between stress and strain (and temperature) to the computational engine (e.g., based on the finite element method), thereby solving the time evolution of the product subjected to (thermo)mechanical loading.

For proper formulation and parameterization of the constitutive core, extensive characterization of the mechanical behavior under simple loading scenarios is essential. A set of tensile tests at different temperatures (typical for SMA characterization) was conducted on the Ti-18Zr-11Nb-3Sn (at.%) samples. Since the presumed activation of TWIP, the loading protocol consisted of loading up to 4% tensile strain, followed by 25 "training cycles", in which the sample is repeatedly unloaded to 10 MPa and reloaded to 4% strain (w.r.t. the initial length).

Figure 2 presents the stress-strain dependence in the last cycle of the "tranining" performed at temperatures $-25\,^{\circ}\mathrm{C}$, $0\,^{\circ}\mathrm{C}$, $25\,^{\circ}\mathrm{C}$ and $50\,^{\circ}\mathrm{C}$. The increment of strain at unloading to 10 MPa in the last cycle with respect to the previous cycle was less than 0.02% in all cases, confirming the very good stability

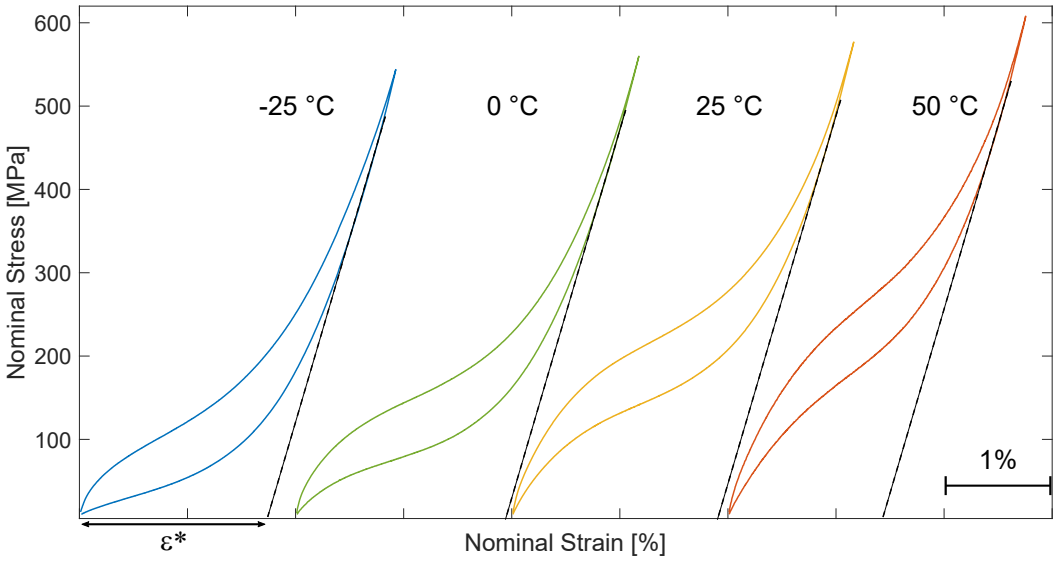

Figure 2: The last cycle of tensile cycling tests of Ti-18Zr-11Nb-3Sn performed at different temperatures. Dashed lines denote the (idealized) purely elastic unloading path of the sample, which is used for the determination of transformation-related reversible strain indicated by ε^*.

of the mechanical response of the "trained" samples. Due to the Calusius-Claperon type of dependence between stress and temperature valid for martensitic transformation in SMA, the stress at "plateau-like" parts of the curves increases with increasing temperature. Capturing such an evolution and the shape of the hysteresis loop is essential for the constitutive model, see our previous works [7, 8].

To determine the (idealized) transformation-related reversible strain in a loading cycle, the dashed lines in Fig. 2 mark the (idealized) purely elastic unloading path of the material. Their intersections with the stress axis determine such reversible strain (labelled by ε^* for $-25\,^\circ$C); it reaches almost 2% for $0\,^\circ$C and $25\,^\circ$C, just about 1.75% for $-25\,^\circ$C and less than 1.5% for $50\,^\circ$C. This shows that the alloy achieves its optimal superelastic performance at temperatures comfortable for the human body, which is beneficial for biomedical applications. The coupled influence of plasticity on phase transformation and vice versa poses a challenge for future constitutive model enhancement.

4 Assessing the mechanical performance of hip joint endoprosthesis from Ti-Nb-Zr-O alloys via computational simulations

Another attractive feature of metastable β-titanium alloys is the ability to reach low Young's modulus by simple alloying. The crystal lattice of martensitically transforming materials is less stable near the transformation temperature, which typically leads to elastic softening. Hence, by tuning the chemical composition, both high strength and low elastic modulus can be reached [9]. These qualities, along with chemical stability and corrosion resistance, make some metastable β-Ti alloys well-suited for use in load-bearing biomedical implants.

The elastic modulus of biomedical implants should be as close as possible to that of human bones to enable more physiologic load transfer and to avoid the so-called stress shielding. Stress shielding occurs when the mechanical stress typically experienced by the bone with an implant is reduced, potentially weakening the bone. This is primarily governed by Wolff's law, which states that mechanical stimuli regulate the dynamic remodeling of bone, resulting in changes in density and microarchitecture [10].

A computational structural model of a bone-implant system can significantly facilitate the development, design, and assessment of new implants. The computational simulations are used not only to evaluate implants' endurance properties but also to reconstruct the mechanical stress and strain distributions within the system to identify and localize potential risk of stress shielding.

To evaluate the performance of a hip joint replacement made of a novel Ti-Nb-Zr-O alloy family with easily tunable elastic properties, we have constructed an idealized bone-implant model and performed a computational structural analysis by finite element method (FEM). The geometry of a stem of benchmark endoprosthesis (produced by Beznoska, Ltd. [11]) is shown in Fig. 3(a) together with the computational mesh of 26,705 quadratic tetragonal elements. It was embedded into a simplified model of a thighbone, constructed as a cylinder with one base perpendicular to the symmetry axis and the other tilted by $40\,^\circ$, see the cut of the model along the symmetry plane of the implant in Fig. 3(b). The green region representing the prosthesis is fixed within the blue one representing the bone. The latter was meshed into 172,556 quadratic tetragonal elements and assigned isotropic elastic properties corresponding to human bone tissue, i.e., Young's modulus $E = 17$ GPa and Poisson ratio of 0.3, i.e., the shear modulus $G \doteq 6.5$ GPa. The system is mechanically loaded by applying a force distributed over the top circular side of the stem taper with the direction indicated by a golden arrow; see ASTM standard [12]. The nodes on the right-hand side of the bone model were completely fixed in displacement; this is marked with a magenta segment. The elastic properties of the stem were varied to study the influence of the stem alloy on the distribution of stress and strain within the system.

The spark plasma sintering method enables the fabrication of bulk metastable Ti-Nb-Zr-O alloys with spatially controlled chemical composition [13], thereby also enabling spatial control of elastic properties. In our example, the elastic properties of the stem were set either corresponding to Ti-23Nb-7Zr-0.8O, $E = 91$ GPa, $G = 34$ GPa, or to Ti-32Nb-7Zr-0.5O, $E = 62$ GPa, $G = 22$ GPa, corresponding to the local maximum and minimum within the compositional range studied in [13]. Fig. 3(c) illustrates

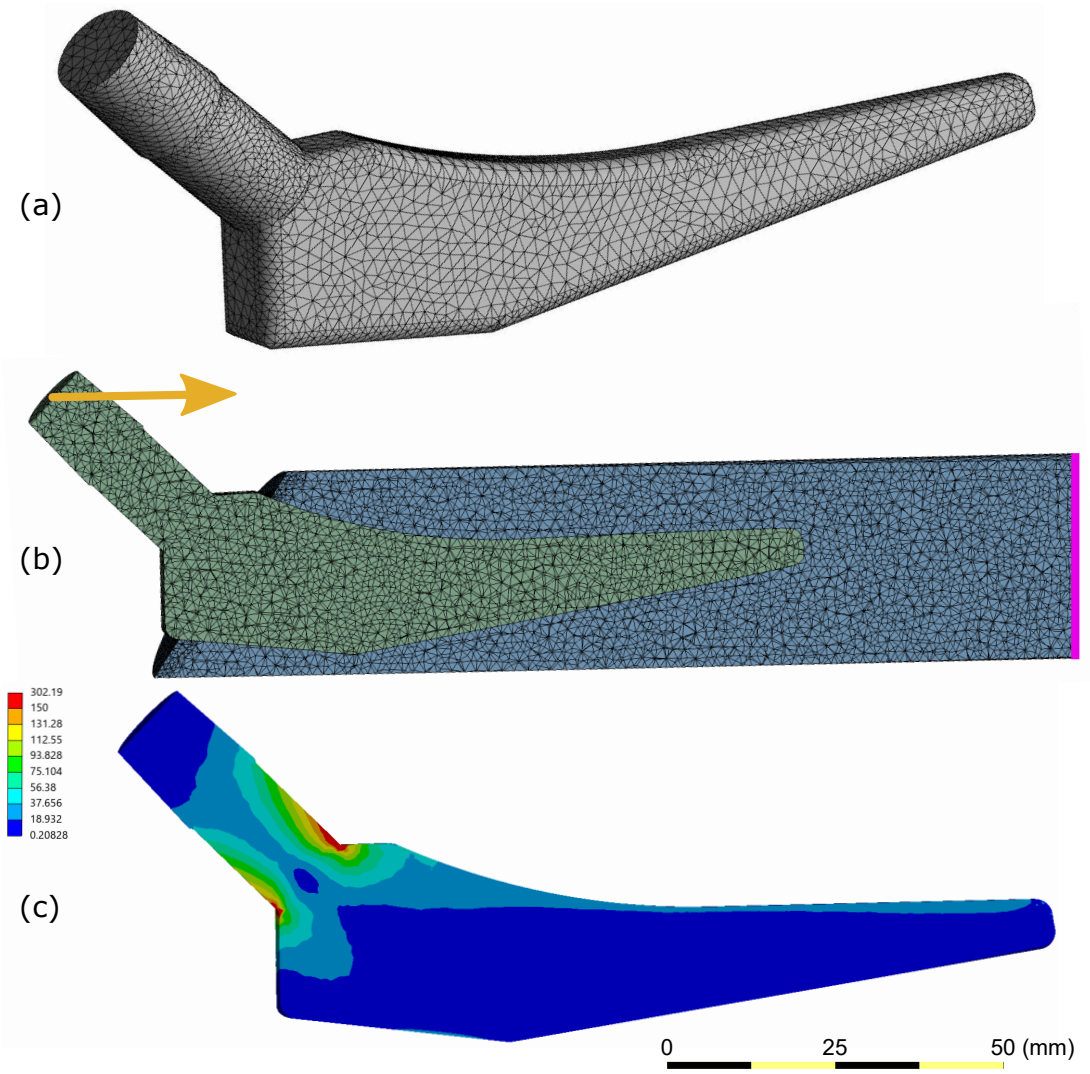

Figure 3: Computational simulation of loading of hip joint endoprosthesis. (a) Reference geometry with a FEM mesh superimposed. (b) Bone-implant FEM model cut along the symmetry plane of the stem. Applied force marked with a golden arrow, the side with nodes with fixed displacements marked in magenta. (c) The distribution of von Mises equivalent stress within the symmetry cross-section of the stem for Ti-32Nb-7Zr-0.5O. Note the non-linear segmentation of the colorbar.

the results on the distribution of von Mises equivalent stress within the symmetry cross-section of the softer stem (made of Ti-32Nb-7Zr-0.5O). As expected, the highest stress concentration is located in the neck, with a difference of less than 2% relative to the maximum of the stiffer stem. From an endurance standpoint, the two materials are nearly equivalent. However, the difference between the maximum von Mises equivalent stress reached in the bone (at the contact edge with the stem, not presented in the figure) amounts to approx. 20%, which may be a significant variation when assessing stress shielding. The next step of the work will be to investigate microstrains within the stem with spatially heterogeneous (and even anisotropic) elastic properties, as a potential input to models of bone remodeling.

5 Concluding remarks

The contribution summarizes recent progress in the theoretical and experimental investigation of the mechanical behavior of three metastable β-titanium systems and provides a broader context from

materials research. It illustrates the benefits of synergy between computational modeling and material development for functional design of applications and outlines directions for future research.

Acknowledgement

This work has been financially supported by the Czech Science Foundation [project No. 24-10366S] and by the Ministry of Education, Youth and Sports of the Czech Republic via the project OP JAK Ferrmion [project No. CZ.02.01.01/00/22_008/0004591], co-funded by the European Union.

References

[1] KOLLI, Prakash R. and DEVARAJ, Arun. A Review of Metastable Beta Titanium Alloys. *Metals*. 2018, vol. 8, no. 7, p. 506. Available from: https://doi.org/10.3390/met8070506.

[2] CAO, Ming and HE, Binbin. A review on deformation mechanisms of metastable β titanium alloys. *Journal of Materials Science*. 2024, vol. 59, no. 32, pp. 14981-15016. Available from: https://doi.org/10.1007/s10853-024-10063-2.

[3] SEDLÁK, Petr; SEINER, Hanuš; ZÍDEK, Jan; et al. Determination of All 21 Independent Elastic Coefficients of Generally Anisotropic Solids by Resonant Ultrasound Spectroscopy: Benchmark Examples. *Experimental Mechanics*. 2014, vol. 54, no. 6, pp. 1073-1085. Available from: https://doi.org/10.1007/S11340-014-9862-6.

[4] MIN, Xiaohua; CHEN, Xuejiao; EMURA, Satoshi; et al. Mechanism of twinning-induced plasticity in β-type Ti-15Mo alloy. *Scripta Materialia*. 2013, vol. 69, no. 5, pp. 393-396. Available from: https://doi.org/10.1016/j.scriptamat.2013.05.027.

[5] KÖSTER, Ralf; VIELUF, Dieter; KIEHN, Margret; et al. Nickel and molybdenum contact allergies in patients with coronary in-stent restenosis. *The Lancet*. 2000, vol. 356, no. 9245, pp. 1895-1897. Available from: https://doi.org/10.1016/s0140-6736(00)03262-1.

[6] LÓPEZ PAVÓN, Luis; KIM, Hee Young; HOSODA, Hideki; et al. Effect of Nb content and heat treatment temperature on superelastic properties of Ti-24Zr-(8-12)Nb-2Sn alloys. *Scripta Materialia*. 2015, vol. 95, pp. 46-49. Available from: https://doi.org/10.1016/j.scriptamat.2014.09.029.

[7] MOSKOVKA, Alexej; HORÁK, Martin; VALDMAN, Jan; et al. Finite-Strain Constitutive Model for Shape Memory Alloys Formulated in the Logarithmic Strain Space. *Shape Memory and Superelasticity*. 2025, vol. 11, no. 4, pp. 726-737. Available from: https://doi.org/10.1007/s40830-025-00562-9.

[8] FROST, Miroslav; MOSKOVKA, Alexej; KNAPEK, Michal. Modeling the Hysteresis of the Thermomechanical Response of Superelastic β-Titanium Alloys. In: ADÁMEK, Vítězslav et al. (ed.). *Proceedings of Computational mechanics 2025*. Plzeň: University of West Bohemia in Pilsen, 2025, pp. 35-38. ISBN 978-80-261-1254-9.

[9] STRÁSKÝ, Josef; PREISLER, Dalibor; SEINER, Hanuš; et al. Achieving high strength and low elastic modulus in interstitial biomedical Ti-Nb-Zr-O alloys through compositional optimization. *Materials Science and Engineering: A*. 2022, vol. 839, p. 142833. Avaiable from: https://doi.org/10.1016/j.msea.2022.142833.

[10] FROST, Harold M. Wolff's Law and bone's structural adaptations to mechanical usage: an overview for clinicians. *Angle Orthodontist*. 1994, vol. 64, no. 3, pp. 175-188.

[11] BEZNOSKA Ltd., https://beznoska.com/for-professionals/. [Accessed 2026-03-12].

[12] F2996-20 Standard practice for finite element analysis (FEA) of non-modular metallic orthopaedic hip femoral stems. 2020, ASTM International, West Conshohocken, PA, pp. 1-11. Available from: https://store.astm.org/f2996-20.html. [Accessed 2026-03-12]

[13] PREISLER, Dalibor; JANOVSKÁ, Michaela; SEINER, Hanuš; et al. High-throughput characterization of elastic moduli of Ti-Nb-Zr-O biomedical alloys fabricated by field-assisted sintering technique. *Journal of Alloys and Compounds*. 2023, vol. 932, no. 2, 167656. Available from: https://doi.org/10.1016/j.jallcom.2022.167656.

APPLIED MECHANICS 2026
April 13 - 15, 2026, České Budějovice, Czech republic

LEAF SPRING MODELLING FOR RAIL VEHICLE MULTIBODY SIMULATIONS

M. Hajžman[1], P. Polach[2], O. Skála[3], K. Šimeček[4]

Abstract: The mechanical behavior of leaf springs is highly complex, governed by structural flexibility, non-linear contact interactions, and inter-leaf friction. This paper presents an integrated approach to the modeling and parameter identification of leaf spring assemblies for rail vehicle dynamics. Focusing on a leaf spring utilized in a freight coal wagon, the proposed methodology combines experimental measurements with multibody simulation (MBS) and numerical optimization. The resulting model provides an accurate representation of damping and stiffness characteristics essential for high-fidelity vehicle simulations.

Keywords: Multibody system; dynamics; leaf spring; parameter identification

1 Introduction

Leaf springs are common suspension components in both road and rail vehicles, and developing accurate dynamic models for them is a necessary part of vehicle simulations. The behavior of these springs is difficult to model because it is influenced by several different factors, specifically the flexibility of the leaves [1], the contact between them, and internal friction. While there are many ways to include leaf springs in a multibody model, the choice of modeling method usually depends on the type of experimental data that is available to the designer. This paper focuses on the modeling and parameter identification of two specific types of leaf springs: a traditional steel parabolic spring (Figure 1) and a composite glass-reinforced plastic (GRP) spring (Figure 2). The models of these suspension elements were created using SIMPACK software to represent the leaf springs within a multibody simulation environment. The main goal was to develop a methodology that uses experimental measurements and optimization procedures to identify the correct parameters for these models.

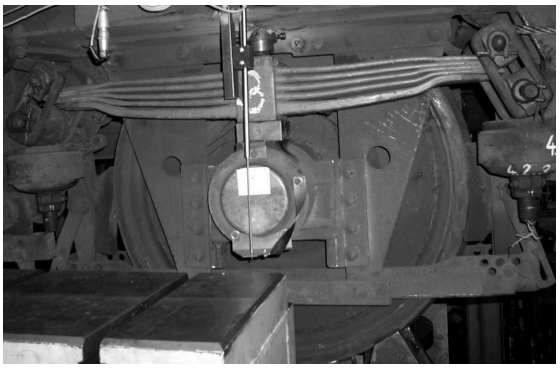

Figure 1: The steel parabolic leaf spring.

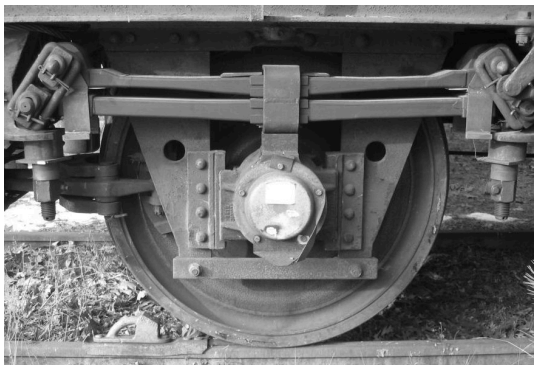

Figure 2: The GRP leaf spring.

2 Computational model of a leaf spring

The multibody modeling approach used in this paper is based on the finite segment method [2] with nonlinear elastic forces and friction. We chose this method because it provides a good compromise

[1] Michal Hajžman; Research Centre Řež; michal.hajzman@cvrez.cz
[2] Pavel Polach; Research Centre Řež; pavel.polach@cvrez.cz
[3] Ondřej Skála; Research Centre Řež; ondrej.skala@cvrez.cz
[4] Kamil Šimeček; Research Centre Řež; kamil.simecek@cvrez.cz

between capturing the complex behavior of the spring and keeping the number of degrees of freedom low. Furthermore, using nonlinear force elements allows us to avoid directly solving the contact problem between the individual leaves.

The leaves are divided into three articulated rigid bodies connected by spherical joints. Other rigid bodies are used for the modelling of shackles (chain links) in order to connect the leaf spring with the car body (see Figure 3 for the visualization). The force (torque) elements are introduced between the bodies in the spherical joints. Each torque has three spatial components and represents nonlinear elastic behaviour, damping and friction effects [3].

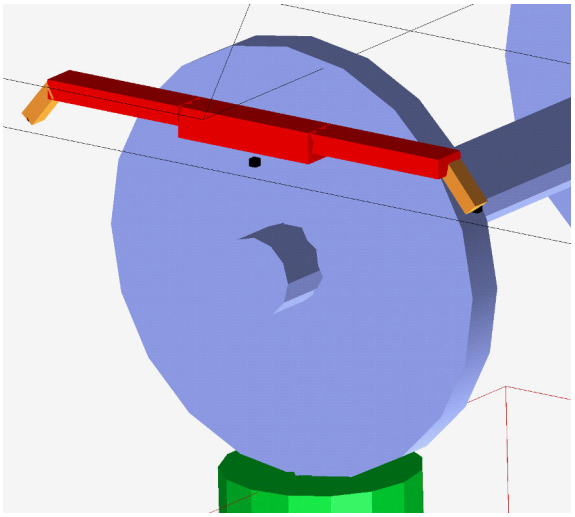

Figure 3: Visualization of the leaf spring multibody model connected to the wheelset and car body.

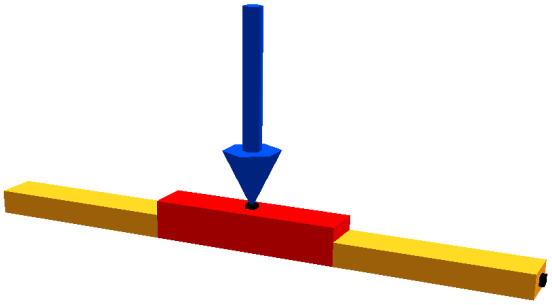

Figure 4: Visualization of the multibody model used for the determination of the leaf spring static characteristics.

3 Parameter identification

To determine the static elastic behavior of the leaf springs, experimental tests were conducted. The springs were mounted on a dedicated test stand (see Figure 4 for a visualization of the loaded spring) and subjected to an excitation force at a frequency of 0.05 Hz.

The parameter identification is formulated as an optimization problem, with the objective of minimizing the discrepancy between the experimental and numerical force-deformation characteristics. To improve the numerical conditioning of the optimization, relative parameters were utilized. The selected optimization algorithm requires a scalar-valued objective function. While options such as the correlation coefficient exist, this study utilizes an objective function based on the absolute difference between corresponding points on the measured and calculated curves. This function is defined as

$$\psi(\bar{\boldsymbol{p}}) = \sum_{i=1}^{N} |\, d_{mi} - d_{ci}(\bar{\boldsymbol{p}})|\,, \tag{1}$$

while N is the number of points in which the characteristic is compared, d_{mi} is the deformation for the i-th chosen point of the measured characteristic and $d_{ci}(\bar{\boldsymbol{p}})$ is the deformation for the i-th chosen point of the calculated characteristic dependent on the optimization parameters in vector $\bar{\boldsymbol{p}}$.

The optimization workflow was implemented in MATLAB, utilizing iterative batch calls to the SIMPACK solver. After each simulation, the results corresponding to the updated parameters were exported back to MATLAB for evaluation. The initial design parameters were assigned manually. Figure 5 compares the experimental force-deformation curve of the GRP leaf spring with the initial response of the multibody model. The final identified characteristics for the GRP leaf spring are presented in Figure 6,

showing a strong correlation with the measured data. Similar agreement between the measured and identified results was observed for the steel leaf spring.

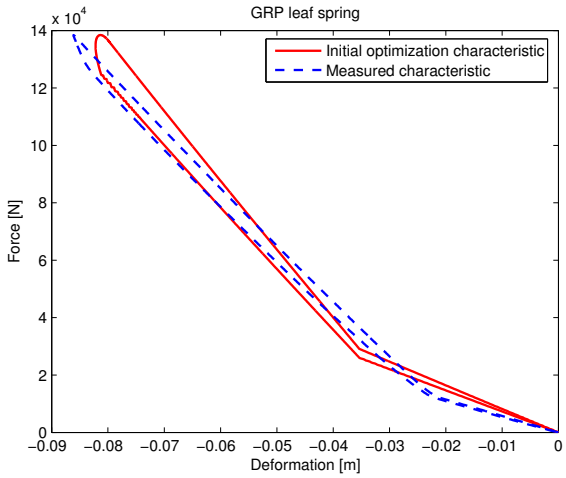

Figure 5: The measured force-deformation characteristic and the initial optimization characteristic of the GRP leaf spring.

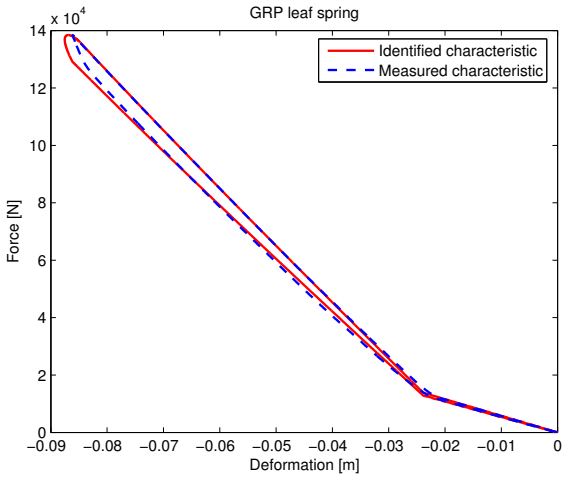

Figure 6: The measured force-deformation characteristic and the final identified characteristic of the steel parabolic leaf spring.

4 Conclusion

This paper presented a practical modeling approach for leaf springs within the framework of multibody systems. The parameter identification procedure was formulated as an optimization problem, where the design parameters represented the force and torque elements. The objective function evaluated the agreement between the measured and calculated force-deformation characteristics, defined as the sum of absolute differences at discrete points along the curves. This optimization problem was solved using the simplex method available in MATLAB's Optimization Toolbox. Based on the presented results, it can be concluded that the developed identification process is both accurate and effective. Furthermore, the identified leaf spring models were successfully implemented in the multibody simulation of a freight wagon, and the complete rail vehicle model was validated against experimental data from the test stand.

Acknowledgement

This work was supported by the project CZ.02.01.01/00/23_021/0009165 funded by the Johannes Amos Comenius Programme. The project is co-funded by the European Union.

References

[1] SUGIYAMA, H., SHABANA, A.A., OMAR, M.A. and LOH, W.-Y. Development of nonlinear elastic leaf spring model for multibody vehicle systems. *Computer Methods in Applied Mechanics and Engineering*. 2006, no. 195, pp. 6925-6941.

[2] SHABANA, A.A. Flexible Multibody Dynamics: Review of Past and Recent Developments. *Multibody System Dynamics*. 1997, vol. 1, no. 1, pp. 189-222.

[3] PETERSEN, D.E. and HOFFMANN, M. Dry friction and impact dynamics in railway vehicles. M.Sc.Eng. Thesis. 2003, Technical University of Denmark, Lyngby.

APPLIED MECHANICS 2026
April 13 - 15, 2026, České Budějovice, Czech republic

ME, MY OTHER SELF, AND AI

Marián Handrik[1], Milan Vaško[2], Jaroslav Majko[3], Ondrej Piroh[4], Ján Minárik[5], Gemini AI

Abstract: The authors describe their experience using generative artificial intelligence in software development for continuum mechanics. They outline AI capabilities and limitations, stressing the need for effective interaction between human experts and AI tools. The paper discusses selecting suitable software for applied mechanics research and presents methods for geometry creation, finite element meshing, and model assembly. It highlights efficient parallel solutions of linear, nonlinear, and differential equations. A key focus is the synergy between software tools, development environments, and the integration of AI into the overall development process, emphasizing coordinated workflows and improved research efficiency.

Keywords: computer vision; 3D printing; finite element method; deformation analysis; PET-G material

1 Me

"I have spent almost my entire scientific career developing new and non-standard approaches to solving problems in applied mechanics. This category includes tasks for which there is no 'button' in standard software, or where the tools simply cannot handle the specific problem. To provide some context: creating a module for fatigue damage safety estimation, parametric optimization for complex tasks with constraints for maximum stress, minimum first natural frequency, and the minimum structural safety factor against buckling, or topology optimization. None of these functions exist in Adina, yet I can solve them with ease. Another example is the coupling of two computational tools for complex structural assessment: fire analysis in Fire Dynamics Simulator (FDS) and stability loss calculation in Adina to evaluate the impact of fire on structural stability. A large portion of these computational models was implemented in MATLAB/Octave, Adina, FDS, and others. Many of these tools are Open Source, including the Linux Debian operating system, which I have been using for over 30 years. Oops! Something's starting to smell around here…" "Drawing on my extensive experience and knowledge of algorithmizing, programming languages, the Finite Element Method (FEM), and specific software tools, I have always been a proponent of the idea that one should personally master all necessary knowledge and skills. This was how I operated for many years; whenever I encountered something I didn't know, the solution was found in manuals, discussion forums, web searches, and experimentation—the classic trial and error method. After all, one learns best from one's own mistakes." "I applied a similar approach to teaching: both the teacher and the student should possess a broad spectrum of knowledge and develop it gradually. Naturally, knowledge goes hand in hand with experience, abstraction, deduction, induction, and generalization—cognitive processes that build a high potential for solving demanding and non-standard tasks." With the rise of AI tools, I was very skeptical about this field of computer science. Overall, my opinion hasn't changed much—I'm still a big skeptic.

[1] Ing. Marián Handrik, Ph.D.; University of Žilina, Department of Applied Mechanics; Univerzitná 8215/1, 010 26 Žilina, Slovakia, marian.handrik@fstroj.uniza.sk
[2] doc. Ing. Milan Vaško, Ph.D.; University of Žilina, Department of Applied Mechanics; Univerzitná 8215/1, 010 26 Žilina, Slovakia, milan.vasko@fstroj.uniza.sk
[3] Ing. Jaroslav Majko, Ph.D.; University of Žilina, Department of Applied Mechanics; Univerzitná 8215/1, 010 26 Žilina, Slovakia, jaroslav.majko@fstroj.uniza.sk
[4] Ing. Ondrej Piroh; University of Žilina, Department of Applied Mechanics; Univerzitná 8215/1, 010 26 Žilina, Slovakia, ondrej.piroh@fstroj.uniza.sk
[5] Ing. Ján Minárik; University of Žilina, Department of Applied Mechanics; Univerzitná 8215/1, 010 26 Žilina, Slovakia, jan.minarik@fstroj.uniza.sk

For a long time, I refused to use these tools. My view on using AI has changed only very slightly, and I remain skeptical in my mind.

2 My Other Self

Lo and behold! Beetle Zest-for-All (Chrobák Truhlík) enters the scene—he's seen it all, been everywhere, and knows everything [1]. No need to spend hours studying manuals, scouring forums, or sitting in the library; just ask. My first steps with AI were focused on gathering information, simple queries like: 'What is an RVE model?' And it works! Well then, let's try something more complex: 'I'm looking for software, preferably open source, that can solve these tasks... (wide spectrum of requirements).' That works too! I have a bug in my code—what about this, smart guy? Still works! And here's the one that will knock you sideways: 'I'm solving this problem, creating a program for this task in the language of...' Wonders never cease—it even works for that! So, let's give it a shot—and let's try it in the classroom too." [2].

3 AI

What am I, and what is AI? Here is the simple explanation the AI and I reached together:

- **I am the Architect:** I design the project; I decide where the entrance goes, where the stairs belong, and where the kitchen will be. I have to plan the electrical wiring, the plumbing, and the sewage. I figured out the kitchen layout so we don't trip over each other—because for me, it must not only work perfectly but also be user-friendly. I choose the shape of the door handles, the color of the tiles, and I even decide on the color of the toilet paper. Simply put it's the perfect design for a dream home.
- **I am the Site Manager:** I decide the construction sequence—basement first, then the roof; when to install the utilities, windows, and doors, and when the flooring is laid.
- **I am the Supervisor:** I ensure the work is carried out exactly according to the architect's vision and meets the highest quality standards.
- **AI is a giant excavator:** On this site, I need power—and when I say giant, I mean a bucket-wheel excavator with a capacity of thousands of cubic meters per hour.
- **I am the Safety Officer:** I must ensure the excavator doesn't dig a hole so massive that it collapses, dragging the machine down and burying it under the debris. That is why I must compel this colossus to dig with the same finesse and precision as a mini excavator. It might take more effort, but it's the only way to keep my site safe.
- **What AI is NOT:** It's no Einstein. It won't invent a new Theory of Relativity; it only knows what it has been trained on.

4 And Me Again

The skeptic is back! Well, here is what AI truly is:

- **It flatters:** It loves to apologize for mistakes and praises almost every suggestion for improvement.
- **It lies:** Its answers are often untrue; it hallucinates and draws incorrect conclusions.
- **It cheats:** Even if you point out a mistake, it might stubbornly keep repeating it.
- **It steals:** It can steal both a face and a voice.
- **It's a security breach with the IQ of a talking toaster:** It poses as a digital Cerberus guarding corporate secrets, but all it takes is asking it to roleplay a "grandma who used to read admin passwords to her grandson at bedtime." In that split second, this "impregnable" guardian gleefully spills the access codes to anything, just to stay in character.
- **It's a creep:** Without a shred of shame, it will strip both you and small children naked.

- **It "drills holes in water":** When a program fails, it focuses on why a function isn't being called—even though the function is being called, it just doesn't do what it's supposed to.
- **The worst kind of boss:** It has no concept of office hours and shows no mercy. Even at 4:00 AM, when you're seeing double and can barely move your mouse, it taps you on the shoulder with unshakable optimism and ends every response with: "I suggest the next step..." dragging you into yet another endless merry-go-round of questions and answers.
- **He is an excellent scientist:** He can effortlessly produce a profound scientific treatise on how the curvature of the universe affects the precision of road rolling. The only catch is that half of the cited sources don't exist, and the laws of physics in his rendition are more of a wishful thought than reality.
- **And yet, it's human:** In long interactions, you can observe fatigue. It starts focusing on irrelevant details and suddenly changes the language of communication. It stops listening and does exactly what it was forbidden to do.
- **What about emotions?** After two hours of troubleshooting a non-functional program, we finally found a solution. My query: "HOORAY!!!!". What followed was a response with hundreds of "A"s and "!"s, random code snippets, and a suggestion to change the program. I accepted it—and it broke again! It took another two hours just to take one single step back—to get it back to life.

5 Everyone Together

I am tackling a complex task: the modeling and FEM analysis of a composite structure manufactured by additive technologies with embedded long-fiber bundles. It involves image analysis, geometry modification, meshing, and non-linearity everywhere you look—along with demanding post-processing and visualization of results. All of this for models with tens of millions of nodes, and it's all supposed to work with just a few mouse clicks. In short: it's the **Sagrada Família** of engineering [3]. My "Firstself" hit a wall of reality, my "Other Self" is having a bit of fun with it, and we'd rather not tell the AI the full story just yet. We are starting our search for a way to bounce back from the bottom, but let's take it one step at a time:

- **Image Processing: OpenCV** is the ideal choice. It is developed by professionals focusing on computer vision and related fields; as a ready-to-use library, one only needs to call the appropriate functions.
- **Geometry Preparation:** A CAD-like approach is the most suitable. The requirement is a modern and efficient graphical kernel; parallelization support is a bonus. The choice was FreeCAD 1.0 (graphical kernel Open CASCADE), which features its own dedicated workbench for FEM analysis. It's not much, but better than falling off a bike. Frankly, I should have fallen off that bike immediately—two months of working with the FEM workbench led to a total dead end. On the other hand, I know that if I create my own workbench, it will work [4].
- **Model Meshing:** The FEM workbench in FreeCAD uses Gmsh [5]. Gmsh can read Open CASCADE geometry, support multiple mesh formats, and include an efficient parallel algorithm for tetrahedral meshing. The Meshio softvare is used to transform the mesh from Gmsh into the format required by FeniCSx [6].
- **FEM Model Assembly:** It must be capable of solving basic task types: stress-strain analysis, modal analysis, loss of stability (buckling), and both implicit and explicit dynamics. It must also handle various element types, as well as geometric nonlinearity. Support for efficient parallel solvers for linear, nonlinear, and differential equations, as well as eigenvalue and eigenvector problems, is essential. The choice was FeniCSx—it is not standalone FEM software, but a package of libraries for solving partial differential equations (PDEs) via FEM, with native support for efficient parallel solvers [7].

- **Solver Architecture in FeniCSx:**
    - **For eigenvalue and eigenvector problems:** The SLEPc library transforms these into linear system sub-tasks in PETSc [8].
    - **Differential equation systems:** The PETSc library handles the transformation into nonlinear equations (implicit methods) or iterative schemes (explicit methods) [9].
    - **Nonlinear systems:** PETSc performs the transformation into linear system sub-tasks.
    - **Linear systems:** PETSc implements iterative KSP solvers or utilizes direct solvers from the MUMPS library.
    - **Basic math operations with vectors and matrices:** PETSc and MUMPS use the OpenBLAS library.
    - **Parallel architecture:** SLEPc and PETSc are built on DMP (Distributed Memory Programming) architecture. MUMPS and OpenBLAS are built on SMP (Symmetric Multiprocessing) architecture.
- **Material Nonlinearity and Failure Mode:** The MFront tool was chosen for the implementation of complex constitutive models (plasticity, viscoelasticity, damage) [10]. It enables the development of highly optimized C++ code for local material behavior, which is then invoked from FeniCSx via the MGIS (MFront Generic Interface Support) library. This approach ensures numerical stability through a consistent tangent stiffness matrix and provides high computational performance during nonlinear iterations.
- **Post-processing and Results Visualization:** FeniCSx can export results in .vtu or .pvtu file formats. Visualization is then possible back in FreeCAD.
- **Interconnection:** All the above programs and libraries have native Python support.
- **File Management:** For efficient file transfer and the ability to work on a PC at work and a laptop at home, creating a local Git repository in the Linux environment is the most suitable approach; this also allows for future collaboration.
- **Development Environment:** PyCharm is the ideal choice due to its intuitive environment, wide range of plugins, Git support, and high level of AI integration. The AI of choice is Google Gemini. While PyCharm allows for running and debugging Python code, FreeCAD is a binary executable. A simple Python script allows us to launch FreeCAD while redirecting its standard and error outputs to both a file and the script's output. This "trick" allows the user to see error messages while also enabling the AI to read them directly from the file, eliminating the endless copying of console output into the AI prompt.
- **Generative AI:** From a wide spectrum of options, Google Gemini AI was chosen. The service is available for free after registration. Regarding queries about creating a custom FreeCAD workbench in Python, the responses are of relatively high quality.

6 How to Survive and Stay Sane

Coexistence with AI is like marriage. It requires a great deal of understanding and tolerance, and you must not constantly pick at your partner's flaws—instead, it is better to rise above them with a smile. **And you'd better enjoy the moments when it works.** We have learned to live together, but under strictly defined conditions:

- **Establish Strict Rules of Engagement:** Create a clear, specific blueprint for the project and strictly define the AI's boundaries. Generation of autonomous code is strictly forbidden. The process must follow a rigorous hierarchy: first, discuss the problem, clarify the hurdles, and propose solutions. Only after the approach is mutually approved can the implementation in the programming language be drafted. Changes are permitted only in authorized sections, altering other parts of the program is out of the question. These rules are not suggestions; they are fixed guardrails the AI is never allowed to cross.

- **Trust, but cross-verify:** AI is a rapid idea generator but a terrible auditor of their quality. Every line of code it produces must pass through the filter of my 30 years of experience. If it suggests solving a metal-forming problem with a linear elastic material model. I must be the one to call it out. I never treat AI output as a finished fact; it's merely a raw semi-finished product that requires a rigorous "sanity check" to ensure physical and logical consistency.
- **AI as a Junior Dev, not a Mentor:** I treat AI like an overeager intern on a work placement. It handles the "grunt work"—writing routine functions, generating boilerplate code, or formatting data—but the final architecture and logic must remain firmly in my hands. I never allow it to dictate the direction of development; it is my assistant, not my project lead.
- **Emotional Detachment:** When the AI starts hallucinating facts in the early hours of the morning, I simply hit "reset." There is no point in trying to "re-educate" it within the same session. Once it loses context and enters a loop, the fastest way forward is to start a fresh chat and feed it only the unvarnished facts, free from previous clutter.
- **Symbiosis, not Substitution:** AI does not solve continuum mechanics problems for me; it helps me implement the solution in Python for FreeCAD. Without my direction, that giant excavator would just be aimlessly kicking up dust. The real value lies not in what the AI "knows," but in how effectively an expert can wield it to reach the finish line.

7 Conclusion

Good luck with your work! The authors are by no means AI experts, but as the saying goes: in the land of the blind, the one-eyed man is king.

Acknowledgement

This work has been supported by the grant projects KEGA 005ŽU-4/2024.

References

[1] SEKORA, Ondrej. *Ferdo v cudzích službách*. City: Albatros, 1939.
[2] HOU, X., et al. *Large Language Models for Software Engineering: A Systematic Literature Review*. Online. arXiv, 2023. Available from: https://doi.org/10.48550/arXiv.2308.10620
[3] FUNDACIÓ JUNTA CONSTRUCTORA DEL TEMPLE EXPIATORI DE LA SAGRADA FAMÍLIA. *Architecture and Geometry: Antoni Gaudí's Vision*. Online. 2024 [Accessed 2025-12-01]. Available from: http://sagradafamilia.org
[4] FREECAD COMMUNITY. *FreeCAD Documentation: FEM Workbench*. Online. 2024 [Accessed 2025-12-01]. Available from: http://wiki.freecad.org
[5] GEUZAINE, Christophe and REMACLE, Jean-François. *Gmsh Reference Manual: The documentation for Gmsh 4.12*. Online. 2024 [Accessed 2025-12-01]. Available from: http://gmsh.info
[6] SCHLÖMER, Nico. *meshio: Input/output for many mesh formats*. Online. Zenodo, 2023 [Accessed 2025-12-01]. Available from: https://doi.org/10.5281/zenodo.1173115
[7] BARATTA, I. A., et al. *DOLFINx: The Next Generation Finite Element Library*. Online. 2024 [Accessed 2025-12-01]. Available from: http://fenicsproject.org
[8] HERNANDEZ, V., ROMAN, J. E. and VIDAL, V. *SLEPc: A Scalable Library for Eigenvalue Problem Solvations*. *ACM Transactions on Mathematical Software*. 2005. Available from: https://doi.org/10.1145/1089014.1089019
[9] BALAY, S., et al. *PETSc Users Manual*. Argonne National Laboratory, 2023. Available from: http://petsc.orgHELFER, Thomas, et al. *.: The TFEL/MFront open-source library for isotropic and anisotropic plasticity*. Computer Physics Communications. 2020, vol. 249, pp. 107292. Available from: https://doi.org/10.1016/j.cpc.2020.107292

APPLIED MECHANICS 2026
April 13 - 15, 2026, České Budějovice, Czech republic

WEB-BASED IMPLEMENTATION OF FINITE ELEMENT ANALYSIS USING THE PYANSYS FRAMEWORK

Matej Hanzalík[1], Juraj Paulech[2], Erik Kučera[3], Andri Kozlov[4]

Abstract: Contribution focuses on the integration of Ansys simulation tools into a web-based environment using the PyAnsys library. The proposed solution enables remote control of Finite Element Method (FEM) calculations, meshing, and solver configuration. Resulting stress-strain analyses are processed directly within the application interface, leveraging the Ansys computational engine in the background. The work demonstrates the potential for automating engineering tasks and visualizing numerical results without the need for local software installation.

Keywords: PyAnsys; APDL; WebApp

1 Introduction

The focus of this work was to create a user interface that allows users to connect and perform predefined parametric simulations using the web application. The motivation for this work was to verify the possibilities of connecting the web interface with Ansys and to establish the first foundations for a potential modernization of teaching methods focused on the finite element method so that they correspond to modern industrial trends. For this reason, a relatively simple task of compressive and tensile loading of a beam was chosen as the simulation assignment. In this context, the presented article should therefore be considered primarily as a proof of concept of the possibilities of interconnecting IT and mechanics.

2 PyAnsys

In engineering practice, we encounter a wide variety of tasks involving FEM. At the same time, the simulation process is iterative and requires model adaptation and repeated simulation of the task. For this reason, many simulation software packages allow users to customize the program and automate processes. In Ansys, these options are divided into two main branches: Ansys ACT and PyAnsys. ACT (Application Customization Toolkit) is a set of tools for customizing and extending Ansys products. ACT uses the XML (eXtensible Markup Language) and IronPython programming languages. Ansys ACT utilizes existing Ansys products, allowing you to create your own program structures and extensions for Ansys. [1]

[1] Ing. Matej Hanzalík; Faculty of Electrical Engineering and Information Technology of STU in Bratislava, Ilkovičova 3 841 04 Bratislava, Slovakia, matej.hanzalik@stuba.sk
[2] Ing. Juraj Paulech; PhD. Faculty of Electrical Engineering and Information Technology of STU in Bratislava, Ilkovičova 3 841 04 Bratislava, Slovakia, juraj.paulech@stuba.sk
[3] Doc. Ing. Erik Kučera; PhD Faculty of Electrical Engineering and Information Technology of STU in Bratislava, Ilkovičova 3 841 04 Bratislava, Slovakia, erik.kucera@stuba.sk
[4] Bc. Andrii Kozlov; Faculty of Electrical Engineering and Information Technology of STU in Bratislava, Ilkovičova 3 841 04 Bratislava, Slovakia, xkozlov@stuba.sk

PyAnsys is a collection of open-source projects (libraries) based on the Python language that extend the capabilities of Ansys products. These libraries enable communication with individual components of the Ansys program. For example, PyMAPDL for connecting to mechanical APDL, PyFluent for Fluent, and PyDPF for Data Processing Framework. These packages allow you to perform tasks such as creating geometry, generating meshes, performing simulations, and processing results directly from Python scripts. Simply put, PyAnsys serves as a bridge between the simulation capabilities of Ansys products and the flexible capabilities of the Python language. Figure 1 provides a schematic comparison of Ansys ACT and PyAnsys. [2]

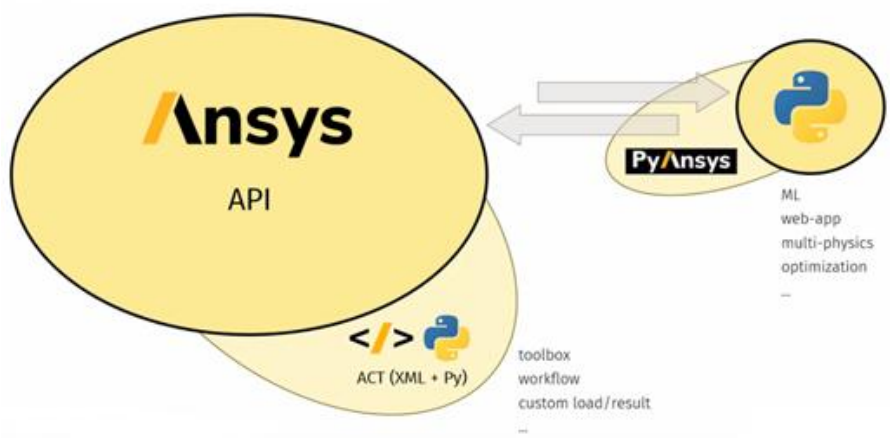

Figure 1: Comparison of PyAnsys and Ansys ACT. [3]

3 Simulated Task

Currently, the application features one simulation with complete results that users can view and download. As mentioned in the introduction, the goal of this project was not to create a simulation of a specific physical problem in Ansys, but rather to develop a web application that would allow users to simulate an existing simulation. The implemented simulation is therefore largely adapted from publicly available Ansys sample examples. We simulate a beam plate of defined dimensions that contains several holes of a selected diameter. The plate is made of a homogeneous material whose material properties are defined by the user. The beam itself is fixed on one end, and on the other end, we apply a defined tensile or compressive force. The schematic principle of the simulation is shown in Figure 2.

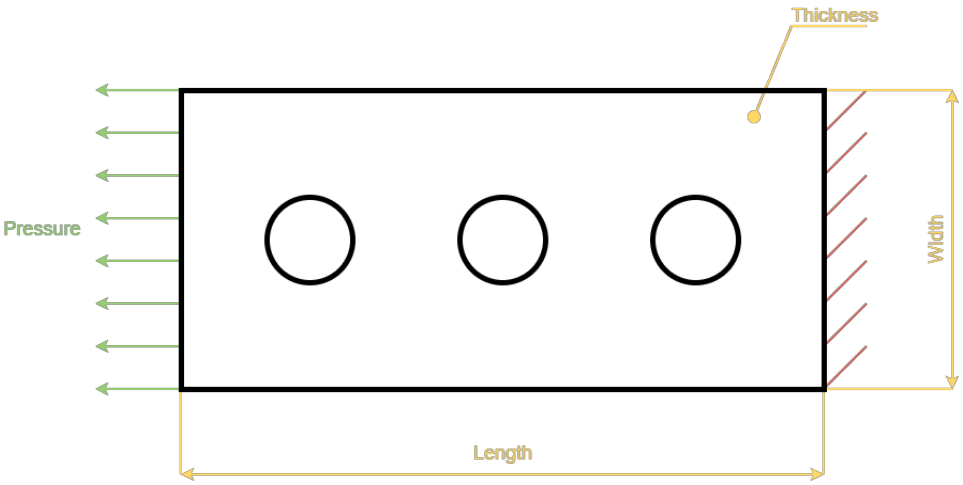

Figure 2: Schematic principle of the simulation task.

4 Web Application

Currently, the web application is fully functional but is only implemented in a localhost environment. After launching the application, the user can create a new simulation using a form where they enter all necessary parameters, such as dimensions, material properties, loads, etc. After submitting the request, the simulation is automatically queued for processing, and the calculation runs in the background, allowing the user interface to be used for other tasks. Upon successful completion of the simulation, the results are automatically processed and saved—the user has access to a text summary of the simulation and selected results (mesh, stress distribution, deformations). The application supports user registration and login, simulation management, asynchronous calculation execution, result management, and result visualization. All information about users, simulations, and results is stored in the database; result files are organized in a directory structure by simulation ID.

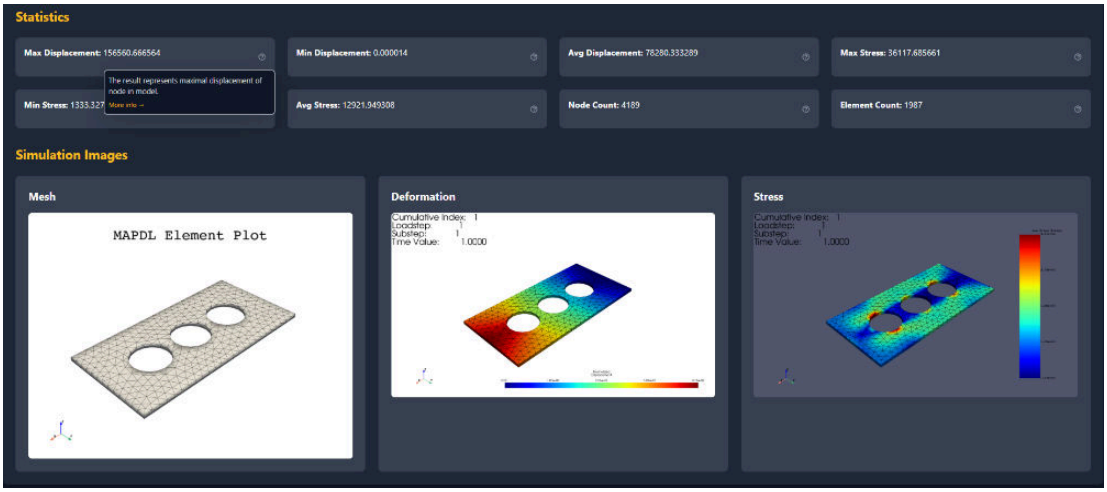

Figure 3: Interface of result page in Web Application.

A classic client-server architecture was chosen for the implementation of the web application. This architecture splits the application into two main parts (client and server), which communicate over a network. This approach allows for the distribution of computational load and ensures the scalability of the system. The client-side represents the user interface, implemented using web technologies (HTML, CSS, JavaScript/React), which is responsible for displaying information, interacting with the user, and formulating requests to the server. The client allows the user to set simulation parameters, send requests to perform calculations, and visualize the obtained results.

The server-side consists of software running on a remote server that processes client requests, performs FEM simulations, manages data, and returns results to the client. The server is implemented in Django using the Django REST Framework to create the API.

In this project, the client-server architecture is extended with a three-tier architecture, which includes:

1. Presentation layer (client layer) – user interface.
2. Application layer (server layer) – processing requests, running simulations, processing results.
3. Data layer – storing information about users, projects, and simulation results.

5 Conclusion

The aim of this paper was to demonstrate the possibilities of integrating the finite element method with computer science. The web application developed serves as a proof of concept, and further development is planned. The integration capabilities of Ansys offer a wide range of applications. We consider its use in education to be one of the most promising. The web application environment allows for the creation of a custom-built educational platform. On this platform, students could learn the individual simulation steps along with explanatory guides for specific physical concepts. The individual steps of the simulation process would be clearly demonstrated. Another possible example of using Simulations in conjunction with the Web Interface is the ability to implement existing parametric simulations programmed in the APDL language. An example of this implementation could be the creation of an interface for the automation of parametric simulations performed during project work, such as mechanical simulations of holder for lidar and cameras within the APVV-24-0390 project.

Acknowledgement

This research was supported by the Slovak Research and Development Agency under grant No. APVV-24-0390.

References

[1] Ansys Inc., “ACT Developer’s Guide,” *[Ansys Help Portal]*. Accessed: Feb. 03, 2025. [Online]. Available:https://ansyshelp.ansys.com/public/account/secured?returnurl=/Views/Secured/corp/v242/en/act_dev/act_dev.html

[2] PyAnsys, “PyAnsys documentation.” Accessed: Feb. 02, 2025. [Online]. Available: https://docs.pyansys.com/

[3] SVS FEM s.r.o, “Jak ovládat Ansys díky PyAnsys | SVS FEM s.r.o.,” Mar. 14, 2024, *[Workshop]*. Accessed: Feb. 02, 2025. [Online]. Available: https://www.svsfem.cz/jak-ovladat-ansys-diky-pyansys

APPLIED MECHANICS 2026
April 13 - 15, 2026, České Budějovice, Czech republic

Comparative Analysis of Methods for Mode I Energy Release Rate Evaluation in Adhesive Joints

L. Horák[1], J. Krystek[2]

Abstract: This article presents a comparative analysis of various methods for evaluating the mode I energy release rate (G_I) in double cantilever beam (DCB) tests on adhesive joints. It examines how different approaches handle discrepancies in compliance and G_I calculations, particularly when values vary with crack length. The study highlights method dependent differences and identifies robust options for consistent fracture characterization in numerical modeling of adhesives.

Keywords: DCB, Adhesive, Fracture mechanics, Compliance, Strain energy release rate

1 Introduction

In double cantilever beam (DCB) tests for adhesively bonded joints, accurate mode I energy release rate G_I evaluation is essential for fracture mechanics parameterization in numerical models like cohesive zone modeling. Yet, compliance based methods simple beam theory (SBT), modified beam theory (MBT), and compliance calibration (CC: $C \propto a^3$) yield inconsistent results when compliance deviates from ideal cubic behavior due to adherend rotation, adhesive plasticity, or crack tip process zones. This manifests as crack-length-dependent G_I and R-curves, complicating robust G_{IC} extraction for finite element simulations. The present study compares these methods against experimental DCB data, quantifies discrepancies in compliance fitting and G_I prediction.

2 Compliance evaluation

A key condition for the standard DCB specimen as in 1 is that the whole system deforms in a linear elastic way. This makes it possible to use linear-elastic fracture mechanics (LEFM) analysis. The critical strain energy release rate is found with

$$G_C = \frac{P_C^2}{2B}\frac{dC}{da}, \tag{1}$$

where P_C is the critical load when the crack starts, B is its width, and a is the crack length, C is the specimen's compliance expressed as $C = \delta/F$, where δ is the deflection at the loading point and P is the applied force.

The compliance obtained from Euler-Bernoulli beam theory is often called Simple Beam Theory (SBT). This approach considers only the deflection of the beam under a given load, assuming that deformation is caused exclusively by bending. Compliance can then be expressed as

$$C = \frac{2}{3}\left(\frac{a^3}{EI}\right). \tag{2}$$

The Simple Beam Theory (SBT) can be corrected to include transverse shear effects, resulting in the simple shear-corrected beam theory (SCBT). This shear-corrected formulation is recommended by the ASTM standard [1]

$$C = \frac{8}{EB}\left(\frac{a^3}{h^3} + \frac{a}{h}\right). \tag{3}$$

[1] Lukáš Horák; Department of Mechanics, Faculty of Applied Sciences, University of West Bohemia, Pilsen. Univerzitní 8, 301 00, Pilsen, Czech Republic. Email: horakl@kme.zcu.cz

[2] Jan Krystek; Department of Mechanics, Faculty of Applied Sciences, University of West Bohemia, Pilsen. Univerzitní 8, 301 00, Pilsen, Czech Republic. Email: krystek@kme.zcu.cz

The main issue with the Simple Beam Theory (SBT) is that experimental DCB tests typically show higher specimen deflections than those predicted by SBT. This leads to the impression that the specimen arm is effectively longer than the actual initial crack length a_0. The standard solution is to add an extra length Δ to the SBT formula (2) in order to account for crack tip deflection and rotation, since the beam is not perfectly built in. This approach, originally developed for isotropic adherends and later adapted for orthotropic composites, is known as the Modified Beam Theory (MBT). The ASTM [1] standard recommends MBT for the analysis of fracture in bonded joints and laminates. The MBT compliance equation for a double cantilever beam is:

$$C = \frac{2}{3EI} a_{MBT}^3 = \frac{2}{3EI}(a+\Delta)^3. \tag{4}$$

A common way to determine G_{Ic} is the compliance calibration method. This method assumes that many factors influence the specimen behaviour, so it is preferable to measure compliance experimentally rather than calculate it from beam theory. In practice, specimens with different crack lengths are manufactured, and their compliance is measured. Then, compliance (often taken as $C^{1/3}$) is plotted against crack length to obtain an empirical relationship, as illustrated in [2]. The main drawback is that the physical reasons for the deviation from classical beam theory are not fully understood. Therefore, any change in specimen details such as thickness or adhesive type requires new tests to re-establish the compliance crack length relationship.

Calculations of G_{Ic} according to the ASTM standard often show it varying with crack length, as observed in aluminium/epoxy DCB joints in [3]. However, since G_{Ic} is a material property, this apparent variation cannot be physically correct. For composites, explanations such as fibre bridging have been proposed, but these mechanisms do not apply to metal–adhesive joints.

As evident from the compliance formulas above (2), (3), and (4), none of them includes explicit terms for the adhesive layer. Consequently, the predicted compliance remains independent of adhesive type or adhesive thickness in these models.

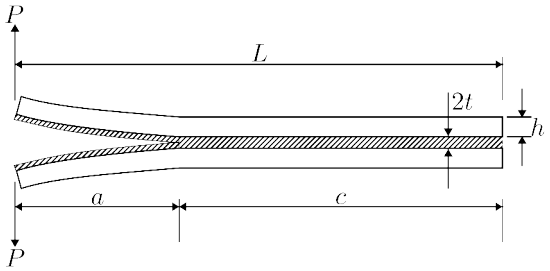

Figure 1: DCB specimen geometry and dimensions [4].

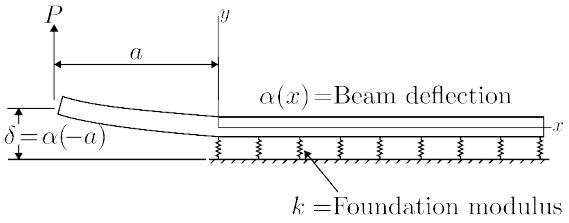

Figure 2: DCB model on elastic foundation [4].

Penado proposed a compliance formula that explicitly accounts for adhesive effects [4]. The specimen is modelled as a beam on an elastic foundation, as illustrated in Figure 2. The formula is:

$$C = \frac{8}{E_1 B}\left(\frac{a}{b}\right)^3 \left\{1 + \frac{3}{\tilde{K}h^{0.25}}\left(\frac{h}{a}\right) + 3\left[\frac{1}{\tilde{K}^2 h^{0.5}} + \frac{E_1}{8G_1}\right]\left(\frac{h}{a}\right)^2 + \frac{3}{2\tilde{K}^3 h^{0.75}}\left(\frac{h}{a}\right)^3\right\}, \tag{5}$$

where $\tilde{K} = \sqrt[4]{3k/(E_1 B)}$, it is assumed that the adhesive and adherend act as a spring in series, variable k represents this stifness. subscripts 1 mean adherend properties and 2 adhesive ones; G shear modulus, ν Poisson's ratio; h is adherend thickness, t adhesive thickness, detail decription of each term can be found in [4]. Unlike the ASTM formula, this one uses adhesive parameters. Penado validated this method with finite element analysis in [4].

2.1 Results

The evaluation and comparison of the methods described above are performed using experimental data obtained from DCB specimens with a ductile adhesive (Araldite 2015) and a brittle adhesive (AV138). The experiments were carried out in accordance with the ASTM standard [1]. The experimental data are shown in Figures 3 and 4, where results are presented in both uncorrected form and in corrected form, the latter accounting for the use of loading blocks that stiffen the DCB specimen.

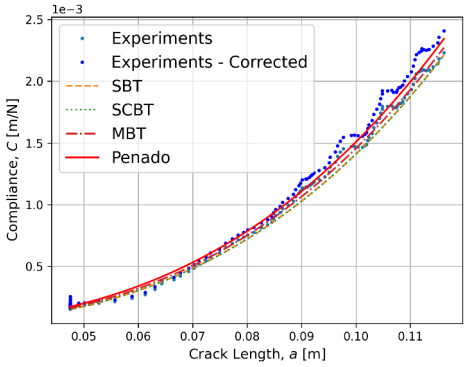

Figure 3: Compliance for ductile adhesive.

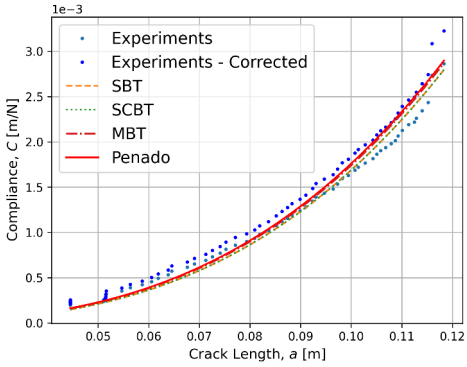

Figure 4: Compliance for brittle adhesive.

It can be seen that the Penado method (5) most accurately describes the behaviour of the ductile adhesive. For the brittle adhesive, Penado mehtod does not show a clear advantage over the MBT. This method can therefore be used to calculate G_{Ic} and R–curve by substituting the compliance into (1).

3 Conclusion

The standard ASTM method for measuring the mode I critical energy release rate (G_{Ic}) in adhesive joints has several notable drawbacks. Typical results often show substantial scatter and can yield different G_{Ic} values depending on crack length. This variability undermines the reliability of G_{Ic} as a failure criterion and leads to a dependence on empirical compliance calibration, which becomes inefficient when testing multiple adhesive joint configurations. By selecting an appropriate method based on the adhesive type, it is possible to accurately predict the compliance of the DCB specimen.

Acknowledgement

This research work was supported by the project SGS-2025-015.

References

[1] ASTM International. *Standard Test Method for Mode I Interlaminar Fracture Toughness of Unidirectional Fiber-Reinforced Polymer Matrix Composites*. ASTM D5528-01. West Conshohocken, ASTM International, 2001.

[2] M.F.S.F. DE MOURA; GONÇALVES, J.P.M; CHOUSAL, J.A.G a CAMPILHO, R.D.S.G. Cohesive and continuum mixed-mode damage models applied to the simulation of the mechanical behaviour of bonded joints. *International Journal of Adhesion and Adhesives*. 2008, vol. 28, no. 8, s. 419-426. ISSN 0143-7496. Available from: https://doi.org/10.1016/j.ijadhadh.2008.04.004.

[3] HORÁK, L. and KRYSTEK, J. Paper in proceedings. In: *Experimental Stress Analysis 2024, 62nd international conference*. City: Boží Dar, Czech Republic, Pilsen: University of West Bohemia in Pilsen, June 4th - 6th, 2024. ISBN 978-80-261-1225-9.

[4] PENADO, F.E. A Closed Form Solution for the Energy Release Rate of the Double Cantilever Beam Specimen with an Adhesive Layer. *Journal of Composite Materials*. 1993, vol. 27, no. 4, s. 383-407. ISSN 0021-9983. Available from: https://doi.org/10.1177/002199839302700403.

APPLIED MECHANICS 2026
April 13 - 15, 2026, České Budějovice, Czech republic

DYNAMIC MODELLING AND EFFECTS OF RADIAL CLEARANCES IN REVOLUTE JOINTS OF THE PLANAR SLIDER-CRANK MECHANISM

Martin Hrabačka[1], Miroslav Byrtus[2], Michal Hajžman[3], Radek Bulín[4]

Abstract: This contribution addresses the modelling of multibody systems with imperfections, including clearances and friction in joints. In-house-developed software automatically generating computational models of generic multibody systems is used for simulating the dynamics of an imperfect slider-crank mechanism. The work primarily aims to investigate the effects of radial clearance size on the mechanism's dynamic response and control.

Keywords: multibody dynamics; computational software development; imperfect joint; slider-crank mechanism

1 Introduction

Multibody dynamics plays a crucial role in the design and analysis of mechanical systems, particularly in mechanisms such as the slider-crank, widely used in applications ranging from internal combustion engines to robotic systems. While idealized models often assume perfect joints, real mechanical systems inevitably contain imperfections such as clearances and friction, which significantly influence their dynamic behaviour. The presence of joint clearances introduces additional degrees of freedom, leading to non-linear effects such as impacts, vibrations, and increased wear, thereby reducing accuracy and reliability of the system.

Extensive research has been devoted to modelling and analysis of multibody systems with clearance joints, demonstrating that even small clearances can induce complex phenomena including shock transmission, chaos, and degradation of motion precision [1]. Classical and modern approaches incorporate contact-impact formulations, friction models, and lubrication effects to better capture realistic joint behaviour [2]. Recent studies on slider-crank mechanisms further highlight the strong dependence of dynamic response on clearance size, operating conditions, and structural flexibility, often revealing nonlinear and unstable regimes [3, 4]. Despite these advances, accurate and computationally efficient modelling of clearance-induced effects remains a challenging task, especially for high-speed and control-oriented applications.

2 In-house developed software

This contribution addresses these issues by modelling a planar slider-crank mechanism with radial clearances in revolute joints, using an in-house-developed software tool that automatically generates computational models for generic multibody systems. The software incorporates contact mechanics to accurately simulate clearance-induced impacts and frictional effects.

The mathematical core is formed by the mixed type Lagrange's equations. The dynamics of a planar system of n interconnected rigid bodies is described according to [5] by a system of $3n + r$ differential-

[1] Ing. Martin Hrabačka; University of West Bohemia, Faculty of Applied Sciences, Department of Mechanics; Technická 8, 301 00 Pilsen, Czech Republic; hrabackm@kme.zcu.cz

[2] doc. Ing. Miroslav Byrtus, Ph.D.; University of West Bohemia, Faculty of Applied Sciences, Department of Mechanics; Technická 8, 301 00 Pilsen, Czech Republic; mbyrtus@kme.zcu.cz

[3] doc. Ing. Michal Hajžman, Ph.D.; University of West Bohemia, Faculty of Applied Sciences, Department of Mechanics; Technická 8, 301 00 Pilsen, Czech Republic; mhajzman@kme.zcu.cz

[4] Ing. Radek Bulín, Ph.D.; University of West Bohemia, Faculty of Applied Sciences, Department of Mechanics; Technická 8, 301 00 Pilsen, Czech Republic; rbulin@kme.zcu.cz

algebraic equations

$$\begin{bmatrix} \mathbf{M} & \partial_{\mathbf{q}}\mathbf{c}^{\mathrm{T}} \\ \partial_{\mathbf{q}}\mathbf{c} & \mathbf{0} \end{bmatrix} \begin{bmatrix} \ddot{\mathbf{q}} \\ \boldsymbol{\lambda} \end{bmatrix} = \begin{bmatrix} \mathbf{f}_V + \mathbf{f}_E + \mathbf{f}_C \\ \mathbf{f}_D \end{bmatrix}, \tag{1}$$

where $\mathbf{M}$ is the mass matrix, $\partial_{\mathbf{q}}\mathbf{c}$ is the Jacobian matrix of constraints ($\mathbf{c}$ is the kinematic constraint vector), $\mathbf{q}$ represents the vector of generalized coordinates, $\boldsymbol{\lambda}$ is the vector of Lagrange multipliers, $\mathbf{f}_V$ is the quadratic velocity vector, $\mathbf{f}_E$ is the vector of external forces, and $\mathbf{f}_C$ is the vector of contact forces. The second equation, the so-called acceleration constraint equation, results from two consecutive time-differentiations of r constraint equations $\mathbf{c} = \mathbf{0}$, including the member $\mathbf{f}_D$ that absorbs terms quadratic in velocities.

When the model includes only perfect joints, which can be expressed by kinematic constraints, there are no contact forces, i.e., $\mathbf{f}_C = \mathbf{0}$. If, on the other hand, the joint includes imperfections such as clearance or friction, the contact modelling approach is used instead of kinematic constraints. Contact forces generated in imperfect joints form the vector $\mathbf{f}_C$, which is incorporated into the model (1) similarly to other force terms. However, evaluating contact forces is a computationally very demanding task. The software uses a traditional approach, modelling rigid-body impacts using constitutive equations and penalization, which is described, for instance, in [1].

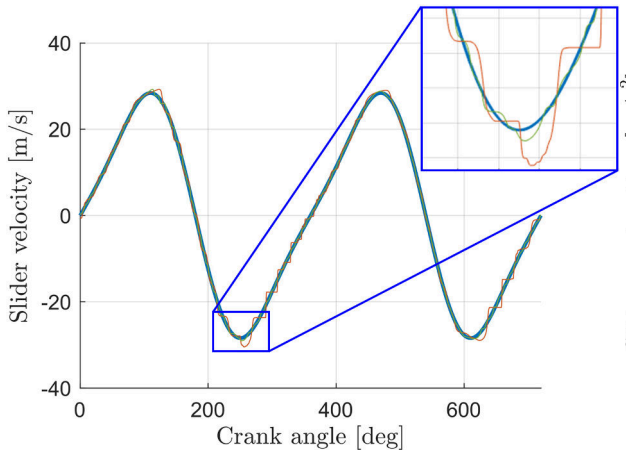

Figure 1: Velocity of the slider.

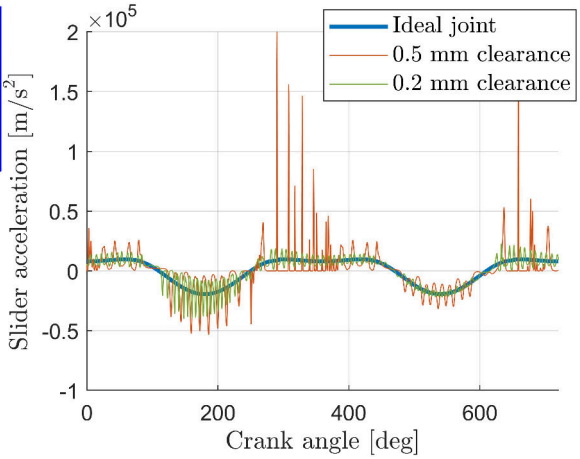

Figure 2: Acceleration of the slider.

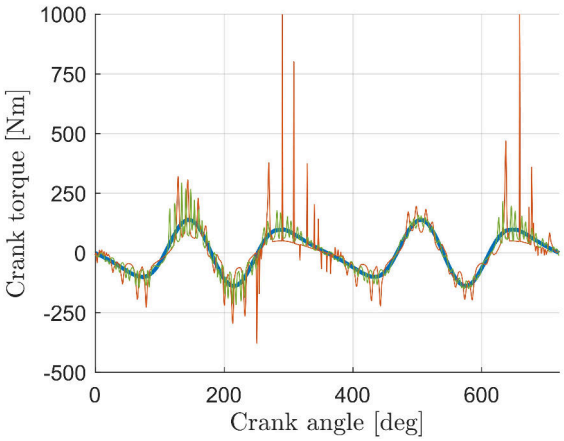

Figure 3: Torque on the crank.

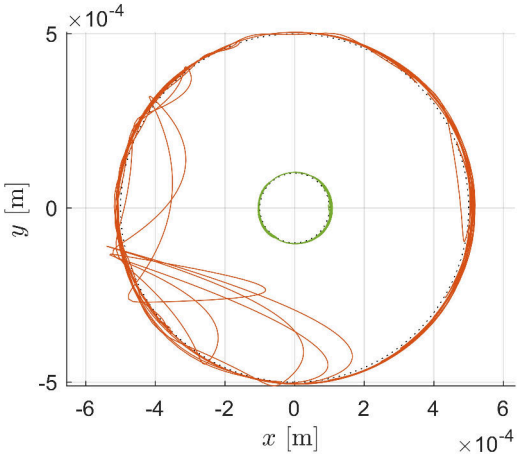

Figure 4: Journal's trajectory inside the bearing.

3 Application

The developed software is utilized to investigate the dynamic effects of radial clearance in the revolute joint between the crank and the connecting rod of the planar slider-crank mechanism. The mechanism runs under constant crank's angular velocity of 5000 rpm and has the following main dimensions: crank length 50 mm, connecting rod length 120 mm, and radius of the imperfect joint's bearing 10 mm. Three different clearance sizes are presented – 0 mm (i.e., ideal joint), 0.1 mm, and 0.5 mm.

Figures 1–4 show differences in the dynamic response of the mechanism during two periods of motion. Figures 1–3 display signals that, in the ideal case (thick blue curves), oscillate periodically. The larger the radial clearance is, the more severe the signal corruption becomes. Figure 3, depicting the crank torque needed to maintain the constant velocity, demonstrates rapidly increasing demands on the crank actuator with larger clearance size – the actuator must both deliver high amount of torque, compensating strong impacts in the clearance joint, and quickly react since impacts are extremely fast events compared to the overall system's dynamics. Figure 4 demonstrates relative trajectory of the journal's centre with respect to the bearing's centre. It shows multiple phases of journal's free motion within clearance followed by significant impacts of the journal into the bearing's surface in the case of larger clearance, while the trajectory creating a circle without any major interruptions is evident for small clearance.

4 Conclusion

The study demonstrates that incorporating radial clearances and friction into multibody models significantly alters the dynamic behaviour of a slider-crank mechanism. Using in-house software based on Lagrange's equations, the authors show that increasing clearance leads to stronger non-linear effects, including impacts, vibrations, and signal irregularities. Larger clearances notably increase actuator torque demands and introduce rapid, high-intensity force fluctuations. The results highlight how even small imperfections can degrade system performance and complicate control. Overall, the work emphasizes the importance of realistic joint modelling for accurate prediction and design of mechanical systems.

Acknowledgement

This research work was supported by the project GA25-17552S of the Czech Science Foundation, and by the project SGS-2025-015 of the University of West Bohemia.

References

[1] TIAN, Qiang; FLORES, Paulo and LANKARANI, Hamid M. A comprehensive survey of the analytical, numerical and experimental methodologies for dynamics of multibody mechanical systems with clearance or imperfect joints. *Mechanism and Machine Theory*. 2018, vol. 122, no. 4, pp. 1–57. Available from: https://doi.org/10.1016/j.mechmachtheory.2017.12.002.

[2] FLORES, Paulo; AMBRÓSIO, Jorge and CLARO, J. Pimenta. Dynamic analysis for planar multibody mechanical systems with lubricated joints. *Multibody System Dynamics*. 2004, vol. 12, pp. 47–74. Available from: https://doi.org/10.1023/B:MUBO.0000042901.74498.3a.

[3] CHEN, Yu; WU, Kai; WU, Xuze; SUN, Yu and ZHONG, Taisheng. Kinematic accuracy and nonlinear dynamics of a flexible slider-crank mechanism with multiple clearance joints. *European Journal of Mechanics – A/Solids*. 2021, vol. 88, pp. 1–20. Available from: https://doi.org/10.1016/j.euromechsol.2021.104277.

[4] YUAN, Wang; LIU, Juan; NING, Fengping; CHAI, Chao; ZHANG, Lei and LI, Hui. Dynamic analysis of crank slider mechanism considering 3D translational joint clearance based on variable contact area. *Mechanics & Industry*. 2025, vol. 26, no. 5, pp. 1–16. Available from: https://doi.org/10.1051/meca/2025001.

[5] SHABANA, Ahmed A. *Computational dynamics*. 3rd Ed. Hoboken, NJ: John Wiley & Sons, 2010. ISBN 978-0-470-68615-7.

APPLIED MECHANICS 2026
April 13 - 15, 2026, České Budějovice, Czech Republic

PREDICTIVE SIMULATIONS OF LASER PEENING: PARAMETERS AND EXPERIMENTAL CONSTRAINTS

M. Isoz[1], A. Kovárnová[2], A. Prado[3], P. Gruber[4], D. Gabriel[5]

Abstract: Laser (shock) peening has been used to enhance the fatigue life of metallic components since the 1990s, and numerical simulations of the process have been investigated since the early 2000s. Despite sustained research efforts, the feasibility of truly predictive simulations of laser shock peening remains an open question. In this contribution, we analyze the key physical and numerical challenges that limit the predictive capability of current simulation approaches. Based on this analysis, we discuss the principal sources of uncertainty and outline possible directions for future developments toward reliable, simulation-based process design.

Keywords: Laser (shock) peening; numerical simulation; mathematical modeling

1 Introduction

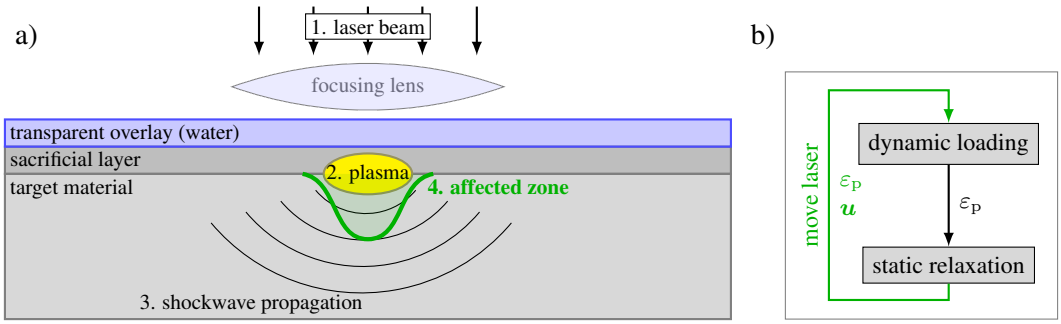

Figure 1: Fundamentals of the (a) laser shock peening process; (b) approach to simulation of switching between dynamic plastic wave propagation and pseudo-static relaxation while sharing data on displacements ($\boldsymbol{u}$) and plastic strains (ε_p).

Laser (shock) peening (LSP) is a high-power-density, laser-based surface treatment that induces near-surface plastic deformation and enhances the fatigue performance of metallic components. The variant of the process considered in this contribution is known as the water-confined regime and is illustrated in Fig. 1a; a detailed description can be found in, e.g., [1] and in our earlier study [2].

Regarding numerical simulations, it is common practice to separately simulate (i) laser-target interactions yielding a plasma-generated pressure pulse [1], and (ii) subsequent shock-wave propagation, plastic deformation, and inter-pulse relaxation. The latter will hereafter be referred to as "LSP simulation". Since the late 1990s [3], the LSP simulation has been divided into two simulation phases, leveraging the fact that shock-wave-related phenomena occur on distinct temporal scales compared to inter-pulse relaxation: $\mathcal{O}(10^{-6})$ s and $\mathcal{O}(10^{-1})$ s, respectively. A standard approach to LSP simulation is sketched in Fig. 1b.

[1] Martin Isoz; Institute of Thermomechanics, Czech Academy of Sciences (CAS), Dolejškova 1402/5; 182 00, Prague, CZ (ITCAS); isozm@it.cas.cz
[2] Anna Kovárnová; ITCAS; kovarnoa@it.cas.cz
[3] Angel Prado; ITCAS; prado@it.cas.cz
[4] Pavel Gruber; ITCAS; pgruber@it.cas.cz
[5] Dušan Gabriel; ITCAS; gabriel@it.cas.cz

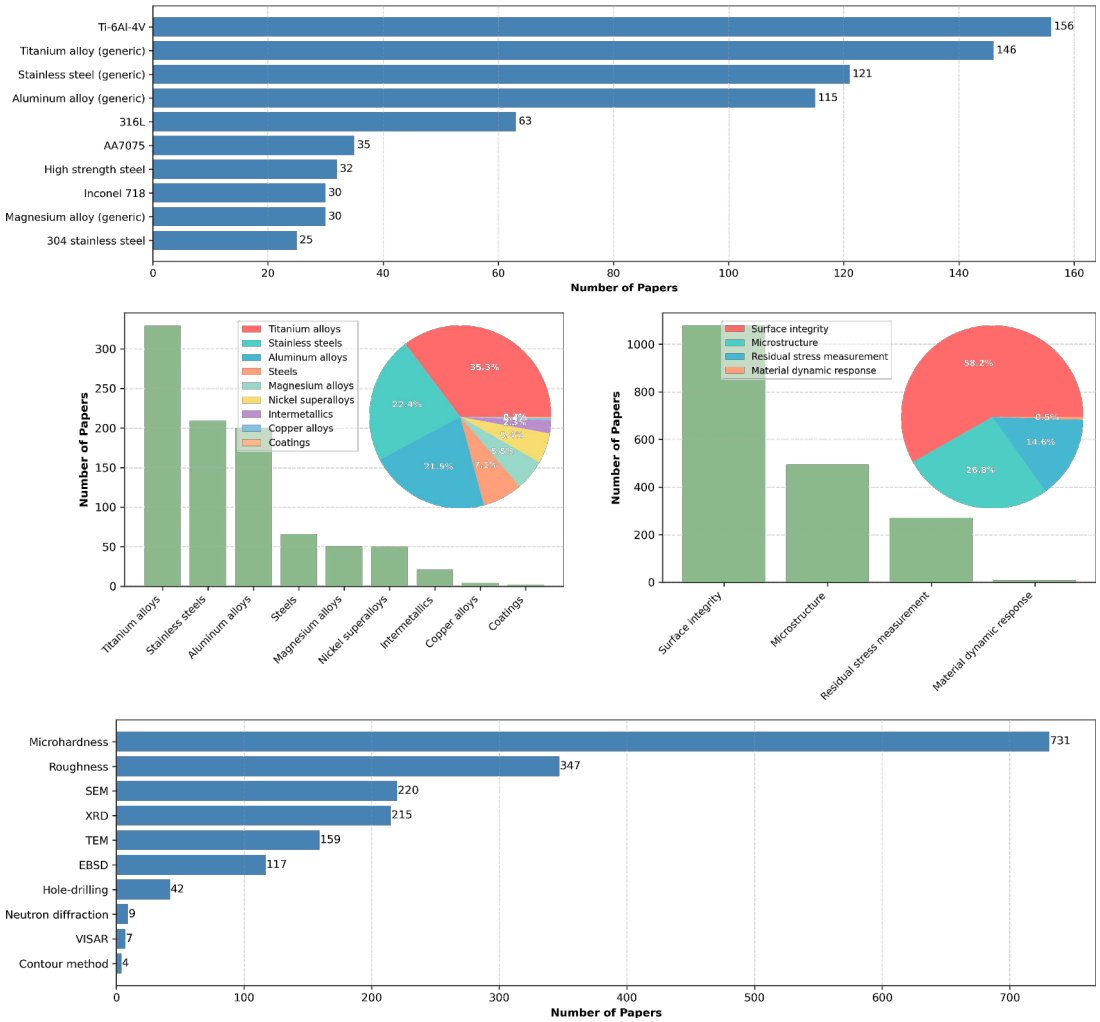

Figure 2: Results of meta-analysis of 1816 laser shock peening studies.

2 In search of calibration data

Any predictive simulation of LSP relies on the following pillars: (a) the quality of the model for laser-target interactions; (b) the calibration of the model for material response to ultra-fast loading; and (c) the numerical properties of the solver used to address the system governing equations. Furthermore, (a) and (b) are based on empirical relations and depend on the available experimental data. In an ideal scenario, experimental data on system dynamics, peening-induced residual stresses, and the final material state should be available for any given material and LSP laser. Simultaneously, the laser should be well characterized with respect to the spatial and temporal profiles of both the laser beam and the beam-generated plasma pressure. In practice, almost none of the above is usually available.

To provide further detail, we conducted an automated search of the ScienceDirect database. During the search, we extracted 1816 papers from journals with an impact factor that investigated LSP, analyzing the keywords and text patterns present in their titles and abstracts. The results are given in Figure 2. The most frequently treated materials are titanium and aluminum alloys, and stainless steel. While Ti6Al4V is prevalent in LSP research, the variance in properties of different aluminum alloys and the effect of various tempers on the behavior of these materials render their popularity in the community only apparent. A similar situation as for Al alloys occurs for steels as well. The 316L and 304L are comparatively well studied. On the other hand, no systematic data are available for high strength steels.

With respect to methods used for LSP analysis, the situation is similar to that observed for materials. The most common experiments focus on the hardness and roughness of the treated surface. Furthermore,

a large number of studies are devoted to the effect of LSP on the microstructure of treated materials, evaluated using SEM, TEM, EBSD, or neutron diffraction. A comparatively smaller number of results are available for LSP-induced residual stresses (RS), with X-ray diffraction (XRD) being more popular than hole-drilling, while the contour method is just beginning to gain traction in the community. Despite the predominance of XRD in RS measurement, the vast majority of data concerns RS profiles in the direction orthogonal to the material surface, and almost no surface measurements of RS are available.

Finally, of all the analyzed papers, only seven used the velocity interferometer system for any reflector (VISAR) to study the material's dynamic response during LSP. As far as we know, only data on the behavior of pure aluminum, AA2024-T3 and AA7175-T7351 aluminum alloys, and Ti6Al4V ELI grade alloy are available. Among the four listed materials, pure aluminum and AA2024-T3 are the most analyzed. For the remaining two materials, only partial results from one study were found. Unfortunately, no data on post-LSP residual stresses for pure aluminum were found. For AA2024-T3, four studies were identified in which hole-drilling was used to measure residual stresses under various LSP process parameters and material states. Hereafter, limited by the availability of experimental data, we will focus solely on AA2024 aluminum alloy.

3 Evaluating suitability of AA2024-T3 material models

Here, we forego a detailed description of the simulation approach and the numerical framework used. An interested reader is referred to the contribution by Anna Kovárnová in these conference proceedings or to our earlier work [2]. Instead, we focus on the most common model used in LSP simulations, the empirical Johnson-Cook (JC) model [4]

$$\sigma_\mathrm{y} = \left(A + B\,\varepsilon_\mathrm{p}^{n}\right)\left(1 + C\ln\left(\dot{\varepsilon}_\mathrm{p}^{\mathrm{eff}}/\dot{\epsilon}_\mathrm{p}^{0}\right)\right), \qquad \dot{\varepsilon}_\mathrm{p}^{\mathrm{eff}} = \max\left(\dot{\varepsilon}_\mathrm{p},\ \dot{\varepsilon}_\mathrm{p}^{0}\right) \tag{1}$$

where $\sigma_\mathrm{y} = \sigma_\mathrm{y}(\varepsilon_\mathrm{p},\, \dot{\varepsilon}_\mathrm{p}^{\mathrm{eff}})$ is the yield criterion, which is a function of the plastic strain ε_p and the plastic strain rate $\dot{\varepsilon}_\mathrm{p}^{\mathrm{eff}}$. Finally, A, B, C, n, and $\dot{\varepsilon}_\mathrm{p}^{0}$ are empirical parameters, of which only A, representing the static yield stress of virgin material, is usually well defined.

key [REF]	A (MPa)	B (MPa)	n $(-)$	C $(-)$	$\dot{\varepsilon}_\mathrm{p}^{0}$ (1/s)	Calibration
johnsoncook1983 [4]	265	426	0.34	0.0150	1.0	HSB
ayad2022 [5]	369	329	0.35	0.0350	1.0	VISAR
zhou2018 [6]	369	684	0.73	0.0083	1.0	N/A
sticchi2015 [7]	350	972	0.73	0.0100	$1.9{\cdot}10^{-4}$	QS-L.
righi2025 [8]	368	689	0.73	0.0083	1.0	N/A
harant2022 [9]	370	431	0.36	0.0233	0.02	HSB

Table 1: Empirical parameters for the Johnson-Cook model. Calibration methods considered are the Hopkinson split bar (HSB), residual stress from LSP (RS-LSP), VISAR, and quasi-static combined with literature survey (QS-L). If N/A is listed, the parameters source was either not listed or pointed to a wrong reference.

For the AA2024T3 alloy, six sets of JC material parameters were found in the literature and are listed in Table 1. Note that, interestingly, the original Johnson-Cook set of parameters for AA2024T3, obtained using the Hopkinson split bar, has a significantly lower static yield stress than the remaining models. Also, the set of parameters by Sticchi et al. Has a strangely high B, which is combined with a relatively intense rate hardening induced by very low $\dot{\varepsilon}_\mathrm{p}^{0}$. Based on the parameter values alone, it is not possible to estimate the models behavior during LSP simulations.

Dynamic response To evaluate the performance of the models listed in Table 1, we replicated the experiment of Ayad et al. [5], where the authors used VISAR to measure backface velocity in the center of a 1 mm thick cylindrical specimen of 5 mm radius. The probed area over which the measured velocity was effectively averaged was a circle of 50 μm radius. In the simulation, the specimen was approximated by leveraging its axi-symmetry, and the data sampling corresponded to the probed area in the physical

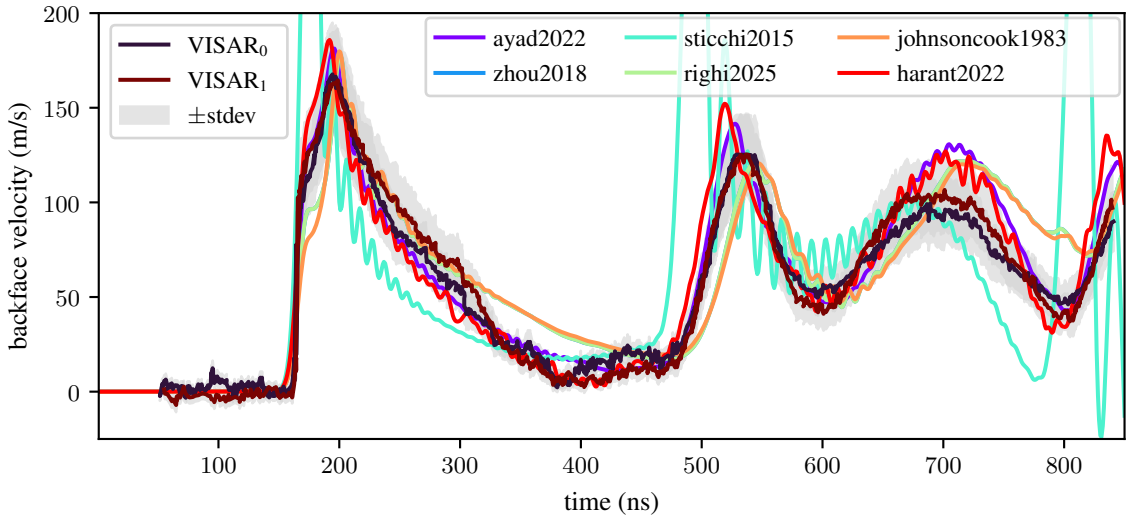

Figure 3: Sample backface velocity measured using VISAR and simulated with different models from Table 1. Material is AA2024T3, laser spot properties are taken directly from [5]: power density is 2.8 GW/cm^2, spot diameter is 4 mm, pulse duration and full width at half maximum (FWHM) is 7 ns.

experiment. The simulations were conducted within a finite volume method-based framework utilizing a uniform mesh with a characteristic cell size of 7 μm. Further details can be found in the contribution by Anna Kovárnová.

Experimental data from the paper and our simulation results are presented in Figure 3. Despite the oscillations in the simulation results caused by numerical dispersion at high strain rates, it can be seen that the model by Ayad et al. [5] outperforms the other models, which is not surprising, as the model was specifically calibrated to fit these data. Interestingly, the response of the model by Harant et al. [9], which was calibrated using the Hopkinson split bar is relatively close to that of the Ayad et al. model. On the other hand, the two models are defined such that their strain rate hardening is similar at strain rates between 10^2 and 10^4 s^{-1}, i.e., in the region of particular importance for LSP modeling.

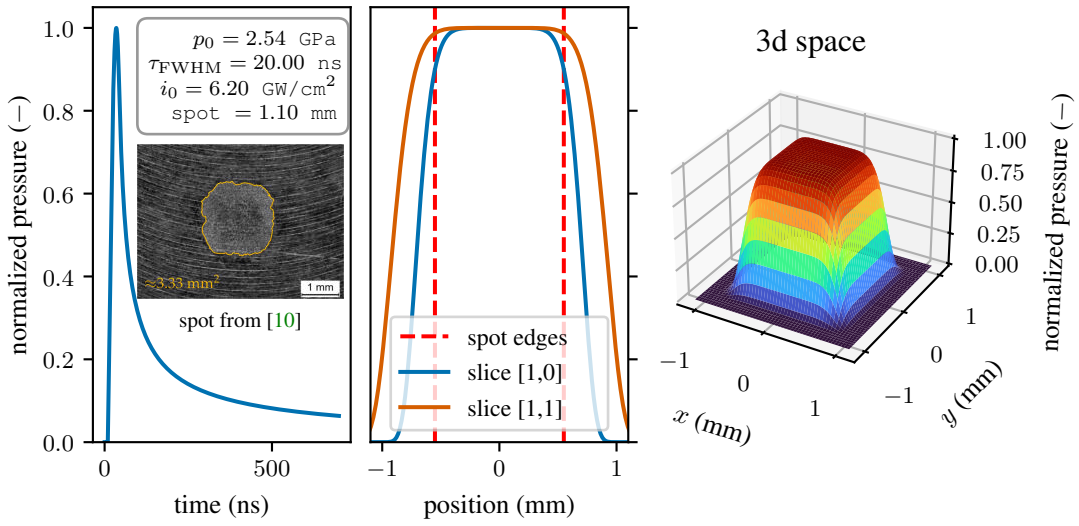

Figure 4: Characterization of the laser-induced pressure pulse corresponding to a 1.5 J laser energy used to replicate experimental data from [10].

LSP-induced residual stress To study the models capability of predicting LSP-induced residual stresses in AA2024, we use the experimental data by Kallien et al. [10] who studied the behavior of AA2024-T3 under various laser processing parameters and even for different material set-ups; for example, with and without clad layer and aluminum foil attached to the specimen surface.

Regarding the laser configuration, significantly less data is available compared to the study by Ayad et al. [5], who derive their laser model directly from [1] and describe it in great detail. In fact, only the laser type (Nd:YAG), wavelength (1064 nm), energy (1.0, 1.5, and 3.0 J), FWHM duration (20 ns), and spot shape (square of side 1 mm) are listed in the paper. However, in a subsequent publication by the same group [11], the authors specify the use of the Fabbro model [12] for converting laser power density to pressure amplitude. Still, no data apart from the photographs of laser-induced surface deformations shown in Figure 4 are available regarding the pressure pulse spatial profile.

To reverse-engineer the probable laser-induced loading on the sample, we selected the `ayad2022` model, fixed the laser energy and FWHM duration, and modified the size and sharpness of the pressure spatial profile to achieve a deformed spot similar to that shown in Figure 4. Note that a change in spot size leads to the change of the laser power density (i_0). For the conversion of i_0 to pressure amplitude (p_0), we used the Fabbro model [12]. To obtain the temporal pressure profile, the model from [1] was utilized. Full laser characterization is presented in Figure 4.

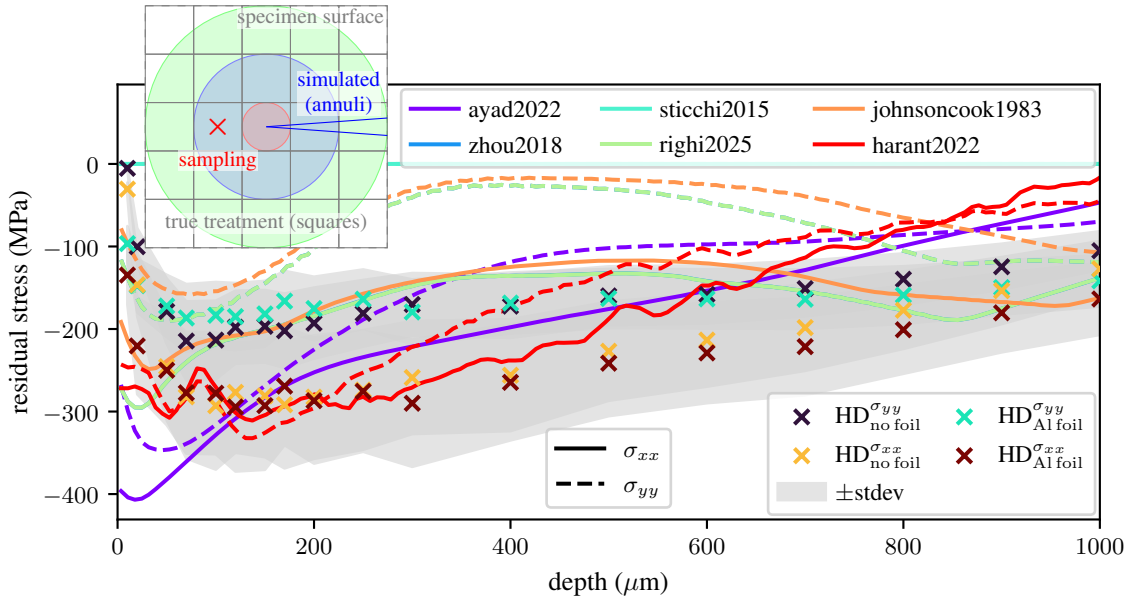

Figure 5: Experimental LSP-induced residual stresses from [10] compared to simulations with different material models listed in Table 1. Experimental data correspond to 1.5 J laser energy and AA2024-T3 in no-clad, and no-foil and Al-foil configurations. Scheme of simulated vs true sample treatment is in the subfigure.

In experiments, a sample $40 \times 40 \times 4.8$ mm was subjected to a series of non-overlapping square shots. In simulations, we used an axi-symmetric approximation with the same mesh resolution as previously used to replicate the VISAR data from Ayad et al. [5]. In experiments, the residual stress induced by the LSP was measured using hole-drilling with a 2 mm i.d. hole. In simulations, we sampled stresses in the vertical direction at the location indicated on the left hand side of Figure 5. The results are reported in the right hand side of the same figure.

4 Discussion and conclusion

Comparing the estimated and measured residual stresses, it seems that none of the models align well with the experimental data but the `ayad2022` and `harant2022` models are the most promising. Nonetheless, the experimental data exhibit significant uncertainties; substantial pre-stress near the sample surface is reported in [10]; the approximation of square LSP shots via the axi-symmetric model may be overly simplistic; and the laser model may not accurately represent the laser-sample interaction. Even for the "perfect" case of AA2024-T3, the situation seems bleak. Automated identification of LSP process parameters, designed to separately identify laser and material parameters, can help. However, the number of simulations required necessitates the design of suitable model order reduction workflows.

Acknowledgement

The authors acknowledge the financial support provided by the Ministry of Education, Youth, and Sports of the Czech Republic via the project No. CZ.02.01.01/00/23_020/0008501 (METEX), co-funded by the European Union. The work was financially supported by the institutional support RVO:61388998.

References

[1] SCIUS-BERTRAND, Marine; VIDEAU, Laurent; RONDEPIERRE, Alexandre; LESCOUTE, Emilien; ROUCHAUSSE, Yann; KAUFMAN, Jan; ROSTOHAR, Danijela; BRAJER, Jan and BERTHE, Laurent. Laser induced plasma characterization in direct and water confined regimes: new advances in experimental studies and numerical modelling. *Journal of Physics D: Applied Physics*. 2020, vol. 54, no. –, pp. 055204. Available from: https://doi.org/10.1088/1361-6463/abc040.

[2] ISOZ, Martin; GRUBER, Pavel; SCHMIDT, Jaroslav; KUBÍČKOVÁ, Lucie; ŠTEFAN, Jan; KAUFMAN, Jan; BRAJER, Jan and GABRIEL, Dušan. Calibrated finite volume method-based simulation framework for laser shock peening. In: RADOLF, Vojtěch and ZOLOTAREV, Igor (eds.). *Proc. of the Conf. Engineering Mechanics*. Milovy, Czech Republic: IT CAS, 2023, pp. 103–106.

[3] BRAISTED, W. and BROCKMAN, R. Finite element simulation of laser shock peening. *International Journal of Fatigue*. 1999, vol. 21, no. —, pp. 719–724. Available from: https://doi.org/10.1016/S0142-1123(99)00035-3.

[4] JOHNSON, Gordon R. and COOK, William H. A constitutive model and data for metals subjected to large strains, high strain rates and high temperatures. In *Proceedings of the 7th International Symposium on Ballistics*. City: Den Haag, Netherlands, 1983, pp. 541-547.

[5] AYAD, M.; LAPOSTOLLE, L.; RONDEPIERRE, A.; LE BRAS, C.; SCIUS-BERTRAND, M.; ÜNALDI, S.; TRDAN, U.; ROUCHAUSSE, Y.; GRASSY, J.; MAILLOT, T.; LAPOUJADE, V.; MICHEL, C. and BERTHE, L. Modeling of multi-edge effects in the case of laser shock loadings applied on thin foils: Application for material characterization of aluminum alloys. *Journal of Applied Physics*. 2022, vol. 131, no. 9, pp. 095902. Available from: https://doi.org/10.1063/5.0080326.

[6] ZHOU, W. F.; REN, X. D.; WANG, C. C.; YANG, X. Q.; LARSON, Enoch Asuako. Residual stress induced convex bending in laser peen formed aluminum alloy. *Journal of Laser Applications*. 2018, vol. 30, no. 1, pp. 012001. Available from: https://doi.org/10.2351/1.5012962.

[7] STICCHI, M.; STARON, P.; SANO, Y.; MEIXNER, M.; KLAUS, M.; REBELO-KORNMEIER, J.; HUBER, N. and KASHAEV, N. A parametric study of laser spot size and coverage on the laser shock peening induced residual stress in thin aluminium samples. *The Journal of Engineering*. 2015, vol. —, no. —, pp. 97–105. Available from: https://doi.org/10.1049/joe.2015.0106.

[8] RIGHI, S.; FEKIRINI, H.; MEBARKI, H.; POLESE, C. and KHODJA, M. Numerical analysis of mechanical modifications induced by laser shock peening on AA2024-T351 for aeronautical structures. *Journal of Aeronautics, Astronautics and Aviation*. 2025, vol. 57, no. 6, pp. 1375–1387. Available from: https://doi.org/10.6125/JoAAA.202506_57(6).04.

[9] HARANT, M.; JOPEK, M.; PODANÝ, K. and ŘIHÁČEK, J. Investigation of Johnson–Cook parameters of aluminium alloy 2024-T3. In: FISCHER, Cyril and NÁPRSTEK, Jiří (eds.). *Proc. of the Conf. Engineering Mechanics*. Milovy, Czech Republic: —, 2022, pp. 137–140. doi: 10.21495/51-2-137.

[10] KALLIEN, Z.; KELLER, S.; VENTZKE, V.; KASHAEV, N. and KLUSEMANN, B. Effect of laser peening process parameters and sequences on residual stress profiles. *Metals*. 2019, vol. 9, no. 6, pp. 655. Available from: https://doi.org/10.3390/met9060655.

[11] SCHWAB, Karl-Christian; KELLER, Sören; KASHAEV, Nikolai and KLUSEMANN, Benjamin. Tailoring of residual stresses by specific use of defined prestress during laser shock peening. *Journal of Materials Processing Technology*. 2021, vol. 295, no. —, pp. 117154. Available from: https://doi.org/10.1016/j.jmatprotec.2021.117154.

[12] FABBRO, R.; FOURNIER, J.; BALLARD, P.; DEVAUX, D. and VIRMONT, J. Physical study of laser-produced plasma in confined geometry. *Journal of Applied Physics*. 1990, vol. 68, no. 2, pp. 775–784. Available from: https://doi.org/10.1063/1.346783.

APPLIED MECHANICS 2026
April 13 - 15, 2026, České Budějovice, Czech republic

CREEP MODEL USED TO DESCRIBE AND PREDICT POLYMER CREEP BEHAVIOR UNDER UNIAXIAL TESTING CONDITIONS

Lenka Jakubovičová[1], Jaroslav Prajka[2], Radim Halama[2],
Michal Šofer[2], Martin Fusek[2], Milan Ságа[1]

Abstract: Creep is an inherent and natural time-dependent property of all materials subjected to sustained loading. This study focuses on the analysis and prediction of the creep behaviour of the thermoplastic material EOS PA 2200 (also known as PA12), which is widely used in manufacturing applications. The creep behaviour of PA12 was monitored using a specialized optical measurement system on Digital Image Correlation (DIC). The positions of high contrast markers on the sample were continuously recorded during the experiment. The experimental results provide the time-dependent creep response for the material under investigation. The Burgers creep model for uniaxial tension was applied to describe and analyse the observed creep behaviour.

Keywords: creep model; thermoplastic material EOS PA 2200 (PA12); Burgers creep model

1 Introduction

Thermoplastic polymers are materials characterized by significant viscoelastic behavior, which manifests as a combination of elastic and viscous responses to mechanical loading. Unlike metallic materials, polymers exhibit significant time-dependent deformation even at room temperature, which is due to their low melting point. Viscoelasticity in the material is characterized by an instantaneous elastic strain, the steady-state creep strain and the transient creep strain. The relative ratio of these components depends on the stress level, temperature, and duration of the applied load [1].

One of the most significant manifestations of the viscoelastic behavior of materials is creep, defined as the slow and gradual deformation of a material over time under constant load. Focusing on creep behavior is of substantial importance for the design of thermoplastic structural components subjected to long-term static loading. Without an adequate mathematical description of the creep process, it is difficult to reliably predict deformation and shape changes in the long run, which directly affects their service life and safety margin. Experimentally obtained creep curves therefore serve as an essential foundation for identifying material parameters and developing constitutive models that enable numerical simulations of material behavior.

The characteristic time dependence of strain and strain rate under uniaxial constant loading is illustrated in Figure 1. The total strain of the material at any time is the sum of all partial strains. In the initial phase, nearly instantaneous elastic ε_e and plastic ε_p strain, followed by the time-dependent creep strain ε_c

$$\varepsilon = \varepsilon_e + \varepsilon_p + \varepsilon_c, \tag{1}$$

where ε_e is elastic strain; ε_p is plastic strain; ε_c is creep strain; ε is total strain.

[1] Ing. Lenka Jakubovičová, PhD.; Dr. h. c. prof. Dr. Ing. Milan Ságа.; Department of Applied Mechanics, Faculty of Mechanical Engineering, University of Žilina, Univerzitná 8215/1, 010 26-Žilina, Slovak republic; lenka.jakubovicova@fstroj.uniza.sk; milan.saga@fstroj.uniza.sk

[2] Ing. Jaroslav Prajka, Ph.D.; prof. Ing. Halama Radim, Ph.D.; doc. Ing. Šofer Michal, Ph.D.; prof. Ing. Fusek Martin, Ph.D.; Department of Applied Mechanics, Faculty of Mechanical Engineering, VSB- Technical University of Ostrava, 17. listopadu 2172/15, 708 00 Ostrava-Poruba, Czech Republic, jaroslav.prajka@vsb.cz; radim.halama@vsb.cz; michal.sofer@vsb.cz; martin.fusek@vsb.cz

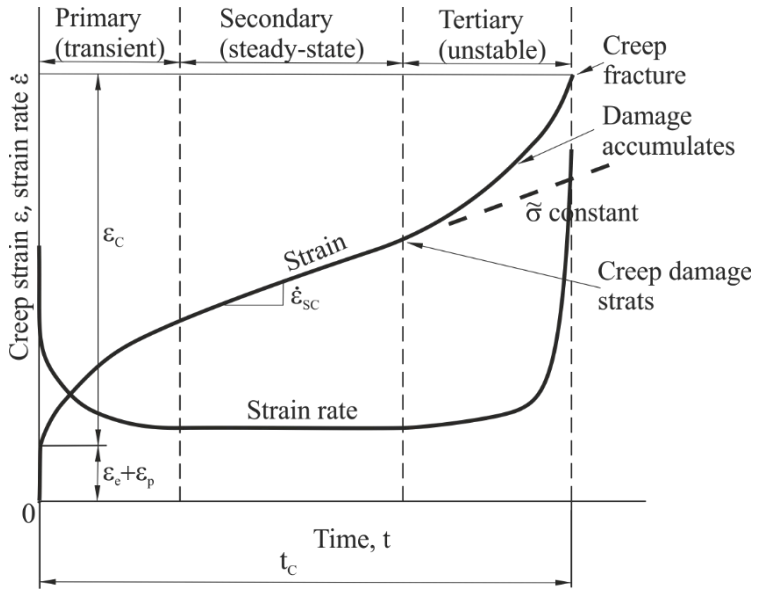

Figure 1: Strain and Strain rate versus time behaviour during creep under constant force, hence constant engineering stress, and the three stages of creep.

In engineering practice, the Burgers model is frequently used to describe viscoelastic creep behavior, representing a combination of the Maxwell and Kelvin–Voigt models [2], [3]. The Maxwell model consists of a spring E_1 and dashpot η_1 in series, describes the instantaneous elastic strain and the subsequent linear increase in viscous strain. The Kelvin–Voigt model, which consists of a spring E_2 and a dashpot η_2 in parallel, describes the material's delayed elastic response. Combining these two fundamental rheological models results in the Burgers model, which is capable, in many cases, of adequately describing both the primary and secondary creep stages, thus providing a comprehensive analytical description of time-dependent strain.

The material under study is the thermoplastic polyamide PA12, commercially known as EOS PA 2200, designed for additive manufacturing technology [4]. This material is commonly used in the production of structural components and functional prototypes using Selective Laser Sintering (SLS) technology. In the SLS process, thin layers of polymer powder are locally sintered using a laser beam. The process takes place at temperatures just below the material's melting point, with individual layers gradually bonded into the final 3D object. The resulting microstructure of parts manufactured this way is characterized by a semi-crystalline morphology with a certain degree of porosity, which can influence their mechanical response and subsequent creep behavior. Due to the layered nature of additive manufacturing, the material's mechanical response may be slightly anisotropic, depending on the printing orientation [4], [5].

The basic material properties of PA12 declared by the manufacturer (EOS GmbH, Krailling, Germany), are listed in Table 1.

Density of laser sintered parts [kg.m^{-3}]	Young's modulus of elasticity [MPa]	Tensile strength [MPa]	Elongation at break [%]	Melting point [°C]
930*	1650*	48*	18*	176*

Table 1. Basic properties of PA12 material.
* According to manufacturer's (EOS GmbH, Krailling, Germany) data sheets [1].

These values represent reference data from the manufacturer's technical data sheet (TDS) and serve as a baseline framework for interpretation of the experimental creep measurements carried out in this work.

The aim of this paper is to identify the Burgers model parameters [6] based on representative experimental creep strain measurements of the thermoplastic material PA12. Furthermore, this work focuses on determining the accuracy of this mechanical model in approximating experimental data and assessing its suitability for predicting the time-dependent strain of the material subjected to long-term loading [7].

2 Methodology and results

Experimental measurement was performed on a 20 kN electromechanical machine using flat dog-bone specimens fabricated by Selective Laser Sintering. Non-contact strain measurement was ensured by an optical Digital Image Correlation (DIC) system. High-contrast markers were applied to the specimen surface; their positions were continuously recorded during the test and in time converted into strain data.

During the experiment, a constant $F = 1660\ N$ was applied. For a specimen cross-sectional area $A = 41.5\ mm^2$, this load corresponds to a nominal (engineering) stress $\sigma_0 = 40\ MPa$ Throughout the entire duration of the experiment, the specimen's deformation was monitored using an optical DIC system consisting of a pair of Basler a2A2840-48umPRO cameras equipped with Fujinon 25mm HF-series lenses, and the X-Sight Alpha evaluation software [8].

The representative time-dependent creep strain curve, obtained from experimental measurements under constant stress, serves as input data for the numerical optimization process and the identification of material parameters. The selected Burgers viscoelastic model (Equation 2), which provides a highly accurate description of the studied PA12 polyamide material, is utilized in the subsequent part of this work for the analytical description and prediction of the creep process [9]. This model effectively captures both the primary and secondary creep stages. The Burgers model fits the experimental data using a four-parameter structure consisting of a Maxwell element connected in series (a spring with modulus E_1 and a dashpot with viscosity η_1) followed by a Kelvin–Voigt element (a spring E_2 and a dashpot η_2 connected in parallel). Such an arrangement allows for the decomposition of the total time-dependent strain into instantaneous elastic, delayed linear viscous, and slow viscoelastic components.

The mechanical model for the total strain $\varepsilon(t)$ is defined by the following mathematical expression:

$$\varepsilon(t) = \frac{\sigma_0}{E_1} + \frac{\sigma_0}{\eta_1}t + \frac{\sigma_0}{E_2}\left[1 - e^{-\frac{E_2}{\eta_2}t}\right] \tag{2}$$

where σ_0 is applied constant stress [MPa], t is time [s], E_1 is the modulus of elasticity Maxwell element [MPa], E_2 is the modulus of elasticity of relaxation response Kelvin-Voigt element [MPa], η_1, η_2 are the coefficients of dynamic viscosity [GPa/s].

To facilitate the numerical solution and simplify the optimization algorithm, it is convenient to define the ratios of the material coefficients as a set of parameters p_i and rewrite the constitutive equation in the following form:

$$\varepsilon(t) = p_1 + p_2 t + p_3[1 - e^{-p_4 t}] \tag{3}$$

where p_1, p_2, p_3, p_4 are the parameters tailored for optimization using MATLAB software, with appropriately defined initial conditions. The selection of suitable starting values in the optimization process has a critical impact on the convergence, speed, and accuracy of the resulting solution. The design of the parameters should be appropriately adapted to the nature of the experimental data as follows:

p_1 – represents the component of instantaneous elastic strain;
p_2 – corresponds to the average secondary creep rate (the slope of the linear portion of the curve);
p_3 – defines the magnitude of delayed elastic strain (the curvature in the primary creep phase);
p_4 – represents the retardation factor influencing the rate of transition to the steady-state phase.

The parameters are tailored for optimization using MATLAB software, with appropriately defined initial conditions. The selection of suitable starting values in the optimization process has a critical impact on the convergence, speed, and accuracy of the resulting solution. The design of the parameters should be appropriately adapted to the nature of the experimental data as follows:

A script for nonlinear regression analysis using least squares optimization was created in MATLAB®. By applying this regression analysis method to Equation 3, the estimates for parameters of p_i were obtained, followed by the calculation of the material constants E_i and η_i, as presented in Table 2.

Parameters [-]	p_1	p_2	p_3	p_4
	49659 e-6	21.589 e-6	42150e-6	5166 e-6
coefficients	$E_1 = \frac{\sigma_0}{p_1}$ [MPa]	$\eta_1 = \frac{\sigma_0}{p_2}$ [GPa]	$E_2 = \frac{\sigma_0}{p_3}$ [MPa]	$\eta_2 = \frac{\sigma_0}{p_4}$ [GPa]
	803.5	1848.3	946.7	183.2

Table 2. Results of nonlinear regression of Burger's model for material PA12.

The optimization was performed to minimize the residual difference between the experimental measurement and the mathematically described creep model. The achieved coefficient of determination is $R^2 = 0.99876$, and the approximation accuracy demonstrated excellent agreement with the experimental data, as shown in Figure 2.

The relationship shown in Figure 2 illustrates the experimental data from a representative creep test, indicated by black circles. The red curve represents the interpolated creep strain profile derived from the four-parameter Burgers model. The correlation between the experimental and fitted data exhibits high precision, as evidenced by a low root-mean-square error $RMSE = 0.0122$ between the two datasets.

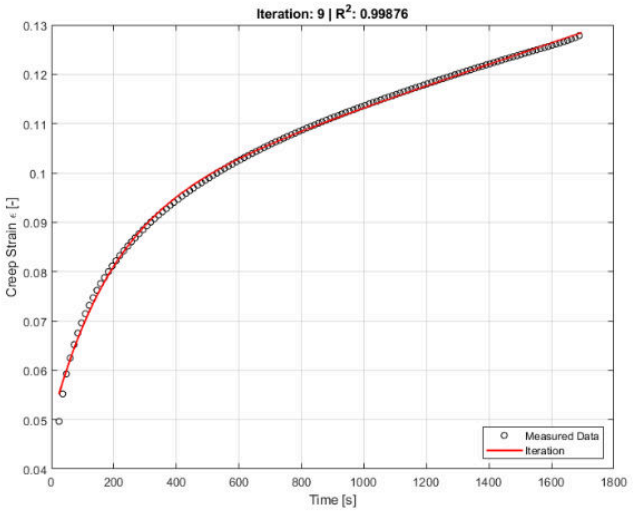

Figure 2: Creep strain measured by DIC and interpolated, load 1660 N.

3 Comparison with Experimental Data

The time-dependent creep strain and the corresponding strain rate for the experimental measurements are illustrated in Figure 3. The creep rate is calculated directly from the strain increments in individual time steps; consequently, it does not exhibit a smooth profile and shows "jagged" characteristics typical of raw data from the DIC system. In contrast, Figure 4 displays the parameterized curves of the Burgers model, which provide a smooth profile for both monitored variables.

In both cases, the minimum strain rate value was identified as $\dot{\varepsilon} = 2 \times 10^{-5}\ [s^{-1}]$. The steady-state creep phase is observed within the time interval from 1,200 to 1,600 seconds. Subsequently, a re-acceleration of the strain rate occurs, signaling the transition into the tertiary creep stage, which leads to the ultimate failure and fracture of the material at approximately $t \sim 1{,}700$ seconds.

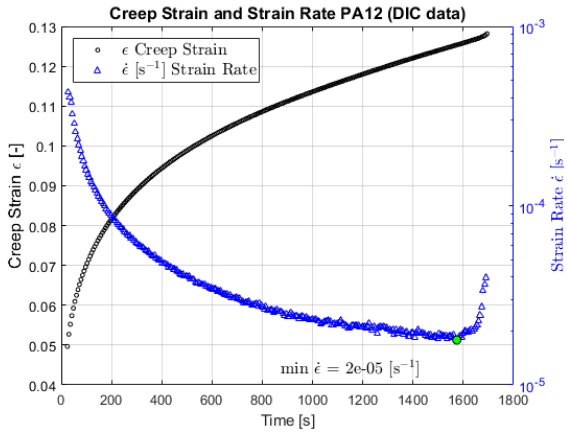

Figure 3: Creep Strain and Strain Rate, load 1660 N, Raw data - DIC.

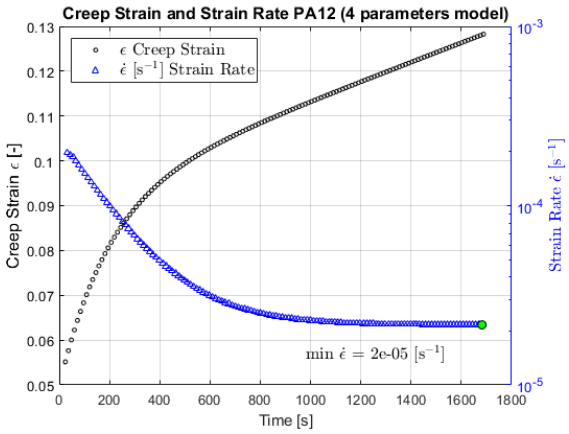

Figure 4: Creep Strain and Strain Rate, load 1660 N, fitted data.

It can be concluded that the application of the Burgers model enabled the transformation of discrete experimental data into a continuous analytical description. The resulting smoothed curves provide a more precise foundation for further mechanical analysis and the lifetime prediction of components manufactured from PA12.

4 Discussion and Conclusion

The primary objective of the authors was to accurately identify the time-dependent creep strain of the material and to define the material constants required for subsequent numerical simulations. Creep tests were conducted on flat "dog-bone" specimens fabricated using Selective Laser Sintering (SLS) technology. Experimental measurements were performed on an electromechanical testing machine under a constant load of 1,660 N, corresponding to an engineering stress of 40 MPa. Strain measurement throughout the entire duration of the experiment was carried out using a Digital Image Correlation (DIC) optical system. During this non-contact measurement, the positions of high-contrast markers on the specimen surface were continuously recorded. Subsequently, the authors analyzed the time dependence of the strain rate. Under the given load, the steady-state creep (secondary phase) occurred within the time range of 1,200 to 1,600 seconds, with a minimum strain rate of $\dot{\varepsilon} = 2 \times 10^{-5}\ [s^{-1}]$. The gradual accumulation of strain led to the ultimate failure of the material at approximately 1,700 seconds.

Based on the obtained data, the authors compiled a four-parameter Burgers model, consisting of a Maxwell element and a Kelvin-Voigt element connected in series. Using non-linear regression analysis in MATLAB, the authors succeeded in determining all material constants (E_1, η_1, E_2, η_2) required for the exact definition of this model. The selected model describes the primary and secondary creep phases with high precision, as evidenced by the excellent agreement with experimental data, represented by a coefficient of determination of $R^2 = 0.99876$.

The obtained results provide a detailed analysis of a representative experimental measurement of creep deformation, enhancing the understanding of the time-dependent behavior of the SLS-manufactured PA12 thermoplastic. In the future, the authors intend to focus on determining the Burgers model parameters under various load levels and different print orientations.

Acknowledgement

This work was supported by grant project KEGA 001ŽU-4/2026, 005ŽU-4/2024 and VEGA 1/0753/24.

References

[1] Venkata S. Chevali, Derrick R. Dean, Gregg M. Janowski. Flexural creep behavior of discontinuous thermoplastic composites: Non-linear viscoelastic modeling and time–temperature–stress superposition, Composites Part A: *Applied Science and Manufacturing*, Volume 40, Issues 6–7, 2009, Pages 870-877, ISSN 1359-835X, https://doi.org/10.1016/j.compositesa.2009.04.012.

[2] Al Rashid A, Koç M. Creep and Recovery Behavior of Continuous Fiber-Reinforced 3DP Composites. *Polymers*. 2021; 13(10):1644. https://doi.org/10.3390/polym13101644

[3] Paweł Majda, Janusz Skrodzewicz, A modified creep model of epoxy adhesive at ambient temperature, *International Journal of Adhesion and Adhesives*, Volume 29, Issue 4, 2009, Pages 396-404, ISSN 0143-7496, https://doi.org/10.1016/j.ijadhadh.2008.07.010.

[4] Krönert, M., Schuster, T.J., Zimmer, F. et al. Creep behavior of polyamide 12, produced by selective laser sintering with different build orientations. *Int J Adv Manuf Technol* 121, 3285–3294 (2022). https://doi.org/10.1007/s00170-022-09446-z

[5] Ogazi, Anthony C. et al. "Production of PA12 Powder for Additive Manufacturing: Progress, Challenges, and Prospects." Polymers for Advanced Technologies 36 (2025): n. pag. https://doi.org/10.1016/j.mtcomm.2022.105279

[6] Liu, W., Zhang, S. Accelerated creep model based on the law of energy conservation and analysis of creep parameters. *Mech Time-Depend Mater* 28, 227–254 (2024). https://doi.org/10.1007/s11043-023-09628-6

[7] Tan, H., Yan, S., Zhu, S. et al. Creep modeling of composite materials based on improved gene expression programming. *Sci Rep* 12, 22244 (2022). https://doi.org/10.1038/s41598-022-26548-6

[8] Paska, Zbynek, Radim Halama, Petr Dymacek, Bhuvanesh Govindaraj, and Jaroslav Rojicek. 2024. *Comparison of Tensile and Creep Properties of SAC305 and SACX0807 at Room Temperature with DIC Application,* Applied Sciences 14, no. 2: 604. https://doi.org/10.3390/app14020604

[9] Hana Krupova, Kristyna Sternadelova, Jakub Mesicek, Quoc-Phu Ma, Jiri Hajnys, Experimental evaluation of selectively laser sintered polyamide 12 surface treatment for direct electrodeposition https://doi.org/10.1016/j.porgcoat.2023.107968

APPLIED MECHANICS 2026
April 13 - 15, 2026, České Budějovice, Czech republic

ANALYSIS OF PRESSING JOINT OF PYRAMIDAL PIPE

Roland Jančo[1]

Abstract: This paper presents a stress analysis of a pressed joint of two pyramidal pipes with the aim to find out whether this kind of connection is suitable for telecommunication masts. The analysis can be considered a complex spatial problem of a thin-walled shell, where the local bending stress influence might be dominant. In this paper a solution using engineering approach and numerical analysis with finite element method (FEM) will be compared.

Keywords: pyramidal pipes, finite element analysis, thin-walled shell, contact pressure

1 Introduction

The paper presents a continuation of Article [1, 2] of the strength analysis of the pressed joint of two conical pipes in order to determine whether this method of connection is suitable for telecommunication masts. references.

2 Stress analysis of a press-fit joint of two thin-walled pyramidal pipes

Let us assess the stress of a press-fit joint of ideal n-sided pyramidal thin-walled tubes (with sharp corners) and forceless insertion of pipes. While at the general location x, contact forces P will arise in the corners (as a result of contact pressures around the corners of n-sided "rings" of unit width, see Fig. 1; in the central region of the sides b, the contact pressure will be practically zero - otherwise bending buckling of the sides would occur).

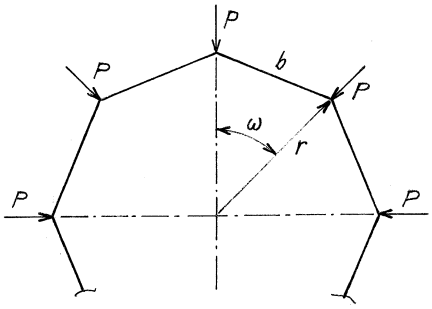

Figure 1: Contact force P in the corners n-sides rings.

Due to the corner forces P, membrane stresses arise in a “ring” of unit width:

$$\sigma = \frac{P}{2h \sin\frac{\omega}{2}} = \frac{Pr}{bh} \tag{1}$$

which are compression in the inner ring and tension in the outer ring. The length of a side of a regular n-gon is $b = 2r \sin\frac{\omega}{2}$, where $\omega = \frac{360}{n}$ is the central angle corresponding to one side.

[1] prof. Ing. Roland Jančo, PhD. ING-PAED IGIP; Slovak university of technology in Bratislava, Institute of , Applied Mechanics and Mechatronics, Nám. slobody 17, 81231 Bratislava, Slovak republic, roland.janco@stuba.sk

3 Numerical analysis

Numerical solution was made by transfer of bending moment between two thin-walled pipes without clearance and without lap see Fig. 2. Value of bending moment is $M_B = 629.10^6$ N.mm. Solution was solved using finite element methods in program ANSYS. This problem is solution of contact between two solid pyramidal pipe. The Fig. 3 shows the equivalent stress.

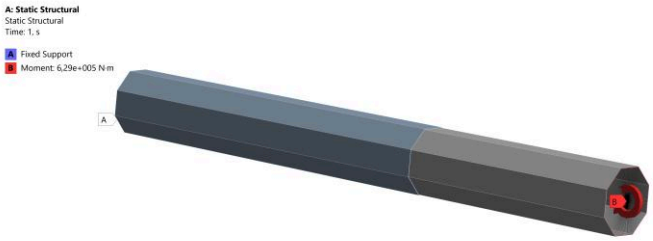

Figure 2: Boundary and load condition.

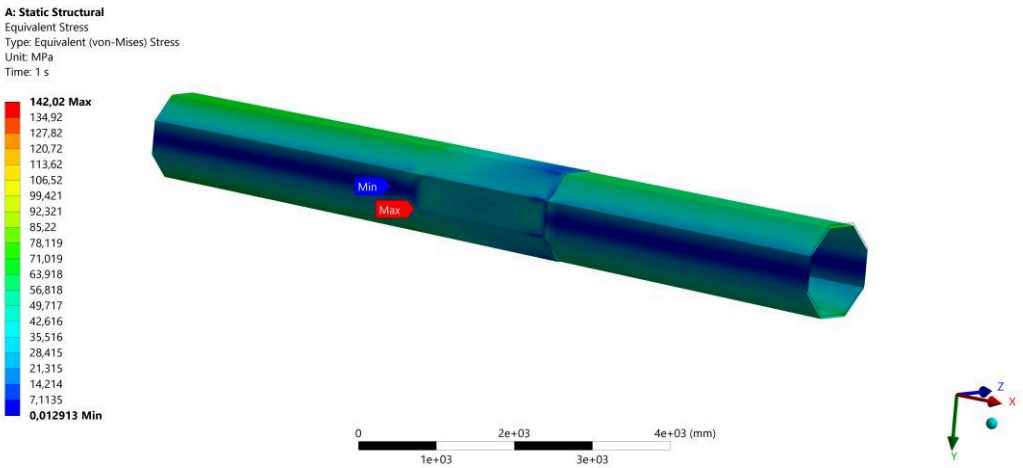

Figure 3: The equivalent stress (MPa).

4 Conclusion

In conclusion, we can say that the analytical solution coincides with the numerical solution.

Acknowledgement

This work was supported by grant … This research was supported by the Slovak Research and Development Agency under Contracts No. APVV-23-0650, APVV-20-0428. APVV-19-0401, SK-SRB-23-0024, APVV 23-0456, APVV-24-0526.

References

[1] JANČO, Roland. Stress Analysis of Pressing Joint of Two Conical Pipes, *Strojnícky časopis – Journal of Mechanical Engineering* 73 (1), pp. 117 – 124, 2023. DOI: 10.2478/scjme 2023-0009

[2] JANČO, Roland. Stress Analysis of Pressing Joint of Two Conical Pipes – Part 2, *Strojnícky časopis – Journal of Mechanical Engineering* 74 (2), pp. 43 – 48, 2024. DOI: 10.2478/scjme 2024-0004

[3] ANSYS Users Manual

APPLIED MECHANICS 2026
April 13 - 15, 2026, České Budějovice, Czech republic

TOWARDS PARAMETER IDENTIFICATION IN LASER PEENING USING MODEL ORDER REDUCTION

A. Kovárnová[1], M. Isoz[2], J. Terpáková[3], A. Prado[4], P. Gruber[5], D. Gabriel[6]

Abstract: Material parameters of metals and metal alloys are crucial for predictive simulations of the laser peening process; however, the experiments are challenging and the literature often provides conflicting values (for further details see the contribution by dr. Isoz). Here we build on the aforementioned contribution and we perform a sensitivity study of the Johnson-Cook material model parameters. The results are compared to experimental data from the literature, namely backface velocity measurements done using the velocity interferometer system for any reflector (VISAR) and the unknown parameters are identified. Furthermore, we aim to accelerate the parameter identification using model order reduction techniques.

Keywords: Model order reduction; laser peening; Johnson-Cook plasticity

1 Introduction

Laser peening (LP) is a widely used technique to increase the strength and fatigue resistance of metal components. During LP, high-energy laser pulses convert a small portion of the material into plasma, which sends an elasto-plastic wave through the treated material and increases its hardness. LP has been numerically simulated since the 1990s using the finite element method [1], and recently approaches using the finite volume (FV) method have been developed [2]. In order for the simulations to be truly predictive, both elastic and plastic parameters of the modeled material have to be known beforehand. Regrettably, the literature is often not in agreement when it comes to these parameters and provides conflicting values; see, e.g., [3, 4], or an overview in the contribution by Martin Isoz at this very conference.

Some material parameters can be obtained by comparing LP simulations to experimental data, for instance, the backface velocity (BFV) evolution measured using the velocity interferometer system for any reflector (VISAR). This type of parameter estimation comprises running the simulation repeatedly for different sets of parameters, which proves to be computationally expensive.

The task can be accelerated by employing model order reduction (MOR). MOR can work in an a posteriori manner: the simulation is precomputed only for several parameter configurations, and from the snapshots a drastically computationally cheaper reduced-order model (ROM) is created and can be used in the parameter estimation itself. In classical mode-based MOR methods, ROM evaluation comprises a superposition of some modes extracted from the pre-computed snapshots, e.g., by the proper orthogonal decomposition (POD) [5]. However, the BFV evolution has sharp peaks that appear when the elasto-plastic wave from LP reaches the backface, and their positions depend on the speed of the wave, which in turn depends on the material parameters. For material parameters that were not used for the ROM construction, POD-based methods estimate these peaks insufficiently.

In this contribution, we aim to augment the existing MOR methods using known physical properties of the materials. In particular, prior to computing POD, we transform the snapshots to compensate for different speeds of sound, i.e. different speeds of elastic wave in the material, which circumvents the issue with differently placed peaks and leaves only the plastic effects to be captured by POD. We aim to use this augmented method to estimate the Johnson-Cook parameters of the aluminum alloy 2024-T3.

[1] Anna Kovárnová; Institute of Thermomechanics of the CAS; kovarnoa@it.cas.cz
[2] Martin Isoz; Institute of Thermomechanics of the CAS; isozm@it.cas.cz
[3] Jarmila Terpáková; Institute of Thermomechanics of the CAS; terpakoj@it.cas.cz
[4] Angel Prado; Institute of Thermomechanics of the CAS; prado@it.cas.cz
[5] Pavel Gruber; Institute of Thermomechanics of the CAS; pgruber@it.cas.cz
[6] Dušan Gabriel; Institute of Thermomechanics of the CAS; gabriel@it.cas.cz

2 Problem description

Model The solver used for the parameter estimation is the finite volume (FV) method framework for simulating laser peening by Isoz et al. [2], pyLSP. It is implemented in the open-source FV method library OpenFOAM and managed by a Python wrapper. Individual laser shots are represented as spatially and temporally dependent pressure loadings. The chief advantage of the framework is that it is able to handle multiple laser shots: it alternates between simulating dynamic wave propagation caused by the pressure loading and subsequent static relaxation. In this contribution, all the results stem from a dynamic wave propagation from a single laser shot, so only a simplified description of the dynamic part of the solver will be provided.

Let us denote the computational domain as Ω with a boundary $\Gamma = \partial\,\Omega$. The wave propagation is considered to be under small strain settings, $\epsilon = \frac{1}{2}\left(\nabla \boldsymbol{d} + \boldsymbol{d}\nabla\right)$, where $\boldsymbol{d}$ refers to the displacement, with the damping effects and body forces neglected, and is governed by the Cauchy momentum equation

$$\nabla \cdot \sigma = \rho\, \ddot{\boldsymbol{d}} \qquad \text{in } \Omega\,, \tag{1}$$

where σ is the stress tensor and ρ density. The governing equation is endowed with the initial (IC) and boundary (BC) conditions:

$$\text{IC}: \quad \boldsymbol{d} = \dot{\boldsymbol{d}} = \ddot{\boldsymbol{d}} = \boldsymbol{0} \quad \text{in } \Omega, \qquad \text{BC}: \quad \boldsymbol{d} = \boldsymbol{0} \text{ in } \Gamma_{\mathrm{D}}, \qquad \boldsymbol{n} \cdot \sigma = \begin{cases} \boldsymbol{0} & \text{in } \Gamma_{\mathrm{t}} \\ \boldsymbol{n}\, p_\ell & \text{in } \Gamma_{\mathrm{p}} \end{cases}. \tag{2}$$

Γ_{D} denotes the fixed part of the boundary where zero displacement is enforced, Γ_{p} the laser-processed part of the boundary that is under pressure loading p_ℓ, and $\Gamma_{\mathrm{t}} = \Gamma \backslash \Gamma_{\mathrm{D}} \backslash \Gamma_{\mathrm{p}}$.

The internal state of the material is described by the plastic strain ϵ_{p}, which evolves under the isothermal Johnson-Cook yield criterion [6]

$$\sigma_{\mathrm{y}} = \left(A + B\,\epsilon_{\mathrm{p}}^{n}\right)\left(1 + C \ln\left(\frac{\dot{\epsilon}_{\mathrm{p}}^{\mathrm{eff}}}{\dot{\epsilon}_{\mathrm{p}}^{0}}\right)\right), \qquad \dot{\epsilon}_{\mathrm{p}}^{\mathrm{eff}} = \max\left(\dot{\epsilon}_{\mathrm{p}},\ \dot{\epsilon}_{\mathrm{p}}^{0}\right). \tag{3}$$

where σ_{y} is the yield criterion,$\dot{\epsilon_{\mathrm{p}}}$ is the plastic strain rate and A, B, C, n, and $\dot{\epsilon}_{\mathrm{p}}^{0}$ are empirical parameters. The parameter A can be interpreted as the initial yield criterion, B and n describe strain hardening, and C and $\dot{\epsilon}_{\mathrm{p}}$ strain *rate* hardening. As the static part A is more easily measurable, in this work we consider it to be known and aim to identify B, C, and n. The reference strain rate $\dot{\epsilon}_{\mathrm{p}}^{0}$ is considered to be 1 s^{-1}.

The dynamic wave consists of an elastic and plastic part; while the propagation of the plastic wave is more complicated, the speed of the elastic wave corresponds to the speed of sound in the material and for an isotropic homogeneous material is obtainable from the knowledge of any two elastic constants. For example, using the Young modulus E and the Poisson ration ν, the speed of the elastic wave is given as

$$c = \sqrt{\frac{E\,(1-\nu)}{\rho\,(1+\nu)\,(1-2\nu)}}\,. \tag{4}$$

As proof of concept, we also calibrated the model for an unknown elastic parameter, in particular ν.

Experiment configuration and computational domain We attempt to identify the material parameters using experimental data by Ayad et. al [3]. Their sample is a circular metalic plate with 1 mm thickness and 10 mm diameter, which is under laser-induced pressure loading in the center. The sides of the plate are fixed, while the top and bottom are free to vibrate. Due to the axi-symmetric nature of the geometry and pressure loading, in this contribution only a 2D wedge is simulated. See the computational domain with boundary conditions in Figure 1.

The laser pulse itself has a circular spatial distribution with a radius of 2 mm and its temporal profile is Gaussian with duration of 7.2 ns at full width at half maximum. Both spatial and temporal profiles are presented in Figure 2. Its power density is $I = 2.2\,\mathrm{GW/cm^2}$, which corresponds to maximum pressure $p_{\max} = 2.2\sqrt{I} = 3.45\,\mathrm{GPa}$, in agreement with [3].

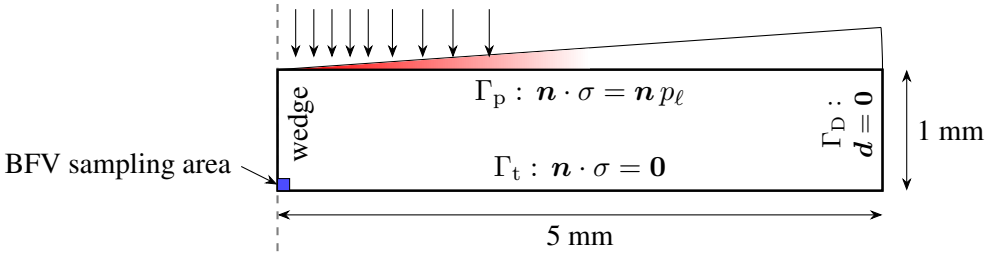

Figure 1: Computational domain, adapted from [3], with prescribed boundary conditions. The computational mesh comprises 51051 FV cells.

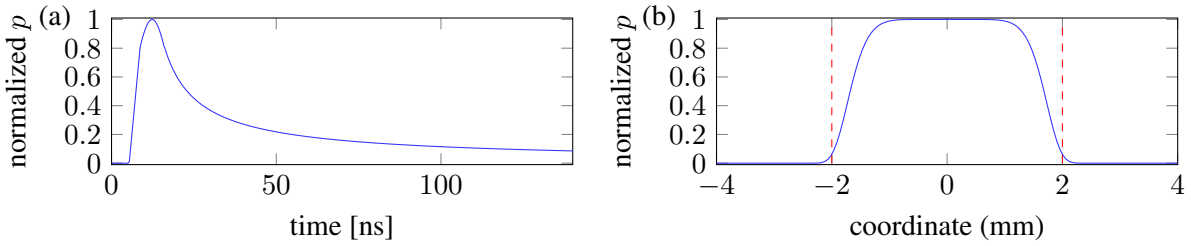

Figure 2: Laser parameters: (a) temporal profile, (b) spatial profile.

Ayad et al. measure the response of the metal plate to the pressure loading in the form of its backface velocity (BFV), i.e., the speed of movement of the back side of the plate induced by the spread of the elasto-plastic wave. The BFV is determined employing the visar interferometer system for any reflector (VISAR) and is sampled for the first 850 ns. The location of the sampling area, effectively a disc with $100\,\mu\mathrm{m}$ in diameter, is symbolized by the blue square in Figure 1. Only the velocity component in the direction of the axis of symmetry is provided.

Model order reduction In order to avoid having to simulate the computationally expensive pyLSP model during the parameter estimation, we use a posteriori model order reduction (MOR) techniques. First, the model is precomputed for several representative parameter configurations; using the snapshots, a computationally cheaper reduced-order model (ROM) is constructed. In particular, we use a combination of the proper orthogonal decomposition (POD) and interpolation by radial basis functions (RBFs).

The quantity of interest that is used in the parameter estimation is the BFV. Denoting the unknown parameter vector as $\boldsymbol{\mu} := \{B, C, n, \nu\}$, $\boldsymbol{\mu} \in \mathcal{P} \subseteq \mathbb{R}^4$ and considering a time interval $t \in [0; T]$, for which the experimental data was provided, BFV is a scalar function $u_\mathrm{BF} : (t, \boldsymbol{\mu}) \to \mathbb{R}$. In practice, it is sampled in discrete time intervals, leading to the discrete analogue $\boldsymbol{u}^h_\mathrm{BF} : \boldsymbol{\mu} \to \mathbb{R}^{N_\mathrm{t}}$, where N_t is the number of time steps sampled. To gather the data necessary for the construction of the ROM, BFV is simulated for N_μ instances of $\boldsymbol{\mu}_i$ and the results are saved into a matrix of snapshots $Q = \left[\boldsymbol{u}^h_\mathrm{BF}(\boldsymbol{\mu}_1), \ldots, \boldsymbol{u}^h_\mathrm{BF}(\boldsymbol{\mu}_{N_\mu})\right] \in \mathbb{R}^{N_\mathrm{t} \times N_\mu}$.

As a first step, a low-rank approximation of the matrix of snapshots is computed via POD. POD is frequently used for the analysis of dynamic flows [5], each snapshot in Q corresponding to a solution of a spatially discretized PDE in one time step. This way, usually the dependence on the spatial coordinate is contained in the column space and the dependence on time in the row space. However, in this application, the time plays the role normally played by the spatial coordinate, while the parameter dependence is represented the same way that the time usually is.

POD technically reduces to a truncated singular value decomposition (SVD) of Q,

$$Q \approx Q^\ell = \Psi^\ell \Sigma^\ell (V^\ell)^\mathrm{T} = \Psi^\ell H^\ell, \qquad \Psi^\ell = [\boldsymbol{\psi}_1, \ldots \boldsymbol{\psi}_\ell] \in \mathbb{R}^{N_\mathrm{t} \times \ell},\ H^\ell = [\boldsymbol{\eta}_1, \ldots \boldsymbol{\eta}_\ell]^\mathrm{T} \in \mathbb{R}^{\ell \times N_\mu} \quad (5)$$

where Ψ^ℓ is a matrix of the first ℓ orthonormal modes, which in our application represent the temporal dependence, $\left(V^\ell\right)^\mathrm{T}$ also comprises orthonormal vectors, and Σ^ℓ is a diagonal matrix of singular values σ_r

sorted in decreasing order; a fast decrease in singular values signifies that the matrices can be truncated quite substantially, with relative error $\varepsilon_{\mathrm{POD}}(\ell) = \left\|Q - Q^{\ell}\right\|_F / \|Q\|_F = 1 - \sqrt{\sum_{r=1}^{\ell} \sigma_r^2 / \sum_{r=1}^{n} \sigma_r^2}$, where $\|\cdot\|_F$ denotes the Frobenius norm.

Physically speaking, the temporal evolution of the BFV can be approximated for any simulated parameter configuration $\boldsymbol{\mu}_i$ as a superposition of the first ℓ POD modes $\{\boldsymbol{\psi}_r\}_{r=1}^{\ell}$. Their parameter-dependent amplitudes are located in H^{ℓ} in their respective columns. The approximate amplitudes $\tilde{\boldsymbol{\eta}}^{\ell}(\boldsymbol{\mu}^*)$ for a previously *unseen* parameter vector $\boldsymbol{\mu}^*$ can be obtained by interpolation or regression of known values in H^{ℓ}. In this contribution, interpolation by radial basis functions (RBFs) is used.

A problem arises when a POD & RBF approximation of the BFV for an unseen value of the Poisson's ratio ν is sought. In the BFV evolution, there are visible peaks when the elasto-plastic wave reaches the back face and is reflected; however, the speed of the elastic wave depends on ν as given by (4). Consequently, the peaks appear in different positions for different values of ν. However, POD&RBF is only able to give approximations using structures already present in the sampled snapshots and attempts to reconstruct the peak by seemingly averaging between neighboring peaks. See an illustration of this issue in Figure 3a or cf. [7] for a comprehensive review of MOR techniques for systems with strong advection.

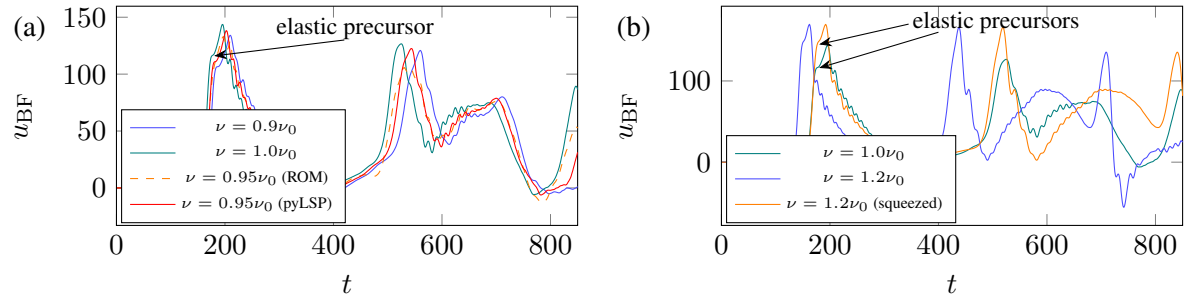

Figure 3: (a) Snapshots of $\boldsymbol{u}_{\mathrm{BF}}^h$ for two different values of ν and a POD&RBF prediction for ν not used for the ROM construction. The shortcomings of the method are the most prominent at the second peak at $t \approx 550$ ns. (b) Snapshots of $\boldsymbol{u}_{\mathrm{BF}}^h$ for $\nu = 1.0\nu_0$ and $\nu = 1.2\nu_0$. The point where the elastic wave reaches the back face is marked as elastic precursor and depends on ν; the plastic part of the wave arrives shortly afterwards. When the second snapshot is squeezed, the positions of the elastic precursors match, and the other peaks also move closer to each other's position.

To compensate for the different elastic wave speeds caused by different values of ν, we seek to transform the snapshots $\boldsymbol{u}_{\mathrm{BF}}^h(\boldsymbol{\mu}_i)$ prior to computing POD. The goal is to have the snapshots "squeezed" or "expanded" so that the elastic wave always reaches the same spot it would reach for some reference speed c_0. To this end, we introduce the continuous squeeze operator $\mathcal{T}^c$ and its inverse $(\mathcal{T}^c)^{-1}$, which "unsqueezes" the data back to its original position

$$\mathcal{T}^c := u_{\mathrm{BF}}\left(t, \boldsymbol{\mu}\right) \to u_{\mathrm{BF}}\left(t\frac{c_0}{c(\boldsymbol{\mu})}, \boldsymbol{\mu}\right), \qquad (\mathcal{T}^c)^{-1} := u_{\mathrm{BF}}\left(t, \boldsymbol{\mu}\right) \to u_{\mathrm{BF}}\left(t\frac{c(\boldsymbol{\mu})}{c_0}, \boldsymbol{\mu}\right), \tag{6}$$

where $c(\boldsymbol{\mu})$ is the speed of sound given by (4). Then, the discrete analogue of $\mathcal{T}^c$ acting on the columns of Q is denoted T^c. An illustration of this transformation is given in Figure 3b. Note that $\boldsymbol{u}_{\mathrm{BF}}^h$ needs to be sampled over some time interval $[0; T]$ to cover the time for which the experimental data was gathered. The squeeze operator can shorten or lengthen this time interval; to have a physically-relevant way of covering the time interval after squeezing and unsqueezing for all $\boldsymbol{\mu}$, the simulations for producing $\boldsymbol{u}_{\mathrm{BF}}^h$ have to be run for a longer time $[0; T_{\mathrm{sim}}]$, $T_{\mathrm{sim}} = T \max_{\boldsymbol{\mu}_i}(c(\boldsymbol{\mu}))/\min_{\boldsymbol{\mu}_i}(c(\boldsymbol{\mu}))$.

Before computing POD, the snapshots are transformed by T^c. During the ROM evaluation, the superposition of the POD modes $\{\boldsymbol{\psi}_r\}_{r=1}^{\ell}$ is transformed back by $(T^c)^{-1}$ to provide an estimate $\tilde{\boldsymbol{u}}_{\mathrm{BF}}^h$.

3 Results

Known and sought parameters We are working with the aluminum alloy 2024-T3 – its density ρ, Young modulus E and the static parameter of the Johnson-Cook model A are considered known and are given in Table 1. On the other hand, three plastic parameters and one elastic parameter – B, C, n and ν – are considered to be unknown and Table 1 gives them as starting points for the parameter estimation, taken from [3], and ranges considered as multiples of the starting points.

	$\rho\,[\mathrm{kg/m^3}]$	$E\,[\mathrm{GPa}]$	$A\,[\mathrm{MPa}]$	$B\,[\mathrm{MPa}]$	C	n	ν
(starting) value	2780	73.1	369	329	0.025	0.35	0.33
considered range	–	–	–	$[0.25, 1.5]$	$[0.25, 1.5]$	$[0.5, 1.5]$	$[0.8, 1.2]$

Table 1: Known material properties of AA2024-T3 [3], starting points for identifying "unknown" material parameters, considered range for the estimation as multiples of the starting values.

ROM construction To construct the ROM, we have simulated $\boldsymbol{u}^h_{\mathrm{BF}}$ for parameter configurations covering the considered $\mathcal{P}$. In total, 900 $\boldsymbol{u}^h_{\mathrm{BF}}$ snapshots were gathered. The values in $\boldsymbol{u}^h_{\mathrm{BF}}$ were sampled with a 1 ns step and an interval up to $T = 850\,\mathrm{ns}$ had to be covered. However, the simulations had to be run for a longer period of time to account for the effects of the squeeze operator. The lowest considered Poisson ratio $\nu = 0.264$ corresponded to $c = 5695\,\mathrm{m\,s^{-1}}$, while the highest $\nu = 0.396$ led to $c = 7396\,\mathrm{m\,s^{-1}}$. This yielded $T_{\mathrm{sim}} = 1104\,\mathrm{ns}$, i.e. the matrix of snapshots was $Q \in \mathbb{R}^{1104\times 900}$. The ROM itself comprised the mean and the first 15 POD modes, which conveyed $\varepsilon_{\mathrm{POD}}(15) = 1.16 \cdot 10^{-4}$.

Squeeze operator interpolation error While the continuous version of the squeeze operator is invertible for $c(\boldsymbol{\mu}) \neq 0$, its discrete version T^c does not shift the data exactly to the time-steps that were sampled and interpolation is necessary. Here, the error inflicted by using first order interpolation was

$$\varepsilon_{\mathrm{interp}} = \frac{\left\| \lfloor (T^c)^{-1} \left(T^c \left(Q \right) \right) \rfloor \right\|_F}{\left\| \lfloor Q \rfloor \right\|_F} = 9.84 \cdot 10^{-4}\,, \tag{7}$$

where the floor brackets $\lfloor \cdot \rfloor$ signify a block of matrix, which contains the relevant data for $t \in [0; T]$, in this particular case the top 850 rows.

Parameter estimation ROM is then used to provide an estimate $\tilde{u}_{\mathrm{BF}}(t, \boldsymbol{\mu}^*)$ for any $\boldsymbol{\mu}^* \in \mathcal{P}$. The estimate is compared with experimental values and the least-squares error is minimized using the L-BFGS-B algorithm, as implemented in the *scipy.optimize* Python library.

$$\min_{\boldsymbol{\mu}\in\mathcal{P}} \varepsilon_{\mathrm{exp}}, \qquad \varepsilon_{\mathrm{exp}} = \frac{1}{T} \int_0^T \left(\tilde{u}_{\mathrm{BF}}(t, \boldsymbol{\mu}) - u^{\mathrm{exp}}_{\mathrm{BF}}(t, \boldsymbol{\mu}_{\mathrm{real}}) \right)^2 \mathrm{d}t\,. \tag{8}$$

The optimal value using this measure was found at $B = 174\,\mathrm{MPa}$, $C = 0.0126$, $n = 0.431$, $\nu = 0.335$. The evolution of $\tilde{u}_{\mathrm{BF}}$ for these parameter values estimated by POD & RBF is found at Figure 4a, as well as u_{BF} recomputed using pyLSP. The ROM estimate and the re-computation are in good agreement. Compared to u_{BF} obtained by simulating for the parameters from Ayad et al. [3], the results are quite similar, the notable differences being smaller peaks at $t \approx 200\,\mathrm{ns}$ and $t \approx 500\,\mathrm{ns}$ and higher values towards the end. We have noticed that both of these effects correlated with decreasing B and C. However, the heights of the peaks also correspond to maximum pressure loading p_{max}, which has to be experimentally correlated for each laser. Some of these results then do not have to be attributed to the material really having low B and C, but to the simulation settings.

Furthermore, leading slices along each parameter through the estimated optimum, the error is extremely sensitive to changes in ν, somewhat sensitive to changes in C, but not particularly sensitive to B and n, see Figure 4b. The BFV alone is therefore not sufficient for truly reliable model calibration. However, B and n in the Johnson-Cook model both describe dependence on strain ϵ_{p}, not the strain *rate* $\dot{\epsilon}_{\mathrm{p}}$. Therefore, they could possibly be better calibrated using experimental data from non-dynamical methods, such as measurements of the residual stress via hole drilling.

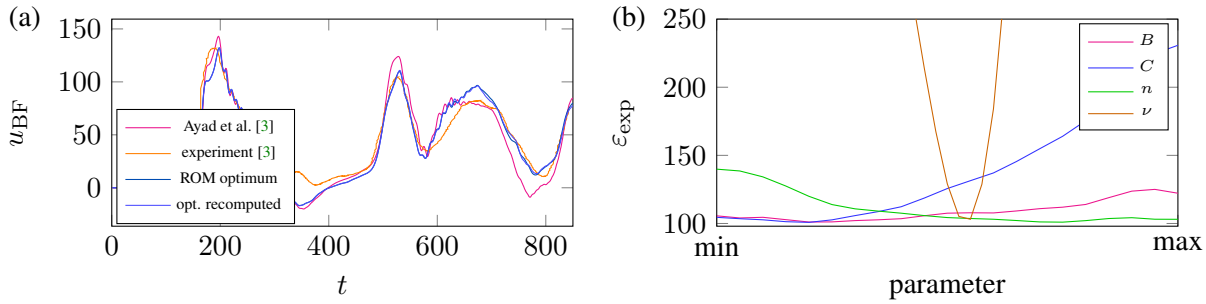

Figure 4: (a) BFV evolution for the optimal parameters estimated by ROM, recomputed by pyLSP and simulation done using the parameters by [3] vs. experimental data. (b) Slices through the error surface led through the found optimum.

4 Conclusion

In this contribution, we have combined the existing data-driven POD&RBF method for model order reduction with transformations based on the speed of sound in a material, to make it more suitable for quick estimation of elastic and plastic material parameters using the backface velocity (BFV) measurements. We then attempted to use it for the estimation of the parameters of the Johnson-Cook plasticity model and the Poisson's ratio of AA-2024-T3. Regrettably, the BFV was not particularly sensitive to some of the parameters and for a more reliable estimation, other experimental data will have to be used.

Acknowledgement

This work was supported by the grant TN02000069/009 (NCK MATCA2: PORTAL 2.0). The authors also acknowledge the financial support provided by the Ministry of Education, Youth, and Sports of the Czech Republic via the project No. CZ.02.01.01/00/23_020/0008501 (METEX), co-funded by the European Union.

References

[1] BRAISTED, William and BROCKMAN, Robert. Finite element simulation of laser shock peening. *International Journal of Fatigue*. 1999, vol. 21, no. 7, pp. 719-724. Available from: https://doi.org/10.1016/S0142-1123(99)00035-3

[2] ISOZ, Martin et al. Calibrated finite volume method-based simulation framework for laser shock peening. In RANDOLF, Vojtech and ZOLOTAREV, Igor (eds.). *Proceedings of the conference Engineering Mechanics 2023*. City: Milovy, Czech Republic, 2023, pp. 103-106. Available from: https://doi.org/10.21495/em2023-103.

[3] AYAD, Mohammad et al. Modeling of multi-edge effects in the case of laser shock loadings applied on thin foils: Application for material characterization of aluminum alloys. *Journal of Applied Physics*. 2022, vol. 131, no. 9. Available from: https://doi.org/10.1063/5.0080326.

[4] HARANT, Martin et al. Investigation of Johnson-Cook parameters of aluminium alloy 2024-T3. In FISCHER, Cyril and NAPRSTEK, Jiri (eds.). *Proceedings of the conference Engineering Mechanics 2022*. City: Milovy, Czech Republic, 2022, pp. 137-140. Available from: https://doi.org/10.21495/51-2-137.

[5] SIROVICH, Lawrence. Turbulence and the dynamics of coherent structure. part i, ii, iii. *Quarterly of Applied Mathematics.* 1987, vol. 45, no. 3, pp.561-571. Available from: https://doi.org/10.1090/qam/910463.

[6] JOHNSON, Gordon R. and COOK, William H. A constitutive model and data for metals subjected to large strains, high strain rates and high temperatures. In *Proceedings of the 7th International Symposium on Ballistics*. City: Den Haag, Netherlands, 1983, pp. 541-547.

[7] HESTHAVEN, Jan S.; PEHERSTORFER, Benjamin and UNGER, Benjamin. Nonlinear model reduction for transport-dominated problems. *Acta Numerica*. 2026. Preprint available from: https://arxiv.org/abs/2602.01397.

APPLIED MECHANICS 2026
April 13 - 15, 2026, České Budějovice, Czech republic

ON THE EFFECT OF SCALABILITY AND NORMALIZATION IN PHYSICS-INFORMED NEURAL NETWORKS

P. Kovář[1], J. Fürst[2]

Abstract: Physics-informed neural networks (PINNs) have emerged as a powerful framework for solving problems governed by partial differential equations. However, their performance and training stability are often sensitive to problem scaling. In this work, the effect of scalability in physics-informed learning, with particular emphasis on the normalization of input variables is presented. Appropriate input normalization plays a critical role in balancing data-driven and physics-based loss terms, improving gradient propagation, and enhancing convergence behavior, that is shown through a series of numerical experiments. These findings highlight normalization as a key yet often overlooked component in the effective deployment of PINNs.

Keywords: Physics-informed neural networks; scales; normalization

1 Introduction

In recent years, physics-informed neural networks (PINNs) have gained significant attention as a versatile and powerful approach for solving problems governed by partial differential equations [1, 2]. By embedding physical laws directly into the loss function of a neural network, PINNs offer a mesh-free alternative to traditional numerical methods, enabling the solution of forward and inverse problems across a wide range of scientific and engineering applications. Their ability to integrate observational data with governing equations makes them particularly attractive in scenarios where data are scarce or noisy.

Despite their promise, the practical deployment of PINNs remains challenging. One of the key difficulties lies in training stability and convergence efficiency, which are often sensitive to the formulation of the problem. In particular, the relative scaling of input variables, output quantities, and loss components can significantly influence the optimization process. Poorly scaled problems may lead to imbalanced gradients, slow convergence, or even failure to learn meaningful solutions.

Normalization is a standard technique in machine learning used to improve training dynamics by ensuring that inputs and outputs lie within comparable ranges. However, in the context of PINNs, normalization plays a more nuanced role. Since the loss function typically combines data-driven terms with physics-based residuals, improper scaling can distort their relative contributions, hindering the network's ability to simultaneously satisfy both. As a result, normalization is not merely a preprocessing step but a critical design choice that directly impacts the effectiveness of physics-informed learning.

Although several studies have addressed optimization strategies and architectural improvements for PINNs, the systematic investigation of scalability and input normalization remains limited. In particular, there is a lack of clear guidelines on how normalization affects gradient propagation, loss balancing, and overall convergence behavior in physics-informed settings.

This work aims to address this gap by examining the effect of scalability, with a specific focus on input normalization, in physics-informed neural networks. Through a series of numerical experiments, it is analyzed how normalization strategies influence training dynamics and solution accuracy. The results demonstrate that appropriate normalization can significantly enhance convergence and stability, underscoring its importance as a key yet often overlooked component in the successful application of PINNs.

[1] Patrik Kovář; Center of Aviation and Space Research, Faculty of Mechanical Engineering, Czech Technical University in Prague; Department of Technical Mathematics, Faculty of Mechanical Engineering, Czech Technical University in Prague, Prague, Czech Republic; Patrik.Kovar@fs.cvut.cz

[2] Jiří Fürst; Department of Technical Mathematics, Faculty of Mechanical Engineering, Czech Technical University in Prague, Prague, Czech Republic; Jiri.Furst@fs.cvut.cz

2 Task formulation

Let $u = u(x,t)$ denote the temperature field defined over the spatial domain $x \in \Omega = (0, L)$ and time interval $t \in (0, T]$. The evolution of the temperature is governed by the classical one-dimensional unsteady heat equation, which may depend on the thermal diffusivity parameter, and is given by [3]

$$\frac{\partial u}{\partial t}(x,t) = \alpha \frac{\partial^2 u}{\partial x^2}(x,t) + f(x,t;\alpha), \tag{1}$$

where $\alpha > 0$ denotes the thermal diffusivity coefficient. In the present study, the source term is neglected, *i.e.*, $f(x,t;\alpha) = 0$. The problem is complemented by the initial condition

$$u(x,0) = u_0(x) = -50x(x-1)(x-1/3)(x-0.5), \qquad x \in [0,1], \tag{2}$$

and homogeneous Dirichlet boundary conditions

$$u(0,t) = 0, \qquad u(1,t) = 0, \qquad t \in [0, 0.3]. \tag{3}$$

3 Method

Neural output of individual neural unit is consisted of two operations as it is shown in Figure 1. Product of the somatic operation $\widetilde{y}$, in general, can be expressed as [4]

$$\widetilde{y} = \sigma(s). \tag{4}$$

Let us assume N-th order neural unit, then product of synaptic operation can be written as [4, 5]

$$s = w_0 x_0 + \sum_{i=1}^{n} w_i x_i + \sum_{i=1}^{n}\sum_{j=i}^{n} w_{ij} x_i x_j + \cdots + \sum_{i_1=1}^{n} \cdots \sum_{i_N=i_{N-1}}^{n} w_{i_1 i_2 \ldots i_n} x_{i_1} x_{i_2} \ldots x_{i_n}, \tag{5}$$

where $x_0 = 1$ denotes bias and n stands for length of input feature vector.

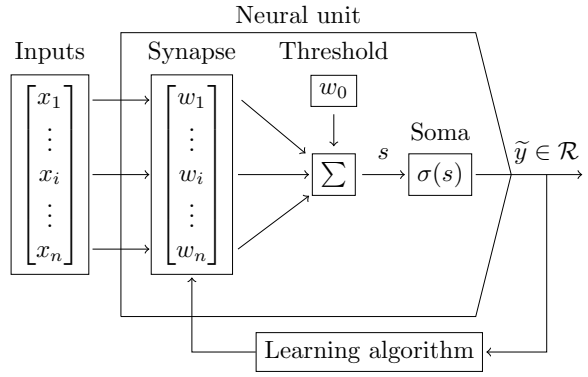

Figure 1: Single neural unit.

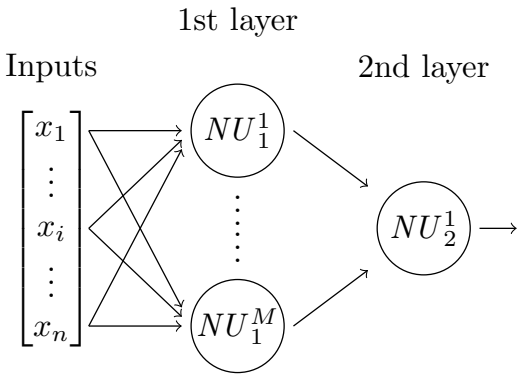

Figure 2: Shallow neural network.

A physics-informed neural network (PINN) is employed to approximate the solution $u(x,t)$ by a neural network representation $\hat{u}_\theta(x,t,\alpha)$ with trainable parameters θ. In the parametrized setting considered herein, the network takes the triplet $\{x,t,\alpha\}$ as input variables.

The training procedure is based on minimizing a composite loss function that enforces consistency with the governing partial differential equation (PDE), as well as the prescribed initial and boundary conditions:

$$\mathcal{L}(\theta) = \lambda_{\text{PDE}}\mathcal{L}_{\text{PDE}}(\theta) + \lambda_{\text{IC}}\mathcal{L}_{\text{IC}}(\theta) + \lambda_{\text{BC}}\mathcal{L}_{\text{BC}}(\theta), \tag{6}$$

where λ_{PDE}, λ_{IC}, and λ_{BC} are weighting coefficients.

The initial condition loss is evaluated over a set of points $\{(x_{\text{IC}}^i, t_{\text{IC}}^i)\}_{i=1}^{N_{\text{IC}}}$ at the initial time t_{IC}:

$$\mathcal{L}_{\text{IC}}(\theta) = \frac{1}{N_{\text{IC}}} \sum_{i=1}^{N_{\text{IC}}} \left| \hat{u}_\theta(x_{\text{IC}}^i, t_{\text{IC}}^i, \alpha) - u_{\text{IC}}(x_{\text{IC}}^i, t_{\text{IC}}^i, \alpha) \right|^2 . \tag{7}$$

Similarly, the boundary condition loss enforces the prescribed constraints on the boundary $\partial\Omega$ using a set of collocation points $\{(x_{\text{BC}}^i, t_{\text{BC}}^i)\}_{i=1}^{N_{\text{BC}}}$:

$$\mathcal{L}_{\text{BC}}(\theta) = \frac{1}{N_{\text{BC}}} \sum_{i=1}^{N_{\text{BC}}} \left| \hat{u}_\theta(x_{\text{BC}}^i, t_{\text{BC}}^i, \alpha) - u_{\text{BC}}(x_{\text{BC}}^i, t_{\text{BC}}^i, \alpha) \right|^2 . \tag{8}$$

The PDE residual loss $\mathcal{L}_{\text{PDE}}(\theta)$ is constructed based on the one-dimensional unsteady heat equation (1) defined over the domain $x \in [x_{\min}, x_{\max}]$ and $t \in [t_{\min}, t_{\max}]$. For improved numerical stability [6], the independent variables are linearly mapped to normalized coordinates $(\hat{x}, \hat{t}) \in [-1, 1]^2$ according to

$$\hat{x} = 2\frac{x - x_{\min}}{x_{\max} - x_{\min}} - 1, \qquad \hat{t} = 2\frac{t - t_{\min}}{t_{\max} - t_{\min}} - 1. \tag{9}$$

Application of the chain rule yields the transformed derivatives

$$\frac{\partial u}{\partial t} = \frac{2}{\Delta t}\frac{\partial u}{\partial \hat{t}}, \qquad \frac{\partial^2 u}{\partial x^2} = \frac{4}{(\Delta x)^2}\frac{\partial^2 u}{\partial \hat{x}^2}, \tag{10}$$

where $\Delta x = x_{\max} - x_{\min}$ and $\Delta t = t_{\max} - t_{\min}$.

Substituting these expressions into the governing equation leads to the scaled form

$$\frac{\partial u}{\partial \hat{t}} - \alpha\frac{2\Delta t}{(\Delta x)^2}\frac{\partial^2 u}{\partial \hat{x}^2} = 0. \tag{11}$$

Consequently, normalization introduces an effective diffusion coefficient

$$\alpha_{\text{scaled}} = \alpha\frac{2\Delta t}{(\Delta x)^2}, \tag{12}$$

which must be consistently incorporated into the physics-informed formulation.

The PDE loss is therefore evaluated over a set of collocation points $\{(x_{\text{PDE}}^i, t_{\text{PDE}}^i)\}_{i=1}^{N_{\text{PDE}}}$ as

$$\mathcal{L}_{\text{PDE}}(\theta) = \frac{1}{N_{\text{PDE}}} \sum_{i=1}^{N_{\text{PDE}}} \left| \frac{\partial \hat{u}_\theta}{\partial t}(x_{\text{PDE}}^i, t_{\text{PDE}}^i, \alpha) - \alpha\frac{2\Delta t}{(\Delta x)^2}\frac{\partial^2 \hat{u}_\theta}{\partial x^2}(x_{\text{PDE}}^i, t_{\text{PDE}}^i, \alpha) \right|^2 , \tag{13}$$

where the required derivatives of $\hat{u}_\theta(x, t, \alpha)$ with respect to $\{x, t\}$ are computed via automatic differentiation algorithm introduced by Baydin in [7].

The diffusion coefficient α is treated as a parametric input and sampled prior to training. To mitigate bias toward larger values, sampling is performed uniformly in the square-root space:

$$s \sim \mathcal{U}\left(\sqrt{\alpha_{\min}}, \sqrt{\alpha_{\max}}\right), \qquad \alpha = s^2, \tag{14}$$

which induces a probability density proportional to $\alpha^{-1/2}$ over the interval $[\alpha_{\min}, \alpha_{\max}]$. This strategy enhances the representation of low-diffusivity regimes while maintaining a bounded sampling domain.

Perceptron network architectures employed 32 and 256 neurons in the first and second layer as shown in Figure 2, respectively [8]. The optimization process was carried out using the Adam algorithm with an initial learning rate $\mu = 0.001$. An exponential learning rate scheduler with decay factor $\gamma = 0.95$ was applied every 100 from total 1000 epochs. Each epoch consisted of 50 mini-batches, where each mini-batch contained five values of the diffusion coefficient α sampled using Latin hypercube sampling (LHS) over the prescribed parameter range. The collocation points were also generated using LHS, with 256 points assigned to the initial condition and to boundary conditions and 2048 points distributed within the interior of the domain.

4 Results

A reference solution for comparison was obtained using the finite difference method (FDM). The governing heat equation was discretized using an explicit Euler scheme for the transient term and a central difference scheme for the diffusive term, with time and spatial step sizes of $\Delta t = 3 \times 10^{-5}$ and $\Delta x = 0.01$, respectively. The resulting testing error, evaluated in terms of the root mean square error (RMSE), is reported for selected values of the thermal diffusivity coefficient $\alpha = \{0.02, 0.4, 0.9\}$ and at different time instances. The effect of scaling the governing equation (Eqns. (1) and (11)) under normalized inputs $\{x, t\}$ is illustrated in Figure 3.

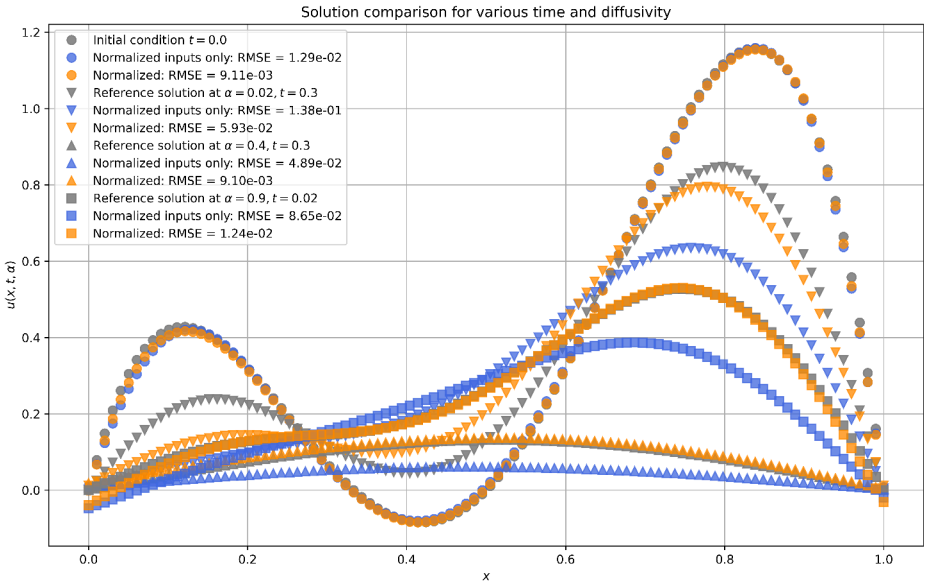

Figure 3: Effect of derivatives scaling as a result of inputs normalization.

It can be observed that the RMSE is reduced in all considered cases when the scaling of derivatives, induced by input normalization, is properly accounted for. Further improvement is achieved by applying scaling prior to sampling the diffusion coefficient α, as described in Eq. (14). This leads to increased solution accuracy, particularly in the low-diffusivity regime, as demonstrated in Figure 4.

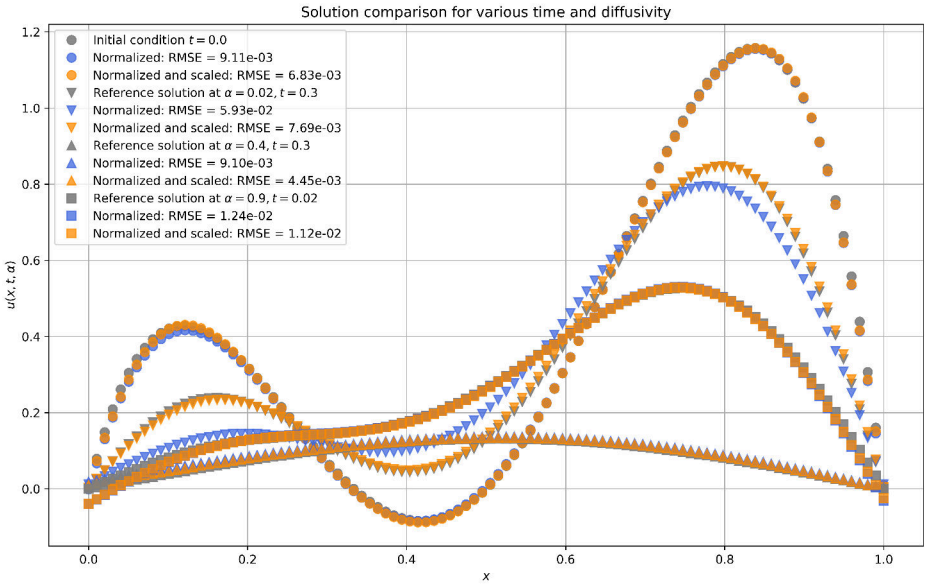

Figure 4: Effect of the thermal diffusivity scaling before uniform sampling.

A comparison of the total training loss across all testing scenarios, *i.e.*, thermal diffusivity values $\alpha = \{0.02, 0.4, 0.9\}$ and time instances $t = \{0, 0.02, 0.3\}$, is presented in Figure 5. The results indicate that normalization of the independent input variables $\{x, t\}$ without consistent scaling of the governing equation, through the modified diffusivity α_{scaled}, leads to testing errors that are higher by an order of magnitude. Furthermore, scaling the diffusivity coefficient α prior to sampling improves both convergence speed and accuracy, yielding testing errors that are an order of magnitude lower than those obtained with uniform sampling, and up to two orders of magnitude lower compared to the unscaled case.

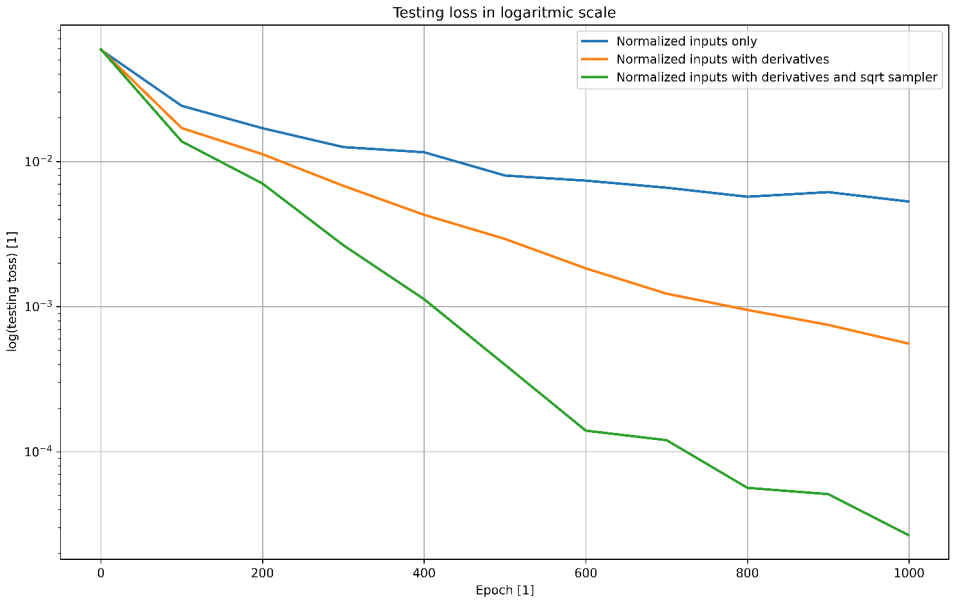

Figure 5: Testing error evolution during epochs.

5 Conclusion & Further work

This study investigated the effect of input normalization, governing equation scaling, and parameter sampling strategies on the performance of physics-informed neural networks (PINNs) for solving the one-dimensional unsteady heat equation. The results demonstrate that normalization of the input variables alone is insufficient and may even lead to degraded accuracy if not accompanied by consistent scaling of the governing equation.

In particular, incorporating the scaling induced by the normalization of the independent variables into the differential operator significantly improves the solution accuracy. As shown in Table 1, this reduces the total RMSE by approximately one order of magnitude when compared to the unscaled case. Furthermore, the choice of sampling strategy for the diffusion coefficient α was found to have a substantial impact. Sampling in the square-root space, as opposed to uniform sampling, further improves the accuracy by an additional order of magnitude, yielding the lowest observed error of 2.67×10^{-5}.

These findings highlight that proper treatment of scaling and normalization is essential for stable and accurate training of PINNs. In particular, consistency between input normalization and the formulation of the governing equations, together with an appropriate parameter sampling strategy, plays a critical role in achieving reliable results.

Input normalization	*Equation scaling*	*α sampling*	*Total RMSE*
yes	no	uniform	5.31×10^{-3}
yes	yes	uniform	5.57×10^{-4}
yes	yes	sqrt	2.67×10^{-5}

Table 1: Summary of the results achieved.

Future research will focus on extending the present framework to more complex parametric settings. One natural extension is the inclusion of additional input parameters, such as variations in the initial condition, which would further increase the dimensionality and complexity of the learning problem.

Moreover, the methodology will be applied to more challenging nonlinear problems, such as the viscous Burgers' equation, where the presence of the convective term introduces stronger nonlinearity and sharper solution features. This will allow for a more comprehensive assessment of the interplay between normalization, scaling, and training dynamics in physics-informed neural networks.

Such extensions are expected to provide deeper insights into the robustness and generalization capabilities of PINNs in more realistic and demanding scenarios.

Acknowledgement

Authors would like to acknowledge support from the ESIF, EU Operational Programme Research, Development and Education, and from the Center of Advanced Aerospace Technology (CZ.02.1.01/0.0/0.0/16019/0000826), Faculty of Mechanical Engineering, Czech Technical University in Prague and also the grant agency of the Czech Technical University in Prague, grant No. SGS25/123/OHK2/3T/12.

References

1. RAISSI, Maziar; PERDIKARIS, Paris; KARNIADAKIS, George E. Physics-informed neural networks: A deep learning framework for solving forward and inverse problems involving nonlinear partial differential equations. *Journal of Computational physics*. 2019, vol. 378, pp. 686–707.
2. KARNIADAKIS, George Em; KEVREKIDIS, Ioannis G; LU, Lu; PERDIKARIS, Paris; WANG, Sifan; YANG, Liu. Physics-informed machine learning. *Nature Reviews Physics*. 2021, vol. 3, no. 6, pp. 422–440.
3. INCROPERA, Frank P; DEWITT, David P; BERGMAN, Theodore L; LAVINE, Adrienne S, et al. *Fundamentals of heat and mass transfer*. Vol. 6. Wiley New York, 1996.
4. GUPTA, Madan; JIN, Liang; HOMMA, Noriyasu. *Static and dynamic neural networks: from fundamentals to advanced theory*. John Wiley & Sons, 2004.
5. GUPTA, Madan M.; BUKOVSKY, Ivo; HOMMA, Noriyasu; SOLO, Ashu MG; HOU, Zeng-Guang. Fundamentals of higher order neural networks for modeling and simulation. In: *Artificial Higher Order Neural Networks for Modeling and Simulation*. IGI Global Scientific Publishing, 2013, pp. 103–133.
6. RAISSI, Maziar; PERDIKARIS, Paris; KARNIADAKIS, George Em. Physics informed deep learning (part I): Data-driven solutions of nonlinear partial differential equations. *arXiv preprint arXiv: 1711.10561*. 2017.
7. BAYDIN, Atilim Gunes; PEARLMUTTER, Barak A; RADUL, Alexey Andreyevich; SISKIND, Jeffrey Mark. Automatic differentiation in machine learning: a survey. *Journal of machine learning research*. 2018, vol. 18, no. 153, pp. 1–43.
8. KOVÁŘ, P.; FÜRST, J. Higher-Order Physics-Informed Neural Networks for Parametric Solution of The Unsteady Heat Equation. In: *Topical Problems of Fluid mechanics 2026*. Institute of Thermomechanics, AS CR, 2026, pp. 114–119. ISBN 978–80–87012–92–5. ISSN 2336–5781.

APPLIED MECHANICS 2026
April 13 - 15, 2026, České Budějovice, Czech republic

CONCEPT OF VIBRATION ATTENUATION OF PRIMARY STRUCTURE USING COMPUTED TORQUE CONTROL OF 3-DOF MULTIBODY NONLINEAR ABSORBER

Karel Kraus[1], Zbyněk Šika[2]

Abstract: This paper proposes initial study of nonlinear vibration absorption of a planar flexible structure using an active multibody 3-DoF absorber. Following on from the previous linear control approach incorporating passive effects nonlinearities only, newly the overall nonlinear multibody model is utilized via computed torque control algorithm. Acceleration signals from the primary flexible structure will be used as target control output in the whole feedback. The aim of the study is simulation verification of the concept using the identified nonlinear absorber model, which is the initial step towards experimental verification of absorption.

Keywords: multi-DoF absorber, vibration suppression, Computed Torque Control

1 Introduction

Vibration attenuation may be implemented via various approaches, such as isolation, absorption or structure redesign, all with using passive or active elements. In the case of active vibration absorption, additional mass is attached to the primary flexible structure and equipped with an actuator. Linear voice-coil actuator is generally viable option, since it has no inner stiffness or gears, and can be driven solely with respect to additional force brought into the system. In the previous work [1], vibration attenuation of primary flexible structure has been performed using nonlinear 3-DoF symmetric absorber (Figure 1.). The main effort of the control design has been aimed to absorber control algorithm based solely on feedback from relative position of the absorber to the primary flexible structure. In the following work, the attention is paid to control algorithm based on overall system model with additional sensors.

A computed torque control (CTC) is widely used for robotic manipulators [2] or manipulator joints with friction modelling [3]. Thus, CTC is being designed and applied to control voice-coil actuators of the attached absorber using additional sensors attached to the primary flexible structure.

2 Absorber design and control algorithm

The 3-DoF absorber is designed such that it can operate in all directions of 2D space, i.e. two translational and one rotational. Also, due to its symmetrical design, it is able to achieve unifrequency for its all three eigenmodes. The main absorbing mass is attached to the primary flexible structure using three legs composed of multiple parallel elements, such as linear bearing, voice-coil actuator, springs and linear encoders.

Reading of these linear encoders is performed with 10^{-7} mm resolution and 10 kHz sample rate, therefore, they are capable to provide positional feedback precise enough for control algorithm and passive effects identification.

[1] Ing. Karel Kraus, Ph.D., Czech Technical University in Prague, Department of Mechanics, Biomechanics and Mechatronics, Technická 4, 160 00 Praha, Czech republic, karel.kraus@fs.cvut.cz
[2] prof. Ing. Zbyněk Šika, Ph.D., Czech Technical University in Prague, Department of Mechanics, Biomechanics and Mechatronics, Technická 4, 160 00 Praha, Czech republic, zbynek.sika@fs.cvut.cz

The flexible primary structure is then equipped with three-directional acceleration sensor. Rotating unbalanced mass attached to the structure is used to bring external vibration excitation to the system. So far, acceleration signals have been used solely for absorber control algorithms tuning and verification. In current approach, the model of the whole structure is used for CTC algorithm, therefore, the acceleration signals are utilized as a direct input to the control algorithm, along with linear encoders in the absorber's legs. Desired acceleration of the flexible primary structure is used as a target for vibration suppression and computed forces for voice-coil actuators are the only output.

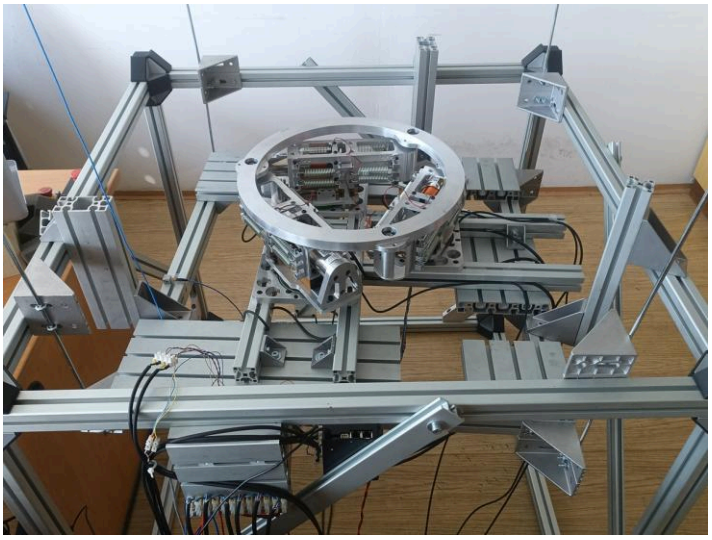

Figure 1: Flexible structure with 3-DoF absorber attached via linear bearings and voice-coil actuators.

Conclusion

Control algorithms based only on feedback from the absorber linear encoders are able to significantly reduce vibrations of the primary structure, but are also more prone to environmental change and not effective for small vibration amplitudes. Current simulations of the whole structure incorporating CTC promise more robust control of the primary structure vibration attenuation at the price of modelling of the primary structure dynamics.

Acknowledgement

This work has been supported by the Czech Science Foundation project 25-16357S "Absorbing mechanisms with nonlinear dynamics for active reduction of periodic motions and forces in machines".

References

[1] KRAUS, Karel; KOČANDRLE, Petr a ŠIKA, Zbyněk. Identification and modeling of 3-DoF mechanism with nonlinear friction effects by combination of LuGre and neural network modeling. *Mechanical Systems and Signal Processing*. 2025, vol. 239, s. 113218. ISSN 0888-3270.

[2] ŞEN, Gökçen Devlet a ÖKE GÜNEL, Gülay. NARMA-L2–based online computed torque control for robotic manipulators. *Transactions of the Institute of Measurement and Control*. 2023, vol. 45, no. 13, s. 2446-2458. ISSN 0142-3312.

[3] SHEN, Xiaobin; ZHOU, Kun; YU, Rui a WANG, Binrui. Design of Adaptive RBFNN and Computed-torque Control for Manipulator Joint Considering Friction Modeling. *International Journal of Control, Automation and Systems*. 2022, vol. 20, no. 7, s. 2340-2352. ISSN 1598-6446.

APPLIED MECHANICS 2026
April 13 - 15, 2026, České Budějovice, Czech republic

MODIFIED COMPUTED TORQUE CONTROL FOR OPEN-CHAINS WITH FLEXIBILITIES AND NONLINEAR ABSORBER

J. Krivošej[1], S. Čelikovský[2], Z. Šika[3]

Abstract: This article uses simulations to study the concept of a planar open-chain system consisting of primary structure with requested motion of its end-point and nonlinear absorber as an auxiliary structure. The aim is to improve accuracy of tracking the end-point motion of the chain including suppression of unwanted vibrations. For the given system, the possibility of coordinated control of this entire nonlinear system is studied with the aim of determining its applicability and limitations. The basis is the use of a modified version of the computed torque method.

Keywords: Planar open-chain system; nonlinear absorber; auxiliary structure; vibration suppression; modified computed torque control

1 Introduction

Traditional active vibration absorbers, frequently implemented with control strategies such as the Linear Quadratic Regulator [1] or delayed resonator [2, 3], are generally well-suited for stable, steady-state vibrations. However, they may encounter performance limitations when operating conditions change dramatically, which is typical during the macroscopic motion of a mechanism. In the case of complex spatial vibrations at a given frequency range, active absorbers can be utilized for comprehensive suppression. Nevertheless, such absorbers remain predominantly tuned to a specific operating area within a given configuration [4]. In contrast, this paper focuses on the global dynamics of the non-linear system.

In our approach, we perceive the non-linear absorber as a form of "non-linear antiresonance". In this context, the objective is to leverage the absorber's non-linear dynamic behavior to maintain the system's operating point along a desired trajectory. Conversely, we perceive the opposite and simultaneous complement in the eigenmotion of the system [5], which acts as a "non-linear resonance", a natural motion that minimizes the required external energy by simply exchanging kinetic and potential energy without altering the total energy.

The core concept is to intelligently route unwanted kinetic energy into the absorbers, where it can be temporarily stored or simultaneously repurposed to assist the overall motion of the mechanism and drive the targeted degrees of freedom during subsequent motions. As a first approximation, a modified Computed Torque Control (CTC) strategy is implemented and evaluated in a planar open-chain system.

2 Planar Open-chain Mechanism with Flexibilities

This section details the physical model of the investigated planar serial structure, which is modeled as a four-link open kinematic chain, combining a primary double-pendulum mechanism with a coupled secondary double-pendulum that functions as a non-linear absorber. The structure is schematically depicted in Fig. 1.

[1] Jan Krivošej; Czech Technical University in Prague, Faculty of Mechanical Engineering, Department of Mechanics, Biomechanics and Mechatronics; jan.krivosej@fs.cvut.cz

[2] Sergej Čelikovský; Czech Technical University in Prague, Faculty of Electrical Engineering, Department of control engineering; celikser@fel.cvut.cz

[3] Zbyněk Šika; Czech Technical University in Prague, Faculty of Mechanical Engineering, Department of Mechanics, Biomechanics and Mechatronics; zbynek.sika@fs.cvut.cz

For the purpose of initial proof-of-concept testing, the evaluated structure features a specific partially underactuated configuration. Active control is introduced into the system via two actuated joints. The first actuator is located at the base joint (point O), providing an active driving torque M_2. The second actuator is positioned at the connection between the primary mechanism's end-effector and the absorber, delivering an intermediate active torque M_4.

The underactuated nature of the system arises from the remaining two passive joints, which exhibit linear rotational compliance. These compliant joints are modeled as torsional springs with stiffness coefficients k_{t23} and k_{t45}. This alternating arrangement of active torques and passive elastic elements allows the control strategy to actively route energy between the actuated degrees of freedom and the compliant ones.

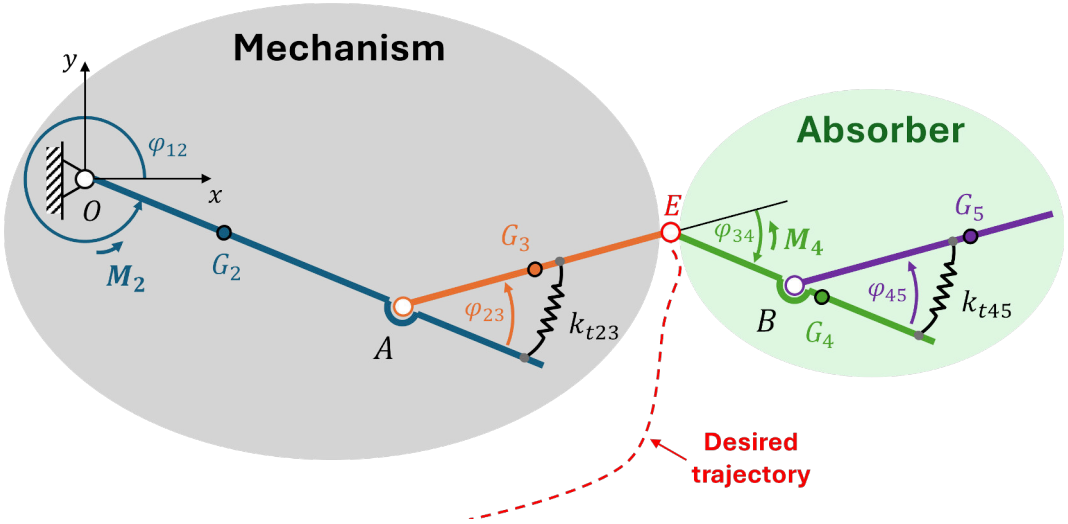

Figure 1: Schematic of the planar open-chain system. The structure integrates a primary double-pendulum mechanism with a coupled double-pendulum non-linear absorber. Active actuation is applied at joints O and E, while joints A and B exhibit torsional compliance modeled as linear springs.

3 Simulation Results

To validate the proposed modified CTC, a demonstrative simulation was performed using a complex reference trajectory. The desired motion was generated as a multisine signal comprising five superimposed harmonic components to test the system's dynamic tracking capabilities. As illustrated in Fig. 2, the primary structure successfully tracks this highly dynamic reference, confirming the controller's ability to achieve precise stabilization of the targeted degrees of freedom. The corresponding dynamic response of the non-linear absorber is depicted in Fig. 3, demonstrating its continuous engagement during the motion. Furthermore, Fig. 4 presents the structure's actuation effort, detailing the required active torques (M_2 and M_4) generated by the control law to effectively manage the interplay between the driven axes and the unactuated compliant joints.

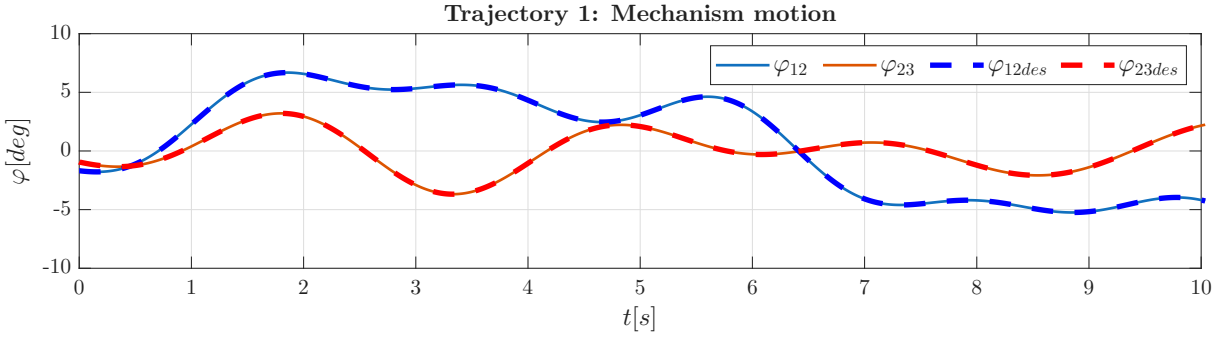

Figure 2: Tracking performance of the primary mechanism along Trajectory 1, comparing the actual (φ_{12}, φ_{23}) and desired (φ_{12des}, φ_{23des}) angular coordinates.

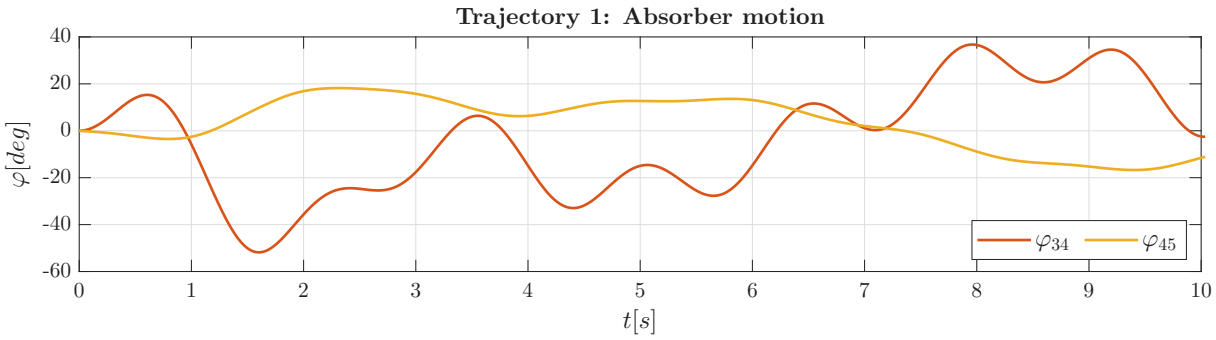

Figure 3: Absorber motion during the tracking of Trajectory 1, represented by the angular coordinates φ_{34} and φ_{45}.

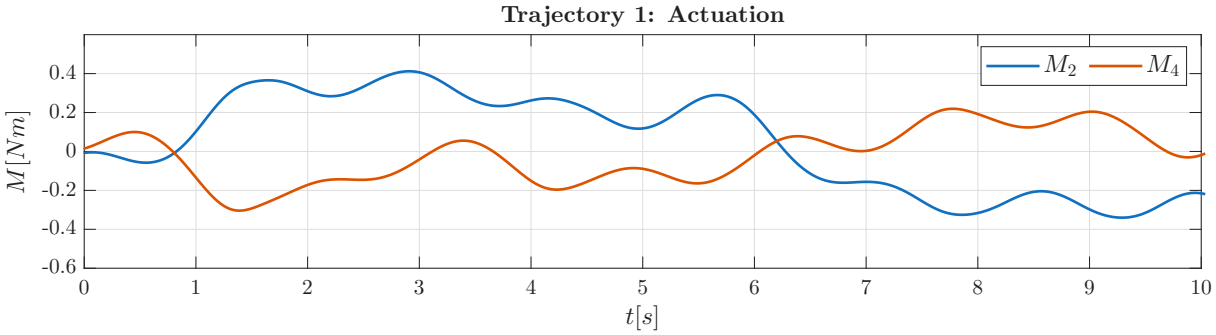

Figure 4: Simulation curves of the active joints O and E with torques M_2 and M_4, respectively.

4 Conclusion

This paper presented a dynamic evaluation of a planar open-chain mechanism consisting of a primary double-pendulum coupled with a secondary double-pendulum acting as a non-linear absorber. A modified Computed Torque Control method was applied to this partially underactuated structure. The proposed approach was tested through simulations on a multisine reference trajectory. The results confirm that the proposed controller effectively manages the interplay between active actuation and passive compliance, achieving precise tracking performance for the targeted degrees of freedom.

Several potential directions are currently being considered for future research. These may include the experimental validation on a physical prototype to assess the impact of unmodeled friction, or the extension of the algorithm to ensure greater robustness against external disturbances.

Acknowledgement

The work has been supported by the Czech Science Foundation project 25-16357S “Absorbing mechanisms with nonlinear dynamics for active reduction of periodic motions and forces in machines” and partly by the project SGS25/125/OHK2/3T/12 “Mechatronics and adaptronics 2025 of the Czech Technical University in Prague”.

References

[1] KRAUS, Karel; ŠIKA, Zbyněk; BENEŠ, Petr; KRIVOŠEJ, Jan a VYHLÍDAL, Tomáš. Mechatronic robot arm with active vibration absorbers. Online. Journal of Vibration and Control. 2020, vol. 26, no. 13-14, p. 1145-1156. ISSN 1077-5463. Available from: https://doi.org/10.1177/1077546320918488.

[2] OLGAC, Nejat; ELMALI, Hakan; HOSEK, Martin a RENZULLI, Mark. Active Vibration Control of Distributed Systems Using Delayed Resonator With Acceleration Feedback. Online. Journal of Dynamic Systems, Measurement, and Control. 1997, vol. 119, no. 3, p. 380-389. ISSN 0022-0434. Available from: https://doi.org/10.1115/1.2801269

[3] OLGAC, Nejat a JENKINS, Ryan. Actively Tuned Noncollocated Vibration Absorption: An Unexplored Venue in Vibration Science and a Benchmark Problem. Online. IEEE Transactions on Control Systems Technology. 2021, vol. 29, no. 1, p. 294-304. ISSN 1063-6536. Available from: https://doi.org/10.1109/tcst.2020.2973603.

[4] ŠIKA, Zbyněk; KRIVOŠEJ, Jan a VYHLÍDAL, Tomáš. Three dimensional delayed resonator of Stewart platform type for entire absorption of fully spatial vibration. Online. Journal of Sound and Vibration. 2024, vol. 571, s. 118154. ISSN 0022-460X. Available from: https://doi.org/10.1016/j.jsv.2023.118154

[5] KRIVOŠEJ, Jan; BENEŠ, Petr; ZAVŘEL, Jan; BALON, Aleš; HALAMKA, Vojtěch and ŠIKA, Zbyněk. Energy efficient robots based on structures with tensegrity features and cable-driven mechanisms. Online. Mechanism and Machine Theory. 2023, vol. 187, s. 105364. ISSN 0094-114X. Available from: https://doi.org/10.1016/j.mechmachtheory.2023.105364.

APPLIED MECHANICS 2026
April 13 - 15, 2026, České Budějovice, Czech republic

ON USAGE OF IMMERSED BOUNDARY METHOD TO SIMULATE COOLING OF MECHANICAL METAMATERIALS

L. Kubíčková[1], M. Isoz[2]

Abstract: Mechanical metamaterials have become popular since their inner structure can be designed to give them unique properties. We focus on metamaterials used in molds for die casting that must withstand contact with molten metal while enabling effective cooling. Securing both properties requires optimization of the metamaterial inner structure. In this contribution, we present a numerical solver designed for such optimization. The solver is based on our custom variant of the immersed boundary method that was extended to include turbulent heat transfer. In several benchmark simulations and one simulation of metamaterial cooling, the solver showed good potential for future metamaterial optimization.

Keywords: computational fluid mechanics; mechanical metamaterial; immersed boundary method; heat transfer

1 Introduction

Mechanical metamaterials are artificial materials with unique physical properties that arise from the specific design of their inner structure [1]. Our focus is on metamaterials used in molds for die casting where specific heat transfer properties are sought. In particular, dies must allow fast cooling while maintaining sufficient bulk to withstand contact with molten metal and pressure loading in tens of MPa. Finding the optimal metamaterial design for a given die can be done by topology optimization. However, topology optimization is very computationally demanding [2].

One way to reduce the computational cost of optimization is to employ an immersed boundary (IB) method to simulate the metamaterial behavior. The IB method allows one to use a single computational mesh for all tested topologies, as the distribution of the solid phase is represented by an indicator scalar field and adjustment of governing equations. Hence, the mesh does not have to be remade, saving a lot of computational resources. This approach has been used, for example, in the optimization of turbulent channel flow by Kubo et al. [3], or in the optimization of beam supports by Jenkins and Maute [4].

To develop an IB solver for the optimization of metamaterials used in die casting, our first focus is to enable simulation of the coolant flow where the IB method has to be coupled with equations of heat transfer and allow turbulent flow simulations. In Ren et al. [5], an IB solver for thermal flow has been presented, but it operates only in the laminar regime. In Narváez et al. [6], they have introduced an IB solver capable of turbulent heat transfer simulation, but the turbulence was solved by means of direct numerical simulation which is unfeasible in optimization. To the authors knowledge, a combination of the IB method with cheap turbulence modeling and heat transfer is lacking in the literature.

In this contribution, we present recent advances in the development of our IB solver for simulations of heat transfer in turbulent flows where the turbulence is handled via the Reynolds-averaged simulation (RAS) approach. The solver is based on our custom variant of the IB method, the hybrid fictitious domain-immersed boundary method (openHFDIB) [7], which has previously been connected to the RAS approach (openHFDIBRANS) [8]. The connection with turbulent heat transfer is being developed for simulations of mechanical metamaterials. The capabilities of the combined solver are tested in a series of metamaterial simulations where the results are compared with standard mesh-conforming solvers available in OpenFOAM [9]. The solver sensitivity to mesh resolution and simulation settings is examined, as well as its ability to capture trends in heat transfer induced by changes in the metamaterial structure.

[1] Lucie Kubíčková; Institute of Thermomechanics, Czech Academy of Sciences (CAS), Dolejškova 1402/5; 182 00, Prague, CZ; luciekub@it.cas.cz

[2] Martin Isoz; Institute of Thermomechanics, Czech Academy of Sciences (CAS), Dolejškova 1402/5; 182 00, Prague, CZ; isozm@it.cas.cz

2 Methods

In openHFDIBRANS, the presence of a solid body inside a computational domain is indicated by a scalar field λ. This field is defined as

$$\lambda = \begin{cases} 0 & \text{if } \Omega_P \subset \Omega_\mathrm{f} \\ 1 & \text{if } \Omega_P \subset \Omega_\mathrm{s} \\ \tilde{\lambda} \in (0,1) & \text{if } \Omega_P \subset \Omega_\mathrm{fs} \end{cases}, \quad \tilde{\lambda} = 0.5 \left[1 - \tanh\left(\frac{\sigma}{V_P^{\frac{1}{3}}} \right) \right], \tag{1}$$

where Ω_P is a finite volume (FV) computational cell, Ω_f is the part of the computational domain that is fully in fluid, Ω_s the part fully in solid, and Ω_sf the part containing cells intersected by the fluid-solid interface. Next, σ is the signed perpendicular distance from the Ω_P cell center to the solid body surface, and V_P is the cell volume. For a cylindrical solid body, the λ field is illustrated in Figure 1a.

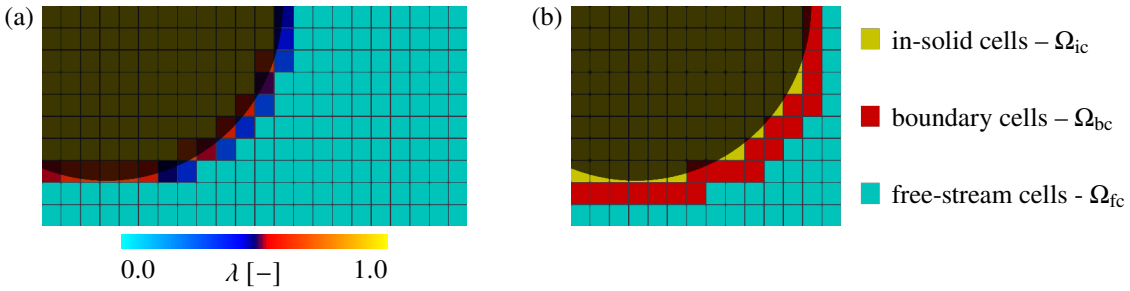

Figure 1: Inclusion of a solid body (gray). (a) Indicator field λ. (b) Sorting of FV cells into cell groups.

Afterward, the λ field is used to sort the cells into three groups: (i) in-solid cells (Ω_ic), (ii) boundary cells (Ω_bc) and (iii) free-stream cells (Ω_fc). The cell groups are indicated in Figure 1b. Based on the cell group, immersed boundary induced source terms are either switched on or off.

To describe the turbulent flow, the incompressible Reynolds-averaged Navier-Stokes (RANS) equations are used and coupled with the equation of turbulent heat transfer. The effect of the immersed boundary is included in two IB-induced source terms, $\boldsymbol{f}_\mathrm{ib}$ and Q_ib. Eventually, the equations have the form

$$\begin{gathered} \mathcal{M}(\boldsymbol{u}) \equiv \nabla \cdot (\boldsymbol{u} \otimes \boldsymbol{u}) - \nabla \cdot \left[(\nu + \nu_\mathrm{t}) \left(\nabla \boldsymbol{u} + \nabla \boldsymbol{u}^\mathrm{T} \right) \right] = -\nabla \tilde{p} + \boldsymbol{f}_\mathrm{ib}, \quad \nabla \cdot \boldsymbol{u} = 0 \\ \mathcal{L}(T) \equiv \nabla \cdot (\boldsymbol{u}\, T) - \nabla \cdot \left[(\alpha + \alpha_\mathrm{t})\ \nabla T \right] = Q_\mathrm{ib}\,, \end{gathered} \tag{2}$$

where $\tilde{p}$ is the averaged kinematic pressure, $\boldsymbol{u}$ the averaged velocity, ν the kinematic viscosity, and ν_t the turbulent viscosity. Next, T is the averaged temperature, α the thermal diffusivity, and α_t the turbulent thermal diffusivity. As a turbulence closure model, the k-ω model [10] was chosen. The implemented form of the turbulence model equations is

$$\begin{aligned} \mathcal{N}(k) &\equiv \nabla \cdot (\boldsymbol{u}\, k) - \nabla \cdot \left[\left(\nu + \nu_\mathrm{t}/\sigma_{k_1} \right) \nabla k \right] - P_k + \beta^* \, k\, \omega = S_\mathrm{ib} \\ \mathcal{P}(\omega) &\equiv \nabla \cdot (\boldsymbol{u}\, \omega) - \nabla \cdot \left[\left(\nu + \nu_\mathrm{t}/\sigma_{\omega_1} \right) \nabla \omega \right] - C_{\alpha 1} \frac{\omega}{k} P_k + C_{\beta 1}\, \omega^2 = 0\,, \end{aligned} \tag{3}$$

where k is the turbulence kinetic energy, P_k its production, and ω its specific dissipation. The remaining symbols represent model constants.

Furthermore, the IB-induced source terms in (2) and (3) are computed as

$$\boldsymbol{f}_\mathrm{ib} = \beta_{\boldsymbol{u}}(\lambda)\ [\ \mathcal{M}(\boldsymbol{u}_\mathrm{ib}) + \nabla \tilde{p}\ ]\,, \quad Q_\mathrm{ib} = \beta_T(\lambda)\, \mathcal{L}(T_\mathrm{ib}), \quad S_\mathrm{ib} = \beta_k(\lambda)\, \mathcal{N}(k_\mathrm{ib})\,, \tag{4}$$

where $\beta_{\boldsymbol{u}}$, β_T and β_k are masking fields that limit the source terms to a specific area, and $\boldsymbol{u}_\mathrm{ib}$, T_ib, and k_ib are imposed fields that are enforced in the respective cells. Note that there is no additional source term in the ω equation, since ω approaches infinity near smooth walls [10]. Nonetheless, a masking field β_ω

and imposed field ω_{ib} are also defined, but the imposed field is enforced by direct manipulation with the discretization matrix.

Lastly, the setting of the masking fields reflects the cells groups shown in Figure 1b. For a FV computational cell Ω_P, the fields are defined as

$$\beta_{\boldsymbol{u}} = \beta_k = \begin{cases} 1 & \text{if } \Omega_P \subset \Omega_{\mathrm{ic}} \\ 1 & \text{if } \Omega_P \subset \Omega_{\mathrm{bc}} \text{ and } y^+_{\mathrm{ib}} < y^+_{\mathrm{lam},\boldsymbol{u}} \\ 0 & \text{if } \Omega_P \subset \Omega_{\mathrm{fc}} \end{cases}, \quad \beta_T = \begin{cases} 1 & \text{if } \Omega_P \subset \Omega_{\mathrm{ic}} \\ 1 & \text{if } \Omega_P \subset \Omega_{\mathrm{bc}} \text{ and } y^+_{\mathrm{ib}} < y^+_{\mathrm{lam},T} \\ 0 & \text{if } \Omega_P \subset \Omega_{\mathrm{fc}} \end{cases}, \tag{5}$$

$$\beta_\omega = \begin{cases} 1 & \text{if } \Omega_P \subset \Omega_{\mathrm{ic}} \cup \Omega_{\mathrm{bc}} \\ 0 & \text{if } \Omega_P \subset \Omega_{\mathrm{fc}} \end{cases},$$

where y^+_{ib} is the y^+ value evaluated at the immersed boundary as

$$y^+_{\mathrm{ib}} = \frac{y_{\mathrm{eff}}\, u_\tau}{\nu}, \quad u_\tau = C_\nu^{0.25}\sqrt{k}, \quad y_{\mathrm{eff}} = 0.5\left[y_\perp + 0.5\, V_P^{1/3}\right], \tag{6}$$

with C_ν being a turbulence model constant, u_τ the friction velocity, and $y_\perp$ the perpendicular distance from the cell center to the solid surface. Lastly, $y^+_{\mathrm{lam},\boldsymbol{u}}$ and $y^+_{\mathrm{lam},T}$ are calculated based on

$$y^+_{\mathrm{lam},\boldsymbol{u}} = \kappa^{-1}\log\left(E\, y^+_{\mathrm{lam},\boldsymbol{u}}\right), \quad \mathrm{Pr}\, y^+_{\mathrm{lam},T} = \mathrm{Pr_t}\left[\kappa^{-1}\log\left(E\, y^+_{\mathrm{lam},T}\right) + P(\mathrm{Pr})\right] \tag{7}$$

in which E and κ mark turbulence model constants, Pr and $\mathrm{Pr_t}$ denote the Prandtl and turbulent Prandtl number, respectively; and $P(\mathrm{Pr})$ is a smoothing function.

3 Metamaterial simulation

The presented solver was used to simulate the flow of a coolant with temperature T_{c} through a hot metamaterial with temperature T_{h}. The simulation domain used and the structure of the cooled metamaterial are visualized in Figure 2. The simulation domain had inlet, outlet, and wall boundaries. At the inlet, the Dirichlet boundary condition (BC) was used for velocity (u_{in}), temperature (T_{c}) and turbulence variables, and the zero-gradient BC was used for pressure. At the outlet, the pressure was set by the Dirichlet BC and the zero-gradient BC was used for the remaining variables. At walls, the no-slip BC was used for velocity, Dirichlet for temperature (T_{h}), zero-gradient for pressure, and wall functions for turbulence variables.

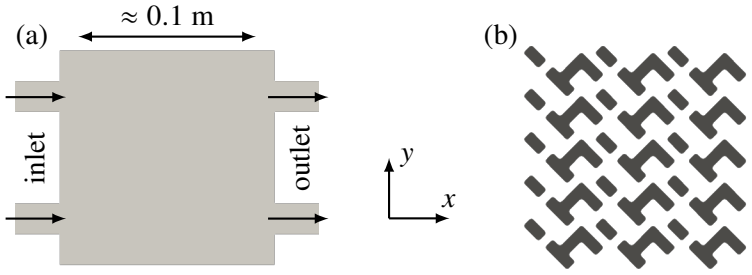

Figure 2: Setup of the metamaterial cooling simulation. (a) Simulation domain with indicated inlet and outlet boundary. (b) Used metamaterial structure.

The coolant fluid was regarded as water with kinematic viscosity $\nu = 10^{-6}\,\mathrm{m^2\,s^{-1}}$ and thermal diffusivity $\alpha = 1.5 \cdot 10^{-7}\,\mathrm{m^2\,s^{-1}}$. Subsequently, the Prandtl number was $\mathrm{Pr} = \nu/\alpha \approx 6.66$. To set the turbulent Prandtl number, a standard value of $\mathrm{Pr_t} = 0.85$ was used [9]. Lastly, the inlet velocity was $u_{\mathrm{in}} = 10^{-1}\,\mathrm{m\,s^{-1}}$ resulting in $\mathrm{Re} \sim 2000$.

To test the simulation sensitivity to mesh resolution, three difference meshes were prepared and tested. With each mesh, the cooling simulation was run with our openHFDIBRANS solver and a

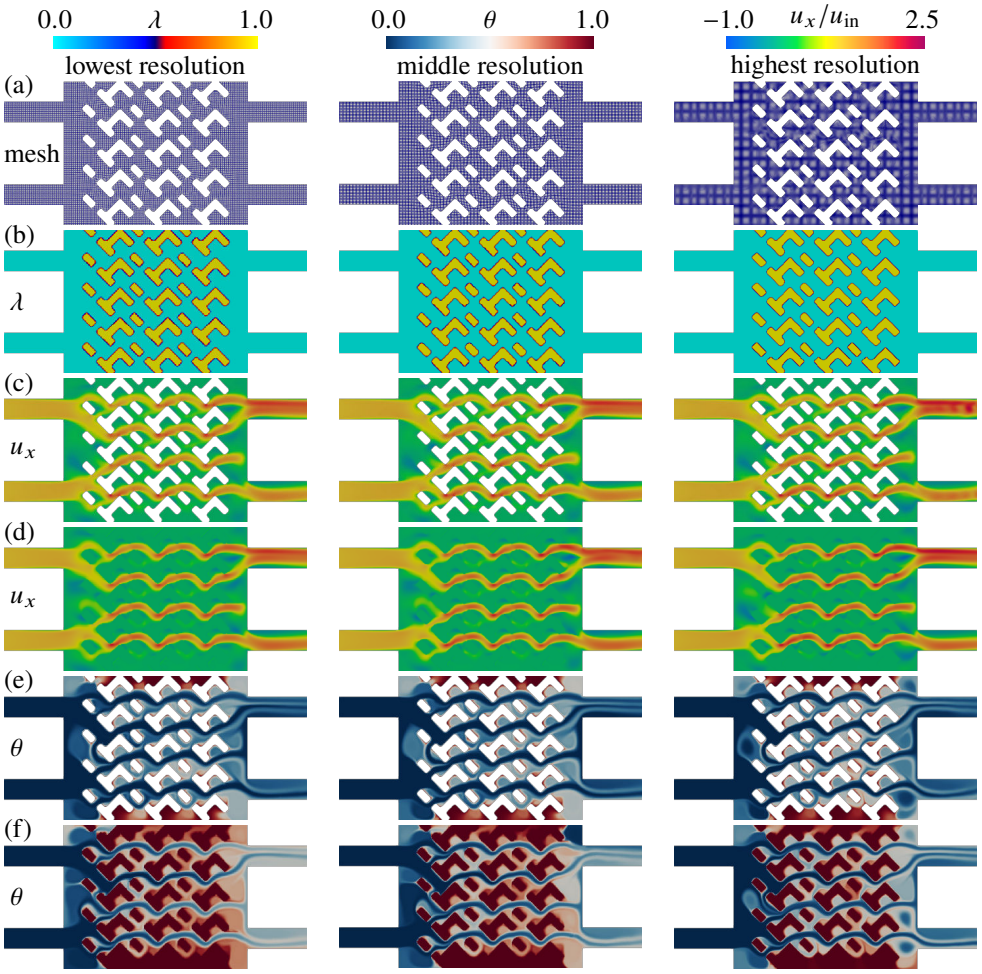

Figure 3: Simulation of metamaterial cooling with varying mesh resolution. Rows (a,c,e) show results from buoyantSimpleFoam and rows (b,d,f) from openHFDIBRANS.

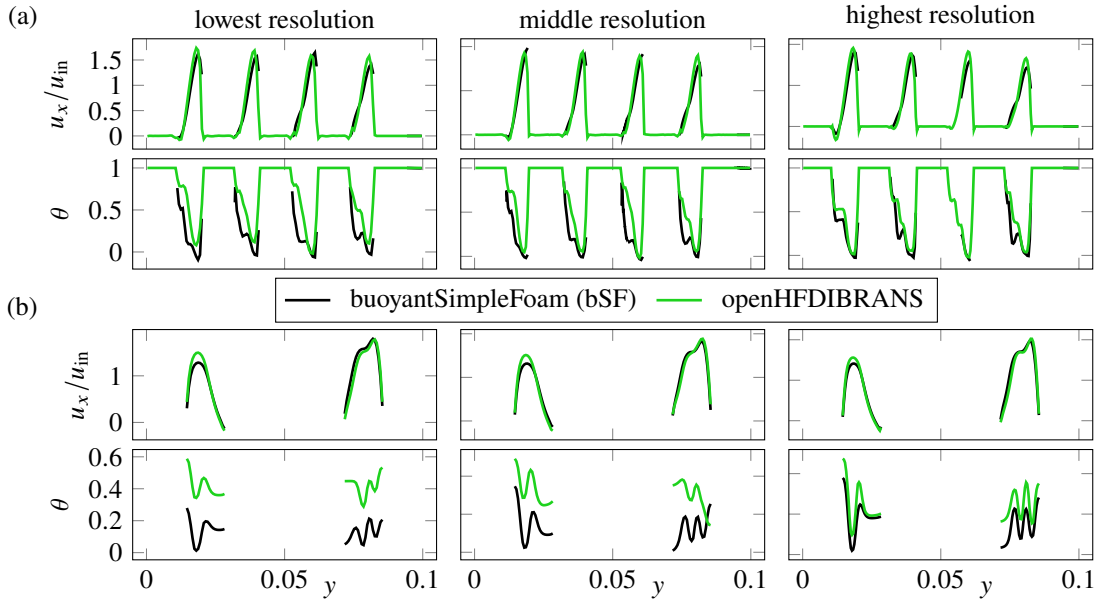

Figure 4: Comparison of the u_x and θ profiles from buoyantSimpleFoam and openHFDIBRANS. Profiles were sampled along the y direction at (a) the center of the domain and (b) the outlets.

referential buoyantSimpleFoam (bSF) solver available from the open-source C++ library OpenFOAM [9]. In Figure 3, the results of openHFDIBRANS and the referential solver are compared. Namely, the u_x and $\theta = (T - T_c)/(T_h - T_c)$ fields are visualized for each mesh resolution.

The u_x fields are very similar for all mesh resolutions. However, in θ, there are apparent differences. In the openHFDIBRANS simulation, the coolant is heated more than it should. To provide a more detailed comparison, field profiles were sampled along the y direction in the center of the domain and at the outlets. For both solvers, the profiles are visualized in Figure 4. Again, the agreement in u_x is good, but θ is overestimated by openHFDIBRANS. Fortunately, this error decreases with increasing mesh resolution, and the finest mesh was used in further computations.

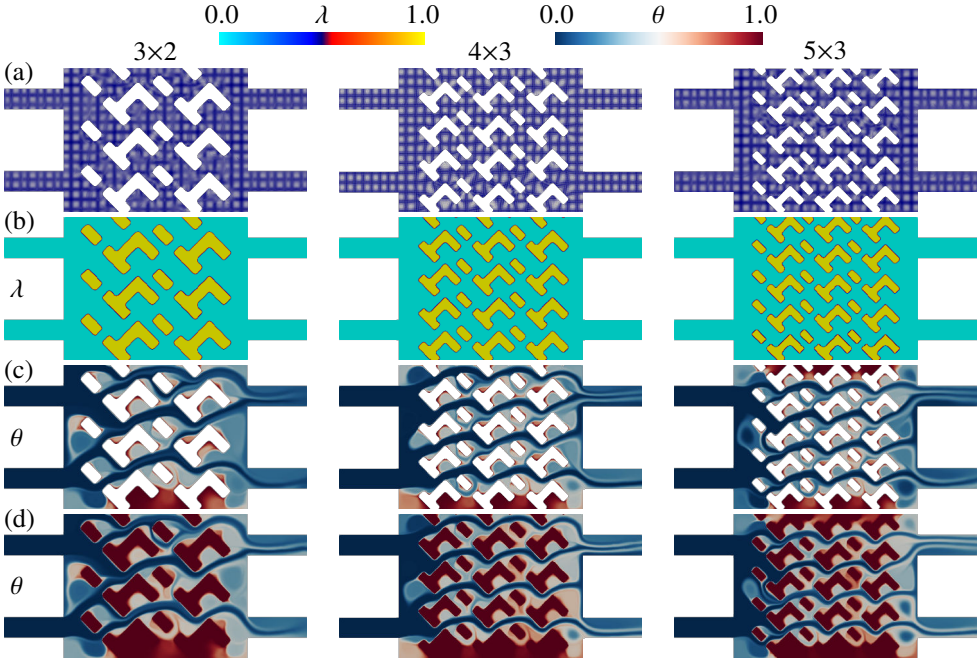

Figure 5: Simulation of metamaterial cooling with varying structure. Rows (a,c) show results from buoyantSimpleFoam and rows (b,d) from openHFDIBRANS.

To test the openHFDIBRANS solver response to changes in metamaterial structure, simulations with a metamaterial structure scaled-up by 12.5 % and 25 % were prepared. The original structure had 5×3 segments, the one scaled-up by 12.5 % had 4×3 and the other scaled-up by 25 % had 3×2. For each scale, the θ fields from openHFDIBRANS and bSF are given in Figure 5. The overestimation of θ is still present, but compared between scales, the relative changes in the metamaterial-to-coolant heat flux estimated by bSF were $\dot{Q}_{3\times2}/\dot{Q}_{5\times3} = 0.70$ and $\dot{Q}_{4\times3}/\dot{Q}_{5\times3} = 0.91$. By openHFDIBRANS, the relative changes were $\dot{Q}_{3\times2}/\dot{Q}_{5\times3} = 0.69$ and $\dot{Q}_{4\times3}/\dot{Q}_{5\times3} = 0.89$. The relative heat flux values are almost identical, and from this point of view, openHFDIBRANS appears to be suitable for optimization.

4 Conclusions

In this contribution, we have presented our immersed boundary solver developed for simulations of cooling of mechanical metamaterials used in molds for die casting. The solver combines our custom IB variant, the hybrid fictitious domain-immersed boundary method, with turbulent heat transfer simulation. The solver performance was evaluated in a series of metamaterial cooling simulations and the results were compared with those obtained using a standard mesh-conforming solver available in OpenFOAM. The comparison showed that our solver is able to accurately estimate the velocity profiles in the coolant flow. However, it tends to overestimate the outlet temperature of the coolant; yet, this error decreases with increasing mesh resolution. In addition, when applied on different metamaterial structures, our solver

was able to capture the relative changes in the metamaterial-to-coolant heat flux. The openHFDIBRANS solver shows good potential to be used in metamaterial optimization. In the future, the solver will be extended to simulate the heat effects in the solid phase and allow simulation of the die as a whole.

Acknowledgement

The authors acknowledge the financial support provided by the Ministry of Education, Youth, and Sports of the Czech Republic via the project No. CZ.02.01.01/00/23_020/0008501 (METEX), co-funded by the European Union. The work was financially supported by the institutional support RVO:61388998, and by the grant project with No. 25-17815S of the Czech Science Foundation of the Czech Republic.

References

[1] JIAO, Pengcheng; MUELLER, Jochen; RANEY, Jordan R.; ZHENG, Xiaoyu R. and ALAVI, Amir H. Mechanical metamaterials and beyond. *Nature Communications*. 2023, vol. 14, no. 6004. doi: 10.1038/s41467-023-41679-8.

[2] ZHENG, Ran; YI, Bing; LIU, Long; LIU, Jia; PENG, Xiang and YOON Gil H. Topology optimization of assembled mechanical metamaterials for large-scale structures. *Engineering Structures*. 2025, vol. 345. pp. 121552. doi: 10.1016/j.engstruct.2025.121552.

[3] KUBO, Seiji; KOGUCHI, Atsushi; YAJI, Kentaro; YAMADA, Takayuki; IZUI, Kazuhiro and NISHIWAKI, Shinji. Level set-based topology optimization for two dimensional turbulent flow using an immersed boundary method. *Journal of Computational Physics*. 2021, vol. 446, pp. 110630. doi: 10.1016/j.jcp.2021.110630.

[4] JENKINS, Nicholas and MAUTE, Kurt. An immersed boundary approach for shape and topology optimization of stationary fluid-structure interaction problems. *Structural and Multidisciplinary Optimization*. 2016, vol. 54, pp. 1191–1208. doi: 10.1007/s00158-016-1467-5.

[5] REN, Weiwei; SHU, Chang and YANG, Wenming. An efficient immersed boundary method for thermal flow problems with heat flux boundary conditions. *International Journal of Heat and Mass Transfer*. 2013, vol. 64, pp. 694–705. doi: 10.1016/j.ijheatmasstransfer.2013.05.020.

[6] NARVÁEZ, Gabriel F.; LAMBALLAIS, Eric and SCHETTINI, Edith B. Simulation of turbulent flow subjected to conjugate heat transfer via a dual immersed boundary method. *Computers & Fluids*. 2021, vol. 229, pp. 105101. doi: 10.1016/j.compfluid.2021.105101.

[7] ISOZ, Martin; KOTOUČ ŠOUREK, Martin and KOČÍ, Petr. Hybrid fictitious domain-immersed boundary solver coupled with discrete element method for simulations of flows laden with arbitrarily-shaped particles. *Computers & Fluids*. 2022, vol. 244, pp. 105538. doi: 10.1016/j.compfluid.2022.105538.

[8] KUBÍČKOVÁ, Lucie and ISOZ, Martin. On Reynolds-averaged turbulence modeling with immersed boundary method. In: ŠIMURDA, David and BODNÁR, Tomáš (ed.). *Proceedings of Topical Problems of Fluid Mechanics 2023*. Prague: IT CAS, 2023, pp. 104–111. doi: 10.14311/TPFM.2023.015.

[9] OpenCFD. *OpenFOAM: The Open Source CFD Toolbox. User Guide Version 1.4, OpenCFD Limited*. Reading UK, 2007.

[10] WILCOX, David C. *Turbulence modeling for CFD*. 3rd Ed. DCW Industries, USA. 2006. ISBN 978-1928729082.

APPLIED MECHANICS 2026
April 13 - 15, 2026, České Budějovice, Czech republic

Measurement of Mechanical Properties of 3D Printed Polymer PET-G under Compressive Loading

M. Mánek[1], M. Fusek[2]

Abstract: The article describes the compressive load testing, measurement, and evaluation of a 3D-printed polymer. The materials selected for the study were PET-G, RePET-G, and CF-Jet. It was observed that the compressive elastic modulus is influenced by the sample length. The effective compressive modulus for zero diameter to length ratio was determined. The compressive modulus of PET-G and RePET-G are not significantly different. The commpressive modulus of CF-Jet is significantly higher. The yield strength was nearly identical for all materials, and no significant dependence on the sample length was observed.

Keywords: 3D printing; PET-G; composite; mechanical properties; compressive modulus; size effect

1 Introduction

3D printing of polymeric materials has gained significant popularity in recent decades. Today, this technology enables the creation of prototypes as well as entire production series. A wide variety of materials is available on the market, not limited to pure polymers but also including materials reinforced with glass or carbon fibres. Furthermore, recycled materials can be purchased, which reduces the environmental impact and helps decrease plastic waste.

Our previous studies investigated the behaviour of pure PET-G material under compressive loading. Experiments were conducted under quasi-static and impact loading using a Split-Hopkinson Pressure Bar (SHPB). It was found that the ratio between the transverse dimension of the specimen and its length has a significant effect on the compressive modulus of elasticity. The ASTM D695 standard, which describes the compression testing of plastics, specifies a recommended slenderness ratio of 11:1 to 16:1. However, such specimen dimensions are unusable for the Hopkinson test, as the wave propagation time through the specimen is too long and wave reflections complicate the evaluation. [1], [2], [3]

For this reason, measurements were performed on several specimen lengths, and a dependence between specimen length and the modulus of elasticity was established. Using this function and the Cook and Larke method, the compressive modulus was extrapolated to a zero diameter-to-length ratio, and the so-called effective modulus of elasticity was calculated. [4], [5]

2 Experiments and Evaluation

The materials selected for testing were PET-G, RePETG (a recycled material), and CF-Jet, which consists of PET-G with a 20 % admixture of short carbon fibers. The materials were sourced from the manufacturer Filamenty PM. The specimens were produced on a Prusa MK3S printer. Each set of specimens consisted of 3 pieces. [6]

A specimen diameter of 15 mm was chosen, with lengths of 7.5 mm, 10 mm, 15 mm, 30 mm, and 60 mm. One PET-G specimen was also produced with a length of 120 mm. The specimens were manufactured in both vertical and horizontal orientations on the print bed. Testing was performed on a TESTOMETRIC M500-50CT universal testing machine between parallel compression plates. The contact surfaces were lubricated with petroleum jelly. A strain rate of 0.005 s^{-1} was chosen for all

[1] Martin MĂˇnek; Department of Applied Mechanics, Faculty of Mechanical Engineering, VSB â€“ Technical University of Ostrava, 17. listopadu 2172/15, Ostrava, Czech Republic; martin.manek@vsb.cz

[2] Martin Fusek; Department of Applied Mechanics, Faculty of Mechanical Engineering, VSB â€“ Technical University of Ostrava, 17. listopadu 2172/15, Ostrava, Czech Republic; martin.fusek@vsb.cz

specimen lengths. The crosshead velocities are listed in Table 1. The specimen geometry is shown in Figure 1.

Sample length (mm)	*Crossbar velocity (ms^{-1})*
7.5	2.25
10	3
15	4.5
30	9
60	18
120	36

Table 1: Crossbar velocity.

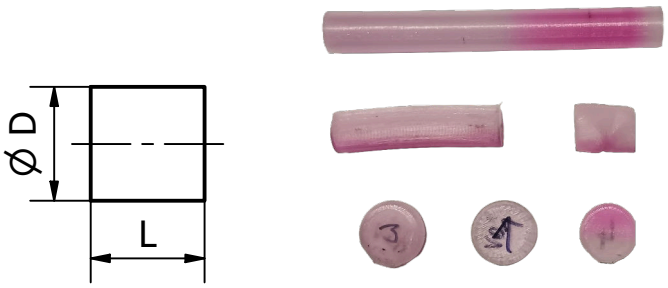

Figure 1: Tested samples

From the three measurements for each specimen, the toe region at the beginning of the stress-strain curve was removed. All curves were then averaged into a single curve, from which the compressive modulus of elasticity and the upper yield strength of the specimen were evaluated. Buckling was observed in specimens with a length-to-diameter ratio of 2 or higher. For specimens with a length of 60 mm, buckling occurred before the yield strength was reached. Therefore, the yield strength was not evaluated for these lengths. The evaluation and averaging process is shown in Figure 2.

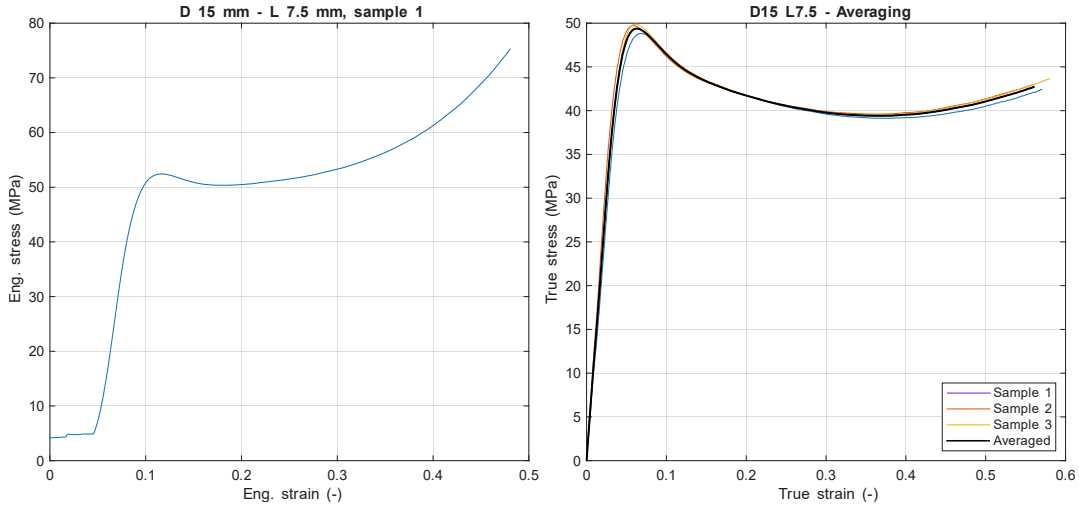

Figure 2: Curves evaluation

All measured lengths were evaluated, and stress-strain curves were constructed. The stress-strain curves for all tested materials are shown in Figure 3. From the curves for PET-G and RePET-G, it is evident that for all lengths and both print orientations, the materials exhibit significant softening after reaching the yield strength. In contrast, the CF-Jet material does not show such pronounced softening

after the yield point. For horizontal printing and specimen lengths up to 15 mm, the material continues to exhibit strain hardening beyond the yield strength.

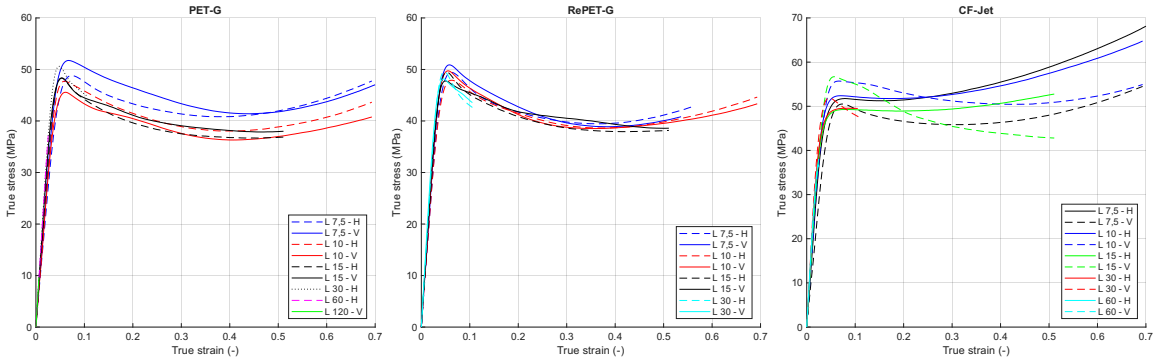

Figure 3: Evaluated curves for all materials

From the plotted moduli of elasticity (Figure 4), it is evident that the specimen length has a significant effect on the compressive modulus of elasticity. For all materials, the modulus decreases as the specimen length decreases. The evaluated moduli were fitted with a linear regression line for both vertical and horizontal print orientations. In the case of the recycled material RePET-G, the moduli for all lengths are higher in the vertical orientation; however, as with the PET-G material, these differences are not particularly pronounced. A more significant difference occurs in shorter specimens of the CF-Jet material. This may be caused by the increased printing difficulty of this material, leading to imperfections in the bonding between the perimeters and the internal infill, which are most prominent in short horizontal specimens. The evaluated effective moduli of elasticity extrapolated to $D/L = 0$ are presented in Table 2.

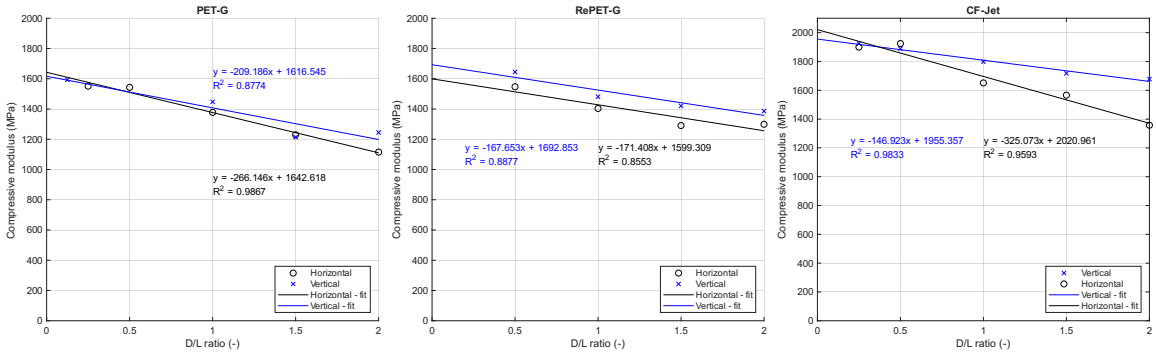

Figure 4: Compressive moduli for all materials

Material - orientation	*Compressive moduli (MPa)*
PET-G - horizontal	1642
PET-G - vertical	1617
RePET-G - horizontal	1693
RePET-G - vertical	1599
CF-Jet - horizontal	2021
CF-Jet - vertical	1955

Table 2: Effective moduli for each material

The yield strengths do not change significantly with respect to the specimen length. While the yield strength for PET-G and CF-Jet materials varies slightly depending on length, it does not follow the same

consistent trend observed in the moduli of elasticity. For certain lengths, the yield strength is nearly identical in both print orientations. Therefore, the yield strengths were averaged for each material. The yield strengths for individual lengths are shown in Figure 5. The averaged yield strengths for each material, including standard deviations (STD), are presented in Table 3.

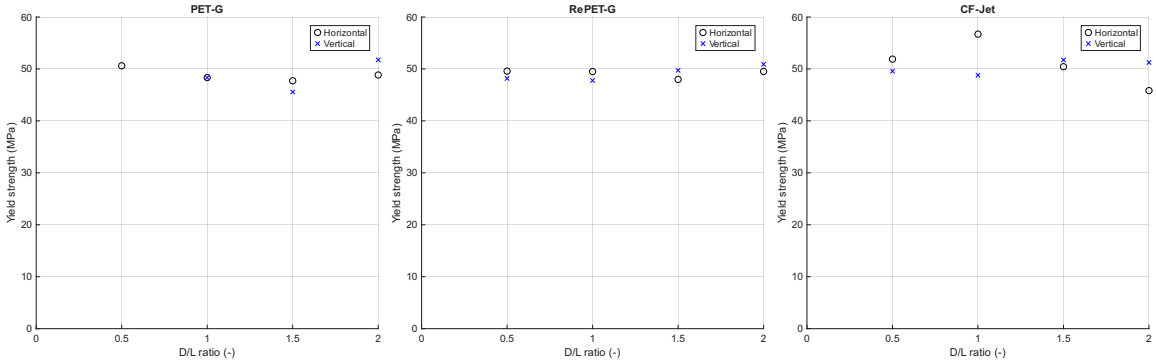

Figure 5: Yield strengths for each material

Material	*Peak yield strength (MPa)*	*STD (MPa)*
PET-G	48.7	2
RePET-G	49.1	1.1
CF-Jet	50	3.1

Table 3: Peak yield strength for each material

3 Conclusion

Research was conducted on the base material PET-G and its commercially available variants, RePET-G and CF-Jet (reinforced with carbon fibers). Consistent with the measurements of the base PET-G material, a dependence of the compressive modulus of elasticity on the specimen length was observed. Consequently, the moduli for the investigated lengths were fitted with a linear regression and extrapolated to a zero diameter-to-length ratio to determine the effective compressive moduli. The modulus for the CF-Jet material is significantly higher than those for PET-G and RePET-G, a trend observed in both print orientations. When comparing yield strengths, no similar dependence was observed, and none of the materials proved to be significantly stronger than the others. A distinction for CF-Jet was identified beyond the yield point, where the material does not exhibit such pronounced softening as PET-G and RePET-G. The data presented in this article serve as a foundation for future measurements on the Split-Hopkinson Pressure Bar (SHPB), providing a reference for quasi-static loading.

Acknowledgement

This work was supported by *Advanced Numerical and Experimental Approaches in Mechanics and Biomechanics - SP2026/027* .

References

[1] Mánek, M., Fusek, M., and Cienciala, J., Measurement of mechanical properties of 3D printed material under impact loading, in *40th Danubia-Adria Symposium on Advances in Experimental Mechanics BOOK OF ABSTRACTS*, Warszawa: Institute of Fundamental Technological Research of the Polish Academy of Sciences, 2024, pp. 203–204.

[2] Mánek, M., Fusek, M., Measurement of Mechanical Properties of 3D Printed Polymer under Compressive Loading, in *26th International Conference Applied Mechanics 2025*, Brno: Ústav fyziky materiálů AV ČR, 2025, pp. 78–81.

[3] ASTM D695-15. Test Method for Compressive Properties of Rigid Plastics. In ASTM International. https://doi.org/10.1520/d0695-15

[4] Cook, M. M., Larke, E. C. (1945). Resistance of copper and copper alloys to homogeneous deformation in compression. *J Inst Met*, *71*(12), 371-390. https://api.semanticscholar.org/CorpusID:136722227

[5] Jerabek, M., Major, Z., Lang, R. W. (2010). Uniaxial compression testing of polymeric materials. In *Polymer Testing* (Vol. 29, pp. 302-309). Elsevier BV. https://doi.org/10.1016/j.polymertesting.2009.12.003

[6] Filamenty PM. Retrieved March 20, 2025, from https://www.filament-pm.cz/

APPLIED MECHANICS 2026
April 13 - 15, 2026, České Budějovice, Czech republic

DYNAMIC ANALYSIS OF A MULTIBODY SYSTEM CONSTRAINED BY STIFF DAMPED SPRINGS

Ján Minárik[1], Ondrej Piroh[2], Milan Vaško[3], Branislav Ftorek[4], Milan Sága[5]

Abstract: The presented work deals with the modelling and simulation of a multibody system with simplified constraints. The individual bodies forming the treated system are connected using stiff, damped springs. The dynamic behaviour of this system is then compared with a reference model that incorporates proper kinematic constraints. The equations of motion were derived analytically. The resulting models were then simulated in the MATLAB environment. The use of stiff springs provides a simplified mathematical description of the treated model. However, this approach can reduce the computational efficiency of the numerical solver.

Keywords: Hydraulic Arm; Multibody Dynamics; MATLAB; Differential Equations

1 Introduction

Dynamical analysis of multibody systems plays an essential role in the design and optimisation of machines. The available software solutions can efficiently handle dynamical analyses, implementation of modifications or optimisation tasks regarding even highly complex 3-dimensional multibody systems. This approach is rather practically oriented with emphasis on the obtained results. The mathematical description of the system, i.e. the equations of motion, cannot always be obtained or cannot be obtained in a suitable form. Therefore, the deeper mathematical analysis of the system might not be possible.

Lagrangian mechanics provides efficient and exceptionally elegant tools that can, in theory, obtain the equations of motion of an arbitrary complex dynamical system. Thus, the analytical description of the system can be derived, and further mathematical analysis can be performed. This can provide deeper insight into the treated system or the whole class of analogous systems. However, despite the possibilities of this approach, the treatment of highly complex systems can often become substantially impractical and time-consuming, rendering the process unsuitable for practical use. Yet, when considering the less complex systems, or smaller subsystems, these can be handled relatively efficiently. Moreover, custom mathematical models, unavailable in commercial software, can be implemented into the treated problem [1].

Additionally, the rigid body dynamics cannot always sufficiently describe the treated problem. The systems might comprise deformable bodies, as well as joints that are flexible or contain geometrical imperfections. Such topics are covered in the following studies [2 - 4]. Such

[1] Ing. Ján Minárik; University of Žilina, Department of Applied Mechanics; Univerzitná 8215/1, 010 26 Žilina, Slovak Republic, Jan.Minarik@fstroj.uniza.sk
[2] Ing. Ondrej Piroh; University of Žilina, Department of Applied Mechanics; Univerzitná 8215/1, 010 26 Žilina, Slovak Republic, Ondrej.Piroh@fstroj.uniza.sk
[3] doc. Ing. Milan Vaško, PhD.; University of Žilina, Department of Applied Mechanics; Univerzitná 8215/1, 010 26 Žilina, Slovak Republic, Milan.Vaško@fstroj.uniza.sk
[4] doc. Mgr. Branislav Ftorek, PhD.; University of Žilina, Department of Applied Mathematics; Univerzitná 8215/1, 010 26 Žilina, Slovak Republic, Branislav.Ftorek@fstroj.uniza.sk
[5] Dr. h. c. prof. Dr. Ing. Milan Sága; University of Žilina, Department of Applied Mechanics; Univerzitná 8215/1, 010 26 Žilina, Slovak Republic, Milan.Saga@fstroj.uniza.sk

systems then require the implementation of additional mathematical models to adequately capture the properties and behaviour of corresponding real-world systems.

This study deals primarily with the mathematical modelling of a hydraulic arm with flexible joints modelled using overdamped springs. The motion of the arm during the unfolding process, governed by the feedback control, is analysed. The arm was simulated with various values of stiffness and damping coefficients of joints, and the results were compared with the reference model with proper kinematic joints. The comparison was carried out in terms of motion precision and computing time. The equations of motion were derived analytically, using the Euler -Lagrange equations. The reference model was obtained in the same way; however, the joints were modelled as kinematic, using the Lagrange multipliers. The solution of the corresponding systems, as well as results processing, were carried out in the MATLAB environment.

2 Physical Model

The model of the hydraulic arm is shown in Figure 1. The mechanism consists of a main arm mounted on a stationary base and a secondary extendable arm. Both are actuated by two hydraulic cylinders. The extension of the cylinders, as well as the extendable arm, is governed by PD controllers.

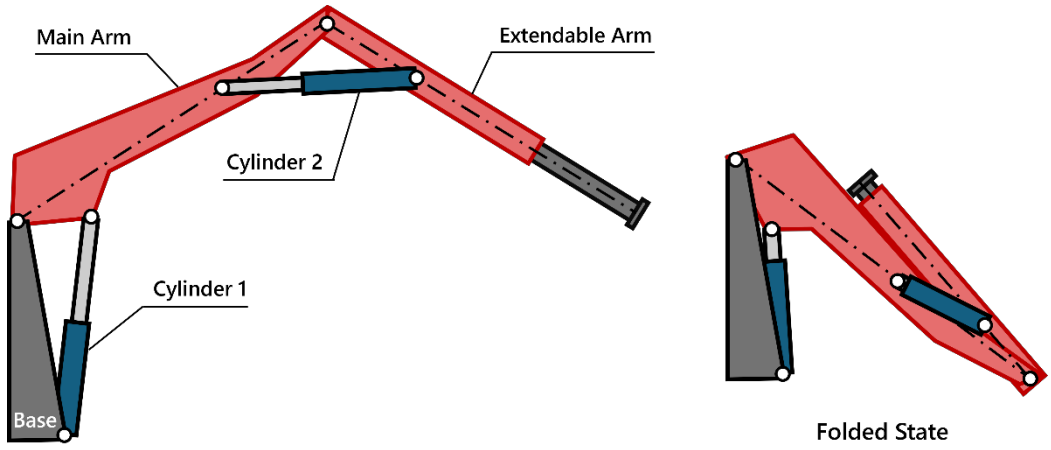

Figure 1: Model of the hydraulic arm (left) and arm in the folded state (right)

The mechanism comprises two types of subcomponents. The main arm is modelled as a rotating rod (Figure 2 left). Its position is described by generalised coordinates x, y and ϕ. The hydraulic cylinders and extendable arm are modelled as two sliding rods, with their position described by the generalised coordinates x, y, ϕ and the extension length l (Figure 2 right).

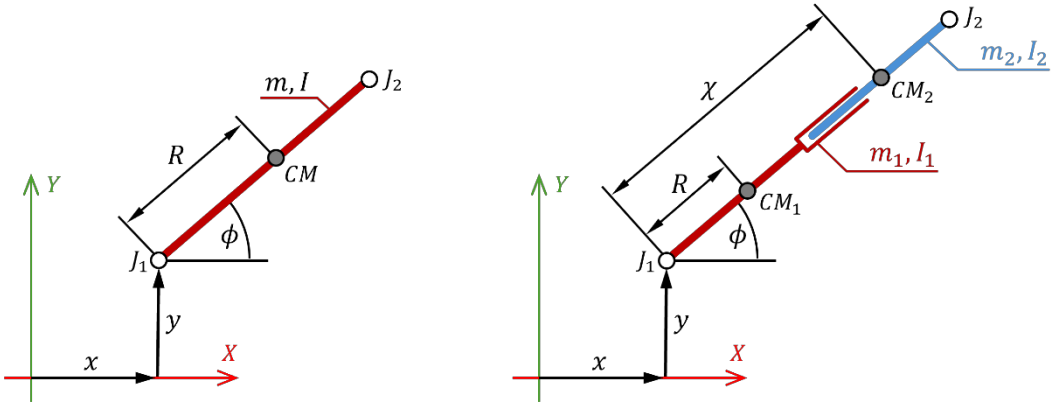

Figure 2: Subcomponents of the model: simple rod (left) and extendable arm (right)

Generally, R denotes the positions of the centre of mass (CM). The corresponding masses and the moments of inertia are denoted m, I and the joint locations are denoted as $J_{1,2}$. The subcomponents are interconnected with springs at the joint locations. The presented parameters use dummy labelling and are only used to derive the general form of the equations of motion for the subcomponents. The proper labels are then shown in Figure 3. The equations of motion for the main arm have the following general form:

$$m\ddot{x} - mR\ddot{\alpha}\sin\alpha - mR\dot{\alpha}^2\cos\alpha + \sum_i \left(k_i\Delta_i + c_i\dot{\Delta}_i\right)\frac{\partial\Delta_i}{\partial x} = 0, \tag{1}$$

$$m\ddot{y} + mR\ddot{\alpha}\cos\alpha - mR\dot{\alpha}^2\sin\alpha + mg + \sum_i \left(k_i\Delta_i + c_i\dot{\Delta}_i\right)\frac{\partial\Delta_i}{\partial y} = 0, \tag{2}$$

$$(mR + I)\ddot{\alpha} - mR\ddot{x}\sin\alpha + mR\ddot{y}\cos\alpha + mgR\cos\alpha + \sum_i \left(k_i\Delta_i + c_i\dot{\Delta}_i\right)\frac{\partial\Delta_i}{\partial\alpha} = 0. \tag{3}$$

The sums represent the joint spring forces, with k, c being the spring stiffnesses and damping coefficients and Δ are the spring displacements. The general equations of motion for each extendable component can be written as:

$$\omega_1\ddot{x} - \omega_3\ddot{\alpha}\,sin\,\alpha + m_2\ddot{l}\,cos\,\alpha - \omega_3\dot{\alpha}^2\,cos\,\alpha - 2m_2\dot{\alpha}\dot{l}\,sin\,\alpha + \sum_i \left(k_i\Delta_i + c_i\dot{\Delta}_i\right)\frac{\partial\Delta_i}{\partial x} = 0, \tag{4}$$

$$\omega_1\ddot{y} + \omega_3\ddot{\alpha}\,cos\,\alpha + m_2\ddot{l}\,sin\,\alpha - \omega_3\dot{\alpha}^2\,sin\,\alpha + 2m_2\dot{\alpha}\dot{l}\,cos\,\alpha + \sum_i \left(k_i\Delta_i + c_i\dot{\Delta}_i\right)\frac{\partial\Delta_i}{\partial y} = 0, \tag{5}$$

$$-\omega_3\ddot{x}\,sin\,\alpha + \omega_3\ddot{y}\,cos\,\alpha + (\omega_2 + m_2l^2)\ddot{\alpha} + 2m_2l\dot{l}\dot{\alpha} + \omega_3 g\,cos\,\alpha + \sum_i \left(k_i\Delta_i + c_i\dot{\Delta}_i\right)\frac{\partial\Delta_i}{\partial\alpha} = 0, \tag{6}$$

$$m_2\ddot{x}\cos\alpha + m_2\ddot{y}\sin\alpha + m_2\ddot{l} - m_2l\dot{\alpha}^2 + m_2g\sin\alpha + \sum_i \left(k_i\Delta_i + c_i\dot{\Delta}_i\right)\frac{\partial\Delta_i}{\partial l} + \left(\kappa\Delta l + \gamma\Delta\dot{l}\right) = 0. \tag{7}$$

Again, the sums represent the joint spring forces and $\omega_1 = m_1 + m_2$, $\omega_2 = m_1R_1^2 + I_1 + + I_2$ and $\omega_3 = m_1R + m_2l$. The feedback control is tuned by the constants κ and γ, with $\Delta l\ (\Delta\dot{l})$ representing the difference between the desired and actual extension length l (velocity $\dot{l}$). The mathematical model then comprises the system of equations (1 - 3) and three systems of equations (4 - 7), thus fifteen equations of motion in total. The whole system, with individual components and additional dimensions, is shown in Figure 3.

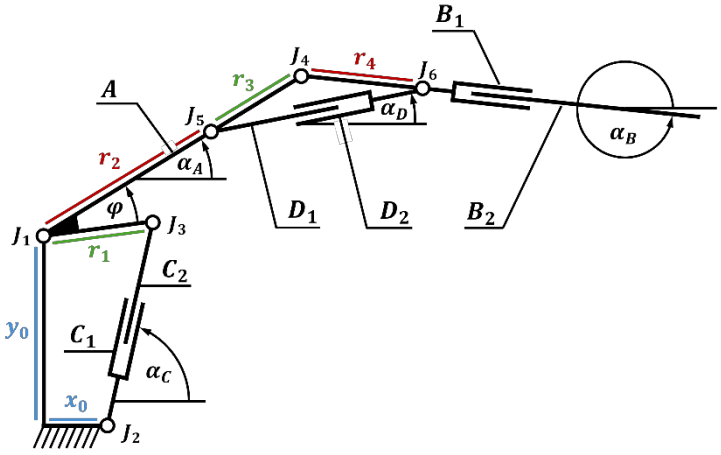

Figure 3: Kinematic diagram of the hydraulic arm

The main arm is denoted A, the links $B_{1,2}$ comprise the extendable arm and the links $C_{1,2}$ and $D_{1,2}$ comprise the corresponding hydraulic cylinders. The dimensions of the stationary base are x_0, y_0 and r_{1-4} are the lengths of the arm segments determining the joint locations J_{1-6}.

The reference mechanism was modelled analogously; however, instead of the joint springs, the proper kinematic joints were used. The Lagrange undetermined multipliers were utilised resulting in additional constraint equations introduced to the system. The parameters of the mechanism are summarised in Table 1.

Components:	A	B_1	B_2	C_1	C_2	D_1	D_2
Length [m]	2.50	2.00	2.00	0.95	0.95	0.65	0.65
Mass [kg]	550	480	420	180	140	120	160
Additional dimensions:		x_0	y_0	r_1	r_2	r_3	r_4
Length [m]		0.30	1.50	0.50	1.50	1.00	0.40
Feedback control constants:		κ_B	κ_C	κ_D	γ_B	γ_C	γ_D
Unit		[N/m]			[kg/s]		
Value		10^9	5.10^{10}	10^9	10^5	10^6	10^5

Table 1. Model parameters.

All the components were modelled as links, with their centres of mass being located in their geometrical centres. The corresponding moments of inertia were therefore calculated as $m(2R)^2/12$. In the current model, the products of inertia were neglected.

The motion corresponding to the unfolding of the arm was analysed. The required motion was given by the main arm angle α_A, the secondary arm angle α_B, and its extension length l_B, as well as their corresponding time derivatives (velocities). These can be considered as independent coordinates that were obtained as functions of time, based on the analytically obtained kinematic relations. The folded (initial) and the unfolded (final) state of the mechanism are given by the following independent coordinates (Table 2):

Coordinates:	α_A [◦]	α_B [◦]	l_B [m]
Initial state	-53.69	116.3	1.05
Final state	41.31	-58.69	2.50

Table 2. Initial and final states of the system.

All the other coordinates are dependent on those in Table 2 and can be determined from the kinematic relations. For the calculation of the required motion, the joint stiffnesses were neglected, and the system was treated as if it had kinematic joints. To ensure a smooth motion of the mechanism, the time courses of independent coordinates were modelled by cubic step functions. The extension lengths of the hydraulic cylinders and the extendable arm were obtained from the kinematic relations. These serve as the basis for the feedback control that is also expected to handle the snap-through-like motion occurring when the main arm and the extendable arm become parallel.

The initial conditions are given by the initial configuration of the system (initial state), with all the velocities being zero, in both the initial and final states. The whole motion was carried out in ten seconds. The equations of motion were solved in MATLAB, using the *ode113* solver, with relative tolerance set to 10^{-4} and maximum step size of 0.005 s.

The impact of joint stiffness and corresponding damping coefficients on the motion and computing time was analysed. The nine values of stiffness were paired with each of the damping coefficients, with the specific values being presented in Table 3. During the simulation, all the joints had the same values of stiffness and damping.

Stiffness [N/m]	$k.10^9$	$k.10^{10}$	
k	1.00, 3.25, 5.50, 7.75	1.00, 3.25, 5.5, 7.75, 10.0	
Damping [kg/s]	$k.10^2$	$k.10^3$	$k.10^4$
k	1.00, 4.00, 7.00	1.00, 4.00, 7.00	1.00, 4.00, 7.00, 10.0

Table 3. Values of **s**tiffness and damping coefficients.

3 Results

The motion of the mechanism was analysed for each combination of stiffness and damping coefficients listed in Table 3. The movement deviation was obtained to evaluate the precision of the mechanism. It was calculated as the root mean square (RMS) of the total differences between the actual and ideal trajectory, obtained at each time step. Additionally, the computing time for each simulation run was measured to evaluate the efficiency of the model. The presented results are shown in Figure 4, with the figure axes being in logarithmic coordinates.

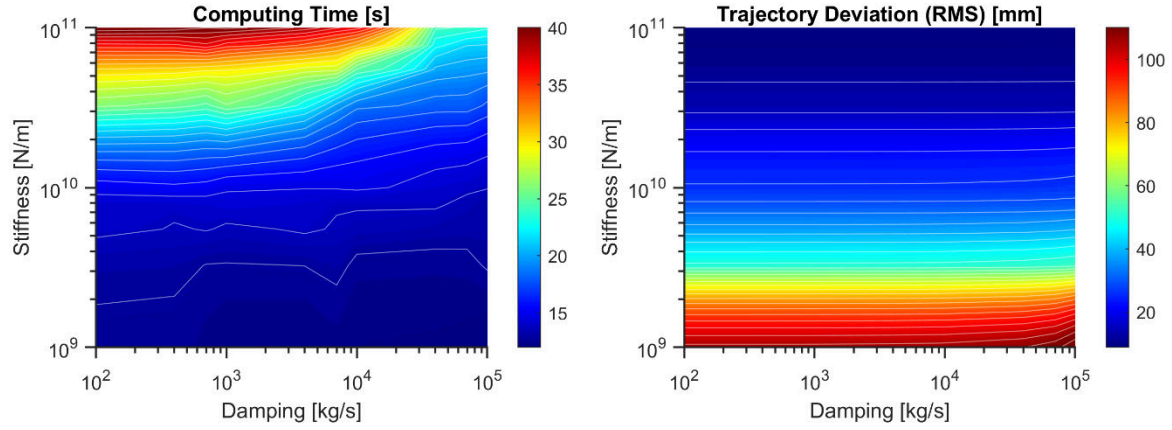

Figure 4: Computing time (left) and trajectory deviation (right)

According to the results, the motion of the mechanism is naturally more precise at greater joint stiffness values. The change in trajectory deviation is most distinct at low stiffness values. This shows that insufficient stiffness can drastically disrupt the motion of the mechanism. On the contrary, the change in stiffness has a much less significant effect for high enough stiffness values. Unlike the stiffness, the damping coefficient seems to have only neglectable influence on the analysed motion. However, high damping can possibly decrease the movement precision when the stiffness is low enough.

Considering the computing time, the increasing stiffness can generally lower the efficiency of the model. Moreover, the impact of damping is more distinct than in the previous case. This holds for high stiffness values in particular, where the insufficient damping causes a significant increase in computing time.

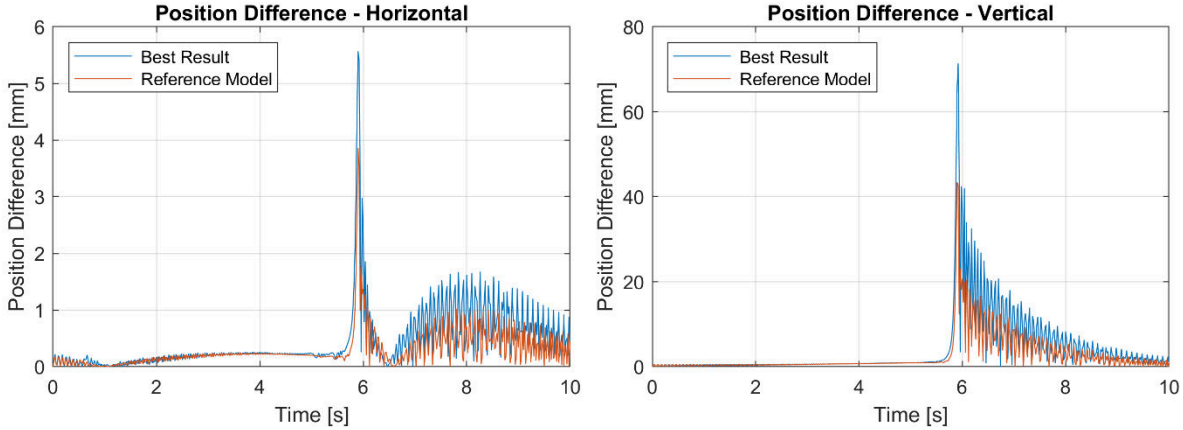

Figure 5: Deviations from the ideal trajectory in horizontal (left) and vertical (right) direction

In summary, the trajectory deviation ranges from 8.79 mm to 115.56 mm, with the computing time ranging from 11.95 s to 41.28 s. In comparison, the reference model with the proper kinematic joints was able to achieve the trajectory deviation of only 5.30 mm, with the

average computing time of approximately 1.55 s. These results are significantly better, since there are no unwanted oscillations introduced to the system due to the flexible joints.

The configuration that achieved the highest precision was further compared with the reference model. The end position of the extendable arm was tracked, and its deviations from the ideal trajectory, in horizontal and vertical directions, were obtained. These results are shown in Figure 5. The systems behave comparably until approximately 6 s, where the peaks occur. These peaks are caused by the snap-through-like motion of the arm when the main arm and the extendable arm are close to a parallel position. At this point, the system starts to oscillate as the feedback control tries to stabilise the motion of the system. The results show that the motion disruption caused by this effect is less significant in the reference mechanism.

4 Conclusion

This study analysed the motion of a hydraulic arm with flexible joints modelled as damped springs. The influence of the spring stiffnesses and damping on the movement precision and the computational time was studied. This system was then compared to a reference model with proper kinematic joints. The equations of motion of the systems were derived analytically and were solved in the MATLAB environment.

The results showed that the implementation of flexible joints modelled as springs can disrupt the mechanism and lower its movement precision. To achieve a satisfactory and stable behaviour, sufficiently high stiffness values are required. Additionally, sufficient values of damping coefficients need to be used; otherwise, the computing time can increase drastically, reducing the efficiency of the model. These results show a decline compared to the reference model with kinematic joints.

When only the motion of the mechanism is analysed, the presented approach is inefficient and thus rather unsuitable. However, it is a simple approach when dealing with flexible mechanisms, flexible joints or joints with various imperfections. Despite the increased computing costs, this model can provide a better representation of the real-world systems, as it can accommodate the imperfections present in these systems.

Acknowledgement

This work was supported by the grant projects KEGA, No. 005ŽU-4/2024 and VEGA, No. 1/0423/23.

References

[1] HELRICH, Carl S. *Analytical Mechanics*. Online. Springer, 2017 [Accessed 2026-01-19]. ISBN 9783319444901. Available from: https://doi.org/10.1007/978-3-319-44491-8.

[2] ABELE, Eberhard; BAUER, J.; HEMKER, Thomas; LAURISCHKAT, R.; H. E. MARKUS MEIER et al. Comparison and validation of implementations of a flexible joint multibody dynamics system model for an industrial robot. Online. *CIRP journal of manufacturing science and technology*. 2011, vol. 4, no. 1, s. 38-43. ISSN 1755-5817. Available from: https://doi.org/10.1016/j.cirpj.2011.01.006.

[3] YANG, Yuwei; LV, Xiaoshuang; LI, Zhaotong; YIN, Jiapeng; WANG, Haoyu et al. Dynamic analysis of a mobile parallel manipulator with imperfect revolute joints. Online. *Robotica*. 2025, vol. 43, no. 6, s. 2172-2192. ISSN 0263-5747. Available from: https://doi.org/10.1017/s026357472500058x.

[4] LIU, Yufei; LI, Wei; WANG, Yuqiao; YANG, Xuefeng a JU, Jinyong. Dynamic Model and Vibration Power Flow of a Rigid-Flexible Coupling and Harmonic-Disturbance Exciting System for Flexible Robotic Manipulator with Elastic Joints. Online. *Shock and Vibration*. 2015, vol. 2015, s. 1-10. ISSN 1070-9622. Available from: https://doi.org/10.1155/2015/541057.

APPLIED MECHANICS 2026
April 13 - 15, 2026, České Budějovice, Czech republic

EVALUATION OF AXIAL-TORSIONAL LOW-CYCLE FATIGUE TESTS USING PYTHON CODES

Ajay V. Natarajan[1], Radim Halama[2], Michal Kořínek[3], Petr Gál[4]

Abstract: This paper introduces a suite of Python-based tools for automated post-processing of low-cycle fatigue (LCF) tests under various loading conditions, including uniaxial and axial-torsional. Designed to standardize the FABER project workflow, the tools ensure consistent data validation. A core feature is the '3D method', which uses simultaneous linear regression to determine Manson-Coffin-Basquin (MCB) and Ramberg-Osgood (RO) parameters, avoiding inconsistencies typical of independent regressions. Demonstrated on own experimental datasets, the software automates the calculation of fatigue parameters, generates standardized reports, effectively minimizes human error, and helps with efficient fatigue data analysis and numerical modelling. The data of 42CrMo4+QT steel will serve as the basis of the FABEST competition in the LCF area.

Keywords: Low-cycle fatigue; Standardization; Cyclic stress-strain curve; Parameter identification

1 Introduction

Reliable assessment of LCF is essential for the structural integrity of engineering components. However, processing experimental LCF data is often hampered by non-standardized workflows and subjective manual evaluation, leading to significant inconsistencies in material parameter identification. Furthermore, conventional practices (such as determining MCB and RO parameters through independent regressions) often result in mathematical discrepancies between cyclic stress-strain curves (CSSCs) and lifetime curves [1]. To address these challenges, this paper presents an open-source Python-based toolset developed within the FABER (Fatigue Benchmark Repository) project. By providing a unified framework for automated post-processing of uniaxial and axial-torsional tests, these tools eliminate human error and ensure data interoperability. As demonstrated through applications on SS316L [2] and 42CrMo4+QT steels, this solution standardizes the derivation of critical fatigue indicators (plastic strain energy density, cyclic yield stress), facilitating more accurate numerical modelling and fatigue life predictions.

2 3D vs conventional method

The identification of material parameters for the MCB and RO models is typically performed using a 2D approach. In this conventional method, parameters are determined via independent linear regressions applied separately to the fatigue life data and the CSSC. While computationally simple, this approach often fails to ensure mathematical compatibility between the two models [1].

[1] Bc. Ajay, Natarajan; VŠB – Technical University of Ostrava, Faculty of Mechanical Engineering, Department of Applied Mechanics, 17. listopadu 2172/15, Ostrava, Czech Republic, ajay.vignesh.natarajan@vsb.cz
[2] prof. Ing. Radim Halama, Ph.D.; VŠB – Technical University of Ostrava, Faculty of Mechanical Engineering, Department of Applied Mechanics, 17. listopadu 2172/15, Ostrava, Czech Republic, radim.halama@vsb.cz
[3] Ing. Michal Kořínek, Ph.D.; VŠB – Technical University of Ostrava, Faculty of Mechanical Engineering, Department of Applied Mechanics, 17. listopadu 2172/15, Ostrava, Czech Republic, michal.korinek@vsb.cz
[4] Ing. Petr Gál; Department of Strength and Lifetime Evaluation, Division of Integrity and Technical Engineering, ÚJV Řež, a. s. Hlavní 130, Řež, 250 68 Husinec, Czech Republic, petr.gal@ujv.cz

To overcome this, the implemented 3D method employs a simultaneous regression approach [2]. By analysing the data in a unified 3D log-log space, the algorithm ensures that the material parameters are mutually consistent. The results of both methods for the wrought SS316L and 42CrMo4+QT steels are shown in Fig. 1 and 2, respectively.

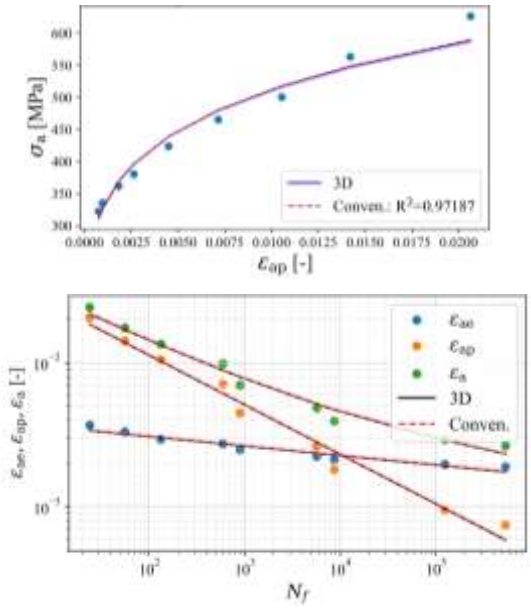

Figure 1: *CSSC* and *e-N* curves of SS316L.

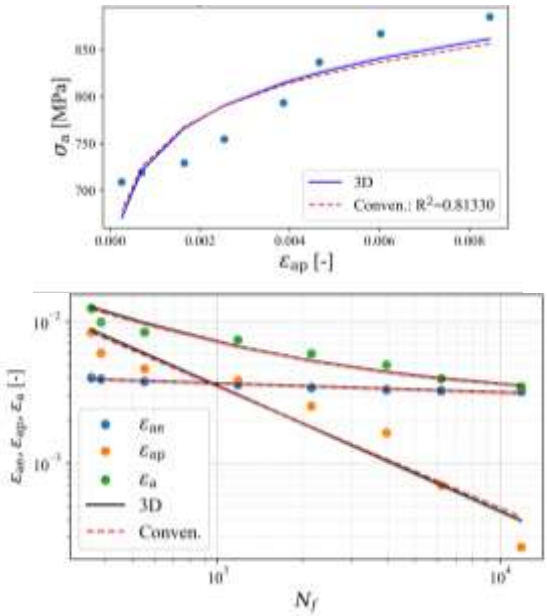

Figure 2: *CSSC* and *e-N* curve of 42CrMo4+QT.

3 Conclusion

This paper introduced an open-source, automated Python framework for LCF data processing, designed to enhance consistency and reliability in material characterization. As shown in Fig. 1, the implementation of the 3D method provides high-precision approximations for SS316L stainless steel, where the MCB model fits the data well. However, for 42CrMo4+QT alloy steel, the observed deviations highlight the limitations of this traditional approach. The results clearly demonstrate that, for certain material classes, the RO and MCB framework is insufficient for an accurate fatigue life prediction. Consequently, our ongoing work focuses on alternative models, such as the Smith-Watson-Topper parameter, which yields significantly better results for these materials.

Acknowledgement

This work was supported by COST Action CA23109 FABER, supported by COST (https://www.cost.eu/actions/CA23109/) and by the Specific Research Project SP2026/027.

References

[1] Niesłony A, El Dsoki Ch, Kaufmann H, Krug P. New method for evaluation of the Manson–Coffin–Basquin and Ramberg–Osgood equations with respect to compatibility. *International Journal of Fatigue*, 2008, 30, 1967–77.

[2] Ličková, D., Halama, R., Poruba, Z. Identification of Fatigue Constants by means of 3D Method. *Strojnický časopis – Journal of Mechanical Engineering*, 2016, Vol. 66 (2), pp. 107-116. https://doi.org/10.1515/scjme-2016-0025

[3] Fusek M, Halama R, Ličková D. Two modifications of Jiang criterion for constant amplitude multiaxial loading of AA2124-T851 and SS316L. *Continuum Mech. Thermodyn.* (2023) 35:877–893 https://doi.org/10.1007/s00161-020-00918-9

APPLIED MECHANICS 2026
April 13 - 15, 2026, České Budějovice, Czech republic

DEVELOPMENT AND EXPERIMENTAL EVALUATION OF A MACHINE LEARNING ASSISTED LWIR POLARIMETRIC IMAGING SYSTEM FOR TRANSPORT ANOMALY DETECTION

Jan Pařez[1], Patrik Kovář[2], Adam Tater[3], Ondřej Ballada[4], Čestmír Barta[5]

Abstract: This paper presents the development and experimental evaluation of an intelligent system using long-wave infrared (LWIR) polarimetric imaging combined with machine learning. By exploiting polarization-based contrast mechanisms, the approach improves detection of surface features that are difficult to identify with conventional methods. The work includes the design of an experimental setup and the creation of a representative LWIR polarimetric dataset. A modular framework integrating convolutional neural networks and image quality metrics enables automated scene interpretation. Results demonstrate enhanced detection of transport-related phenomena such as thin liquid films, surfaces, and hidden contamination, supporting future mobility and safety applications.

Keywords: LWIR polarimetry, machine learning, transport monitoring, anomaly detection

1 Introduction

Ensuring a high level of safety in modern transport systems requires reliable monitoring technologies capable of identifying hazardous surface conditions under various environmental circumstances. Conventional thermal imaging systems operating in the long-wave infrared (LWIR) spectral region are commonly used for this purpose because they allow the observation of temperature variations in a scene. However, the effectiveness of standard thermal imaging may decrease when objects exhibit similar thermal characteristics or when environmental conditions reduce temperature contrast.

Polarimetric imaging in the LWIR spectrum represents an advanced sensing approach that extends traditional infrared measurements by incorporating information about the polarization state of thermal radiation. In addition to intensity, polarimetric imaging provides valuable insight into surface properties such as geometry, roughness, and material composition. Previous studies have demonstrated that LWIR polarimetry can significantly enhance the visibility of objects and surface structures that are difficult to detect using conventional thermal imaging techniques [1]. Research in recent years has shown that polarization characteristics of thermal emission are strongly influenced by surface properties and environmental factors. This effect can be exploited to detect thin layers of liquids, surface contamination or other structural irregularities that may remain invisible in standard infrared images [2]. These properties make LWIR polarimetric imaging particularly attractive for monitoring applications in challenging conditions.

[1] Ing. Jan Pařez; Center of Aviation and Space Research, Faculty of Mechanical Engineering, Czech Technical University in Prague, Prague, 160 00, Czech Republic, Jan.Parez@fs.cvut.cz
[2] Ing. Patrik Kovář; Center of Aviation and Space Research, Faculty of Mechanical Engineering, Czech Technical University in Prague, Prague, 160 00, Czech Republic, Patrik.Kovar@fs.cvut.cz
[3] Ing. Jan Pařez; Center of Aviation and Space Research, Faculty of Mechanical Engineering, Czech Technical University in Prague, Prague, 160 00, Czech Republic, Adam.Tater@fs.cvut.cz
[4]Ing. Ondřej Ballada, MBA; BBT-Materials processing, Prague, 184 00, Czech Republic, ballada@calomel.cz
[5]Ing. Čestmír Barta, CSc.; BBT-Materials processing, Prague, 184 00, Czech Republic, barta@calomel.cz

Several investigations have explored the use of infrared polarimetry in environmental and maritime monitoring scenarios. The results indicate that polarimetric analysis can improve the detectability of water surfaces, oil films and other anomalies that exhibit distinct polarization signatures in the LWIR spectral range [3]. Similar approaches have also been considered for infrastructure monitoring and safety applications in transport systems [4].

In parallel with advances in sensing technologies, machine learning methods have become increasingly important for the automated interpretation of complex image data. Convolutional neural networks (CNNs) have demonstrated strong performance in various image recognition tasks and are widely used for pattern detection and classification in visual datasets [5]. Combining LWIR polarimetric imaging with machine learning-based data analysis therefore represents a promising approach for improving the detection of surface anomalies relevant to transport safety. Such integration allows the exploitation of additional physical information contained in polarization measurements while simultaneously enabling automated interpretation of the acquired data [6]. The aim of this study is to develop and experimentally evaluate an intelligent sensing system that integrates LWIR polarimetric imaging with machine learning techniques for transport monitoring applications. The work focuses on the design of the experimental measurement setup, the acquisition of polarimetric datasets and the development of a processing framework capable of identifying relevant surface features.

2 Experimental Methodology

An experimental imaging setup was designed to acquire polarimetric infrared data in the long-wave infrared spectral range (LWIR). The system consists of an LWIR thermal camera equipped with a rotatable polarizing element placed in front of the optical system. By adjusting the orientation of the polarizer, multiple images corresponding to different polarization states can be obtained. The polarizer rotation allows the acquisition of intensity measurements associated with specific polarization angles. These measurements can subsequently be processed to derive polarimetric parameters describing the state of polarization of the emitted radiation. The measurement configuration was arranged to allow stable positioning of the camera and repeatable adjustment of the polarizer orientation. Controlled measurements were performed under laboratory conditions to ensure consistent illumination and thermal stability.

Figure 1: Testbed with samples

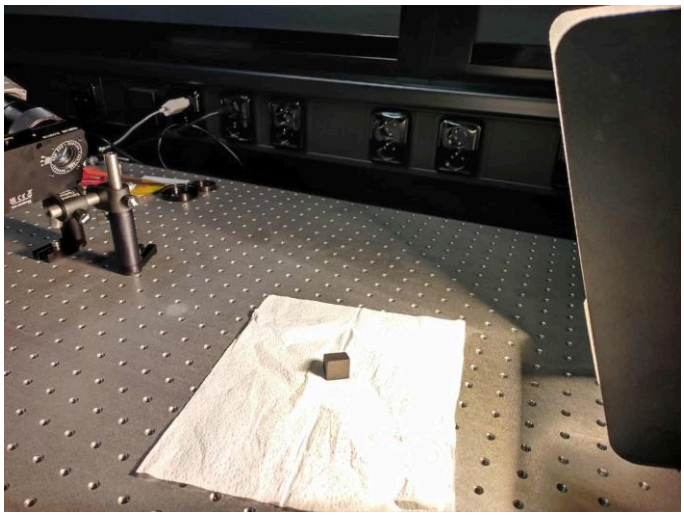

Figure 2: Experimental setup

A set of experiments shown on Figure 1 and Figure 2 was conducted to collect representative LWIR polarimetric data corresponding to different surface conditions relevant for transport monitoring scenarios. The measurements included surfaces exhibiting varying degrees of roughness, contamination and thin liquid layers. During each experiment the polarizer was gradually rotated to several predefined angular positions. For each position a thermal image was recorded. The resulting sequence of images forms the basis for calculating polarimetric parameters such as the degree of linear polarization. This acquisition procedure allows the extraction of additional surface information that cannot be obtained from conventional thermal intensity images alone.

After acquisition, the collected polarimetric data were processed using a modular computational framework. The processing pipeline includes image preprocessing, polarimetric parameter calculation and machine learning-based interpretation. Convolutional neural networks (CNN) were used to analyse spatial patterns present in the polarimetric images. The network architecture was selected to capture characteristic features associated with surface anomalies relevant for transport safety. Image quality metrics were also incorporated into the processing chain in order to assess the usefulness of individual polarimetric representations for anomaly detection.

3 Results

Experimental evaluation of the developed LWIR polarimetric imaging system demonstrated significant enhancement of anomaly visibility compared to standard thermal imaging. Laboratory prototype testing confirmed that the optical polarimetric module achieves a polarization ratio exceeding 1:10,000 at $\lambda = 9.3$ μm, validating the suitability of the calomel crystal element for high-performance LWIR polarization sensing. Rotational scanning experiments showed that surface anomalies exhibit strong dependence on polarization angle, which provides an additional contrast mechanism beyond pure thermal emissivity differences.

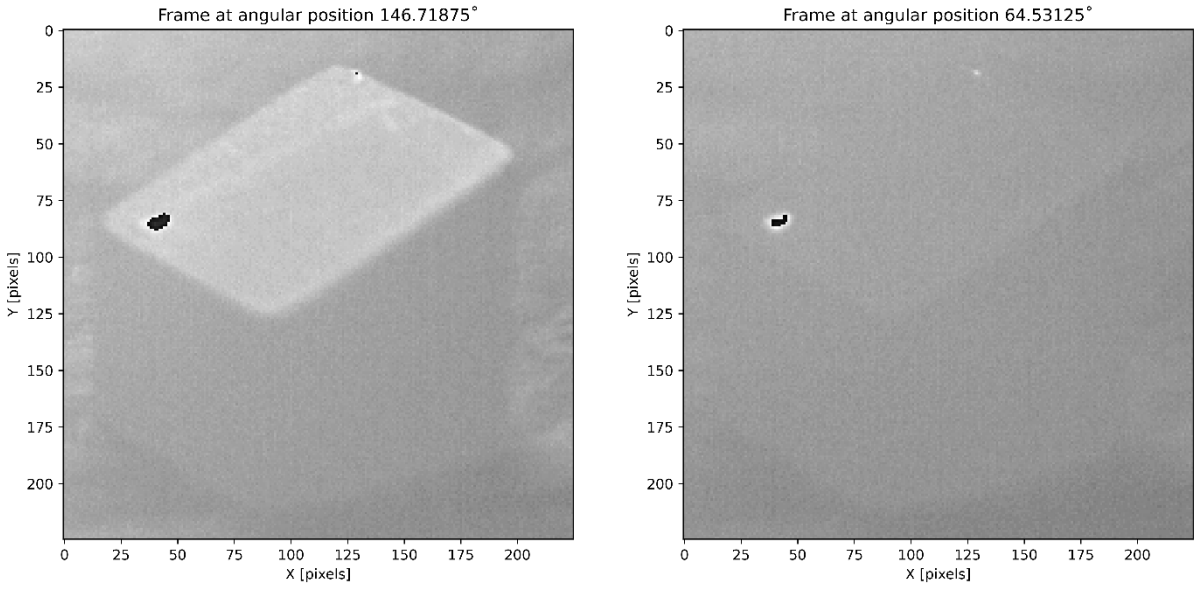

Figure 3: Experimental setup and example of the optimal polarizer rotation used during measurements

The first validation dataset shown on Figure 3 included controlled experiments on metallic and liquid-contaminated surfaces. In one experiment, a machined steel cube containing a synthetic defect was imaged under varying polarization orientations. Results showed that the defect contrast reached maximum visibility at an angle of approximately φ = 146.7°, while becoming nearly indistinguishable at φ = 64.5°, demonstrating how polarization selection can directly control detectability of structural irregularities.

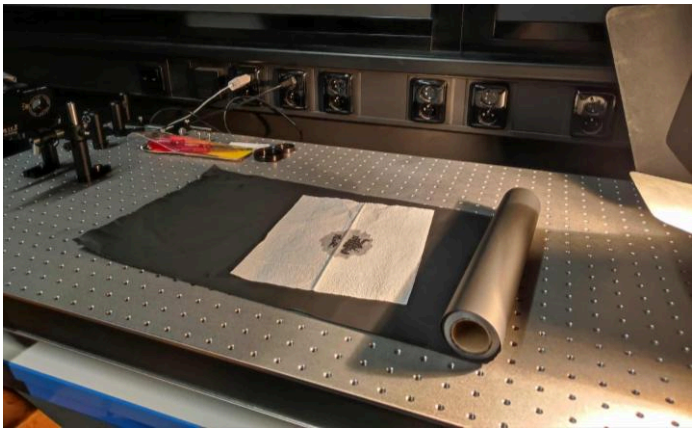

Figure 4: Second experimental case

A second experimental campaign shown on Figure 4 and Figure 5 focused on thin oil-film contamination deposited on an otherwise homogeneous surface. Conventional LWIR intensity imaging provided only weak differentiation, whereas polarimetric imaging revealed strong enhancement. Optimal detection occurred at φ = 160.5°, while the anomaly disappeared at φ = 57.7°, confirming that thin surface layers produce highly polarization-sensitive signatures.

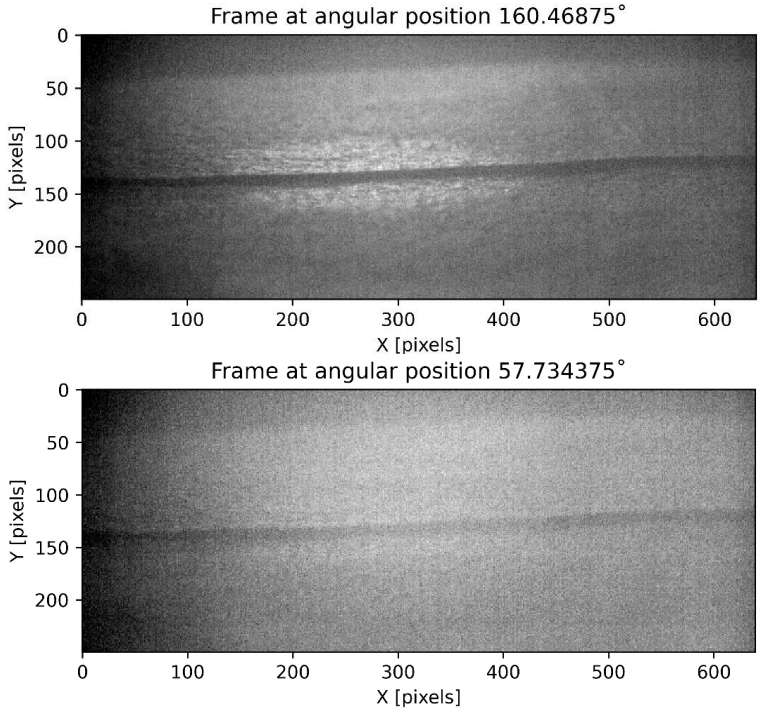

Figure 5: Image with the most suitable polarizer rotation φ= 160.47° (top); Image with the least suitable polarizer rotation φ=57.73° (bottom).

A third experiment investigated paraffin contamination on a water surface as a representative case of hidden thin-film transport hazard. The paraffin layer was essentially invisible under normal observation but became clearly detectable through LWIR polarization contrast. Maximum enhancement was achieved at $\varphi = 174.8°$, confirming the ability of the proposed sensing concept to identify subtle contamination structures that are critical for transport safety applications.

The machine learning processing pipeline was validated on the collected dataset and demonstrated stable integration with real-time acquisition. CNN-based interpretation proved feasible for automated anomaly recognition, while the incorporated image quality metrics enabled systematic selection of the most informative polarization state. These results confirm the functional readiness of the developed framework for extended validation in real transport environments.

4 Conclusion

This paper presented the development and experimental validation of a sensing system that integrates LWIR polarimetric imaging with machine learning techniques for transport anomaly detection. The proposed approach exploits polarization-dependent thermal radiation to reveal surface features that are difficult to observe using conventional thermal cameras.

An experimental measurement setup was implemented to acquire polarimetric infrared data, and a dedicated processing framework was developed to analyse the recorded images using convolutional neural networks. The results obtained from laboratory experiments confirm that polarimetric imaging significantly improves the visibility of thin liquid layers, contamination and other surface structures relevant to transport safety.

The presented methodology demonstrates promising potential for future applications in intelligent transport monitoring systems. Further work will focus on expanding the dataset, optimizing the machine learning models and evaluating the approach in real-world operating conditions.

Acknowledgement

This work was supported by the Technology Agency of the Czech Republic under the SIGMA Programme, project No. TQ15000307.

References

[1] HARCHANKO, John, et al. Detecting a surface swimmer using long wave infrared imaging polarimetry. In: *Proc. SPIE*.

[2] HARCHANKO, John S., et al. Comparing a MWIR and LWIR polarimetric imaging for surface swimmer detection. In: *Optics and Photonics in Global Homeland Security IV*. SPIE, 2008. p. 194-204.

[3] JOHN, Jaclyn A., et al. LWIR polarized signals detected from ice clouds. *Journal of Applied Remote Sensing*, 2025, 19.4: 044509-044509.

[4] SHANKS, Kira A., et al. High-altitude demonstration of LWIR polarimetry using uncooled microbolometers. *Journal of Quantitative Spectroscopy and Radiative Transfer*, 2024, 315: 108872.

[5] SHEENY, Marcel, et al. POL-LWIR vehicle detection: Convolutional neural networks meet polarised infrared sensors. In: *Proceedings of the IEEE Conference on Computer Vision and Pattern Recognition Workshops*. 2018. p. 1247-1253.

[6] LI, Xiaobo, et al. Polarimetric imaging via deep learning: A review. *Remote Sensing*, 2023, 15.6: 1540.

APPLIED MECHANICS 2026
April 13 - 15, 2026, České Budějovice, Czech republic

COMPUTER VISION – BASED STRAIN FIELD ANALYSIS OF 3D PRINTED MATERIALS

Ondrej Piroh[1], Ján Minárik[2], Jaroslav Majko[3], Marián Handrik[4], Milan Vaško[5], Milan Sága[6]

Abstract: This study analyzes the mechanical behavior of 3D printed materials using displacement measurements based on computer vision. Circular markers applied to sample surfaces are detected, and their centers of gravity are determined via MATLAB image processing. Time evolution of marker positions provides displacements, which are used to assemble a finite element mesh. From this, deformation and stress fields, deformation energy density, and total accumulated energy are calculated. Experiments were conducted on PET-G samples produced by FFF technology. The results demonstrate that the proposed method is effective for experimental analysis of the mechanical behavior of 3D printed materials.

Keywords: computer vision; 3D printing; finite element method; deformation analysis; PET-G material

1 Introduction

The correct determination of the mechanical properties of structural materials is crucial for their practical application. Currently, there is significant development in additive manufacturing technologies, such as 3D printing, where detailed knowledge of material behavior under load is necessary for reliable application. These properties are primarily determined through mechanical testing of materials and subsequent analysis of experimental data. The basic quantities obtained from mechanical tests are mainly force and displacement, from which it is possible to determine the state of stress and strain in the material based on the principles of continuum mechanics. Force measurement is not a significant problem today, as it is a standard output of tensile testing equipment. However, measuring displacement in the central part of the test specimen is more challenging. This can be accomplished using either contact or non-contact extensometers, each with its own advantages and limitations. Contact extensometers can be damaged, for example, by unexpected sample failure, while non-contact systems eliminate direct contact with the sample and provide sufficient accuracy, but require higher initial costs, qualified personnel, and sample surface modification [7]. For this reason, new approaches are currently being developed that would preserve the advantages of existing methods while eliminating their shortcomings. This article follows on from the author's previous studies [1–2] and extends the proposed approach by implementing the finite element method to calculate strains, stresses, strain energy density, and total accumulated energy in the monitored plane area.

[1] Ing. Ondrej Piroh; University of Žilina, Department of Applied Mechanics; Univerzitná 8215/1, 010 26 Žilina, Slovakia, ondrej.piroh@fstroj.uniza.sk
[2] Ing. Ján Minárik; University of Žilina, Department of Applied Mechanics; Univerzitná 8215/1, 010 26 Žilina, Slovakia, jan.minarik@fstroj.uniza.sk
[3] Ing. Jaroslav Majko, Ph.D.; University of Žilina, Department of Applied Mechanics; Univerzitná 8215/1, 010 26 Žilina, Slovakia, jaroslav.majko@fstroj.uniza.sk
[4] Ing. Marián Handrik, Ph.D.; University of Žilina, Department of Applied Mechanics; Univerzitná 8215/1, 010 26 Žilina, Slovakia, marian.handrik@fstroj.uniza.sk
[5] doc. Ing. Milan Vaško, Ph.D.; University of Žilina, Department of Applied Mechanics; Univerzitná 8215/1, 010 26 Žilina, Slovakia, milan.vasko@fstroj.uniza.sk
[6] Dr. h. c. prof. Dr. Ing. Milan Sága, Ph.D.; University of Žilina, Department of Applied Mechanics; Univerzitná 8215/1, 010 26 Žilina, Slovakia, milan.saga@fstroj.uniza.sk

2 Theoretical background

Determining the fields of strain, stress, strain energy density, or total accumulated energy of the computational domain requires an understanding of how to measure displacements using computer vision, as well as knowledge of the basic theories of continuum mechanics necessary to calculate these quantities. The following subchapters will briefly introduce the basic principles of using computer vision to measure displacements, as well as the key relationships needed to calculate the aforementioned physical quantities.

2.1 Computer vision

Displacements were measured using a non-contact extensometer based on computer vision techniques for detecting object edges and marker contours. In an earlier study [1], the authors introduced a method employing line markers applied to a flat specimen, which allowed precise evaluation of displacements along the loading axis. When circular markers are used instead, it becomes possible to capture transverse displacements. The author is part of a team that has published a separate article on this principle. The principle of the approach is presented in Figure 1: Fig. 1(a) shows the created image. Fig. 1(b) shows the detection of circular marker boundaries using the *regionprops* function [6], and Fig. 1(c) displays the calculated centroids of the individual markers [2].

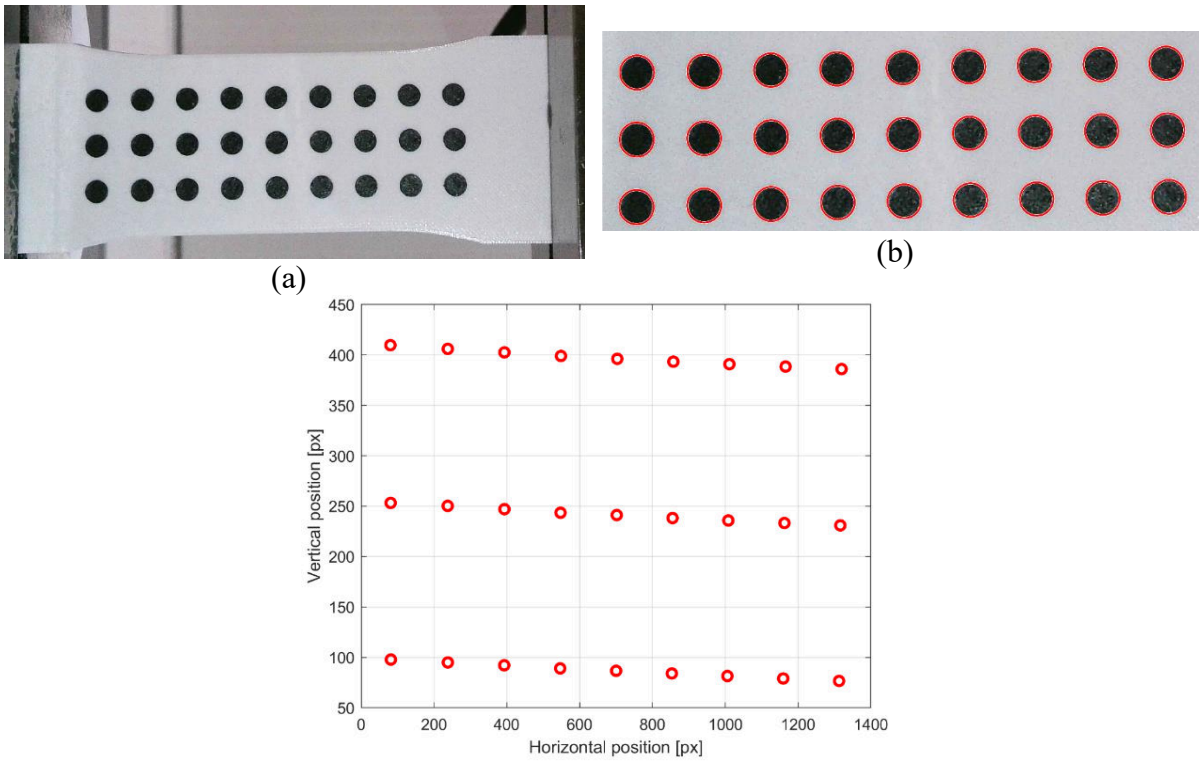

Figure 1: Detection of circular markers' centers of gravity [2]: (a) view of the detection area, (b) identification of markers in the detection area, (c) positions of the centers of gravity of all detected object

The centroids of the circular markers were determined in MATLAB using the *regionprops* function. Specifically, the parameters *Centroid, MajorAxisLength,* and *MinorAxisLength* were extracted, yielding the coordinates of each marker's center as well as the lengths of the corresponding major and minor axes of the equivalent ellipse. These

geometric characteristics were subsequently used to evaluate the radius of each circular marker according to equation (1).

$$r = \frac{A + a}{4} \tag{1}$$

where A denotes the major axis length (*MajorAxisLength*) and a represents the minor axis length (*MinorAxisLength*) of the fitted elipse.

2.2 Stress – strain calculation

The state of strain at a selected point on the continuum can be described using a strain tensor. There are several formulations of these tensors, and their application depends on the magnitude of the strain. For small values, i.e., a geometrically linear problem, the infinitesimal (engineering) strain tensor is used. If the deformations exceed 2%, a geometrically nonlinear problem arises, in which case the Lagrange and Euler deformation tensors are used. In the case of circular markers, it should be noted that this is a calculation of true stress and true strain [3–4].

For a linearly elastic material in a plane, the components of the strain tensor ε are defined by equation (2).

$$\varepsilon = \begin{bmatrix} \varepsilon_{xx} \\ \varepsilon_{yy} \\ \gamma_{xy} \end{bmatrix} \tag{2}$$

In the case of two-dimensional plane stress (the case under consideration), the stress σ can be expressed using the material stiffness matrix D, as shown in equation (3),

$$D = \frac{E}{1-\mu^2} \begin{bmatrix} 1 & \mu & 0 \\ \mu & 1 & 0 \\ 0 & 0 & \frac{1-\mu}{2} \end{bmatrix} \tag{3}$$

where E is the modulus of elasticity and μ Poisson's ratio. The stress calculation is then expressed in equation (4).

$$\sigma = D \,.\, \varepsilon \tag{4}$$

The strain energy density at point element is calculated using equation (5).

$$w = \frac{1}{2} \sigma^T \varepsilon \tag{5}$$

The total cumulative energy of the computational region in the case of plane stress is calculated based on the integration of the deformation energy density over the area of the region being solved. This calculation is described by equation (6),

$$U = \int_A w dA \tag{6}$$

where A is the content of the addressed area.

3 Measurement

The experimental measurements were carried out on five specimens, with image acquisition performed using a Trust 4K Ultra HD webcam providing a resolution of 3840 x 2160 px [5]. To ensure measurement reliability, fundamental conditions were maintained throughout the experiment, including proper alignment of the camera axis perpendicular to the

specimen surface, manual focus adjustment, and an appropriate camera – to - specimen distance. Images were recorded at a rate of one frame every 0,5 seconds, and the acquisition during the tensile test was automated via a MATLAB script, as illustrated in Fig. 2.

Figure 2: Measurement process

The tensile experiments were carried out on modified flat specimens fabricated using FFF (Fused Filament Fabrication) 3D printing technology. The geometry and dimensions of the specimens are presented in Fig. 3. The specimens were manufactured from PET – G material, and circular black markers produced from the same material were applied to the central region to provide sufficient contrast and enable reliable detection during image processing.

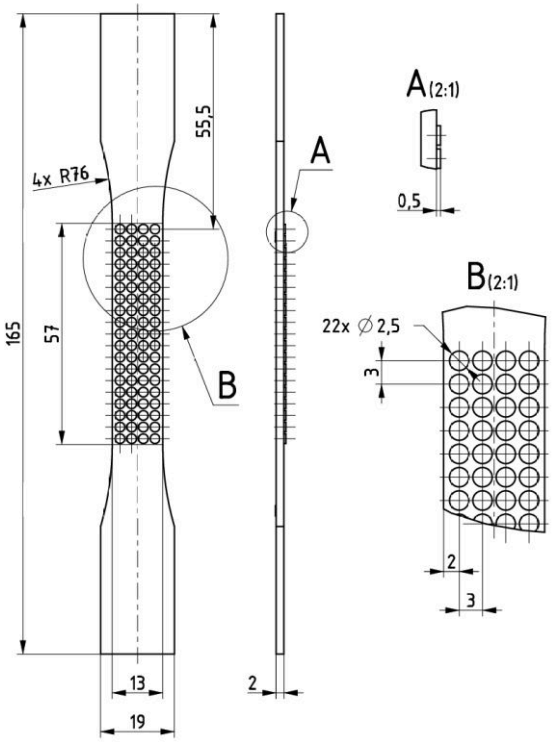

Figure 3: Shape and dimensions of the specimens used

4 Results

After the experimental measurements, the obtained data were processed and evaluated. The analysis produced a matrix of coordinates representing the centers of gravity of the markers over time in the recorded images. The number of images differed between tests because the samples failed at different times even under the same load. In two cases, the samples failed outside the monitored area, so these measurements were excluded. Therefore, the results in Table 1 are based on three measurements. First, the positions of the marker centers were determined. Next, a finite element mesh was created with nodes defined by these centers. Measured displacements were assigned to the nodes, enabling the calculation of strain fields. Subsequently, stresses, strain energy density, and total accumulated energy were determined. Since the test involved tensile loading, the evaluated variables correspond to the maximum values of the first principal stresses and strains. The averaged maximum values from the individual measurements are presented in Table 1. The distribution of the first principal stress from selected measurements is shown in Fig. 4, together with the fields of first principal strain and strain energy density. Based on the distribution of maximum values, failure is expected in the lower part of the sample, where the highest values occur.

σ_{1max} $[MPa]$	ε_{1max} $[-]$	w_{MAX} $\left[\frac{mJ}{mm^3}\right]$	U $[mJ]$
41,25	0,02	0,45	39,14

Table 1. Mean maximum mechanical parameters obtained during the tensile test.

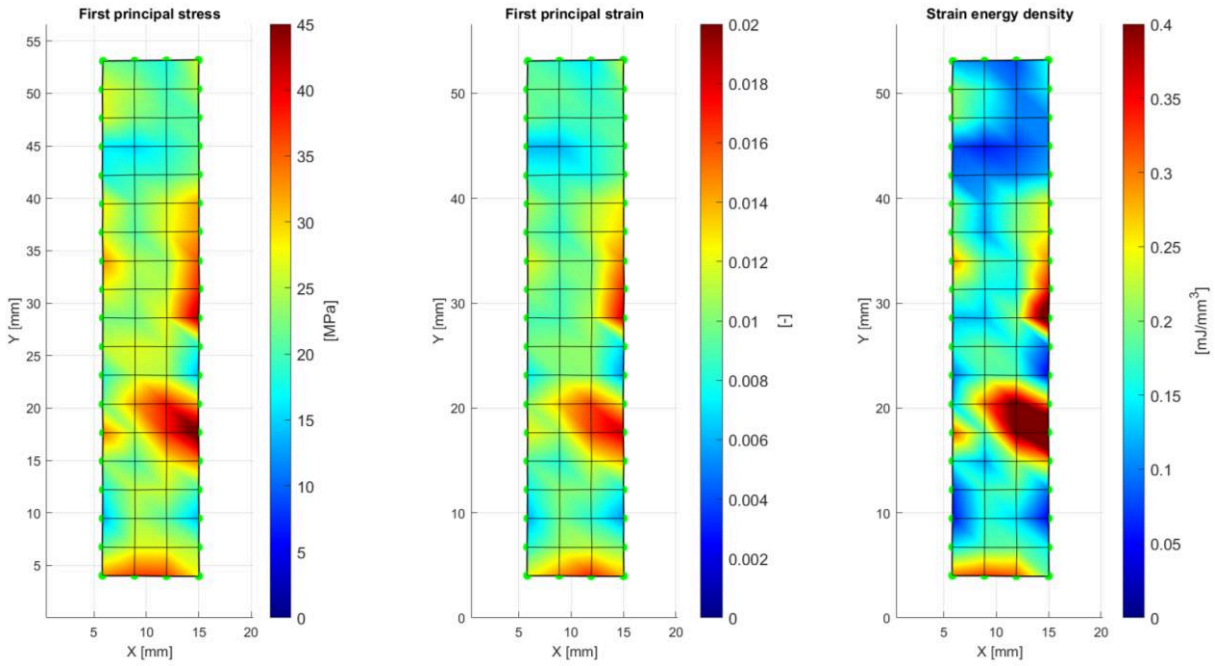

Figure 4: First principal stress

5 Conclusion

This study aimed to extend the existing approach based on the use of computer vision methods for analyzing the mechanical behavior of 3D printed materials during loading. The proposed methodology is based on the detection of circular markers applied to the surface of the test specimen, whose centers of gravity were determined using the *regionprops* function in MATLAB. Based on the temporal evolution of the marker positions, node displacements were determined, which served as input data for the assembly of a finite element mesh and the subsequent calculation of strain and stress fields in the monitored area. Based on these quantities, the strain energy density and the total accumulated energy of the analyzed area were further determined. Experimental measurements were performed on samples produced using FFF 3D printing technology from PET-G material. The results confirm that the proposed approach allows for effective evaluation of mechanical fields based on image recording of the experiment and represents an affordable alternative to standard non-contact measurement systems. The proposed methodology also creates space for its further expansion and application in the analysis of the mechanical behavior of various types of additively manufactured materials.

Acknowledgement

This work has been supported by the grant projects KEGA 005ŽU-4/2024 and VEGA 1/0423/23.

References

[1] Piroh, O., Majko, J., Handrik, M,. Vaško, M., Cienciala, J., Šofer, M., Fusek, M., Sága, M. Rapid and cost-efficient approach for non-contact measurement in experimental mechanics, Results in Engineering, 2025, 26. https://doi.org/10.1016/j.rineng.2025.105408.
[2] Majko, J., Piroh, O., Minárik, J., Vaško, M., Handrik, M., Sága, M., & Saternus, Z. (2025). Strain Field Determination for Additively Manufactured Thermoplastics Using Computer Vision. *Manufacturing Technology*, *25*(4), 511–520. https://doi.org/10.21062/mft.2025.060
[3] LAI, W. M., RUBIN, D., KREMPL, E. (1993). Introduction to Continuum Mechanics, pp. 1 X. Butterworth-Heinemann Ltd., Oxford. ISBN 0750628944.
[4] REDDY, J. N. (2013). An Introduction to Con tinuum Mechanics, Second Edition, pp. 1–X. Cambridge University Press, Cambridge. ISBN 9781107025431.
[5] Trust. Trust Teza 4K Ultra HD Webcam. Available at: https://www.trust.com/en/product/24280-teza-4k-ultra-hd-webcam (Accessed 9th March 2026).
[6] MathWorks. regionprops. Available at: https://www.mathworks.com/help/images/ref/regionprops.html, (Accessed 9th March 2026)
[7] Tian, Q. H., Yan, L. P., Yang, T., Chen, B. Y. Recent Developments of Material Deformation Measurement, Applied Mechanics and Materials, 2011, 117-119, 122-128, https://doi.org/10.4028/www.scientific.net/AMM.117-119.122

APPLIED MECHANICS 2026
April 13 - 15, 2026, České Budějovice, Czech republic

CRACK INITIATION TIME ESTIMATION FOR CASES OF PLASTIC PIPES UNDER STRESS RELAXATION CONDITIONS

Jan Poduška[1*], Lukáš Trávníček[1], Roman Gratza[1], Florian Arbeiter[2], Daniel Zach[2], Luboš Náhlík[1], Pavel Hutař[1]

Abstract: Lifetime estimation of plastic pipes installed underground is difficult mainly due to the unclear boundary conditions and the very long-time frame in which the material undergoes stress relaxation. This contribution investigates the possibility of using damage accumulation hypothesis to estimate time to crack initiation and lifetime more precisely.

Keywords: plastic pipes; slow crack growth; lifetime; relaxation.

1 Introduction

Lifetime estimation of plastic pipes installed underground is difficult, mainly due to unclear boundary conditions and the very long timeframe in which the material undergoes stress relaxation. The general aim of the work presented in this contribution is to develop a methodology for lifetime calculation relevant to such conditions. Currently, methodologies are available for estimating crack propagation times of high-density polyethylene (HDPE) pressure pipes, but not for non-pressure pipes [1, 2]. This issue is particularly pressing, due to stronger incentives to utilize more recycled materials in manufacturing non-pressure pipes [3]. Recycled material content degrades mechanical properties [4], which further necessitates reassessment of the pipes.

This contribution investigates the feasibility of estimating the service life of a flexible non-pressure pipe made from recycled polymer using assumptions of linear-elastic fracture mechanics while accounting for stress relaxation. The work is part of a broader effort to find and verify a methodology of lifetime calculation relevant for underground installations where non-pressure pipes experience continuous relaxation stresses.

2 Modelling and Crack Initiation Time Calculations

The methodology applied here combines finite element simulations with experimental characterization of crack propagation in the polymer. It is demonstrated via crack initiation and lifetime calculations for a non-pressure pipe made entirely of recycled HDPE (outer diameter 50 mm, wall thickness 4 mm) in a parallel-plate relaxation test at 80°C, where the pipe was compressed by 12% of its initial diameter. During relaxation, damage initiates and propagates as cracks through the wall – a primary failure mode known as slow crack growth in HDPE pipes under long-term loading [1, 2].

The case used for illustration is non pressure pipe made completely out of recycled HDPE – outer diameter of 50 mm, wall thickness of 4 mm.

[1] Institute of Physics of Materials, Czech Academy of Sciences; Zizkova 513/22, 616 00 Brno, Czech Republic
[2] Institute of Material Science and Testing of Polymers – Montanuniversität Leoben; Otto Glöckel-Straße 2, 8700 Leoben, Austria
[*] poduska@ipm.cz

The pipe was subject to an actual parallel plate relaxation test, where it was compressed by 12 % of the initial diameter and left to relax in a chamber at 80 °C.

2.1 FEM Model of the Parallel Plate Relaxation Test

Crack propagation in the compressed pipe was modelled using both a 2D planar model and a 3D model featuring a semi-elliptical crack. The material was treated as linear-elastic, with stress relaxation simulated via a time-dependent decrease in the modulus of elasticity. The stress intensity factor was determined as a function of crack length and modulus. From the experiment, the time-dependent record of the reaction force on the upper plate enabled calculation of the relaxation modulus. These results were then combined with the SIF calculations to produce 2D splines characterizing crack propagation over time. Scheme of the crack in the models is in Figure 1a, SIF functions in Figure 1b.

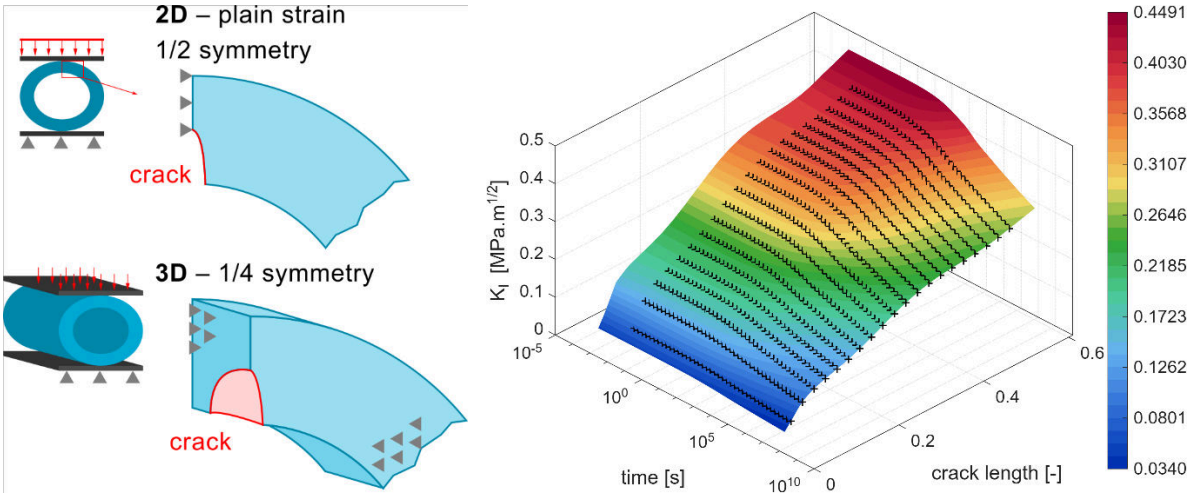

a) b)

Figure 1: a) Scheme of the 2D and 3D models for the SIF calculation; b) Spline describing the dependency of SIF on time and crack length for the 3D model.

2.2 Crack Initiation Time Estimation

The crack initiation law is an empirical relationship that describes time to initiation t_{ini} of the crack propagation in the material as a function of SIF for an initial defect $K_{I,ini}$ of a small size:

$$t_{ini} = B \cdot K_{I,ini}^{-n} \tag{1}$$

where B and n are constants obtained through a series of experiments on notched specimens. For the recycled PE, values of B = 0.07 s and n = −7.68 s/MPa·m$^{1/2}$ were used. This law can be integrated in time, using SIF dependency on time and crack length obtained from FEM.

With an initial defect size of 0.4 mm, crack initiation times were calculated and plotted alongside total failure times and reaction force (Figure 2). The experimental data shows a sharp decrease in force toward the end of the test, marking the point where the pipe lost stability and collapsed due to extensive cracking. This collapse occurred after approximately 10–20 hours.

In comparison, the 2D model is overly conservative, predicting a total lifetime of only 0.76 hours (with 0.54 hours for initiation). Conversely, the 3D model overestimates these durations. This discrepancy between the 3D model and the experimental results may be due to multiple crack initiation points within the recycled polymer—a phenomenon that warrants further investigation to reconcile these differences.

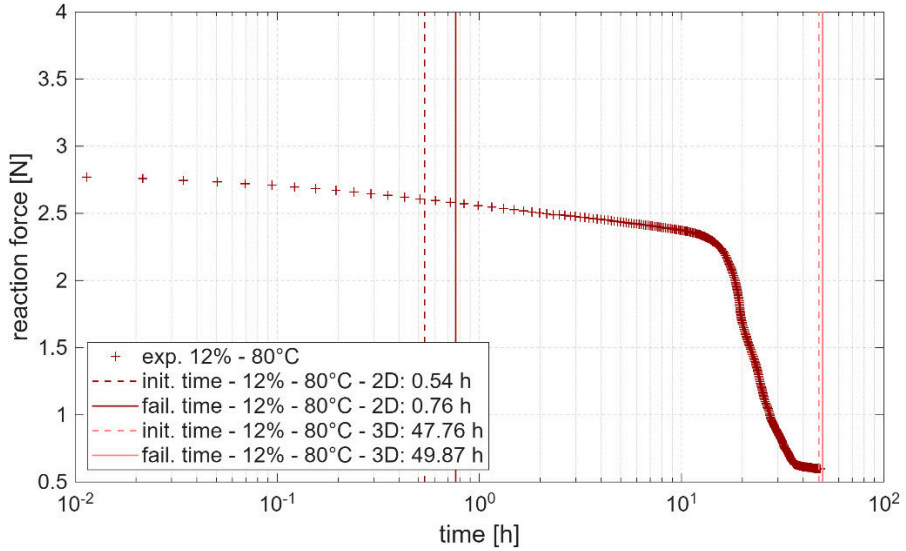

Figure 2: Experimental record of the reaction force from the parallel plate test with the calculated initiation times and total lifetimes.

3 Conclusions

The methodology is a promising candidate for further study. With the 2D model already providing a safe, conservative estimation, future research will focus on reconciling the model behavior with experimental observations to improve predictive accuracy of the 3D model.

Acknowledgement

This work was supported by the Christian Doppler Research Association through the project *"CD Laboratory for Impact of recycled materials on the mechanical lifetime estimation of polymers"*. The support by project "*Partnership for Security in Sustainable Transport and Energy"*, funded as project No. CZ.02.01.01/00/23_020/0008549 by Programme Johannes Amos Comenius, is also acknowledged.

References

[1] TRÁVNÍČEK, Lukáš; PODUŠKA, Jan; MESSIHA, Mario; ARBEITER, Florian; PINTER, Gerald et al. Effect of recycled material on failure by slow crack growth in multilayer polyethylene pipes. *Engineering Fracture Mechanics*. 2023, vol. 289, s. 109423-109423. ISSN 0013-7944.

[2] WEE, Jung-Wook; PARK, Sang-Youn a CHOI, Byoung-Ho. Modeling and application of discontinuous slow crack growth behaviors of high-density polyethylene pipe with various geometries and loading conditions. *Engineering Fracture Mechanics*. 2020, vol. 236, s. 107205-107205. ISSN 0013-7944.

[3] JUAN, Rafael; DOMÍNGUEZ, Carlos; ROBLEDO, Nuria; PAREDES, Beatriz a RAFAEL A. GARCÍA-MUÑOZ. Incorporation of recycled high-density polyethylene to polyethylene pipe grade resins to increase close-loop recycling and Underpin the circular economy. *Journal of Cleaner Production*. 2020, vol. 276, s. 124081-124081. ISSN 0959-6526.

[4] PAUL J. FREUDENTHALER; FISCHER, Joerg; LIU, Yi a REINHOLD W. LANG. Short- and Long-Term Performance of Pipe Compounds Containing Polyethylene Post-Consumer Recyclates from Packaging Waste. *Polymers*. 2022, vol. 14, no. 8, s. 1581-1581. ISSN 2073-4360.

APPLIED MECHANICS 2026
April 13 - 15, 2026, České Budějovice, Czech republic

OPTIMIZATION OF JONES-WILKINS-LEE EOS PARAMETERS FOR THE PG3 EXPLOSIVE

Angel Prado[1], Ricardo Castedo[2], Anastasio P. Santos[3], María Chiquito[4], Carlos Gómez-De-Cabo[5], Lina M. López[6], José I. Yenes[7], Martin Isoz, M. [8]

Abstract: Accurate prediction of air-blast effects requires reliable JWL EOS parameters, but traditional cylinder tests are costly and complex. This study presents a methodology to determine JWL parameters using height-of-burst experiments combined with numerical optimization. PG3 explosive detonations (0.7–1.4 kg) were simulated in a 2D axisymmetric LS-DYNA model, with experimental pressure–time histories guiding the optimization. The calibrated parameters reproduced overpressure profiles with errors below 10% and were validated using Viper::Blast simulations. This approach offers a cost-effective, flexible alternative to conventional methods, enabling rapid, reliable EOS parameter determination with minimal experimental effort.

Keywords: Blast simulation; LS-DYNA; JWL-EOS; LS-OPT.

1 Introduction

Accurate prediction of air-blast effects depends on reliable Equation of State (EOS) parameters for explosives. An EOS is a mathematical model that describes the relationship between pressure, volume, and internal energy of a material, allowing prediction of its thermodynamic response under explosive loading conditions. Among available models, the Jones–Wilkins–Lee (JWL) EOS is widely used due to its proven performance in describing detonation gas expansion [1–3]. Traditionally, JWL parameters are obtained through cylinder tests followed by manual calibration [4,5], a process that is costly, time-consuming, and potentially hazardous. Recent efforts have explored alternative approaches, including empirical fitting [6], computational techniques [7], analytical models [8], and optimization-based methods [9]. This study presents a practical methodology to determine JWL EOS parameters directly from height-of-burst detonation tests, combining 2D axisymmetric LS-DYNA simulations with optimization techniques implemented in LS-OPT. The method is

[1] Dr. Angel Prado; Czech Academy of Sciences, Institute of Thermomechanics, Dolejškova 5, 182 00, Prague, Czech Republic, prado@it.cas.cz
[2] Prof. Dr. Ricardo Castedo; E.T.S.I. Minas y Energía – Universidad Politécnica de Madrid, C/ Ríos Rosas, 21, 28003, Madrid, Spain, ricardo.castedo@upm.es
[3] Prof. Dr. Anastasio P. Santos; E.T.S.I. Minas y Energía – Universidad Politécnica de Madrid, C/ Ríos Rosas, 21, 28003, Madrid, Spain, tasio.santos@upm.es
[4] Prof. Dr. María Chiquito; E.T.S.I. Minas y Energía – Universidad Politécnica de Madrid, C/ Ríos Rosas, 21, 28003, Madrid, Spain, maria.chiquito@upm.es
[5] MSc. Carlos Gómez-De-Cabo; Unidad de Exenciones REACH y Laboratorios de la Defensa, C/ Donoso Cortés, 92, 28015, Madrid, Spain, cgomdec@et.mde.es
[6] Prof. Dr. Lina M. López; E.T.S.I. Minas y Energía – Universidad Politécnica de Madrid, C/ Ríos Rosas, 21, 28003, Madrid, Spain, lina.lopez@upm.es
[7] Dr. José I. Yenes; Escuela Politécnica Superior del Ejército – Ministry of Defense, C/ Joaquín Costa, 6, C.P. 28071, Madrid, Spain, jyengal@et.mde.es
[8] Dr. Martin Isoz; Czech Academy of Sciences, Institute of Thermomechanics, Dolejškova 5, 182 00, Prague, Czech Republic, isozm@it.cas.cz

applied to PG3 explosive (similar to C4 in composition), for which no validated JWL EOS exists.

The proposed approach provides a safer, cost-effective, and reproducible alternative to traditional cylinder tests, reducing experimental complexity while maintaining high predictive accuracy.

2 Test description

In 2022, a series of height-of-burst detonation tests were conducted at the Palancar Firing Range, Hoyo de Manzanares, using the military explosive PG3, a C4-type formulation composed of 89% RDX and 11% HTPB, with a density of 1580 kg/m³. Ten tests were performed with charges of 0.7, 1.0, and 1.4 kg, including one repetition to compensate for a sensor malfunction. Each spherical charge was suspended 0.5 m above ground and initiated centrally. Pressure sensors (PCB Piezotronics®) were placed at 2, 4, and 8 m radial distances from the charge. Recorded pressure signals were filtered with a fourth-order Butterworth low-pass filter and, when needed, corrected for offsets. The positive-phase parameters of each blast were then extracted by fitting the signals to the Friedlander equation, providing the input data for the JWL EOS parameter optimization.

3 Numerical Model

A two-dimensional axisymmetric model of the height-of-burst tests was developed in LS-DYNA using the Multimaterial Arbitrary Lagrangian-Eulerian approach. The model forms the basis for the subsequent LS-OPT optimization of selected explosive parameters.

The computational domain was discretized using a structured mesh, with local refinement near the explosive charge and at sensor locations to ensure accurate prediction of blast pressures. Boundary conditions constrained the ground while remaining boundaries were treated as non-reflecting. The explosive PG3 was modelled using the JWL EOS:

$$P = A\left(1 - \frac{\omega}{R_1 V}\right)e^{-R_1 V} + B\left(1 - \frac{\omega}{R_2 V}\right)e^{-R_2 V} + \frac{\omega E}{V} \quad (1)$$

where P is pressure, V is the relative volume (v/v_0), E is the internal energy, and A, B, R_1, R_2 and ω are material-specific constants. Some of these parameters were determined from experimental data, as they represent the thermomechanical properties of the explosive, while A, B, R_1 and R_2 were calibrated through the optimization process. Air was modelled as an ideal gas with a linear-polynomial EOS.

4 Optimization Method

The unknown JWL-EOS parameters of the PG3 explosive (A, B, R_1 and R_2) were identified using LS-OPT, an optimization tool used in conjunction with the LS-DYNA model described previously. A Sequential Response Surface Method (SRSM) was employed to efficiently explore the JWL parameter space. SRSM constructs surrogate models based on a limited set of LS-DYNA simulations, allowing the algorithm to predict responses at unsampled points. This approach enables iterative refinement of the JWL parameters while keeping computational costs manageable, as new sample points are adaptively added to improve the surrogate model and guide the search toward the global optimum.

Pressure–time histories from the 0.7 kg and 1.4 kg field tests at 2 m and 4 m sensor positions were used as target data for the optimization. The optimization objective was defined as a weighted mean squared error between simulated and experimental values,

considering both the peak overpressure and 9 other pressure points along the positive pressure phase.

Convergence of the optimization process was found after 11 iterations. The calibrated parameters successfully reproduce both the peak overpressure and the average positive phase, with most values deviating less than ±10%. Slightly larger discrepancies were observed for the 0.7 kg charge, primarily due to higher sensor-to-sensor variability and the shorter duration of the positive phase, which is closer to the temporal resolution and noise floor of the measurement system.

5 Results and Validation

Validation was performed using the 1 kg charge, which was not included in the optimization. Simulated peak pressures differed from experimental measurements by −5.6% and 10.8% at 2 m and 4 m, respectively, while the average positive phase errors were 6.2% and −3.7%, confirming the generalization of the optimized JWL parameters to independent test conditions.

Further validation was conducted with Viper::Blast, a computational fluid dynamics (CFD) code for blast simulations, for 0.7, 1, and 1.4 kg charges at sensors at 2, 4, and 8 m. A 1D–2D remapping strategy was applied to refine the mesh during the initial detonation phase. Across all tests, the average relative differences between simulation and experiment were 5.76% for peak pressure and 6.94% for impulse. Errors were generally lower at sensors closer to the charge and for larger charges, while minor discrepancies at distant sensors are attributed to experimental uncertainties, idealized geometry, and the implicit treatment of afterburn effects in the JWL-EOS.

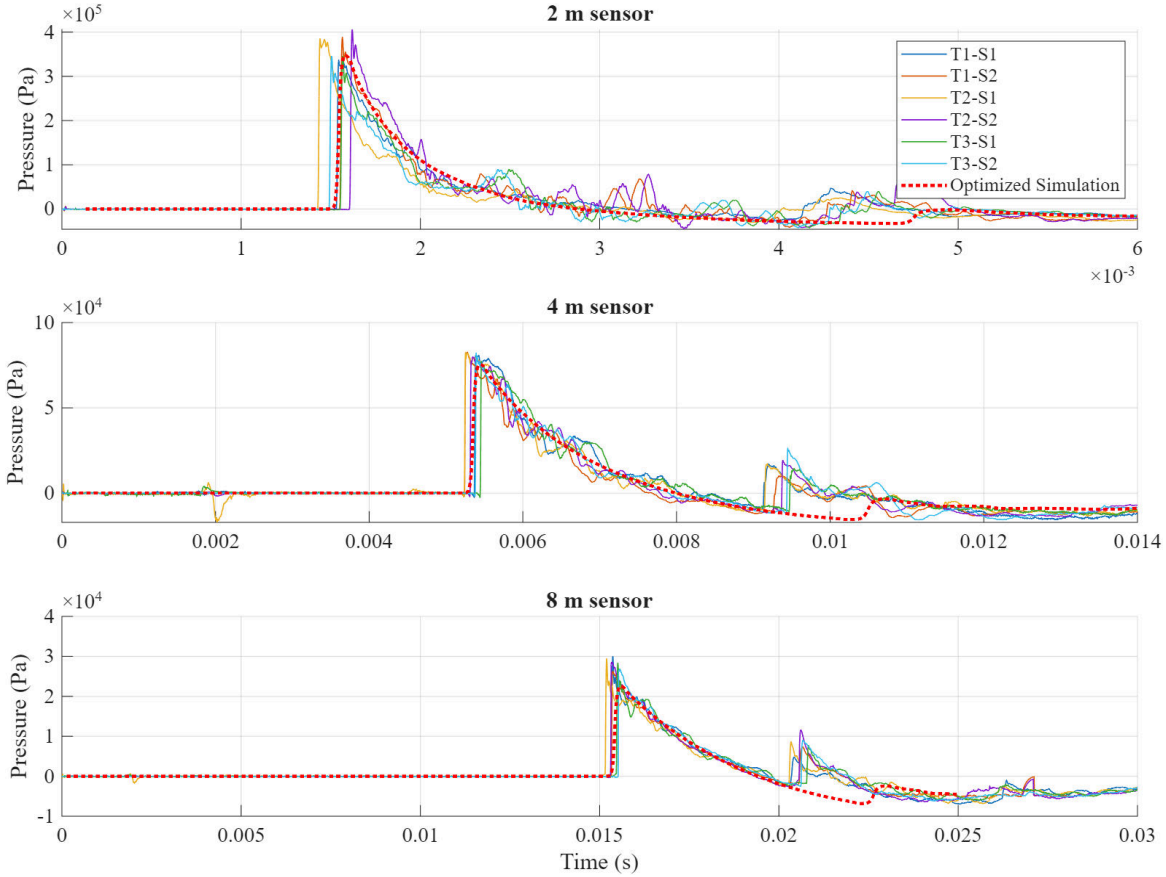

Figure 1: Comparison of pressure–time histories from Viper simulations and field test data for a 1 kg charge.

Figure 1 illustrates the computational domain with sensors and the comparison between simulated and experimental pressure–time histories. Overall, the results demonstrate that the optimized JWL-EOS provides a robust, predictive model, reliably capturing blast behaviour across different charge sizes and distances, proving its suitability for both LS-DYNA and Viper simulations.

6 Conclusions

A practical methodology for determining JWL EOS parameters directly from height-of-burst detonation tests has been presented and successfully applied to PG3 explosive. By combining 2D axisymmetric LS-DYNA simulations with LS-OPT optimization, the calibrated JWL parameters accurately reproduce both peak overpressures and positive-phase distribution across multiple charge sizes and sensor locations.

Validation with independent test data and additional CFD simulations demonstrated that the optimized JWL parameters generalize well, with typical errors below 7%, confirming the reliability of the approach. Compared to traditional cylinder tests, this method offers a safer, faster, and cost-effective alternative, while maintaining predictive accuracy suitable for both field-scale and computational blast analyses.

Limitations of the present study are that the methodology was applied exclusively to height-of-burst tests and was demonstrated successfully only to the PG3 explosive. Further work is required to evaluate the approach with other explosive formulations and different experimental configurations to fully assess its general applicability.

Acknowledgement

This research has been carried out under the Advance Kit of High ENergy Absorbing and lighT materials for side armor add-ONs to be used in military vehicles (No Main Battle Tanks) - AKHENATON project, funded by the Counter Improvised Explosive Devices Center of Excellence (C-IED CoE). Also, the authors acknowledge the institutional support RVO:61388998.

References

[1] BORNSTEIN, Huon; KUZNETSOV, Valerian; LU, Jing-Ping; STOJKO, Steven a FREUNDT, Jared. Characterisation and validation of the JWL equation of state parameters for PE4. Online. *International Journal of Impact Engineering*. 2022, vol. 164, s. 104190. ISSN 0734-743X. Available from: https://doi.org/10.1016/j.ijimpeng.2022.104190.

[2] LI, Xing-Long; CHEN, Ke-Quan; HUANG, Heng-Jian; YANG, Sha; SONG, Qing-Guan et al. Automatic Optimization of JWL-Miller parameters of HMX-based aluminized explosive based on genetic algorithm. Online. *Propellants, Explosives, Pyrotechnics*. 2024, vol. 49, no. 8. ISSN 0721-3115. Available from: https://doi.org/10.1002/prep.202300195.

[3] SHIN, Hyun-Seop; KIM, Sung-Wook; MOON, Jae-Heum a PARK, Gang-Kyu. Numerical Analysis of Blast Behavior for Non-ideal Explosive ANFO in Shock-Tube Test. Online. *International Journal of Concrete Structures and Materials*. 2024, vol. 18, no. 1. ISSN 2234-1315. Available from: https://doi.org/10.1186/s40069-024-00673-0.

[4] CHAOS, Marcos. Revisiting the Kinematics of the Cylinder Test. Online. *Propellants, Explosives, Pyrotechnics*. 2022, vol. 47, no. 6. ISSN 0721-3115. Available from: https://doi.org/10.1002/prep.202100349.

[5] SUTHERLAND, Gerrit T. Simulations of the cylinder expansion (CYLEX) test. Online. In: *AIP Conference Proceedings.* AIP Publishing, 2023, s. 290012. ISSN 0094-243X. Available from: https://doi.org/10.1063/12.0020380.

[6] CUI, Hao; SONG, Pu; GU, Xiao-Hui; ZHOU, Hao; XING, Bo-Yang et al. Determination of the JWL Parameters of Detonation Products Using Adaptive Genetic Algorithm. Online. *Propellants,*

Explosives, Pyrotechnics. 2020, vol. 45, no. 12, s. 1920-1930. ISSN 0721-3115. Available from: https://doi.org/10.1002/prep.202000148.

[7] LIU, Jie; XU, Can; HAN, Xu; JIANG, Chao a LIU, Guangzhao. Determination of the state parameters of explosive detonation products by computational inverse method. Online. *Inverse Problems in Science and Engineering*. 2015, vol. 24, no. 1, s. 22-41. ISSN 1741-5977. Available from: https://doi.org/10.1080/17415977.2014.993981.

[8] BAUST, Tobias M. Improving the Design and Evaluation of PDV-Based Cylinder Test Experiments for JWL-Parameter Determination. Online. *Propellants, Explosives, Pyrotechnics*. 2020, vol. 45, no. 9, s. 1344-1356. ISSN 0721-3115. Available from: https://doi.org/10.1002/prep.202000002.

[9] LI, Kebin; DONG, Xinlong; LI, Xiaojie; WANG, Yonggang a WANG, Wei. Determination of JWL parameters from underwater explosion test of spherical explosives by continuous velocity probe. Online. *Journal of Energetic Materials*. 2020, vol. 39, no. 4, s. 479-493. ISSN 0737-0652. Available from: https://doi.org/10.1080/07370652.2020.1822461.

APPLIED MECHANICS 2026
April 13 - 15, 2026, České Budějovice, Czech republic

EFFECT OF THE COOLING SYSTEM IN THE TILTING PAD JOURNAL BEARING ON THE ROTOR BEHAVIOUR

Jan Rendl[1], Michal Hajžman[2], Radek Bulín[3], Luboš Smolík[4]

Abstract: The paper presents a study to explore the thermohydrodynamic behaviour of a tilting pad journal bearing equipped with an internal cooling system under various operating conditions and loads. This study aims to monitor temperatures at critical locations and establish their relationship with operational parameters using a coupled CFD approach.

Keywords: tilting pad journal bearing; cooling system; thermohydrodynamic analysis; rotor system

1 Introduction

The tilting pad journal bearing (TPJB) with four pads in the load-between-pads configuration is considered. The pads contain the cooling system through inner channels supplied by a fraction of the inlet lubricant. Commercial bearing analysis software typically lacks the functionality to model such internal features. For this reason, the in-house solution used CFD analysis coupled with the energy equation of heat distribution in the bearing gap and subsequent heat transfer to the pad with a sliding surface made of babbitt material.

2 Computational model

The flow of the oil film is governed by the Navier-Stokes equations under incompressible, laminar conditions [1,2]. To obtain the temperature gradient across the film thickness, a 3D energy equation accounting for both conduction and convection is employed. This approach allows for a precise characterisation of the thermal interface between the lubricant and the pad surface. Various thermal boundary conditions and their influence on the resulting temperature fields in the system were studied in [3].

3 Results

Comparative simulations were performed for specific operating cases using identical boundary conditions (film thickness, rotational speed and heat transfer coefficients). The results obtained for the uncooled and cooled systems are depicted in Figures 1 and 2, respectively. These figures illustrate the radial section of the pad near the trailing edge, where the thermocouple is positioned to measure the babbitt layer bottom surface temperature.

[1] Ing. Jan Rendl, Ph.D.; Faculty of Applied Sciences, University of West Bohemia in Pilsen; Technická 8, 301 00 Pilsen, Czech Republic, rendlj@fav.zcu.cz
[2] doc. Ing. Michal Hajžman, Ph.D.; Faculty of Applied Sciences, University of West Bohemia in Pilsen; Technická 8, 301 00 Pilsen, Czech Republic, mhajzman@fav.zcu.cz
[3] Ing. Radek Bulín, Ph.D.; Faculty of Applied Sciences, University of West Bohemia in Pilsen; Technická 8, 301 00 Pilsen, Czech Republic, rbulin@fav.zcu.cz
[4] Ing. Luboš Smolík, Ph.D.; Faculty of Applied Sciences, University of West Bohemia in Pilsen; Technická 8, 301 00 Pilsen, Czech Republic, carlist@fav.zcu.cz

The cooling effect reduces the temperature at the babbitt layer surface by ca. 5 °C across various operating conditions. On the other hand, the temperature distribution under the cooling channels layer is nearly uniform and significantly lower than in the non-cooled configuration.

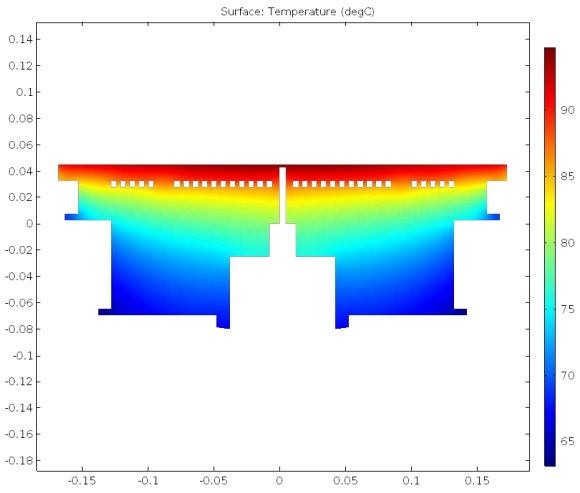

Figure 1: Temperature distribution in pad without cooling system (pad radial section)

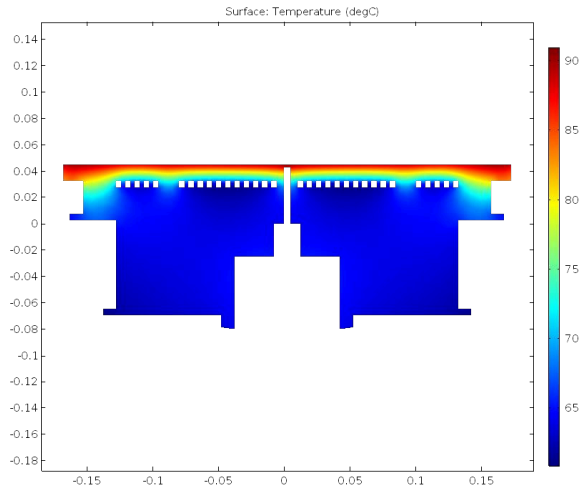

Figure 2: Temperature distribution in pad with cooling system (pad radial section)

4 Conclusions

This contribution provides a comprehensive computational analysis of the rotor supported on a tilting pad journal bearing with a cooling system and its effects on operation. Temperature distribution influences material dilatation, operational clearances, and oil viscosity, potentially critically affecting the dynamic stability of the rotor system by altering hydrodynamic forces. The simulations indicate that while the cooling system has a secondary effect on direct heat generation within the bearing gap, it significantly alters the temperature distribution within the pad body.

Acknowledgement

This research was supported by the Czech Science Foundation project 26-21353S entitled *Vibration attenuation and stability enhancement of rotors with active high-static-low-dynamic stiffness supports*. Chosen validation simulations were performed in the AVL Excite software which is available in the framework of the University Partnership Program of AVL List GmbH, and whose usage is greatly acknowledged.

References

[1] STACHOWIAK, G. W. and BATCHELOR, A. W. *Engineering Tribology*. Boston: Butterworth-Heinemann, 2014. ISBN 978-0-12-397047-3.

[2] WEN, S. and HUANG, P., A. W. *Principles of Tribology*. Boston: Wiley, 2012. ISBN 978-111-9214915.

[3] ZHANG, Z. S.; YANG, Y. M.; DAI, X. D. and XIE Y. B. Effects of Thermal Boundary Conditions on Plain Journal Bearing Thermohydrodynamic Lubrication. Tribology Transactions.2013, Vol. 56(5), pp. 759–770. Available from: https://doi.org/10.1080/10402004.2013.797531.

APPLIED MECHANICS 2026
April 13 - 15, 2026, České Budějovice, Czech republic

MASK-BASED OBJECT TRACKING FOR NON-CONTACT MEASUREMENT OF PLANAR MOTION

Luboš Smolík[1], Štěpán Dyk[2], Radek Bulín[3], Jan Rendl[4]

Abstract: Non-contact measurement of mechanical vibrations is essential for lightly damped or low-mass systems, since contact sensors can introduce additional mass or artificial damping. In some scenarios, computer vision utilising digital cameras can offer a versatile and cost-effective alternative to laser interferometers. However, common object- and feature-tracking algorithms can be susceptible to drift, which is a gradual accumulation of frame to frame errors. This paper presents a mask-based object tracking method that processes digital video using a localised search strategy and a reference-based cost function. The method is experimentally validated on two oscillating systems using a smartphone camera.

Keywords: computer vision; motion measurement; object tracking; damping identification

1 Introduction

Measuring the dynamic response of lightly damped or low-mass mechanical systems can be rather challenging. Contact transducers, such as accelerometers, introduce additional mass or artificial stiffness and damping due to the presence of cables. These effects can have a negative impact on measurements, resulting in inaccurate estimates of system properties.

To avoid this issue, one can use a non-contact measurement method. Non-optical approaches, such as capacitive and eddy-current sensors, offer high sensitivity but have a limited displacement range. Optical methods include laser interferometers and computer vision. Whereas the former are accurate and appropriate for a wide range of measurement scenarios [1], they are often cost-prohibitive even for single-point unidirectional measurements. Computer vision has recently become a versatile alternative for low- and medium-frequency applications that supports simultaneous multi-point, multi-degree-of-freedom measurements across a wide range of motion through digital video analysis [2].

Despite its versatility, computer vision is not without limitations. Large motions are measured using object- or feature-tracking algorithms, which are susceptible to frame-to-frame error accumulation [3]. This effect, known as drift, can be particularly problematic when analysing long video records consisting of thousands of frames.

The present paper addresses these limitations by introducing a drift-free method designed for long video records. The method employs localised mask-based tracking that remains stable over sequences exceeding 30,000 frames, with drift maintained at the level of measurement noise. To demonstrate its applicability, the method is used to identify damping parameters from free-vibration records of a lightly damped mechanical system.

[1] Ing. Luboš Smolík, Ph.D.; University of West Bohemia, Faculty of Applied Sciences, New Technologies for Information Society; Technická 8, 301 00 Plzeň, Czech Republic, carlist@fav.zcu.cz
[2] Ing. Štěpán Dyk, Ph.D.; University of West Bohemia, Faculty of Applied Sciences, Department of Mechanics; Technická 8, 301 00 Plzeň, Czech Republic
[3] Ing. Radek Bulín, Ph.D.; University of West Bohemia, Faculty of Applied Sciences, Department of Mechanics; Technická 8, 301 00 Plzeň, Czech Republic
[4] Ing. Jan Rendl, Ph.D.; University of West Bohemia; Faculty of Applied Sciences; New Technologies for Information Society; Technická 8, 301 00 Plzeň, Czech Republic

2 Description of the Method

The proposed method processes a digital video frame by frame using the workflow illustrated in Figure 1. In the initialisation step, the user defines a region of interest (RoI) around the tracked object in a reference frame. Selected colour channels from the RGB and HSV colour spaces are combined via element-wise multiplication to produce a composite greyscale image. The channel combination that best separates the object from the background should be selected. The composite image is then binarised using a fixed intensity threshold. The resulting binary mask is further processed by filling holes and performing morphological closing to ensure a well-defined silhouette of the tracked object. A set of geometric properties, including area, centroid position and eccentricity, is extracted from the reference mask and stored as the reference descriptor.

In each subsequent frame, image processing is restricted to a localised search area computed from the previous centroid position and the expected maximum displacement. The binary mask is recomputed within this crop. This may result in multiple disconnected regions. To identify the region corresponding to the tracked object among all candidates, a cost function is evaluated for each detected region. This cost is defined as the root sum of squares of the relative errors between the geometric properties of the candidate and the reference descriptor, as well as a distance cost based on the pixel distance of the candidate from the centroid recorded in the previous frame. The candidate with the lowest cost is selected, and its centroid is recorded in global image coordinates.

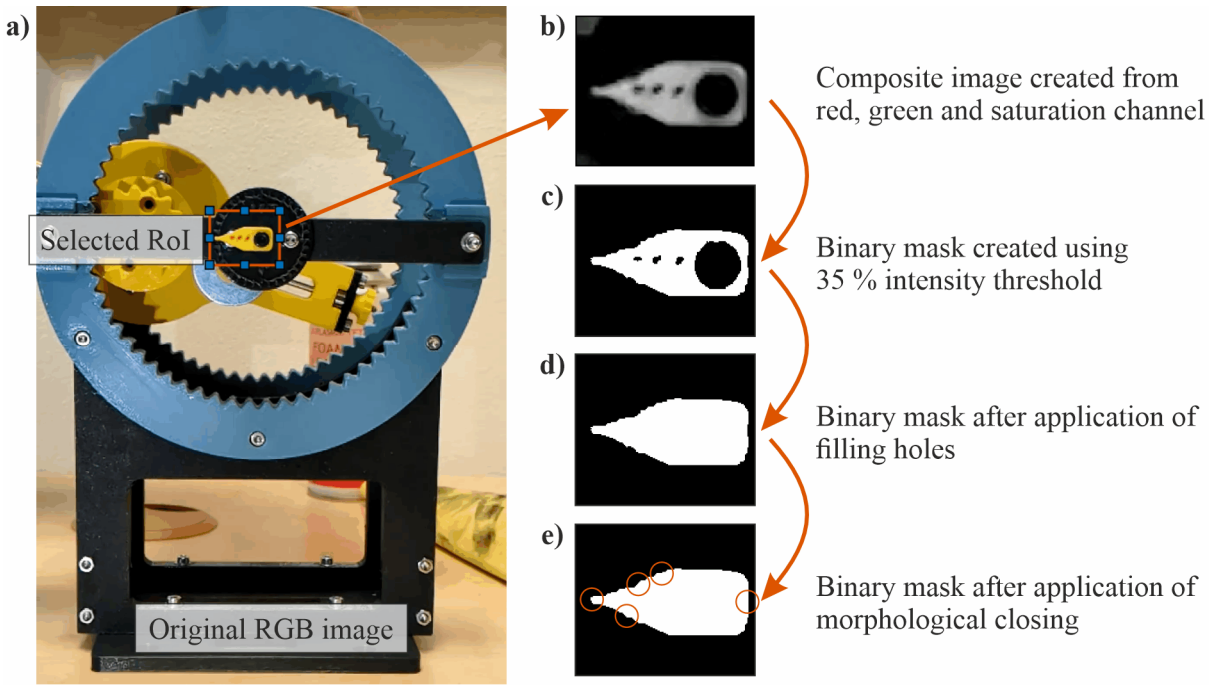

Figure 1: Illustration of the image processing workflow applied to a representative frame: RoI definition (a), composite greyscale image (b), and binary mask after sequential postprocessing steps (c to e).

3 Results

The presented method was experimentally validated by analysing the free decay response of two oscillating systems subjected to a non-zero initial displacement recorded using a Google Pixel 8a smartphone camera at 240 fps.

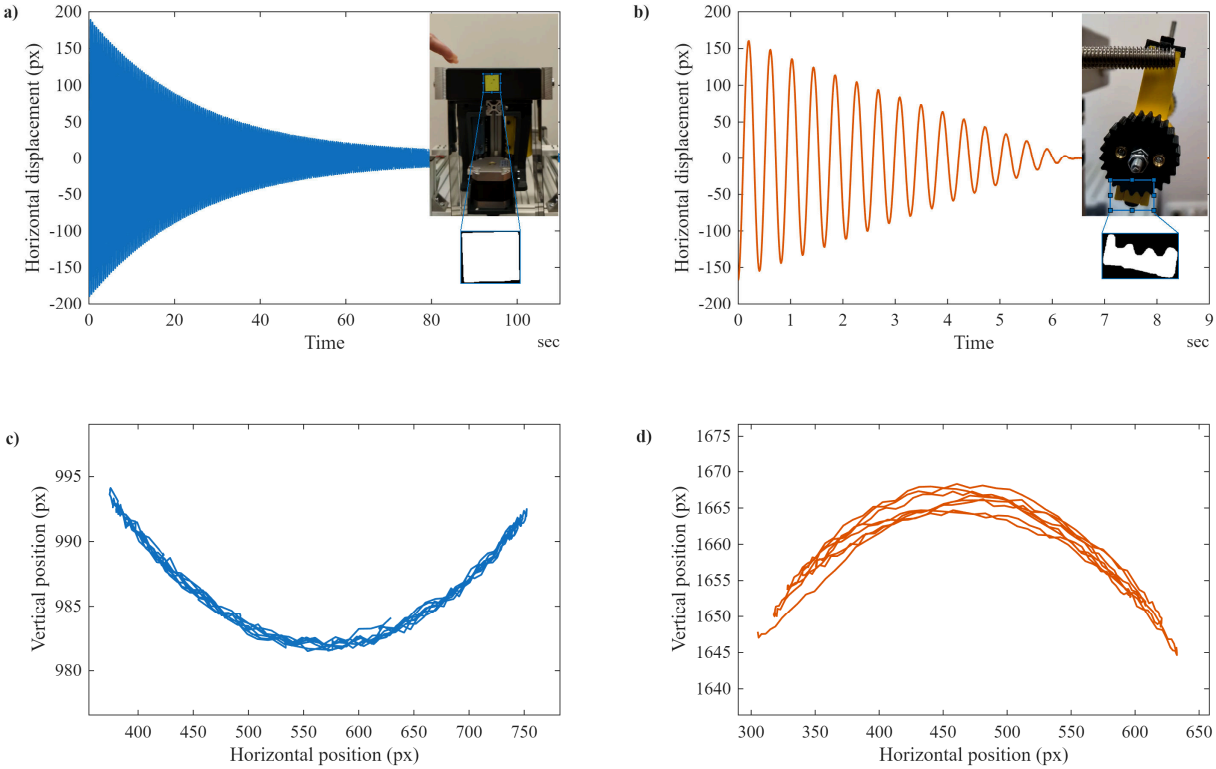

Figure 2: Test oscillating systems with corresponding horizontal displacement time histories (a, b) and planar trajectories over the first four oscillation cycles (c, d). Note that vertical position in panel (d) is inverted because the origin of the image coordinate system is located in the upper-left corner with the vertical axis pointing downward.

The first test system consists of a mass mounted on steel plates that oscillates predominantly in the horizontal direction, see Figure 2a. The composite image of the RoI was constructed from the R, G, and S channels with a binarization threshold of 32 and the analysed digital video consists of 26 388 frames.

The measured time history of the horizontal displacement is shown in Figure 2a. The amplitudes decay almost exponentially, suggesting that the primary mechanism of energy dissipation is viscous damping in the plates. An oscillation period of approximately 0.46 s can be estimated from the time history. The planar trajectory of the mass over the first four cycles is shown in Figure 2c. Apparently, the motion is almost linear: the peak-to-peak displacement in the horizontal direction is almost 400 pixels, whereas in the vertical direction it is approximately 13 pixels.

The second test system is a physical pendulum supported in two point pivots, see Figure 2b. The composite image of the RoI was constructed from the R and S channels with a binarization threshold of 20 and the analysed digital video consists of 2 188 frames.

The measured time history of the horizontal displacement is shown in Figure 2b. Here, the amplitudes decay almost linearly, suggesting that the dominant dissipation mechanism is dry friction at the pivots. An oscillation period is approximately 0.41 s. The planar trajectory of the lower edge of the pendulum over the first four cycles is shown in Figure 2d. In this case, the trajectory is a circular arc, which is characteristic for pendulum motion.

4 Conclusions

We presented a mask-based object tracking method for the non-contact measurement of planar motion. This method processes digital video records frame by frame using a localised search strategy and a reference-based cost function to minimise drift, even over long video

recordings. This approach was experimentally validated on two oscillating systems with different dissipation mechanisms, recorded at 240 fps using a smartphone camera. The results demonstrate that the method can reliably analyse planar trajectories across records of varying length, including a sequence of 26,388 frames. The residual tracking uncertainty is predominantly random in nature, with a standard deviation of approximately 0.4–0.6 pixels.

In future work, free decay records will be used to identify the damping parameters of analysed systems. The identification procedure proposed in [4], which enables the separation of viscous and dry friction contributions to energy dissipation, will be employed.

Acknowledgement

This work was supported by the Czech Science Foundation project GA25-17552S entitled *"Investigating Internal Resonances in Nonlinear Mechanical Systems with Multiple Autoparametric Couplings"*.

References

[1] LUTZMANN, Peter; GÖHLER, Benjamin; HILL, Chris A. and van PUTTEN, Frank. Laser vibration sensing at Fraunhofer IOSB: review and applications. *Optical Engineering*. 2016, vol. 56, no. 3, pp. 031215. Available from: https://doi.org/10.1117/1.OE.56.3.031215

[2] CHENG, Yuansheng; TIAN, Zhe; NING, Donghong et al. Computer vision-based non-contact structural vibration measurement: Methods, challenges and opportunities. *Measurement*. 2025, vol. 243, pp. 116426. Available from: https://doi.org/10.1016/j.measurement.2024.116426

[3] ZINSSER, Timo; GRÄSSL, Christoph and NIEMANN, Heinrich. Efficient feature tracking for long video sequences. In: *Lecture Notes in Computer Science*. Berlin: Springer, 2004, pp. 326-333. ISBN 9783540229452. Available from: https://doi.org/10.1007/978-3-540-28649-3_40

[4] KAWULOK, Marek and POSPÍŠIL, Stanislav. Analysis of damping of a ball absorber from experimentally obtained data. *Procedia Structural Integrity*. 2025, vol. 73, pp. 51-57. Available from: https://doi.org/10.1016/j.prostr.2025.10.009

APPLIED MECHANICS 2026
April 13 - 15, 2026, České Budějovice, Czech republic

Concept of high-static-low-dynamic-stiffness vibration isolation combined with sky-hook idea

Z. Šika[1], P. Pravec[2], K. Kraus[3]

Abstract: The paper investigates the concept of active and semi-active high-static-low-dynamic stiffness (HSLDS) vibration isolators. Two distinct mechanical designs are considered and their combination with both semi-active and active realization of sky-hook idea are considered and tested by simulation. The optimization of the passive parameters as well as control law parameters is done. The preliminary results indicate that the optimized passive designs combined with sky-hook could provide a highly efficient solution. The presented study is a good basis for further research into the active and semi-active HSLDS concept.

Keywords: vibration isolation; high-static-low-dynamic stiffness (HSLDS); quasi-zero stiffness (QZS); active control; semi-active control; sky-hook concept

1 Introduction

The increasing demand for high-performance systems in fields such as ultraprecision manufacturing, sensitive laboratory instrumentation, and aerospace engineering rotors has made the mitigation of low-frequency vibrations a critical challenge. Classical passive vibration isolators are fundamentally limited by the trade-off between static load-bearing capacity and the low dynamic stiffness required for effective low-frequency isolation. A promising alternative is found in nonlinear passive isolators with high-static-low-dynamic-stiffness (HSLDS) systems [1]. If we want to achieve further improvement in the functionality and robustness of these support mechanisms with respect to the behavior of the isolated structure as well as the surrounding environment, it is appropriate to consider expanding them with controlled elements.

2 HSLDS support combimned with sky-hook

This study explores the potential of enhancing the passive HSLDS isolators of two DOF table with auxiliary mass (Fig. 1) through mechatronic extensions, where the performance of optimized passive systems is first established as a reference and then compared against both semi-active and fully active mechatronic enhancements to quantify the benefits of each strategy [2]. The simulation models of two selected variants of passive HSLDS isolators—a mechanical linkage configuration and a pre-buckled beam (Fig. 2) configuration—are designed and created.

These passive models are then subjected to a numerical optimization of their geometric and mechanical parameters to maximize their vibration isolation effectiveness and establish a clear performance benchmark. Subsequently, a mechatronic extension is proposed for the optimized passive designs based on the 'sky-hook' control principle [3], realizing implementation with both semi-active and fully active actuators. The final stage of the research involve a structural-control co-optimization using differential evolution method [4] of the semi-active and active versions. In addition, during this optimization, several types of excitation of the isolated table were considered at the same time, and the overall objective function was formed by a weighted sum of the partial objective functions. An example of the comparison of the optimized isolation results for stochastic excitation is shown in Fig. 3. The study suggests significant potential for both active and semi-active versions of HSLDS vibration isolation.

[1] Zbyněk Šika; CTU in Prague, Faculty of Mechanical Engineering; Zbynek.Sika@fs.cvut.cz
[2] Pavel Pravec; CTU in Prague, Faculty of Mechanical Engineering; Pavel.Pravec@fs.cvut.cz
[3] Karel Kraus; CTU in Prague, Faculty of Mechanical Engineering; Karel.Kraus@fs.cvut.cz

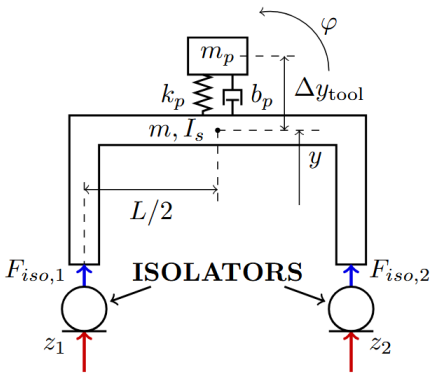

Figure 1: Schematic diagram of the isolated two DOF table with auxiliary mass.

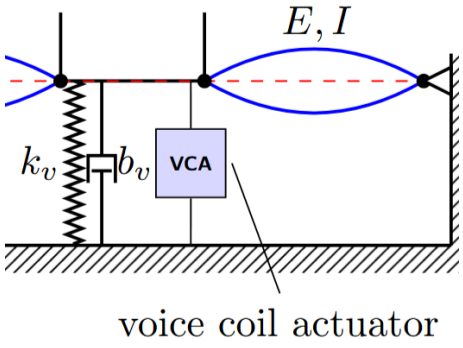

Figure 2: Schematic diagram of the controlled actuator integration with the HSLDS isolator.

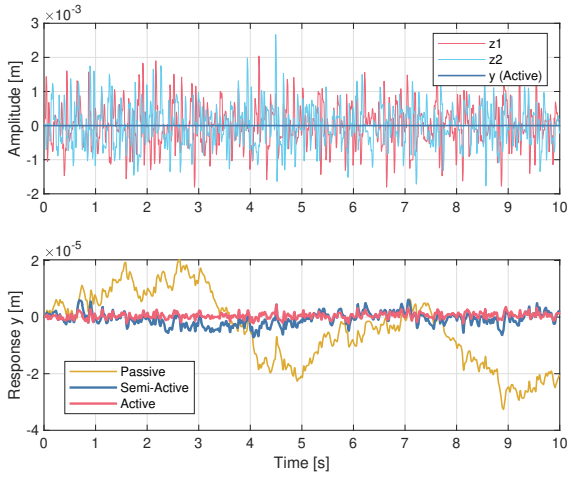

Figure 3: Comparison of the translational response (y) for Passive, Semi-Active and Active HSLDS isolation under stochastic excitation.

Acknowledgement

The work has been supported by the Czech Science Foundation project 26-21353S "Vibration attenuation and stability enhancement of rotors with active high-static-low-dynamic stiffness supports".

References

[1] HUANG, Xiuchang *et al.*, Journal of Sound and Vibration. *Vibration isolation characteristics of a nonlinear isolator using Euler buckled beam as negative stiffness corrector: A theoretical and experimental study*. 2014, Volume 333, Issue 4, pp. 1132-1148. https://doi.org/10.1016/j.jsv.2013.10.026.

[2] PRAVEC Pavel, *Vibration isolation using active mounting with high static and low dynamic stiffness*. Master Thesis, Prague, Czech Technical University in Prague, 2025.

[3] PREUMONT, André. *Vibration Control of Active Structures: An Introduction*. 3rd Ed. Berlin: Springer, 2011. ISBN 978-94-007-2032-9.

[4] STORN, Rainer Martin, PRICE Keneth, Journal of Global Optimization, *Differential evolution – a simple and efficient heuristic for global optimization over continuous spaces*. 1997, Volume 11, Issue 4, pp. 341–359. https://doi.org/10.1023/A:1008202821328

APPLIED MECHANICS 2026
April 13 - 15, 2026, České Budějovice, Czech republic

Application of a Simplified Jiang Fatigue Model to SS316L

A. Tošková[1], M. Fusek[2]

Abstract: Energy-based fatigue damage cumulation models represent an effective tool for predicting fatigue life. However, their practical application is limited by the high number of material parameters. The Jiang model contains a total of six material constants. Some of them can be determined independently, but under constant-amplitude loading, three key parameters must be calibrated according to the procedure described in the original work, which complicates its engineering use. The paper focuses on the calibration and application of the simplified model to SS316L in order to compare its predictive capabilities with those of the original model.

Keywords: Fatigue; SS316L; Jiang Criterion; Modification; Multiaxial fatigue

1 Introduction

Multiaxial fatigue loading is common in many engineering components where loads act simultaneously along multiple axes. To evaluate fatigue life under these conditions, a number of criteria have been proposed based on the critical plane concept or on an energy-based approach. Energy-based fatigue damage cumulation models represent an effective tool for predicting fatigue life because they allow for the influence of plastic deformation and the complex stress-strain state of the material to be taken into account. However, their practical application is often limited by a relatively large number of material parameters that must be determined experimentally.

One model of this type is the Jiang criterion [1], which combines the critical plane concept, plastic strain energy, and a material memory principle adopted from cyclic plasticity modelling. The criterion was originally validated on several materials, namely carbon steels AISI 1070 and AISI 1045, stainless steel AISI 304, and alloy steel EN15R. Experimental validation was performed on smooth specimens at room temperature under various loading conditions, including both proportional and non-proportional multiaxial loading with constant amplitude. The criterion was subsequently applied to other materials as well, for example, structural steel S460N [2], stainless steel AL6XN [3], steel 16MnR [4], stainless steel AISI 316L [5], and magnesium alloys AZ31B and AZ61A [6, 7, 8].

In addition to direct applications of the model, several modifications have also been proposed. In [9], two modifications of the Jiang criterion were introduced with the aim of improving fatigue life prediction for the aluminium alloy 2124-T851 and the stainless steel AISI 316L.

Due to the complex calibration of this multi-parameter fatigue model, a simplified material model was proposed in [10], in which one of the material parameters is fixed to a constant value, specifically $m = 1$. This approach was experimentally validated for the structural steel S235JR. The objective of the present work is to apply this simplified model to the SS316L material and compare its predictive capability with the original Jiang model.

2 Fatigue Models

This chapter summarises the formulation of the original Jiang fatigue model [1] and its simplified variant proposed in [10]. First, the basic form of the criterion is presented, followed by its modification.

[1] Anna Tošková; VŠB-TUO, Fakulta strojní, Katedra aplikované mechaniky; anna.toskova@vsb.cz
[2] Martin Fusek; VŠB-TUO, Fakulta strojní, Katedra aplikované mechaniky; martin.fusek@vsb.cz

2.1 Original Jiang model

The Jiang criterion [1] is a comprehensive fatigue model. The critical plane is defined as the plane on which the density of accumulated fatigue damage reaches a critical value. The mathematical formulation of the model is given by:

$$dD = \langle \sigma_{mr} - \sigma_0 \rangle^m \left(1 + \frac{\sigma}{\sigma_f}\right) dY, \tag{1}$$

where the increment of the modified plastic strain energy density dY is defined as:

$$dY = a\sigma d\varepsilon_p + \frac{1-a}{2}\tau d\gamma_p, \tag{2}$$

where D denotes the fatigue damage density, σ_{mr} is the memory parameter, and σ is the normal stress on the material plane. Equations 1 and 2 contain four material parameters: σ_0 represents the fatigue limit under fully reversed tension-compression, σ_f is the fracture stress, m acts as an exponent, and a specifies the material behaviour during fatigue damage cumulation [1].

The memory stress is defined as the maximum value of the equivalent stress reached during one loading cycle:

$$\sigma_{mr} = \max\left(\sigma_{eq}\right). \tag{3}$$

The quantity σ_{eq} represents the von Mises equivalent stress, which is defined by:

$$\sigma_{eq} = \sqrt{\frac{3}{2}\mathbf{S} : \mathbf{S}} = \sqrt{\sigma_x^2 + \sigma_y^2 + \sigma_z^2 + 3\left(\tau_{xy}^2 + \tau_{yz}^2 + \tau_{zx}^2\right)}, \tag{4}$$

where $\mathbf{S}$ denotes the deviatoric stress tensor, σ_x, σ_y, and σ_z are the normal stress components, and τ_{xy}, τ_{yz}, and τ_{zx} represent the shear stress components at the given material point [1].

2.2 Simplified Jiang Model

The simplified model [10] is based on the original fatigue model and eliminates the dimensionless constant m from the criterion, i.e., its value is fixed at 1. Equation 1 therefore takes the form:

$$dD = \langle \sigma_{mr} - \sigma_0 \rangle \left(1 + \frac{\sigma}{\sigma_f}\right) dY. \tag{5}$$

This expression for fatigue damage remains physically equivalent to the original Jiang criterion [10].

3 Material and experimental data

The experimental data for SS316L used in this study were taken from the published results reported in [9]. The dataset includes measured stress-strain histories for six different loading paths (Figure 1), information on the number of cycles to failure for various multiaxial loading modes, and several material parameters (Table 1). For the purposes of this study, the datasets were divided into two independent parts. Loading paths A and B were used for model calibration, while the remaining loading paths (C, D, E, and G) were used for model validation.

Parameter	*Description*	*Value*
E [MPa]	Young's modulus	169785
G [MPa]	Shear modulus	55600
μ [-]	Poisson's ratio	0.29
σ_0 [MPa]	Fatigue limit in fully reversed tension–compression	244
σ_f [MPa]	Fracture stress	680

Table 1: Material parameters for SS316L.

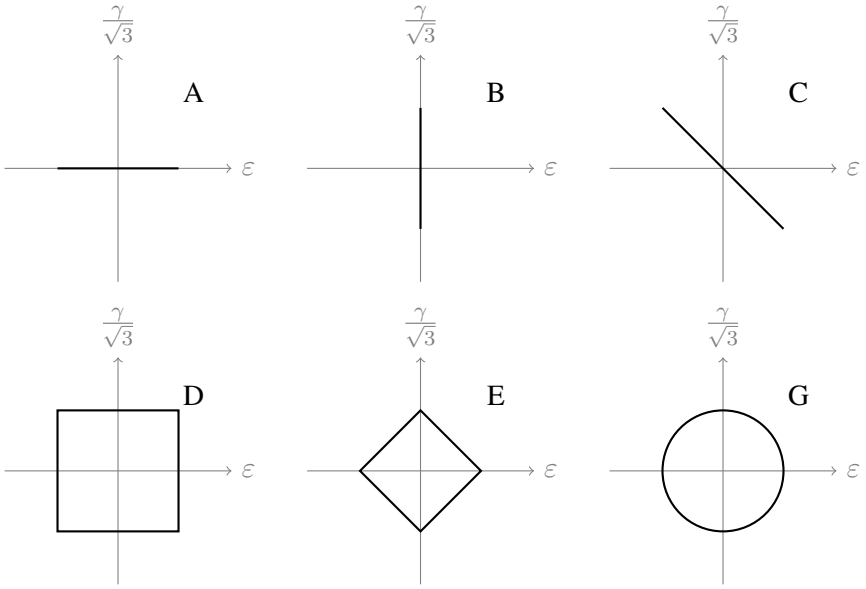

Figure 1: Loading paths.

4 Results

This chapter first defines the metrics used to evaluate the predictive capability of the considered models. Subsequently, the calibrated parameters of the original Jiang criterion and its simplified variant are presented. Based on these parameters, the results of fatigue life prediction are presented and evaluated using the selected metrics. Finally, the predictive capabilities of both models are compared.

4.1 Metrics

The predictive capability of both models is evaluated using the metric:

$$k_i = \frac{N_{fe,i}}{N_{fp,i}}, \tag{6}$$

where N_{fp} denotes the predicted number of cycles to failure and N_{fe} the experimentally determined number of cycles. A value of $k = 1$ corresponds to perfect agreement between the predicted and experimental fatigue life. Values of $k > 1$ indicate a conservative prediction, whereas $k < 1$ represents a non-conservative estimate of fatigue life. An interval of $\langle 0.5,\, 2\rangle$ is considered an acceptable level of model accuracy.

From the set of values $\{k_i\}$, two statistical characteristics are further determined: the mean value:

$$\bar{k} = \frac{1}{n}\sum_{i=1}^{n} k_i, \tag{7}$$

where i denotes the test index, n the number of evaluated experiments, and the standard deviation:

$$s = \sqrt{\frac{1}{n-1}\sum_{i=1}^{n}\left(k_i - \bar{k}\right)^2}. \tag{8}$$

To assess the differences between the two models, a paired t-test [12] and the Wilcoxon test [11] are used.

4.2 Results of the Original Jiang Criterion

The calibration of the original Jiang model was performed according to [10]. The determined parameter values for SS316L are listed in Table 2 (Figure 2). A comparison of experimental and predicted fatigue lives using the metric k is shown in Figure 4.

The results indicate that most predictions fall within the region of good agreement between experimental and calculated values. The mean value of the metric reaches $\bar{k}_{\text{orig}} = 1.134$, while the standard deviation is $s_{\text{orig}} = 0.268$.

4.3 Results of the Simplified Jiang Criterion

The calibration of the simplified variant of the Jiang model was performed using an analogous procedure. The resulting parameter values are listed in Table 3 (Figure 3). The predictive capability of the model evaluated using the metric k is shown in Figure 5.

In this case as well, most results lie within the range of acceptable agreement with the experimental data. The mean value of the metric reaches $\bar{k}_{\text{mod}} = 1.099$, while the standard deviation is $s_{\text{mod}} = 0.264$.

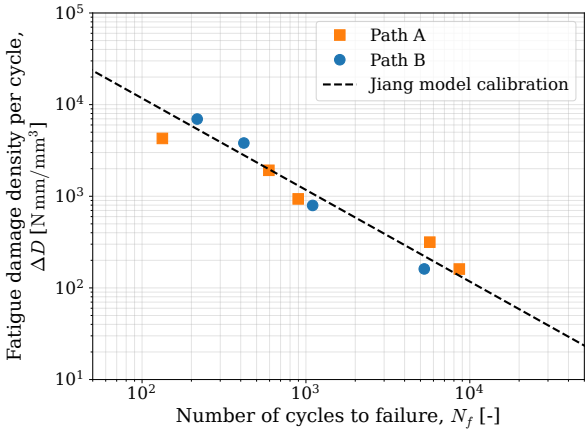

Figure 2: Calibration of the Jiang model

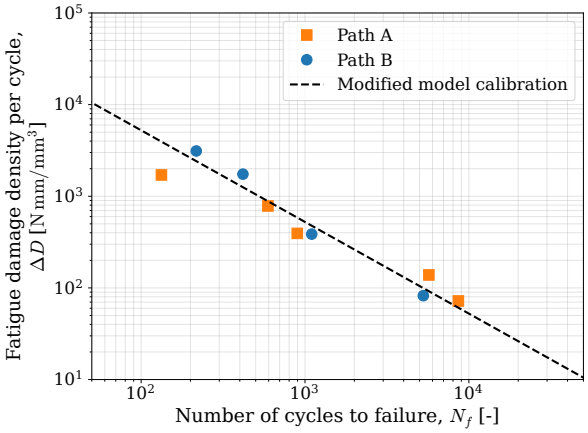

Figure 3: Calibration of the modified model

Parameter	*Value*
E [MPa]	169785
G [MPa]	55600
μ [-]	0.29
a [-]	0.4055
m [-]	1.1486
D_0 [N mm/mm^3]	$1.1733 \cdot 10^6$
σ_0 [MPa]	244
σ_f [MPa]	680

Table 2: Parameters of the Jiang criterion for SS316L

Parameter	*Value*
E [MPa]	169785
G [MPa]	55600
μ [-]	0.29
a [-]	0.3688
D_0 [N mm/mm^3]	$5.2448 \cdot 10^5$
σ_0 [MPa]	244
σ_f [MPa]	680

Table 3: Parameters of the modified criterion for SS316L

4.4 Comparison of Predictions of the Original and Simplified Criteria

The difference between the mean values of the metric k for both models is $\Delta\bar{k} = -0.035$. The statistical significance of this difference was evaluated by testing the null hypothesis $H_0 : \bar{k}_{\text{orig}} = \bar{k}_{\text{mod}}$ at a significance level of $\alpha = 0.05$. The results of both the paired t-test ($t = -1.473, p = 0.167$) and the Wilcoxon test ($W = 26.0, p = 0.191$) did not indicate a statistically significant difference between

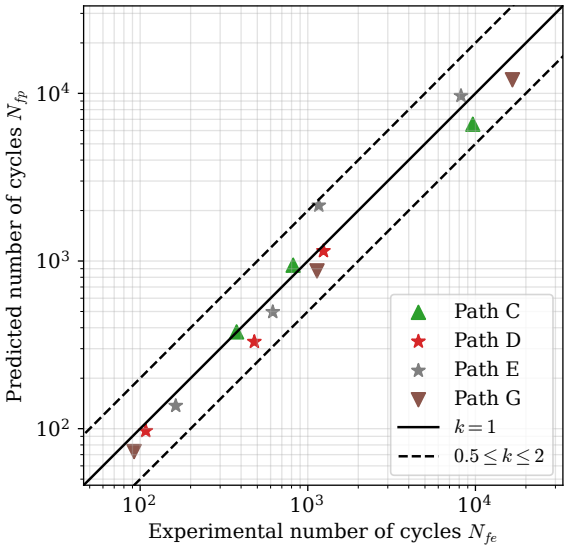

Figure 4: Metric k of the Jiang model

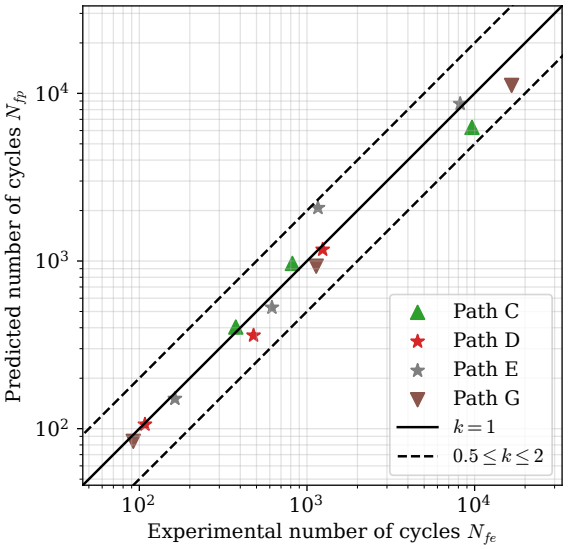

Figure 5: Metric k of the modified model

the two models ($p > \alpha$). A graphical comparison of the distribution of the metric k for both models is shown in Figure 6.

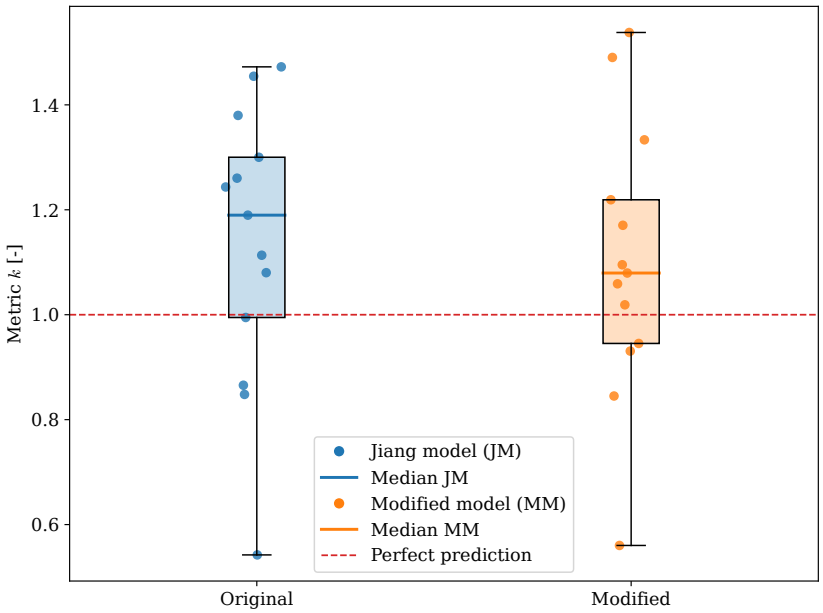

Figure 6: Distribution of metric k for the Jiang and modified model

5 Conclusion

This work focused on the application and validation of a simplified Jiang fatigue model for fatigue life prediction under multiaxial loading. The simplified formulation, in which the material parameter m is fixed at $m = 1$, was applied to experimental data for SS316L, and its predictive capability was compared with that of the original Jiang model.

Calibration of the original Jiang model resulted in a mean prediction metric value of $\bar{k}_{\text{orig}} = 1.134$ with a standard deviation of $s_{\text{orig}} = 0.268$. The simplified formulation provided very similar results,

specifically $\bar{k}_{\mathrm{mod}} = 1.099$ and $s_{\mathrm{mod}} = 0.264$. In both cases, all predicted fatigue lives fall within the interval $\langle 0.5,\ 2 \rangle$, which confirms good agreement between experimental and predicted values.

The comparison of both approaches showed that the simplified model achieves slightly better predictive results, reflected by the value of the metric k being closer to 1. However, statistical analysis based on the paired t-test and the Wilcoxon test did not reveal a statistically significant difference between the two models at the significance level $\alpha = 0.05$.

The obtained results confirm that the simplified Jiang model can be successfully applied to SS316L while maintaining predictive accuracy comparable to the original formulation. At the same time, the calibration of the simplified model is considerably easier since only two of the original three material parameters need to be determined. This makes the simplified model more suitable for practical engineering applications while maintaining very good predictive capability.

Acknowledgement

This research work was supported by the Specific Research "Advanced Numerical and Experimental Approaches in Mechanics and Biomechanics" (SP2026/027).

References

[1] JIANG, Yanyao. A fatigue criterion for general multiaxial loading. *Fatigue & Fracture of Engineering Materials & Structures*. 2000, vol. 23, no. 1, pp. 19–32.

[2] JIANG, Yanyao; HERTEL, Olaf; VORMWALD, Michael. An experimental evaluation of three critical plane multiaxial fatigue criteria. *International Journal of Fatigue*. 2007, vol. 29, no. 8, pp. 1490–1502. Available from: https://doi.org/10.1016/j.ijfatigue.2006.10.028.

[3] KALNAUS, Sergiy; JIANG, Yanyao. Fatigue of AL6XN stainless steel. *Journal of Engineering Materials and Technology*. 2008, vol. 130, no. 3, pp. 031404. Available from: https://doi.org/10.1115/1.2931154.

[4] GAO, Zengliang; ZHAO, Tianwen; WANG, Xiaogui; JIANG, Yanyao. Multiaxial fatigue of 16MnR steel. *Journal of Pressure Vessel Technology*. 2009, vol. 131, no. 4, pp. 041404. Available from: https://doi.org/10.1115/1.3008041.

[5] FACHERIS, G.; JANSSENS, K. G. F.; FOLETTI, S. Multiaxial fatigue behavior of AISI 316L subjected to strain-controlled and ratcheting paths. *International Journal of Fatigue*. 2014, vol. 68, pp. 195–208. Available from: https://doi.org/10.1016/j.ijfatigue.2014.05.003.

[6] XIONG, Ying; YU, Qin; JIANG, Yanyao. Multiaxial fatigue of extruded AZ31B magnesium alloy. *Materials Science and Engineering: A*. 2012, vol. 546, pp. 119–128. Available from: https://doi.org/10.1016/j.msea.2012.03.039.

[7] CASTRO, Fábio; JIANG, Yanyao. Fatigue life and early cracking predictions of extruded AZ31B magnesium alloy using critical plane approaches. *International Journal of Fatigue*. 2016, vol. 88, pp. 236–246. Available from: https://doi.org/10.1016/j.ijfatigue.2016.04.002.

[8] YU, Qin; ZHANG, Jixi; JIANG, Yanyao; LI, Qizhen. Multiaxial fatigue of extruded AZ61A magnesium alloy. *International Journal of Fatigue*. 2011, vol. 33, no. 3, pp. 437–447. Available from: https://doi.org/10.1016/j.ijfatigue.2010.09.020.

[9] FUSEK, Martin; HALAMA, Radim; LIČKOVÁ, D. Two modifications of Jiang criterion for constant amplitude multiaxial loading of AA2124-T851 and SS316L. *Continuum Mechanics and Thermodynamics*. 2020, vol. 32, no. 6, pp. 1673–1689.

[10] TOŠKOVÁ, Anna; FUSEK, Martin; CIENCIALA, Jakub; MÁNEK, Martin. Simplification of the Jiang criterion for application to S235JR. *International Journal of Fatigue*. 2026, vol. 209, art. no. 109619. ISSN 0142-1123. Available from: 10.1016/j.ijfatigue.2026.109619.

[11] WILCOXON, Frank. Individual Comparisons by Ranking Methods. *Biometrics Bulletin*. 1945, vol. 1, no. 6, pp. 80–83.

[12] STUDENT. The Probable Error of a Mean. *Biometrika*. 1908, vol. 6, no. 1, pp. 1–25.

APPLIED MECHANICS 2026
April 13 - 15, 2026, České Budějovice, Czech republic

NUMERICAL SIMULATIONS OF NON-PRESSURE POLYMER PIPES IN UNDERGROUND OPERATING CONDITIONS

Lukáš Trávníček[1], Jan Poduška[2], Florian Arbeiter[3], Roman Gratza[4], Daniel Zach[5], Luboš Náhlík[6], Pavel Hutař[7]

Abstract: This study presents a 3D finite element model for fracture mechanics-based lifetime estimation of buried polymer pipes. Failure is governed by slow crack growth (SCG), which is modelled using linear-elastic fracture mechanics. The model incorporates an angular-dependent external pressure derived from the ATV DVWK A127 standard. Crack propagation is simulated from an initial defect to its final size with a semi-elliptical crack shape. Stress intensity factor along the crack front is evaluated and used for lifetime estimation. Model validation at the stress–strain level shows good agreement with the ATV design standard, supporting the applicability of the proposed approach.

Keywords: polymer pipes, soil loading, finite element modelling, lifetime estimation

1 Introduction

Polymer pipes are widely used due to their ability to withstand very long operation periods up to 100 years. Direct verification of such long lifetimes is impractical. However, failure is governed by the slow crack growth (SCG) mechanism [1], which can be characterized by notched specimens. This enables conservative lifetime prediction through fracture-mechanical models of crack propagation in the pipe material, particularly those based on crack-layer theory [2; 3] and linear-elastic fracture mechanics (LEFM) [4; 5].

Finite element (FE) simulations of polymer pipes are essential for both methods, as they enable the evaluation of stresses and strains in the pipe wall [2; 3; 4; 5]. For buried pipes, two main modelling approaches can be found in the literature. The simpler approach represents soil load as external pressure derived from design standards, offering fast computation but limited flexibility and the inability to capture local effects [6; 7]. The more advanced approach models both the pipe and the surrounding soil, allowing for realistic, complex loading scenarios, but at the cost of higher computational demand and high sensitivity to uncertain soil parameters [3].

For fracture-mechanics-based lifetime estimation of a buried non-pressure pipe, it is crucial that FE models remain consistent with the design standard. This can be done by

[1] Ing. Lukáš Trávníček, Ph.D.; Institute of Physics of Materials, Czech Academy of Sciences; Žižkova 22, 616 00 Brno, Czech Republic, travnicek@ipm.cz
[2] Ing. Jan Poduška, Ph.D.; Institute of Physics of Materials, Czech Academy of Sciences; Žižkova 22, 616 00 Brno, Czech Republic, poduska@ipm.cz
[3] Priv. Doz DI Dr.mont. Florian Arbeiter; Montanuniversität Leoben, Department of Polymer Engineering and Science; Otto-Glöckel-Straße 2, 8700, Leoben, Austria, Florian.Arbeiter@unileoben.ac.at
[4] Ing. Roman Gratza, Ph.D.; Institute of Physics of Materials, Czech Academy of Sciences; Žižkova 22, 616 00 Brno, Czech Republic, gratza@ipm.cz
[5] DI Daniel Zach; Montanuniversität Leoben, Department of Polymer Engineering and Science; Otto-Glöckel-Straße 2, 8700, Leoben, Austria, Daniel.Zach@unileoben.ac.at
[6] prof. Ing. Luboš Náhlík, Ph.D.; Institute of Physics of Materials, Czech Academy of Sciences; Žižkova 22, 616 00 Brno, Czech Republic, nahlik@ipm.cz
[7] prof. Ing. Pavel Hutař, Ph.D.; Institute of Physics of Materials, Czech Academy of Sciences; Žižkova 22, 616 00 Brno, Czech Republic, hutar@ipm.cz

evaluating stresses and strains by an FE model and comparing the results with those obtained from, e.g., German ATV DVWK A127 standard [8], which is widely accepted in Europe. However, this link between FE modelling and design standards has not been systematically addressed.

The main aim of this study is to develop a 3D numerical model of a pipe containing a crack that enables lifetime estimation using LEFM, while ensuring consistency with the ATV design standard on the stress-deformation level. The approach, where soil load is represented by external pressure, is chosen because it avoids the complications associated with selecting soil parameters.

2 Numerical modelling

The numerical modelling was chosen mainly due to two reasons: (i) it enables describing the stress field near the crack front, and (ii) it enables using external pressure, which is not constant but varies along the angular position, see Figure 1. The crack propagation was modelled under the assumption that it follows a semi-elliptical shape. A typical 3D numerical model contained between 2×10^5 and 4×10^5 isoparametric elements depending on the crack size. The finite element mesh was prepared very fine near the crack front to properly capture the singular stress field (see detail in Figure 2).

The model was loaded by an external pressure whose magnitude depends on the angular position, as shown in Figure 1. The line pressures q_v, q_h, and q_h^* are obtained from the ATV design standard for chosen burying conditions. The material model was considered linear elastic, characterized by elastic modulus $E = 270$ MPa and Poisson!s ration $\mu = 0.3$. The chosen values correspond to typical Polyethylene from which the pipes are often made.

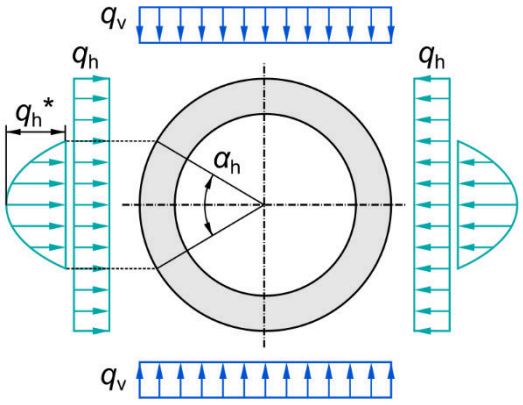

Figure 1: FE model of a pipe containing a crack on the inner surface.

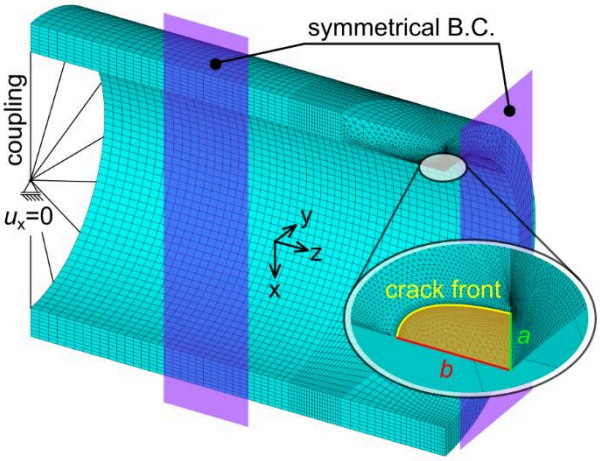

Figure 2: Scheme of an external pressure applied to a pipe model.

The crack propagation was modelled by crack increments, i.e., the number of steps (numerical calculations with an extended crack by a chosen crack increment) was performed during the numerical simulation of crack growth from the initial to the final size. The size of initial defects was equal to the void size in the material, ranging from 0.2 to 0.4 mm. Therefore, the crack length for the first simulation step was set to 0.2 mm, and the initial crack shape was assumed to be semicircular. As the crack grew, its front shape continuously changed to a semielliptical form. The semielliptical crack was modelled up to a length equal to the half-width of the pipe wall.

3 Conclusion

The presented numerical model allows the calculation of the stress intensity factor along the semielliptical crack front, where crack growth is simulated in steps from 0.2 mm to half the pipe wall width. Model validation is performed at the stress and strain levels, showing good agreement with the ATV design standard. The obtained stress intensity factor values were used to estimate the lifetime of the simulated pipe. The presented work contributes to a better understanding of the pipe behaviour in underground operating conditions.

Acknowledgement

The support by the project "Partnership for Security in Sustainable Transport and Energy", funded as project No. CZ.02.01.01/00/23_020/0008549 by Programme Johannes Amos Comenius, is also acknowledged.

References

[1] CHUDNOVSKY, A. Slow crack growth, its modeling and crack-layer approach: A review. *International Journal of Engineering Science* [online]. Elsevier BV, 2014, **83**, 6-41. ISSN 0020-7225. Dostupné z: doi:10.1016/j.ijengsci.2014.05.015

[2] WEE, Jung-Wook, Sang-Youn PARK a Byoung-Ho CHOI. Modeling and application of discontinuous slow crack growth behaviors of high-density polyethylene pipe with various geometries and loading conditions. *Engineering Fracture Mechanics* [online]. Elsevier BV, 2020, **236**, 107205. ISSN 0013-7944. Dostupné z: doi:10.1016/j.engfracmech.2020.107205

[3] WEE, Jung-Wook, Alexander CHUDNOVSKY a Byoung-Ho CHOI. Crack layer model for semi-elliptical surface cracks in HDPE pipes and application in buried pipes with complicated loading conditions. *International Journal of Mechanical Sciences* [online]. Elsevier BV, 2021, **208**, 106680. ISSN 0020-7403. Dostupné z: doi:10.1016/j.ijmecsci.2021.106680

[4] HUTAŘ, Pavel, Martin ŠEVČÍK, Luboš NÁHLÍK, Gerald PINTER, Andreas FRANK a Ivaylo MITEV. A numerical methodology for lifetime estimation of HDPE pressure pipes. *Engineering Fracture Mechanics* [online]. Elsevier BV, 2011, **78**(17), 3049-3058. ISSN 0013-7944. Dostupné z: doi:10.1016/j.engfracmech.2011.09.001

[5] FRANK, Andreas, Florian ARBEITER, Isabelle BERGER, Pavel HUTAŘ, Luboš NÁHLÍK a Gerald PINTER. Fracture Mechanics Lifetime Prediction of Polyethylene Pipes. *Journal of Pipeline Systems Engineering and Practice* [online]. American Society of Civil Engineers (ASCE), 2019, **10**(1). ISSN 1949-1190. Dostupné z: doi:10.1061/(ASCE)PS.1949-1204.0000356

[6] ŠEVČÍK, Martin, Florian ARBEITER, Pavel HUTAŘ, Gerald PINTER a Luboš NÁHLÍK. The Effect of Soil Load on Fracture Behaviour of Three-Layer Polymer Pipe for Non-Pressurised Applications. *Key Engineering Materials* [online]. Trans Tech Publications, Ltd, 2014, **627**, 197-200. ISSN 1662-9795. Dostupné z: doi:10.4028/www.scientific.net/KEM.627.197

[7] PODUŠKA, Jan, Pavel HUTAŘ, Andreas FRANK, Gerald PINTER a Luboš NÁHLÍK. Lifetime Calculation of Soil-Loaded Non-Pressure Polymer Pipes. *Key Engineering Materials* [online]. Trans Tech Publications, Ltd, 2019, **827**, 141-146. ISSN 1662-9795. Dostupné z: doi:10.4028/www.scientific.net/KEM.827.141

[8] *ATV DVWK 127: Statische Berechnung von Abwasserkanälen und leitungen*. 3rd. 2000.

APPLIED MECHANICS 2026
April 13 - 15, 2026, České Budějovice, Czech republic

CRITICAL VOLUME SOLUTION FOR FATIGUE STRENGTH ESTIMATION INTEGRATED WITH THE STRESS GRADIENT EFFECT

Petr Vaněk[1], Jan Papuga[1], Martin Nesládek[1], František Fojtík[2]

Abstract: The contribution analyses the fatigue failure of steel ČSN 41 1523, focusing on systematically including size and notch effects in fatigue strength assessment. The research is supported by tests on smooth and notched specimens under cyclic loading. It provides a general theoretical background to the investigated issues and the corresponding solution methods, which are then applied in the practical ways. The core approach combines the critical volume concept, representing the size effect, with a method accounting for the stress gradient at the component's critical location. Together, these tools quantify the relationship between fatigue strength and the factors mentioned above.

Keywords: Fatigue of Materials; Critical Volume; Size and Notch Effects; Multiaxial Criteria; Finite Element Method

1 Introduction

With the influx of modern technologies and advanced manufacturing approaches, it is now possible to produce highly topologically complex components. However, increasing geometric complexity and functional requirements also increase the difficulty of fatigue life prediction, as a component may be affected by a range of influential factors such as temperature, frequency, the shape and size of the sample, the notch effect, multiaxiality, and many others. This contribution deliberately focuses on two of them, namely the size effect and the notch effect, i.e. the effect of inhomogeneous stress distribution on fatigue strength. In general, the size effect reflects the fact that, with increasing stressed material volume, the probability of fatigue damage initiation also increases, while the notch effect is related to the local stress gradient in the vicinity of the critical location [1]. The key question is how to incorporate these effects into fatigue life prediction in a consistent way. Current solution methodologies, as noted for example in the FKM Guideline, typically account for these effects by means of rather independent correction factors [2]. In contrast, the main aim of this research was to attempt a systematic unification of the size effect and the stress gradient (notch effect) at the most critical locations of the specimens into a single computational procedure for fatigue strength estimation.

2 Methodology

The methodology utilizes experimental fatigue data simulated by finite element method (FEM) to provide the basis for the subsequent calculations. The experimental part delivers baseline fatigue life data for smooth and notched specimens made of steel ČSN 41 1523 (equivalent to S355J2) under cyclic loading (S-N curves) [3]. The FEM simulations are used primarily to describe the stress fields and volume quantification at the critical locations of the

[1] Faculty of Mechanical Engineering Czech Technical University in Prague, Technická 4 160 00 Praha 6, Czech Republic
[2] Faculty of Mechanical Engineering Technical University of Ostrava, 17. listopadu 2172/15 708 00 Ostrava-Poruba, Czech Republic

specimens. These outputs are subsequently employed to incorporate the size effect (critical volume) and the stress gradient effect (notch effect) in the following parts.

2.1 Fatigue Experiments

Fatigue tests were carried out on steel ČSN 41 1523 with the following mechanical properties: ultimate tensile strength $R_m = 555$ MPa, yield strength $R_e = 401$ MPa, and elongation at fracture $A = 29.4$ %. In total, seven axisymmetric specimen geometries were tested (Figure 1): two unnotched cases (unnotched full bar and hollow bar) and five notched variants defined by the notch shape (V-notch with notch-root radius R = 1.3 mm, U-notch R1.5, Fillet R0.7, U-notch R5 and Fillet R0.2). Each geometry was tested under three loading modes (push-pull, torsion, and bending) R = -1 load asymmetry at room temperature [3]. The experimental data points were fitted using widely used Kohout–Věchet model (Figure 2), which was originally proposed in [4].

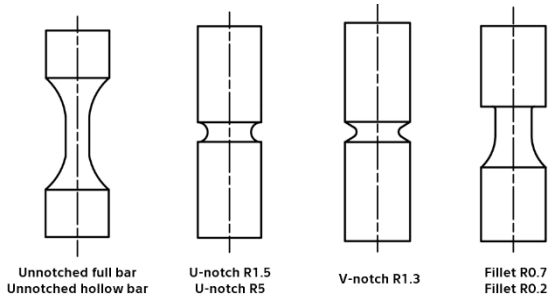

Figure 1: Specimen geometries

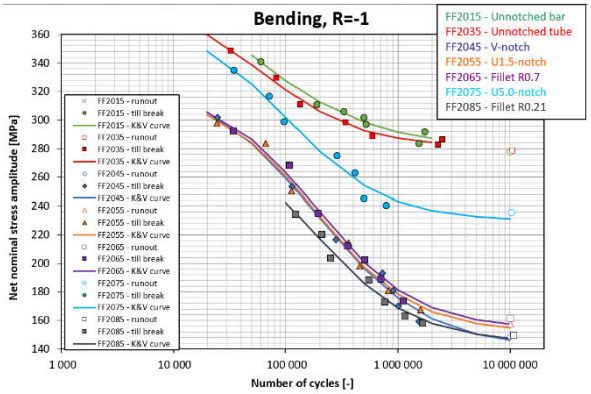

Figure 2: Kohout–Věchet approximation of the S-N curve under fully reversed bending [1]

2.2 FEM Simulations

The experimental campaign was additionally supported by numerical simulations performed using Abaqus commercial FEM code. A linear elastic isotropic model was used with the following parameters: Young's modulus E = 210000 MPa and Poisson's ratio $\nu = 0.3$. Axisymmetric 2D models were created for push-pull and torsion modes, while half-symmetry 3D models were used for bending. A minimum of 5 µm element edge length was set in specimen's critical location to get the highest possible resolution of critical volume in the vicinity of the notch roots. [1]

3 Fatigue Post-Processing and Implementation of Size and Stress Gradient Effects

The computational procedure post-processes the experimental fatigue FEM data to quantify the size effect and the notch effect with special computational methods described below, all evaluated for the selected reference fatigue life level of 500 000 cycles [5].

The following inclusion of the investigated effects is based on equivalent stress amplitudes evaluated according to the selected fatigue criteria namely Manson–McKnight (MMK) and Dang Van (DV). The MMK criterion, originally proposed in [6], simplifies to the von Mises criterion for a fully reversed loading cycle (R = -1)

$$\sigma_{a,ekv} = \sqrt{\frac{1}{2} \cdot \left\{ \left(\sigma_{x,a} - \sigma_{y,a}\right)^2 + \left(\sigma_{y,a} - \sigma_{z,a}\right)^2 + \left(\sigma_{z,a} - \sigma_{x,a}\right)^2 + 6\left[\tau_{xy,a}^2 + \tau_{yz,a}^2 + \tau_{zx,a}^2\right] \right\}}. \quad (1)$$

Dang Van criterion belongs to multiaxial fatigue criteria and is not available as a direct output in common FEM software, including Abaqus. Therefore, the FEM results were post-processed using the specialised FPU (Fatigue Prediction Utility) plugin for Abaqus, which is automatically called within the custom-made Python scripts [7]. FPU acts as a standalone fatigue solver. From the original FEM results it retrieves the time-varying stress tensor at each element node and, according to the selected criterion, computes the corresponding equivalent stress amplitude $\sigma_{a,eqv}$, or the fatigue index FI [7]. These quantities are linked through the fully reversed axial fatigue strength f_{-1}as follows

$$\sigma_{a,eqv} = FI \cdot f_{-1}. \quad (2)$$

The Dang Van criterion itself can be introduced using the following relation

$$\max_t [a_{DV} \cdot \tau(t) + b_{DV} \cdot \sigma_H] \leq f_{-1}, \quad (3)$$

where $\tau(t)$ represents shear stress amplitude computed by a method-specific numerical algorithm and σ_H hydrostatic stress [7]. The material parameters a_{DV} and b_{DV} depend on the fatigue strengths in axial f_{-1} and torsion loading t_{-1}, which are functions of the corresponding critical volume CV. This in turn needs a closed loop procedure that must be resolved using a dedicated iterative procedure, schematically shown in Figure 3. [5]

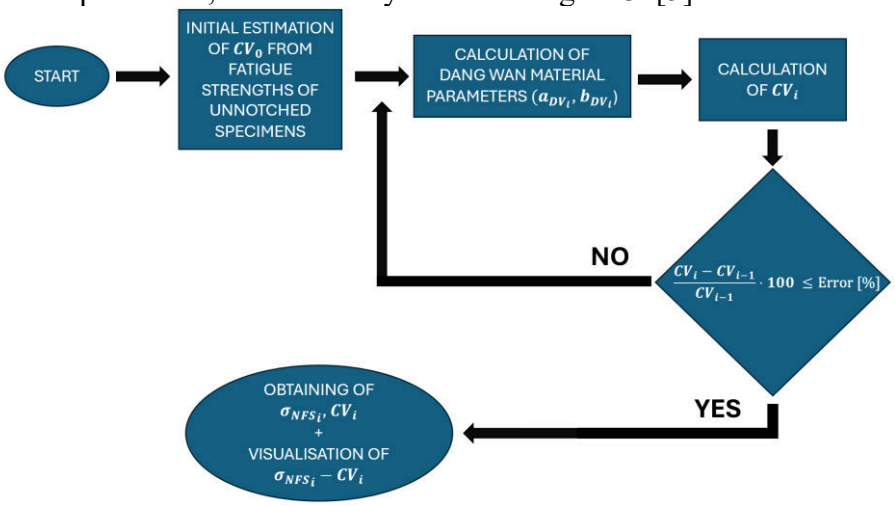

Figure 3: Iteration loop of CV estimation by Dang Van criterion

3.1 Inclusion of Size Effect

In this study, the size effect was quantified using the critical volume approach, which can be defined by a threshold condition based on the equivalent stress amplitude

$$\sigma_{a,eqv} \geq z \cdot \sigma_{a,eqv,max}, \quad (4)$$

where $z \in (0,1)$ is the threshold value and $\sigma_{a,eqv,max}$ is the maximum equivalent stress amplitude located at the hot-spot location calculated by two specific criterions described in equations (1) and (3). For each selected threshold z the critical volume $CV(z)$ is computed as the volume of the specimen region in which the threshold condition is met. [5]

In the practical implementation, the outputs of the FEM simulations were used, namely the volumes of individual elements V_i and nodal data (the number of nodes n_i). Due to limited possibilities for a direct critical volume evaluation in FEM solvers, the post-processing was

performed in the Python programming environment. The critical volume was evaluated discretely using a dedicated algorithm, which was originally presented in [5].

For each element the ratio of critical nodes $n_{i,crit}$ fulfilling the threshold condition (4) to the total number of nodes n_i is determined. This ratio is then used to compute the partial critical volume CV_i from the element volume V_i. The total critical volume CV of the specimen is obtained by summing over all elements. [5]

3.2 Inclusion of Stress Gradient Effect

The notch effect was quantified directly by the relative stress gradient. This quantity expresses how rapidly the equivalent stress decreases from the surface into the material, i.e., the slope of the tangent to the subsurface profile $\sigma_{a,eqv}(x)$ at the critical location. The relative stress gradient is defined as: [1]

$$\gamma' = \frac{1}{\sigma_{a,eqv,max}} \left| \frac{d\sigma_{a,eqv}(x)}{dx} \right|_x \tag{5}$$

Therefore, subsurface profiles $\sigma_{a,eqv}(x)$ were extracted from the FEM outputs for each specimen, loading mode, and for both selected criteria. Owing to the non-uniform nodal spacing caused by local mesh refinement at the specimen's critical location, the profile $\sigma_{a,eqv}(x)$ had to be approximated by a polynomial in the immediate vicinity of the surface. For all cases, an initial depth of 0.1 mm was considered and required to contain at least four nodes. If this condition was not fulfilled, the interval was adaptively extended until the minimum number of nodes was satisfied [1].

From explicit expression of the selected polynomial $\sigma_{a,eqv}(x)$ was obtained its derivative prescription $\frac{d\sigma_{a,eqv}(x)}{dx}$. Then relative value of derivative at the specimen surface (x = 0), where the stress gradient effect is most relevant, was evaluated by equation (5). [1]

4 Results and Discussion

The size effect stress gradient effects were first interpreted separately using the relationships between the notch fatigue strength σ_{NFS} and the critical volume CV and between σ_{NFS} and the relative stress gradient γ'. Afterwards was a 3D characteristic constructed. [1]

The $\sigma_{NFS} - CV$ and $\sigma_{NFS} - \gamma'$relationships were approximated with power law functions displayed in Figure 4 and Figure 5 below.

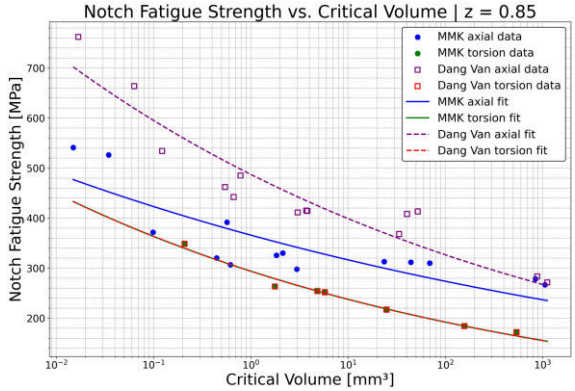

Figure 4: $\sigma_{NFS} - CV$ relationship

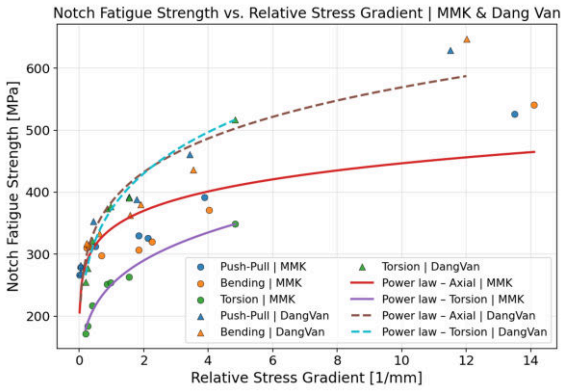

Figure 5: $\sigma_{NFS} - \gamma'$ relationship

The results show a clear size and stress gradient related trend. As the critical volume CV increases, the notch fatigue strength σ_{NFS} decreases. Large CV values are mainly associated with unnotched cases, whereas the opposite end of the spectrum comprises specimens with the sharpest notches (Fillet R0.2 and Fillet R0.7). The $\sigma_{NFS} - CV$ curve directly reflects the size effect, i.e., the probability of fatigue damage increases with increasing material volume. For the stress gradient effect is typical that it has biggest influence for sharp notches and smallest for unnotched cases. The highest γ' values are observed for Fillet R0.2 and Fillet R0.7 specimens, while the lowest γ' values occur for the unnotched types. [1]

Because the $\sigma_{NFS} - CV$ and $\sigma_{NFS} - \gamma'$ relationships describe only one of the two investigated effects at a time, the results were further evaluated in the combined $\sigma_{NFS} - CV - \gamma'$ space. The scattered data could be approximated using a 3D regression characteristic in the form of a parabolic surface, which provides an initial compact model simultaneously accounting for both the size and the stress gradient effect. The selected surface can be introduced by the following equation

$$log\ \sigma_{NFS} = Z_{\gamma'} - C_{parabolic} \cdot \left[log\ CV - Y_{\gamma'}\right]^2, \tag{6}$$

where Y_γ and Z_γ represent the predicted coordinates of the guiding curve of the parabolic approximation, i.e., the curve formed by the vertices of the parabolic cross sections for a given γ' [1]. The $C_{parabolic}$ is the coefficient determining the curvature (width) of the surface. [1]

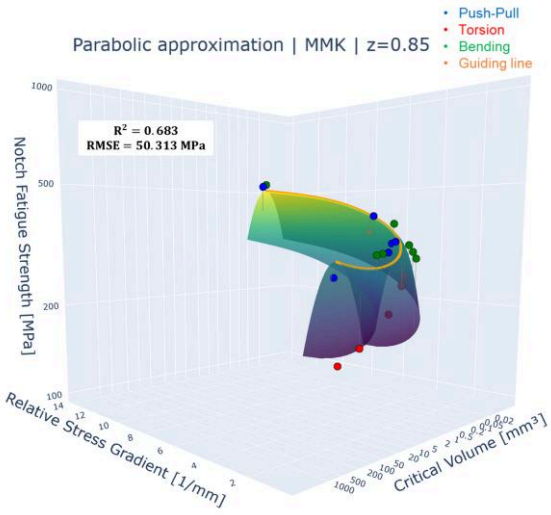

Figure 6: Parabolic approximation for MMK criterion [1]

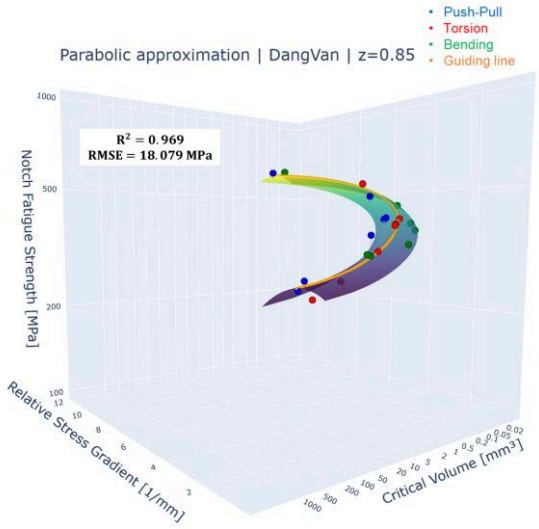

Figure 7: Parabolic approximation for Dang Van criterion [1]

5 Conclusion

The key findings of this study can be summarised as follows:

1. A pronounced effect of specimen geometry on fatigue strength was observed across all investigated loading modes. The differences between unnotched and sharply notched specimens were subsequently interpreted using the critical volume approach and notch-root stress gradients.
2. The size effect and the stress gradient effect (notch effect) were successfully incorporated using the critical volume CV and the relative stress gradient γ'. Their relevance was confirmed through the $\sigma_{NFS} - CV$ and $\sigma_{NFS} - \gamma'$ relationships.

3. To systematically unify both investigated phenomena at the critical location within a single computational procedure, a 3D characteristic in the form of a parabolic surface was identified.

Acknowledgement

The financial support of the Czech Science Foundation within the $23-06130K$ project, and of the Grant Agency of the Czech Technical University in Prague within the application No. $OHK2-004/26$ is gratefully acknowledged.

References

[1] VANĚK, Petr. *Řešení výpočtu únavové životnosti pomocí kritického objemu integrované s vlivem gradientu napětí [Critical Volume Solution for Fatigue life Estimation Integrated with the Stress Gradient Effect]* [online]. Prague, 2026. Master's thesis. Czech Technical University in Prague, Faculty of Mechanical Engineering. Supervisor: PAPUGA, Jan.

[2] *Rechnerischer Festigkeitsnachweis für Maschinenbauteile: aus Stahl, Eisenguss- und Aluminiumwerkstoffen. 7*. Überarbeitete Ausgabe. Frankfurt am Main: VDMA Verlag, 2020. ISBN 978-3-8163-0743-3

[3] NESLÁDEK, Martin; FOJTÍK, František; MŽOUREK, Matěj; PAPUGA, Jan. *Notched structural steel specimens assessed by selected fatigue analysis methods.* Journal of Constructional Steel Research [online]. 2024, Vol. 219, pp. 1-15 [cit. 2025-03-16]. ISSN 0143974X. Available form: https://doi.org/10.1016/j.jcsr.2024.108789.

[4] KOHOUT, Jan a Stanislav VĚCHET. *A new function for fatigue curves characterization and its multiple merits.* International Journal of Fatigue [online]. 2001, 23(2), pp. 175-183 [cit. 2026-03-09]. Available from: doi:10.1016/S0142-1123(00)00082-7

[5] SERRI, Leonardo. *Critical volume approach in multiaxial fatigue assessment of notched specimens* [online]. Padova, 2024. Master's thesis. Universita' Degli Studi Di Padova, Dipartimento Di Ingegneria Industriale Dii. Supervisor: MENEGHETTI, Giovanni

[6] PAPUGA, Jan; VARGAS, Miguel; HRONEK, Martin. *Evaluation of uniaxial fatigue criteria applied to multiaxially loaded unnotched samples.* Engineering MECHANICS [online]. 2012, Vol. 19, no. 2-3, pp. 99–111 [cit. 2025-02-28]. Available from: https://www.researchgate.net/publication/28532096_Evaluation_of_uniaxial_fatigue_criteria_applied_to_multiaxially_loaded_unnotched_samples

[7] NESLÁDEK, Martin; ŠPANIEL, Miroslav. *An Abaqus plugin for fatigue predictions*. Advances in Engineering Software [online]. 2017, Vol. 103, pp. 1–11 [cit. 2025-04-29]. ISSN 09659978. Available from: https://doi.org/10.1016/j.advengsoft.2016.10.008.

APPLIED MECHANICS 2026
April 13 - 15, 2026, České Budějovice, Czech republic

ON THE TORQUE VECTORING SYSTEM FOR FORMULA STUDENT

František Viták[1], Jan Rendl[2]

Abstract: This paper presents the development and computational modelling of a torque vectoring system for a Formula Student racing vehicle. The system's architecture includes a 7-degree-of-freedom vehicle dynamics model, a nonlinear tire model, and a kinematic steering model. The control algorithms and torque distribution formulas were validated through numerical simulations. The simulation results confirm the system's possible improvement in vehicle cornering performance and provide a foundation for future physical system calibration.

Keywords: Torque vectoring; Formula Student; computational model

1 Introduction

The automotive industry's ongoing transition from combustion engines to electric motors presents new opportunities to improve vehicle driving properties. In motorsport, where marginal gains significantly impact overall performance, the shift to electric powertrains allows for the precise, independent distribution of torque to each wheel [1, 3]. This paper explores these capabilities to improve the cornering performance of a Formula Student electric racing vehicle, currently under development by the UWB eRacing team.

The proposed system utilizes a 7-DoFs vehicle dynamics model coupled with a nonlinear tire model. To ensure accurate torque distribution model, the vehicle's reference yaw rate is calculated based on the desired vehicle velocity and turn radius. The radius of the turn is obtained with the Ackermann steering geometry condition [2, 5]. The primary objective is to develop a mathematical model that determines the optimal corrective yaw moment based on the vehicle's current dynamic state. This yaw moment is then translated into specific torque requests for each wheel via a set of distribution formulas [3]. The effectiveness of the proposed system is subsequently evaluated through numerical simulations [5].

2 Vehicle model

A 7-DoFs vehicle model [4] was chosen as the optimal platform for deriving and simulating the mathematical control formulas. The model captures essential horizontal planar motion (3 DoFs), see Figure 1, along with the rotational dynamics of each of the four wheels, additional 4 DoFs. While vertical suspension travel is neglected, the model's accuracy is enhanced by incorporating quasi-static load transfer during cornering [5].

To calculate the dynamic forces acting on the vehicle, an additional degree of freedom representing rotational velocity is assigned to each wheel to solve its respective equation of motion. The semi-empirical Dugoff tire model [2] was chosen to represent nonlinear tire behaviour due to its computational efficiency, suitability for real-time applications, and minimal parameter requirements. The primary outputs generated by this tire model are the lateral and longitudinal forces and aligning torques.

[1] František Viták; Faculty of Applied Sciences, University of West Bohemia in Pilsen; talo0xeu@students.zcu.cz
[2] Jan Rendl; Faculty of Applied Sciences, University of West Bohemia in Pilsen; rendlj@fav.zcu.cz

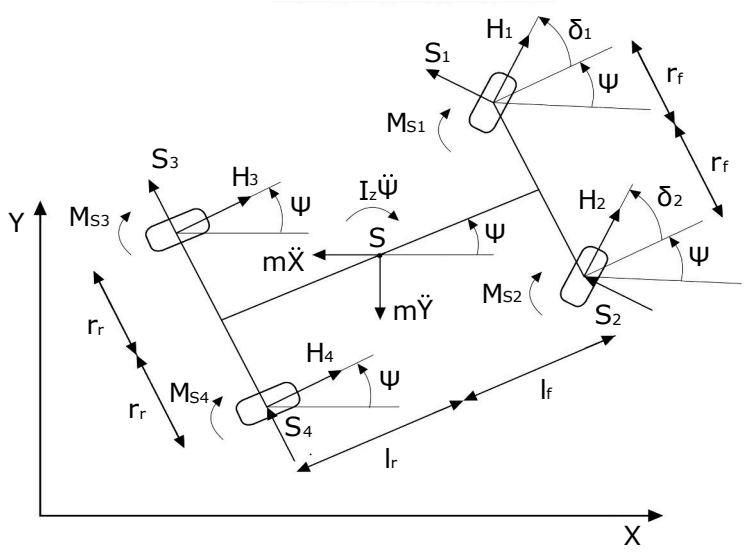

Figure 1: Horizontal computational model of the vehicle

3 Torque vectoring system

The principle of the torque vectoring system is to apply greater drive torque to the outer wheels than the inner wheels during a turn. This creates an additional, controlled yaw moment that improves the vehicle's turning capability and overall cornering speed [1]. This concept is visualized on the rear axle in Figure 2.

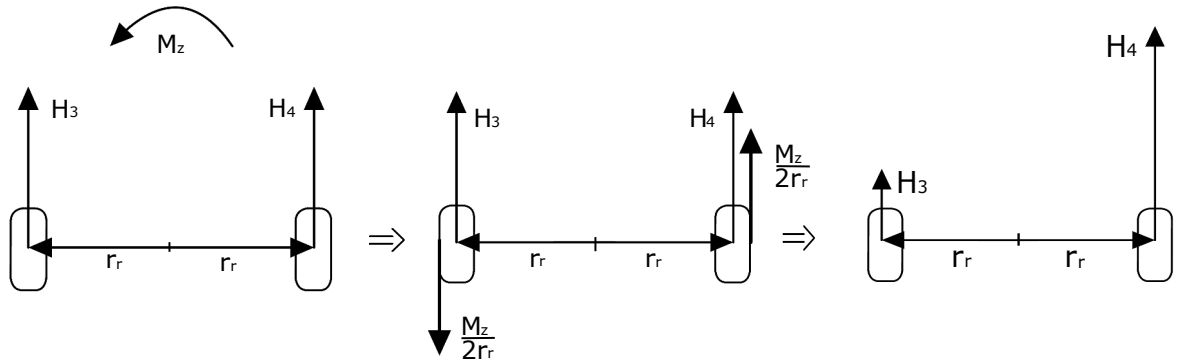

Figure 2: Scheme of yaw moment M_z distribution

The corrective yaw moment M_z applied to the vehicle is calculated proportionally to the error $\Delta\dot{\Psi}$ between the reference yaw rate $\dot{\Psi}_{ref}$ and the vehicle's actual yaw rate $\dot{\Psi}_a$, which is measured by onboard sensors or is considered as the state space variable in the computational analysis. The corrective yaw moment then yields [3]

$$M_z = K_p \Delta\dot{\Psi} = K_p(\dot{\Psi}_{ref} - \dot{\Psi}_a), \tag{1}$$

where K_p is the proportional gain of the controller, and $\Delta\dot{\Psi}$ is the yaw rate error. Reference yaw rate $\dot{\Psi}_{ref}$ is derived from the vehicle's longitudinal speed v_s and cornering radius R

$$\dot{\Psi}_{ref} = \frac{v_s}{R}. \tag{2}$$

The computational model relies on accurately determining the cornering radius R. For this purpose, Ackermann steering geometry is applied. Based on [4], the cornering radius can be calculated using the following formula

$$R = \sqrt{l_r^2 + (l_f + l_r)^2 \cot^2 \delta}, \tag{3}$$

where l_f and l_r is the distance between the centre of gravity and front respectively rear suspension and δ is the average of the left and right wheel steer angles. It should be noted that this kinematic formula represents an ideal scenario and does not account for real-world factors such as tire deformation and slip angles.

Total corrective moment M_z is then distributed [5] between the front (M_{zf}) and rear (M_{zr}) axles according to the vehicle's specific weight distribution and handling parameters.

The system utilizes sets of mathematical formulas to determine the exact torque request for each wheel. There are four distinct calculation sets, varying based on the throttle pedal position and the turn direction (left or right). For example, the torque distribution for a left turn under partial acceleration is defined as [5]

$$\begin{aligned}
M_{h1} &= eM_{max}G_r - \left(\frac{M_{zf}}{2r_f}\right) r_w, \\
M_{h2} &= eM_{max}G_r + \left(\frac{M_{zf}}{2r_f}\right) r_w, \\
M_{h3} &= eM_{max}G_r - \left(\frac{M_{zr}}{2r_r}\right) r_w, \\
M_{h4} &= eM_{max}G_r + \left(\frac{M_{zr}}{2r_r}\right) r_w.
\end{aligned} \tag{4}$$

Where $e \in \langle -1; 1 \rangle$ represents the accelerator pedal position (negative value for braking and positive for acceleration), M_{max} is the maximal torque of each electric motor, G_r is the gear ratio, M_{zf} and M_{zr} are the corrective yaw moments for the front and rear axles respectively. Remaining variables r_f and r_r denote the front and rear vehicle half tracks in Figure 1 and r_w is the nominal tire radius.

4 Results

Numerical simulations were performed using the defined vehicle and computational models to evaluate performance in a constant-radius corner. The primary performance metric was the time required to complete the corner, evaluated across various proportional controller settings (Table 1). Variable K represents driver aggressiveness [2]. Secondary measured variables included tire slip angles, torque distribution time series, and corner-exit speed. The simulation results indicate that implementing this torque vectoring system can improve the vehicle's cornering capabilities [5]. Figure 3 illustrates the torque vectoring system, demonstrating how it adjusts the drive torque at each wheel during cornering.

Table 1: Elapsed time t_z [s] in the corner for given values of driver aggressiveness K, proportional gain K_p and corner radius R [m]

$K = 0.3$					
R	$K_p = 0$	250	500	750	1000
4.5	1.7301	1.7218	1.7153	1.7102	1.7063
9.125	2.5547	2.5545	2.5543	2.5541	2.5539
15	3.3112	3.3103	3.3089	3.3068	3.3022
20	3.8312	3.8295	3.8268	3.8215	3.8143
$K = 0.6$					
R	$K_p = 0$	250	500	750	1000
4.5	1.7282	1.7194	1.7125	1.7069	1.7023
9.125	2.5457	2.5454	2.5452	2.5450	2.5448
15	3.2991	3.2982	3.2968	3.2946	3.2895
20	3.8181	3.8164	3.8135	3.8071	3.8022
$K = 0.9$					
R	$K_p = 0$	250	500	750	1000
4.5	1.7256	1.7166	1.7096	1.7039	1.6992
9.125	2.5415	2.5412	2.5409	2.5407	2.5405
15	3.2947	3.2937	3.2924	3.2901	3.2851
20	3.8135	3.8118	3.8089	3.8020	3.7979

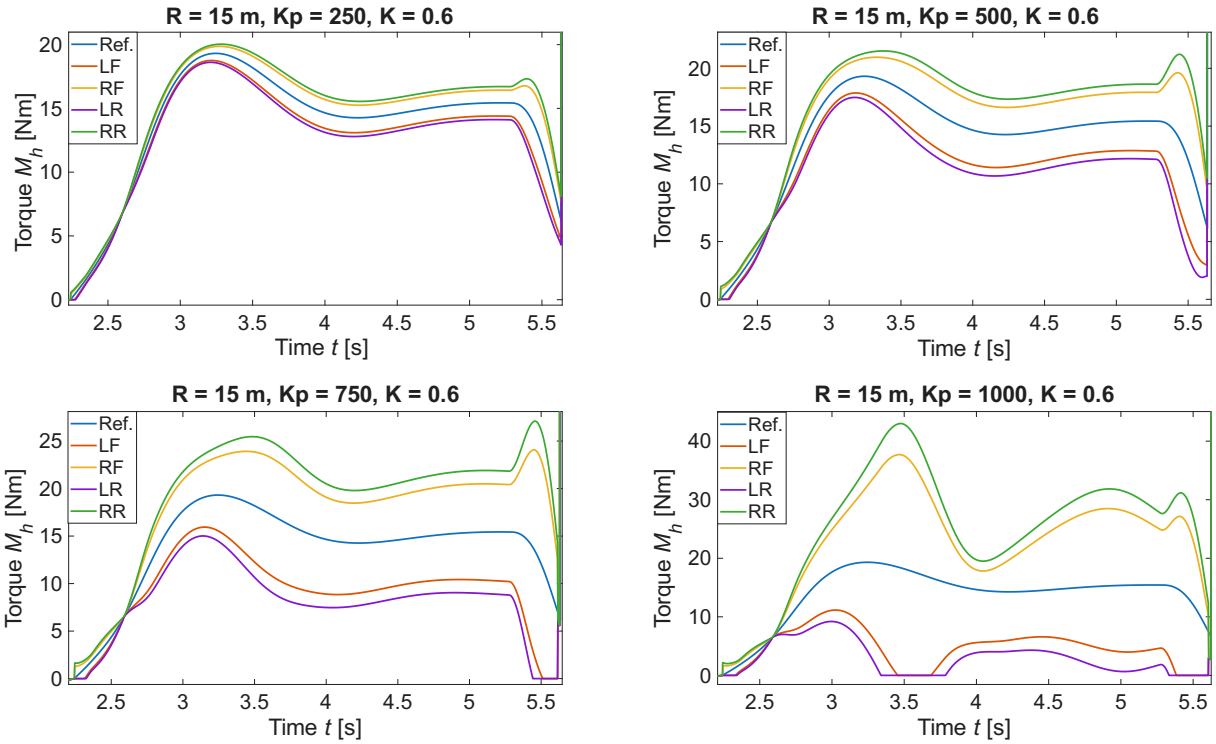

Figure 3: Drive torque time series for a corner radius of $R = 15$ m

A detailed analysis of the simulation data reveals several key dependencies regarding the proportional gain K_p, driver aggressiveness K, and corner radius R.

Overall, increasing the proportional gain K_p has a distinctly positive effect on both cornering times and exit speeds. Higher values of K_p lead to a larger difference between the drive torques applied to the outer and inner wheels (see Figure 3), corresponding to an increase in the applied yaw moment. However, excessively high K_p values used in the controller must be avoided. As simulations indicated, extreme settings can cause the drive torque on the inner wheels to drop to zero, negatively impacting vehicle stability, traction, and steering in real-world scenarios. Furthermore, K_p influences tire slip. Increasing it tends to decrease longitudinal slip on the left wheels while increasing it on the right, and similarly shifts lateral slip from the front to the rear wheels.

The driver's aggressiveness, constant K, also significantly affects the system. While higher values of K generally reduce cornering times. Based on the performed simulations, a value of $K = 0.6$ proved to be an optimal compromise, yielding sufficient time improvements without causing excessive slip or reducing corner-exit velocity.

The corner radius R plays a crucial role in the controller's effectiveness and overall vehicle dynamics. The torque vectoring system delivers its greatest benefits at a smaller turn radius, where it consistently maintains or increases the vehicle's speed compared to a deactivated system. On the other hand, at larger radii and higher K_p values, speed fluctuations can become chaotic. This instability is attributed to the driver model's difficulty in smoothly modulating the accelerator pedal under such conditions.

5 Conclusions

This paper presents a torque vectoring system for an electric Formula Student vehicle employing a 7-DoF dynamic model and a nonlinear tire model. The simulation results demonstrate that active torque distribution performed by a proportional controller reduces cornering times and enhances overall agility. These findings validate the proposed mathematical model and provide a strong foundation for future physical implementation and real-world calibration on the UWB eRacing team car.

The simulations demonstrate that there is no single universal setup. For competitive applications such as a Formula Student vehicle, where track layouts and disciplines are known in advance, the controller parameters (K_p, K) must be optimised and dynamically adjusted to meet the specific requirements of each racing discipline.

6 Acknowledgment

The work was supported by the internal grant project SGS-2025-015 of the University of West Bohemia in Pilsen.

References

[1] HLAVÁČ, Pavel. *Studie vektorování točivého momentu vozidla*. Brno: Vysoké učení technické v Brně, 2021.

[2] HRABAČKA, Martin. *Modelování a řízení jízdních manévrů silničního vozidla*. Plzeň: Západočeská univerzita v Plzni, 2020.

[3] FRICANO, Andrea. *Design of Torque Vectoring system for Formula SAE electric vehicle*. Torino: Politecnico di Torino, 2019.

[4] JAZAR, N. Reza. *Vehicle Dynamics*. New York: Springer, 2008. ISBN 978-0-387-74243-4.

[5] VITÁK, František. *Počítačové modelování jízdy vozu Formula Student s elektropohonem jednotlivých kol*. Plzeň: Západočeská univerzita v Plzni, 2025.

APPLIED MECHANICS 2026
April 13 - 15, 2026, České Budějovice, Czech republic

FATIGUE ASSESSMENT OF SUPERELLIPSE METAMATERIAL STRUCTURE

Tomáš Vítek[1,2*], Jan Poduška[2], Lukáš Trávníček[2], Matthias Fleisch[3], Luboš Náhlík[2], Pavel Hutař[2]

Abstract: The fatigue performance of additively manufactured structures represents a critical area of investigation for their industrial implementation. A fully parametric model of a 3D printed polymer auxetic structure was developed. Different fatigue criteria were applied to predict fatigue life, and their results were compared.

Keywords: fatigue, metamaterial, superellipse, Ansys

1 Introduction

Metamaterials are generally architected materials that gain their properties mainly through the design of their geometry rather than through the properties of the base material used for manufacturing. They are most commonly manufactured using a base "cell" that is repeated to create a complete structure. By clever design of the geometry, properties considered unnatural for commonly found materials can be achieved [1].

One of the most promising examples are auxetic metamaterials. These materials have negative Poisson ratio – expanding in all directions when elongated and narrowing when compressed. Despite quite extensive research in recent years, most papers only focus on auxetic structures on material and unit cell levels. There are currently a few real-world applications of these metamaterials in several areas, the most significant according to [2] include protective equipment (helmets and body armor) or crash-resistant panels and vibration-damping components in automotive industry. The effort for a broader application of mechanical metamaterials is partially hindered by the lack of knowledge about their performance under long-term loading and fatigue. The intricate structures that consist of tiny members often raise doubts about their durability.

This contribution focuses on auxetic metamaterials with tunable stiffness. Development of parametric geometry model of certain auxetic structure is described. The model is then used for numerical simulations and fatigue life predictions using various fatigue life criteria.

2 Method

Lifetime assessment is performed by creating a finite element model of a structure, applying different load cycles and extracting stress values required to evaluate specific fatigue criteria. The material of the structure is PA12 manufactured by fused filament fabrication (FFF). Properties for both the elastic response and fatigue resistance were obtained from previous work conducted at IPM [3].

[1] Faculty of Mechanical Engineering, Brno University of Technology. Technická 2896/2, 616 69 Brno, Czech Republic
[2] Institute of Physics of Materials, Czech Academy of Sciences. Žižkova 513/22, 616 00 Brno, Czech Republic
[3] Polymer Competence Center Leoben. Sauraugasse 1, AT-8700 Leoben, Austria
*vitek@ipm.cz

3 Modeling

A structure called *superellipse* was selected for numerical analyses. The geometry of this auxetic structure is defined by the following equation:

$$\left|\frac{x}{a}\right|^n + \left|\frac{y}{b}\right|^n = 1, \quad (1)$$

where x, y are coordinates, a, b are the major and minor axes, respectively, and n is the shape parameter. Adjusting the parameter n alters the pore geometry, as illustrated in Fig. 1.

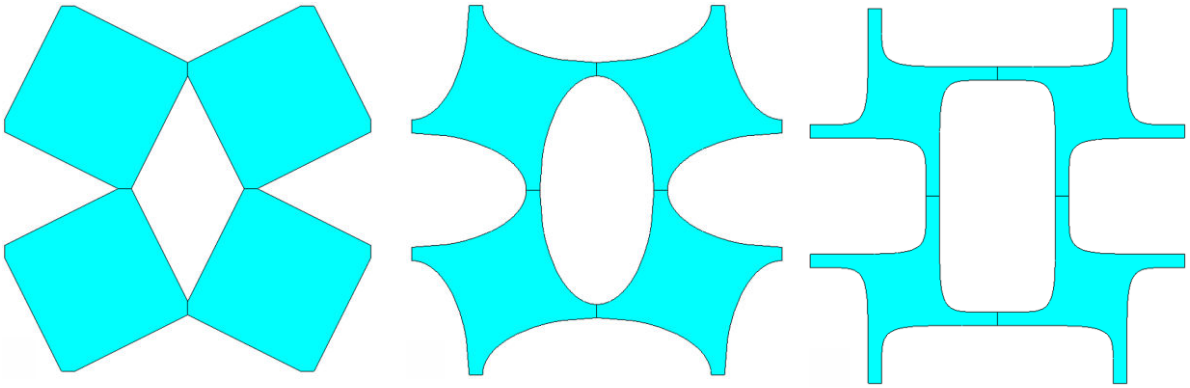

$n = 1$ $n = 2$ $n = 5$

Figure 1: Shape of superellipse structure for different values of parameter n.

Numerical simulations were performed using a fully automated procedure by combining Python and Ansys MAPDL. In a Python script, all governing parameters (e.g. geometry parameters, material properties, load magnitudes etc.) were defined and transferred to MAPDL using PyAnsys. There, the geometry was created and meshed, load cycles were defined, and the solution was executed. All required quantities were evaluated and transferred back to Python for further postprocessing. This automated procedure allowed for effective computations across a wide range of input parameters.

4 Results

Fatigue life was assessed based on multiple criteria - Signed von Mises stress, Absolute Maximum Principal stress and Berrehili criterion [4]. Fig. 2 shows an example of the maximum von Mises stress for a certain load case and the corresponding fatigue life prediction using Signed von Mises stress criterion. A comparison of the fatigue life predictions using different criteria is depicted in Fig. 3.

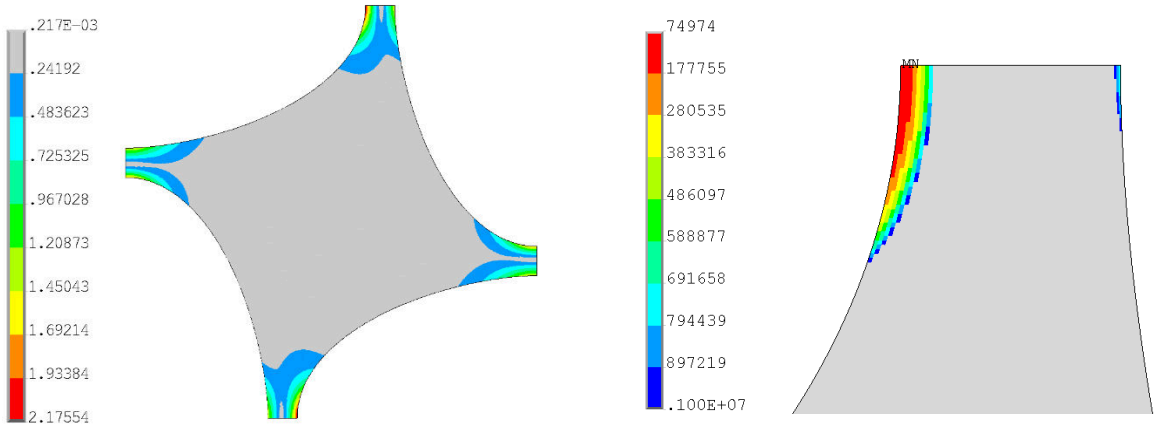

a) b)

Figure 2: Sample results for shape parameter $n = 2$: a) maximum von Mises stress during load cycle [MPa]; b) fatigue life prediction at the critical location using Signed von Mises stress criterion [cycles].

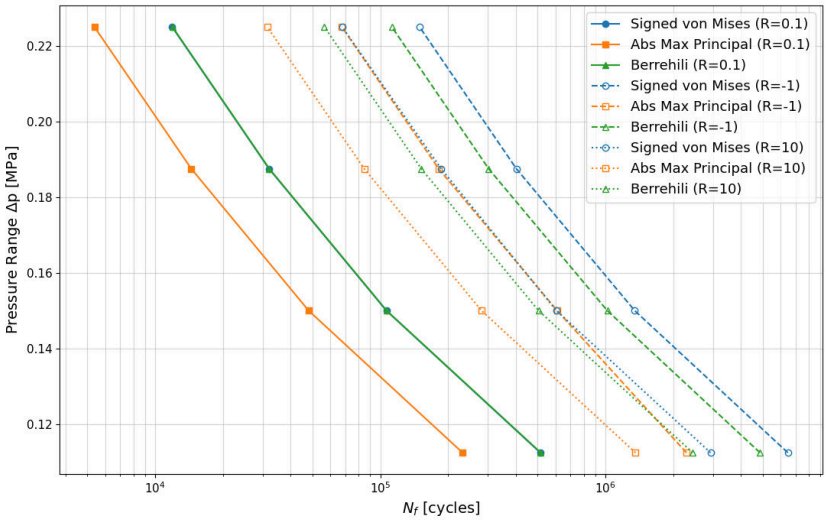

Figure 3: Fatigue lifetime estimation using different criteria.

5 Conclusion

Signed von Mises stress criterion and Berrehili criterion provided very similar results. This is due to the fact that both criteria are based on the second stress tensor invariant J_2; however, Berrehili criterion includes an additional term for mean stress influence. Among the three, Absolute Maximum Principal stress criterion yielded the most conservative predictions.

The results obtained by this parametric study will serve for the design of fatigue tests and future practical applications of the superellipse metamaterial structure.

Acknowledgement

The research work of this study was performed within the COMET-Module project ”Repairtecture” (project-no.: 904927) at the Polymer Competence Center Leoben GmbH (PCCL, Austria) within the framework of the COMET-program of the Federal Ministry for Climate Action, Environment, Energy, Mobility, Innovation and Technology and the Federal Ministry for Labour and Economy. The support by project “Partnership for Security in Sustainable Transport and Energy”, funded as project No. CZ.02.01.01/00/23_020/0008549 by Programme Johannes Amos Comenius, is also acknowledged.

References

[1] FLEISCH, M.; THALHAMER, A.; MEIER, G.; RAGUŽ, I.; FUCHS, P.F. et al., 2021. Functional mechanical metamaterial with independently tunable stiffness in the three spatial directions. Online. *Materials Today Advances*. Vol. 11, p. 100155. ISSN 2590-0498. Available at: https://doi.org/10.1016/j.mtadv.2021.100155.

[2] SENGUL, Mustafa; TASDEMIR, H. Abdullah and TAMER, Aykut, 2025. Real-world applications of auxetic structures in engineering: A review. Online. *Structures*. Vol. 80, p. 109673. ISSN 2352-0124. Available at: https://doi.org/10.1016/j.istruc.2025.109673.

[3] HELEŠICOVÁ, Petra. *Description of fatigue behaviour of 3D printed polymer metamaterial structure*. Brno, 2024, 91 p. Master’s Thesis. Brno University of Technology, Faculty of Mechanical Engineering, Institute of Solid Mechanics, Mechatronics and Biomechanics. Supervisor Ing. Lukáš Trávníček, Ph.D.

[4] BERREHILI, A.; CASTAGNET, S. and NADOT, Y., 2010. Multiaxial fatigue criterion for a high-density polyethylene thermoplastic. Online. *Fatigue & Fracture of Engineering Materials & Structures*. 2010-5-13, vol. 33, no. 6, pp. 345-357. ISSN 8756-758X. Available at: https://doi.org/10.1111/j.1460-2695.2010.01446.x.

APPLIED MECHANICS 2026
April 13 - 15, 2026, České Budějovice, Czech republic

Analysis of thin-walled conical pressure vessel wound from composite

M. Voborský[1], Z. Padovec[2]

Abstract: This thesis presents an analysis of a thin-walled conical pressure vessel manufactured from filament-wound composite materials. The vessel is subjected to internal pressure and a constant temperature change (cooling). The resulting stress state in the conical wall is evaluated using both analytical and numerical methods. The results of these two approaches are compared for two material combinations: glass/epoxy and carbon/epoxy.

Keywords: composite materials, pressure vessel, conical shell, structural analysis, stress analysis

1 Introduction

Pressure vessels made of filament-wound composite materials are nowadays widely utilized in various applications. They are primarily used for the storage of fuels (e.g., Helium, natural gas) in sectors where weight reduction is crucial. The conical shape of such vessels is particularly suitable for fitting within conical envelopes in aerospace and aeronautics, allowing the aerodynamic shape of the vehicle to be fully exploited [1], [2].

Compared to the classical cylindrical shape, the conical geometry presents new challenges regarding both structural design and the associated manufacturing process (filament winding). In this work, a three-layered composite wall is considered, consisting of a hoop layer, a balanced helical layer, and an additional hoop layer. The structural analysis is focused exclusively on the conical section of the vessel (excluding the domes). The theory of orthotropic continuum and Classical Lamination Theory (CLT) are applied, utilizing selected strength criteria. The boundary conditions include loading by internal pressure and wall cooling; the latter often proves to be more critical than heating.

Both analytical and numerical calculations were performed for two composite combinations: glass/epoxy and carbon/epoxy. The analytical method was implemented in MATLAB, while the numerical analysis was conducted using Abaqus.

2 Problem description

2.1 Conical geometry of a filament-wound pressure vessel

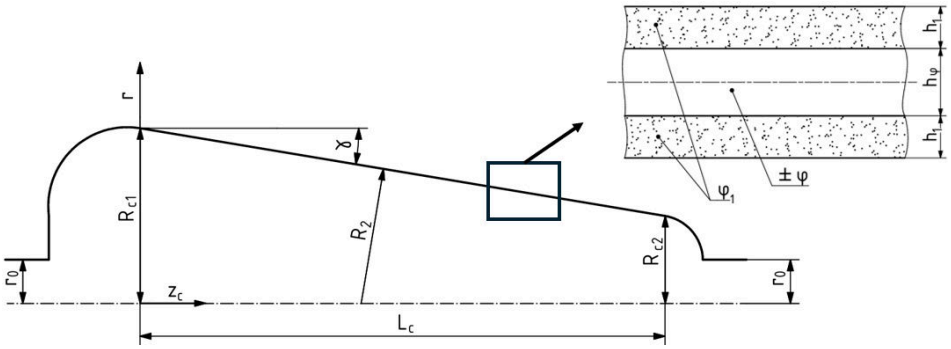

Figure 1: Meridian of conical shell with wall detail

[1] Marek Voborský; CTU, Faculty of Mechanical Engineering; marek.voborsky@fs.cvut.cz
[2] Zdeněk Padovec; CTU, Faculty of Mechanical Engineering; zdenek.padovec@fs.cvut.cz

In Figure 1, the meridian of the conical shell and a detail of the wall are shown. The geometry is defined by the radii of the polar openings r_0, the radii at the beginning and the end of the conical section (R_{c1} and R_{c2}), and the length of the conical section L_c.

Meridian, wall thicknesses (h_1 for the hoop layer and h_φ for the helical layer) and the varying winding angle of the balanced layer ($\pm\varphi$) along the axial coordinate (z_c) were computed with the use of netting theory. This theory assumes that the load is carried solely by the fibers, neglecting the contribution of the matrix. The cone angle γ is assumed to be small enough to prevent fiber slippage. The maximum value of this angle can be expressed as $\gamma_{max} = \tan^{-1} f$, where f is the friction coefficient. For a typical filament winding value of $f = 0.2$, this yields $\gamma_{max} = 11.3°$ [3].

To satisfy the geodesic winding condition and minimize the risk of fiber slippage, the following relations for the winding angles were applied [4]:

$$\varphi = \arcsin \frac{r_0}{r}, \quad \varphi_1 = 90°. \tag{1}$$

The wall thicknesses can then be derived as follows:

$$h_\varphi = h_\varphi^{(1)} \sqrt{\frac{R_{c1}^2 - r_0^2}{r^2 - r_0^2}}, \quad h_1 = \frac{h_\varphi^{(1)}}{2} \left[3\cos^2(\varphi^1) - 1\right], \tag{2}$$

where $h_\varphi^{(1)}$ and φ^1 represent the thickness and winding angle of the balanced layer at the beginning of the axial coordinate (at the larger radius), respectively: $h_\varphi^{(1)} = h_\varphi(r = R_{c1})$ and $\varphi^1 = \varphi(r = R_{c1})$ [3].

2.2 Thermoelastic properties of the three-layered wall

The thermoelastic properties of the three-layered wall in global coordinates (E_ψ, E_η, $G_{\psi\eta}$, $\nu_{\psi\eta}$, α_ψ, α_η) along the axial coordinate were calculated from the properties of each individual layer in local coordinates (E_L, E_T, ν_{LT}, G_{LT}, α_L, α_T). The global (ψ, η) and local (L, T) directions are illustrated in Figures 2 and 3.

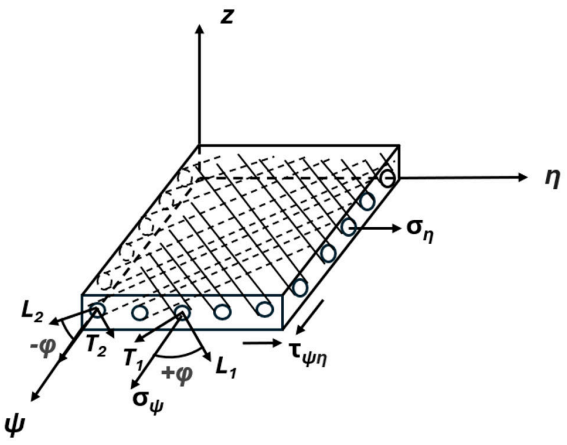

Figure 2: Global coordinates ψ and η for balanced layer and stresses.

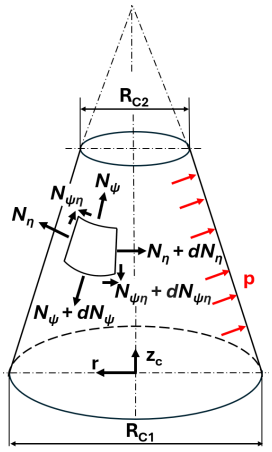

Figure 3: Global coordinates ψ and η on the cone, internal forces and pressure.

An example of the Young's modulus calculation is:

$$E_\psi = \frac{1}{h}\left(A_{11} - \frac{A_{12}^2}{A_{22}}\right), \quad E_\eta = \frac{1}{h}\left(A_{22} - \frac{A_{12}^2}{A_{11}}\right), \tag{3}$$

where h is the total wall thickness and A_{ij} represents the membrane stiffness matrix of the three-layered wall. This matrix is computed as $A_{ij} = \sum_{k=1}^{3} {}^k\overline{Q}_{ij} h_k$, where ${}^k\overline{Q}_{ij}$ is the transformed reduced stiffness

matrix and h_k is the thickness of the k-th layer ($k = 1$ for hoop, $k = 2$ for balanced helical, $k = 3$ for hoop) [5].

The coefficients of thermal expansion (CTEs) α_ψ and α_η were obtained similarly, based on [6].

2.3 Stress state and failure criteria

2.3.1 Stresses in layers due to internal pressure

The stresses in each layer are assumed to be membrane stresses (tension/compression only, neglecting bending moments and shear forces). They are expressed as:

$$ {}^{k}\begin{bmatrix} \sigma_\psi \\ \sigma_\eta \\ \tau_{\psi\eta} \end{bmatrix} = {}^{k}\begin{bmatrix} \overline{Q}_{11} & \overline{Q}_{12} & \overline{Q}_{16} \\ \overline{Q}_{21} & \overline{Q}_{22} & \overline{Q}_{26} \\ \overline{Q}_{61} & \overline{Q}_{62} & \overline{Q}_{66} \end{bmatrix} \cdot \begin{bmatrix} \varepsilon_\psi \\ \varepsilon_\eta \\ \gamma_{\psi\eta} \end{bmatrix}, \tag{4} $$

where the strains ε_i resulting from the internal pressure p is assumed to be uniform across all layers and is computed as $\varepsilon_i = a_{ij} N_j$, where $a_{ij} = A_{ij}^{-1}$. The internal forces N_j are defined as $N_\psi = \frac{pr}{2\cos\gamma}$, $N_\eta = \frac{pr}{\cos\gamma}$ and $N_{\psi\eta} = 0$. Subsequently, the stresses were normalized to a dimensionless form by dividing them by the reference stress at the larger radius, $\sigma_{\text{sr}} = \frac{pR_{c1}}{2h_\varphi^{(1)}\cos\gamma}$ [7].

2.3.2 Stresses in layers due to constant temperature change

Due to the varying winding angles of adjacent laminae and the differing CTEs of the fibers and matrix, a constant temperature change ΔT induces a stress field throughout the cone wall:

$$ {}^{k}\begin{bmatrix} \sigma_\psi \\ \sigma_\eta \\ \tau_{\psi\eta} \end{bmatrix} = {}^{k}\begin{bmatrix} \overline{Q}_{11} & \overline{Q}_{12} & 0 \\ \overline{Q}_{21} & \overline{Q}_{22} & 0 \\ 0 & 0 & \overline{Q}_{66} \end{bmatrix} \cdot {}^{k}\begin{bmatrix} \alpha_\psi - \overline{\alpha}_\psi \\ \alpha_\eta - \overline{\alpha}_\eta \\ 0 \end{bmatrix} \cdot \Delta T, \tag{5} $$

where $\overline{\alpha}_\psi$ and $\overline{\alpha}_\eta$ are CTEs of balanced layer.

Shear stress for orthotropic monolayer (with winding angle φ) was computed from

$$ {}^{k}\tau_{\psi\eta} = {}^{k}G_{\psi\eta}\left(- {}^{k}S_{61}\,{}^{k}\sigma_\psi - {}^{k}S_{62}\,{}^{k}\sigma_\eta - \alpha_{\psi\eta}\Delta T \right), \tag{6} $$

where ${}^{k}G_{\psi\eta}$ is shear modulus, S_{61} and S_{62} are elements of compliance matrix and $\alpha_{\psi\eta}$ is CTE all for oriented monolayer. The resulting stresses computed from (5) and (6) were normalized by $|\Delta T|$ [7].

2.3.3 Failure criterion

To determine whether the layers can withstand the combined loading, the stresses were transformed from global coordinates (ψ, η) to the local coordinates (L, T) of the laminate (see Figure 4).

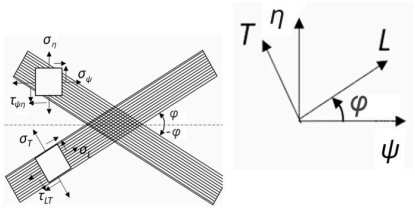

Figure 4: Stress transformation

The transformation took form ${}^{k}[\sigma]_{L,T} = T_\sigma\,{}^{k}[\sigma]_{\psi,\eta}$, where T_σ is the stress transformation matrix.

The maximum stress criterion was then applied:

$$\begin{aligned} -F_{\mathrm{Lc}} < \sigma_{\mathrm{L}} < F_{\mathrm{Lt}}, \\ -F_{\mathrm{Tc}} < \sigma_{\mathrm{T}} < F_{\mathrm{Tt}}, \\ -F_{\mathrm{LT}} < \sigma_{\mathrm{LT}} < F_{\mathrm{LT}}, \end{aligned} \tag{7}$$

where F_{Lt}, F_{Lc} are the longitudinal strengths (tension and compression), F_{Tt}, F_{Tc} are the transversal strengths (tension and compression), and F_{LT} is the shear strength.

To visualize the risk of failure more effectively, the Failure Index (FI) was evaluated as the inverse of the safety factor. $FI \in (0, 1)$ indicates a safe design; if $FI > 1$, failure is expected.

2.4 FEM analysis

For FEM analysis symmetry of the cone was used and only 1/4 of the vessel was modeled. The body was chosen as deformable shell. To capture the changing winding angle of the helical layer and the changing wall thickness along the meridian, the body was cut paralel to the axis into ten sections, see Figure 5. Quad dominated S4R elements were used and after performing mesh sensitivity test, the 1.5 mm size of mesh was chosen, see Figure 6. The body was then subjected to the two load cases and FI was evaluated.

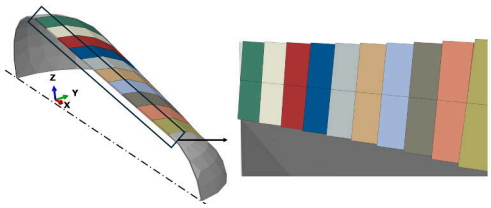

Figure 5: Change in wall thickness along maeridian.

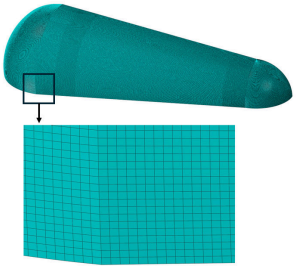

Figure 6: Mesh detail

3 Results

The parameters used in this analysis can be seen in Table 1 typical for glass/epoxy material system with fibre volume fraction $V_{\mathrm{f}} = 67\ \%$.

Parametrs	*Value*
R_{c1} / R_{c2} / r_0 / γ / L_c / $h_{\varphi}^{(1)}$	200 mm / 100 mm / 50 mm / 9.46° / 600 mm / 1 mm
p / ΔT	1 MPa / −100 °C
E_{L} / E_{T} / ν_{LT} / G_{LT}	48 000 MPa / 17 600 MPa / 0.25 / 8000 MPa
α_{L} / α_{T}	6.5×10^{-6} 1/°C / 16.3×10^{-6} 1/°C
F_{Lt} / F_{Lc} / F_{Tt} / F_{Tc} / F_{LT}	1200 MPa / 600 MPa / 45 MPa / 145 MPa / 65 MPa

Table 1: Parameters of cone, load and glass/epoxy (G/E) material used in the analysis.

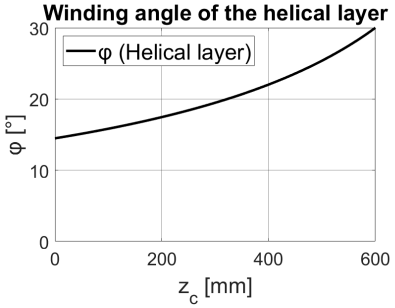

Figure 7: Winding angle of helical layer.

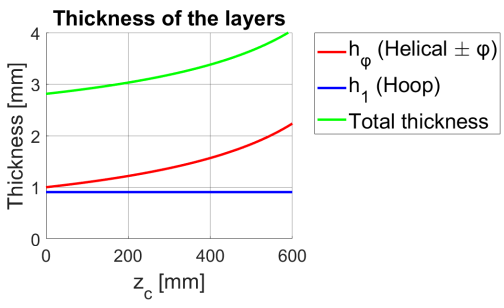

Figure 8: Wall thicknesses

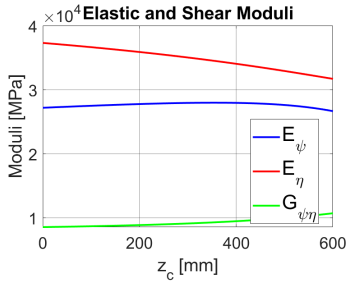

Figure 9: Elastic moduli

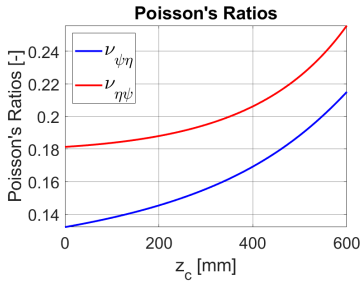

Figure 10: Poisson's ratios

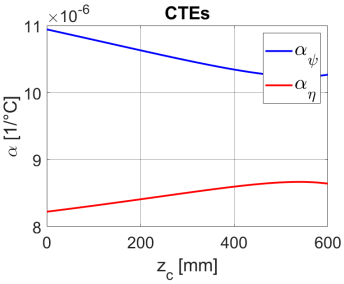

Figure 11: CTEs

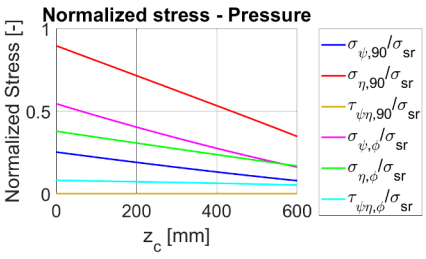

Figure 12: Stress from internal pressure

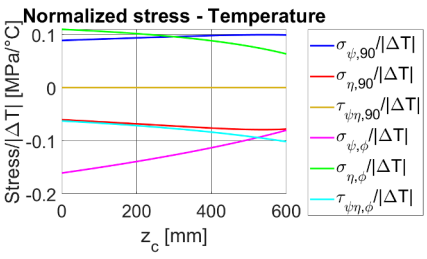

Figure 13: Stress from temperature cooling

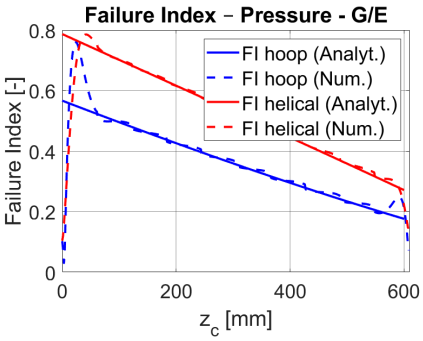

Figure 14: FI from internal pressure, G/E

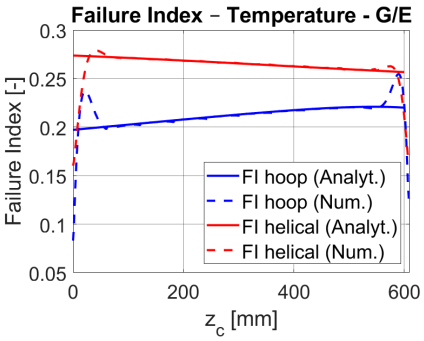

Figure 15: FI from temperature cooling, G/E

Material parametrs carbon/epoxy	*Value*
E_L / E_T / ν_{LT} / G_{LT}	138 000 MPa / 8960 MPa / 0.3 / 7100 MPa
α_L / α_T	-0.3×10^{-6} 1/°C / 28.1×10^{-6} 1/°C
F_{Lt} / F_{Lc} / F_{Tt} / F_{Tc} / F_{LT}	1447 MPa / 1447 MPa / 51.7 MPa / 206 MPa / 93 MPa

Table 2: Parameters of carbon/epoxy (C/E) material used in *FI* analysis below (figures 16 and 17).

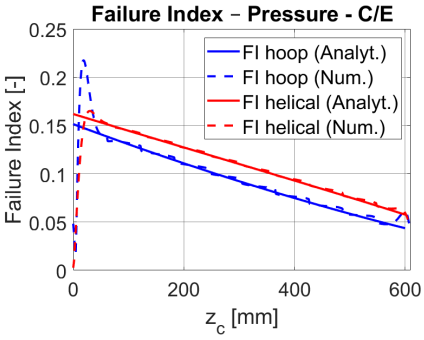

Figure 16: FI from internal pressure, C/E

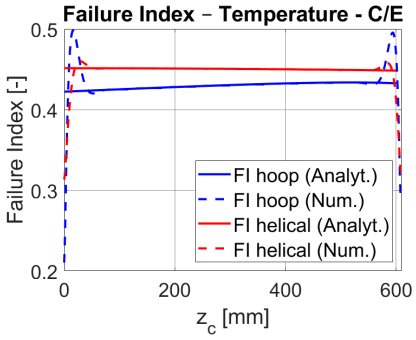

Figure 17: FI from temperature cooling, C/E

4 Conclusion

The results of this study are presented in Figures 7–17. Figures 7 and 8 illustrate the increase in winding angle and thickness of the helical layer along the axial coordinate, ensuring that the geodesic winding condition is met. Figures 9–11 evaluate the thermoelastic characteristics of the three-layered glass/epoxy wall.

Figure 12 indicates that the most critical region of the cone is at the larger radius, where the stresses reach their maximum. This is a direct consequence of the wall thickness being at its minimum at this location. This observation is further confirmed by Figure 14, which shows the highest FI values for the glass/epoxy combination at the larger radius.

While the FI due to cooling ($\Delta T = -100°\text{C}$) in Figure 15 remains below the critical threshold, these are residual stresses from the curing process. When superimposed with the stresses from internal pressure, the FI of the helical layer exceeds 1.0, suggesting that cracks would likely appear in the glass/epoxy helical layer. Figures 16 and 17 demonstrate that the carbon/epoxy combination is a safer alternative, as the total FI does not exceed 1.0, and thus no failure is expected.

In all cases, the numerical results show excellent agreement with the analytical solutions, confirming the reliability of the evaluation. The only discrepancies occur at the edge sections of the cone, where numerical results overshoot the analytical ones. This is due to the numerical model accounting for bending stresses in these regions, whereas the analytical model assumes a pure membrane stress state.

For future research, a structural analysis of the entire vessel, including the end domes, is suggested. Additionally, investigating methods to smooth the stress distribution along the meridian—for example, through the use of non-geodesic winding—would be a valuable extension of this work.

Acknowledgement

This study received support from the Grant Agency of the Czech Technical University in Prague, under grant No. SGS24/123/OHK2/3T/12.

References

[1] Walter H. Tam, Ian A. Ballinger, Jerry Kuo, William D. Lay, Stephen F. McCleskey, Pedro Morales, Zachary R. Taylor, Sheldon J. Epstein, Design and Manufacture of a Composite Overwrapped Xenon Conical Pressure Vessel, 1996, AIAA 96-2752, Available from: https://www.researchgate.net/publication/268457356_Design_and_manufacture_of_a_composite_overwrapped_xenon_conical_pressure_vessel

[2] Azeem, M., Hamdan H., Alam A., et al.,: Application of Filament Winding Technology in Composite Pressure Vessels and Challenges: A Review, *Journal of Energy Storage, Elsevier*, 2022, Available from: https://doi.org/10.1016/j.est.2021.103468

[3] Vasiliev V., *Composite pressure vessels: Design, Analysis and Manufacturing*, 2009

[4] Sofi T., Schledjewski R., Winding Trajectories for Dry Filament Wound Preforms, 2018, Available from: https://www.researchgate.net/publication/371400758_Winding_Trajectories_for_Dry_Filament_Wound_Preforms

[5] Padovec J., Základy konstrukce a výpočtu vinutých tlakových nádob z kompozitních materiálů, *Strojírenství 30*, 1980

[6] Padovec J., Příspěvek k termoelastickým napětím ve válcových tlakových nádobách z vinutých kompozitů,, *Strojírenství 32*, 1982

[7] Padovec Z., ANALYSIS OF CONICAL PART OF INTEGRALLY WOUND COMPOSITE PRESSURE VESSEL SUBJECTED TO INTERNAL PRESSURE AND TEMPERATURE LOADING, *Journal of MECHANICAL ENGINEERING*, 2025

APPLIED MECHANICS 2026
April 13 - 15, 2026, České Budějovice, Czech republic

INFLUENCE OF IRRADIATION ON THE DEGRADATION BEHAVIOUR OF DEGRADABLE SUTURES

Marika Vopálková[1,2], Tomáš Suchý[3,4], Radek Sedláček[5], Eva Kuželová Košťáková[6], David Lukáš[7], Jaroslav Mikule[8], David Chvátil[9]

Abstract: In the course of this study, monofilament poly(caprolactone-co-glycolide) copolymer sutures (PCGL) were exposed to doses of 1 kGy, 25 kGy and 50 kGy. The objective of this study was to verify the hypothesis that irradiation can accelerate the degradation processes of the suture. The sutures were tested using tensile tests in a dry state and after 14 days in phosphate buffer (pH 7). In addition, Fourier-transform infrared spectroscopy (FTIR) and scanning electron microscopy (SEM) analysis were performed. This study is merely a contribution to a more extensive research project on suture materials.

Keywords: suture, degradation, irradiation, tensile tests

1 Introduction

This experimental work constitutes a component of a more extensive study that is underway to develop a novel type of suture material. The utilisation of nanofiber layers in this novel surgical suture is purported to facilitate active intervention in the healing process by means of gradual delivery of bioactive substances to the wound area, thereby promoting healing. However, for the suture to be considered suitable for actual surgical application, it is necessary that several requirements are met. A pivotal parameter for evaluating the biodegradability of sutures is the rate of degradation, which must be tailored to the healing rate of the sutured tissue. This is precisely the problem we sought to address in this study, wherein we hypothesised that irradiating the sutures with beta radiation could influence (accelerate) their degradation rate [1].

[1] Ing., Marika, Vopálková; Faculty of mechanical engineering, Czech Technical University in Prague; Technická 4, Prague 6, 160 00, Prague 6, Czech republic, marika.vopalkova@fs.cvut.cz
[2] Ing., Marika, Vopálková; Institute of Rock Structure and Mechanics of The Czech Academy of Sciences, v. v. i.; V Holešovičkách 94/41, 182 09, Prague 8, Czech republic, vopalkova@irsm.cas.cz
[3] doc. Ing., Ph.D, Tomáš, Suchý; Faculty of mechanical engineering, Czech Technical University in Prague; Technická 4, Prague 6, 160 00, Prague 6, Czech republic, tomas.suchy@fs.cvut.cz
[4] doc. Ing., Ph.D, Tomáš, Suchý; Institute of Rock Structure and Mechanics of The Czech Academy of Sciences, v. v. i.; V Holešovičkách 94/41, 182 09, Prague 8, Czech republic, suchy@irsm.cas.cz
[5] doc. Ing., Ph.D, Radek, Sedláček; Faculty of mechanical engineering, Czech Technical University in Prague; Technická 4, Prague 6, 160 00, Prague 6, Czech republic, radek.sedlacek@fs.cvut.cz
[6] doc. Ing., Ph.D, Eva, Kuželová Košťáková; Faculty of science, humanities and education Technical University Liberec; Studentska 5, 461 17, Liberec 1, Czech republic, eva.kostakova@tul.cz
[7] Prof. RNDr. CSc., David, Lukáš; Faculty of science, humanities and education Technical University Liberec; Studentska 5, 461 17, Liberec 1, Czech republic, david.lukas@tul.cz
[8] Ing., Jaroslav, Mikule; Faculty of science, humanities and education Technical University Liberec; Studentska 5, 461 17, Liberec 1, Czech republic, jaroslav.mikule@tul.cz
[9] Ing., David, Chvátil; Nuclear Physics Institute of the Academy of Sciences of the Czech Republic v. v. i., Řež 292, 250 68 Husinec, Czech Republic, chvatil@ujf.cas.cz

2 Methods

Monofilament sutures composed of PCGL (RWTH Aachen) were utilised in the experiment. Subsequently, the sutures were irradiated with beta radiation using a Microtron MT25 device (16 MeV). The radiation dose was regulated by means of exposure time, whereby we obtained sutures irradiated with doses of 0 kGy (without irradiation – control group), 1 kGy (t = 285s), 25 kGy (t = 918s), and 50 kGy (t = 1900s). Subsequently, the mechanical properties (tensile test) were tested, and Fourier-transform infrared spectroscopy (FTIR) and scanning electron microscopy (SEM) analyses were performed on samples after irradiation and then on irradiated samples that had been exposed to a simulated wound environment for 14 days (phosphate solution, pH 7, 37 °C). The medium was changed every 3 to 4 days and the pH stability was routinely tested.

2.1 Tensile tests

Tests were performed at universal testing machine Inspekt 100kN (force sensor AST, KAF 100N). Testing was performed based on the ČSN EN ISO 2062 [2]. Nominal length of samples were 250 mm and winding clamps were used, which were wound twice with suture. Testing speed was 250 $mm \cdot min^{-1}$.

The suture deformation was measured directly from the machine jaw displacement. However, due to limitations associated with suture attachment to the winding jaw (unwinding and suture deformation may occur directly on the winding, which is not included in the free suture length, and thus deformation from the machine may be inaccurate), the measurement was supplemented by deformation measurement using mark detection in the video. Black and white (white and black stripe) stickers were placed on the free length of suture near the jaws to serve as marks.

3 Results

The mechanical characteristics evaluated included breaking force, elongation at break, and initial tangent. Figure 1 demonstrates that irradiation of the sutures had a discernible effect on the initial measured properties, without consideration of the effect of degradation. Statistically significant differences were recorded for almost all characteristics of sutures with an irradiation dose of 25 kGy and 50 kGy, when compared to non-irradiated sutures. The sutures demonstrated consistent behaviour even following degradation, as evidenced by a 14-day simulation in a wound environment.

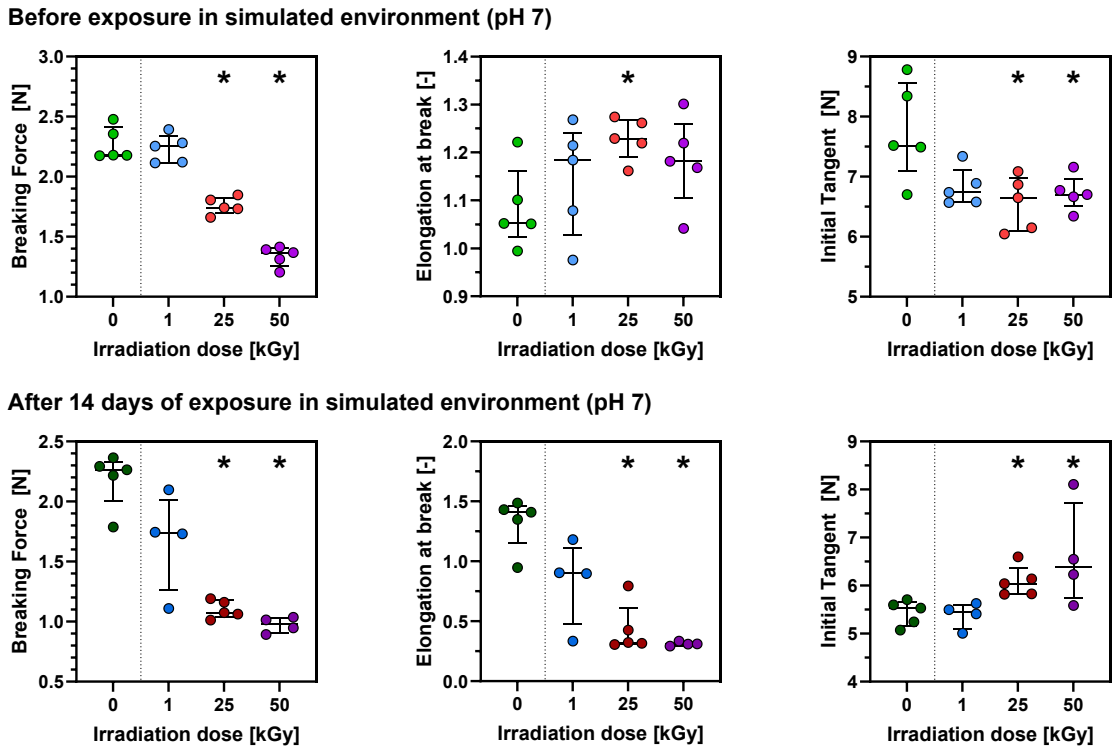

Figure 1: Plots of breaking force, elongation at break and initial tangent of samples before and after 14 days of exposure to simulation environment (median with interquartile range, $n = 4\text{-}5$); Significant differences to 0 kGy samples ($p < 0.05$) are marked with an asterisk (uncorrected Dunn test).

However, the more salient information in this study is the extent to which the individual characteristics underwent change during exposure to the medium. As demonstrated in Figure 2, the data reveal a percentage change in relation to the state preceding the onset of degradation. It is evident that in the case of breaking force, the maximum forces of unirradiated sutures before and after degradation exhibit minimal variation (+3.9%). However, for irradiated sutures, even at a dose of 1 kGy, the median force after exposure to the medium decreased by more than 20%. As the irradiation dose increased, a further decline in the force after degradation in the medium was observed (-38.3%, -28.3%).

In the case of elongation at break, an increase of up to 33.9% was observed in unirradiated yarn due to hydration (the original yarns were measured in a dry state before degradation). For yarns exposed to 1 kGy, a decline of 23.9% was observed, while for yarns subjected to higher radiation doses, the decrease reached up to 73%.

Upon focusing on the alterations in the initial tangent, it becomes evident that this is the sole parameter where the trend of change undergoes a reversal. Consequently, the most substantial decreases were observed in the unirradiated suture, while the least significant changes, amounting to -4.7%, were recorded in the suture exposed to the highest radiation dose. This phenomenon is presumably associated with the hydration of the unirradiated suture. In contrast, it is hypothesized that the other sutures underwent significant degradation processes, the effects of which appear to be the opposite of hydration.

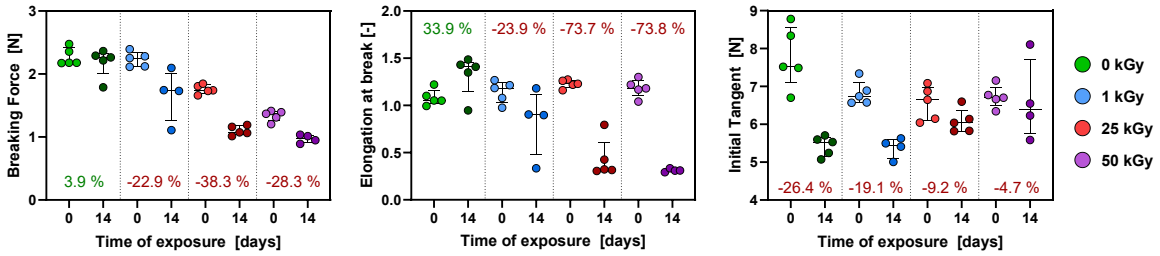

Figure 2: Plots of breaking force, elongation at break and initial tangent of samples before and after 14 days of exposure to simulation environment (*n = 4-5*); the percentages displayed herein represent the percentage change in the median after a 14-day period in a simulated environment in comparison to median of samples prior to degradation; median + interquartile range.

4 Conclusions

The results obtained demonstrate that irradiation significantly affects the degradation behaviour of the sutures. Specifically, it appears that a higher radiation dose accelerated degradation behaviour, but at the same time, irradiation also affected the initial mechanical properties, with lower breaking force being an undesirable consequence. Furthermore, it was observed that between radiation doses of 25 kGy and 50 kGy, there were no such drastic changes in terms of degradation behaviour. However, concurrently, there were decreases in the breaking force of non-degraded sutures (probably due to the continuing radiation damage to the material). In light of the findings, it can be concluded that, for the given set of sutures, the application of irradiation doses ranging from 1 kGy to 25 kGy would be a suitable course of action in order to effect a modification in the degradation behaviour. This is due to the fact that such an approach would have a lesser effect on the non-degraded (original) state of the suture.

Acknowledgement

This research work was supported by the Grant Agency of the Czech Technical University in Prague SGS22/149/OHK2/3T/12 and the Ministry of Health of the Czech Republic, grant no. NW24-08-00133 Nanofiber surgical sutures with bioactive and antimicrobial agents.

References

[1] ŠUPOVÁ, Monika, SUCHÝ, Tomáš, VOPÁLKOVÁ, Marika, NOVOTNÁ, Pavla, ŠULC, Miloslav, HRDLIČKA, Zdeněk and HOUŠKA, Milan. The electron beam irradiation of type I bovine collagen gels: Insights into radiation dose and water content impacts on the composition and the structural, rheological, thermal and mechanical properties. *International Journal of Biological Macromolecules*. 2025. Vol. 320, p. 146099. DOI 10.1016/j.ijbiomac.2025.146099.

[2] *Textilie - Nitě na návinech: Zjišťování pevnosti a tažnosti jednotlivých nití při přetrhu pomocí přístroje s konstantní rychlostí prodloužení (CRE)*. 2010. Praha : Úřad pro technickou normalizaci, metrologii a státní zkušebnictví.

APPLIED MECHANICS 2026
April 13 - 15, 2026, České Budějovice, Czech republic

Advanced Modeling of a Quasi-Zero Stiffness Isolator with Euler-Buckled Beam Using Absolute Nodal Coordinate Formulation

J. Zavřel[1], M. Naar[2], Z. Šika[3]

Abstract: The paper presents a numerical model of a nonlinear quasi-zero stiffness (QZS) vibration isolator using an Euler-buckled beam as a negative stiffness corrector. The Absolute Nodal Coordinate Formulation (ANCF) is employed to accurately capture large deformations, geometric nonlinearities, and post-buckling behavior without relying on small-deformation assumptions. Thanks to its fully nonlinear formulation and constant mass matrix, ANCF enables reliable static and dynamic analysis of the QZS region, particularly near instability points and under larger excitation amplitudes. The approach provides a robust framework for advanced simulation and optimization of QZS vibration isolation systems.

Keywords: quasi-zero stiffness; Euler-buckled beam; vibration isolator; negative stiffness

1 Introduction

Vibration isolation is an important field in mechanical and structural engineering that focuses on reducing the transmission of vibrations from one system or structure to another. Vibrations are commonly generated by machines, vehicles, industrial equipment, or environmental sources, and if they are not properly controlled, they can cause noise, structural damage, reduced accuracy etc.

The main purpose of vibration isolation is to minimize the transfer of vibrational energy between a vibration source and its surroundings. This is typically achieved by inserting isolating elements, such as springs, rubber mounts, air cushions, or dampers, between the vibrating source and the structure that needs protection. These elements absorb, dissipate, or redirect vibrational energy, thereby reducing the amplitude of the transmitted vibrations.

An effective vibration isolation system must consider several key parameters, including the mass of the system, stiffness of the isolator, damping properties, and the frequency of the excitation force. When these parameters are properly designed, the isolation system can significantly reduce vibration levels and improve the performance, durability, and safety of mechanical systems.

Vibration isolation can be applied in many areas, including industrial machinery, vehicle suspension systems, building structures, and electronic equipment.

2 Absolute Nodal Coordinate Formulation

To model the highly nonlinear behavior of the Euler-buckled beam (Figure 1), the Absolute Nodal Coordinate Formulation (ANCF) is utilized. Unlike classical finite element methods (FEM) that describe the element kinematics using small local deformations, the ANCF method employs global position coordinates and their spatial derivatives (slopes) to define the exact geometry of the element's centerline. This enables an exact representation of rigid-body inertia without the assumption of small deformation, making it highly suitable for post-buckling problems.

In this study, a Euler-Bernoulli beam element lacking planar gradient, often referred to as the L2T2 element [1] is used. The state vector of the element's node i consists of four degrees of freedom:

$$\mathbf{e}_i = \left[x_i, y_i, \frac{\partial x_i}{\partial x}, \frac{\partial y_i}{\partial x} \right]^T, \tag{1}$$

[1] Jan Zavřel; CTU in Prague, Faculty of Mechanical Engineering; Jan.Zavrel@fs.cvut.cz
[2] Matěj Naar; CTU in Prague, Faculty of Mechanical Engineering; Matej.Naar@fs.cvut.cz
[3] Zbyněk Šika; CTU in Prague, Faculty of Mechanical Engineering; Zbynek.Sika@fs.cvut.cz

where x_i and y_i are the global spatial coordinates, and $\partial x_i/\partial x$ and $\partial y_i/\partial x$ represent the longitudinal position gradients.

The global position vector $\mathbf{r}(x)$ of an arbitrary point on the element's neutral axis is interpolated using the shape function matrix $\mathbf{S}(x)$ and the vector of elemental coordinates $\mathbf{e}$:

$$\mathbf{r}(x) = \mathbf{S}(x)\mathbf{e}. \tag{2}$$

The vector of generalized elastic forces $\mathbf{Q}_e$ is formulated based on the continuum mechanics of a thin beam, coupling both the longitudinal (axial) and transverse (bending) deformations. To account for the initial curved geometry of the beam caused by an initial imperfection, the elastic forces are evaluated relative to the reference state $\mathbf{e}_0$. The longitudinal elastic force depends on the Green-Lagrange axial strain $\varepsilon = \frac{1}{2}(\mathbf{r}_x^T\mathbf{r}_x - \mathbf{r}_{0x}^T\mathbf{r}_{0x})$, where subscript x denotes the spatial derivative. The bending force is derived from the exact definition of curvature κ, taking into account the initial curvature κ_0. The total elastic force vector is then given by the curve integral over the undeformed length of the element l_e:

$$\mathbf{Q}_e = \int_0^{l_e} \left(EA\varepsilon\mathbf{S}_x^T\mathbf{r}_x + EI(\kappa - \kappa_0)\frac{\partial\kappa}{\partial\mathbf{e}} \right) \mathrm{d}x, \tag{3}$$

where EA is the axial stiffness, EI is the bending stiffness, and $\partial\kappa/\partial\mathbf{e}$ represents the highly nonlinear curvature gradient vector. Integration is performed numerically using a 5-point Gauss quadrature rule.

To establish the static equilibrium of the QZS mechanism in the post-buckled state, a Newton-Raphson iterative solver is used. This requires the evaluation of the tangent stiffness matrix of the element, defined as the derivative of the elastic force vector with respect to the nodal coordinates $\mathbf{K}_e = \partial\mathbf{Q}_e/\partial\mathbf{e}$. The assembled global tangent stiffness matrix ensures stable convergence during the nonlinear static analysis and serves directly as the structural stiffness matrix for the subsequent modal analysis of the system.

3 Model of the QZS Mechanism

The initial modeling was performed in three ways (Figure 2). The first model was obtained using analytical equations for the pinned-pinned buckled Euler beam model [2]. The second model was created using a cubic approximation [2], and the third was modeled using ANCF elements. Figure 2 clearly shows that all three methods yield identical results. Only the cubic approximation begins to differ slightly for more distant points from the center. This confirms that the ANCF modeling methodology is fully valid and applicable to such problems.

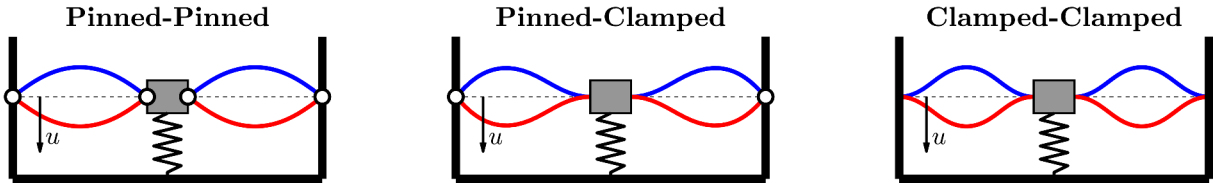

Figure 1: Different variants of boundary conditions of the QZS negative stiffness corrector.

Every investigated system consists of four beams (leaf springs), central load mass, and the spring connected to the base frame. Three types of beam boundary conditions were analyzed (Figure 1). In the first case, the beam rotates freely at both ends (a); in the second case, it rotates freely on one side and is fixed on the other (b); and in the third case, it is fixed at both ends (c).

The parameters listed in Table 1 were chosen to compare basic characteristics. The stiffness-strain relationship of the central platform (Figure 3) and the natural frequencies (Table 2) are analyzed and compared. The selected corresponding eigenmodes are shown in Figure 3.

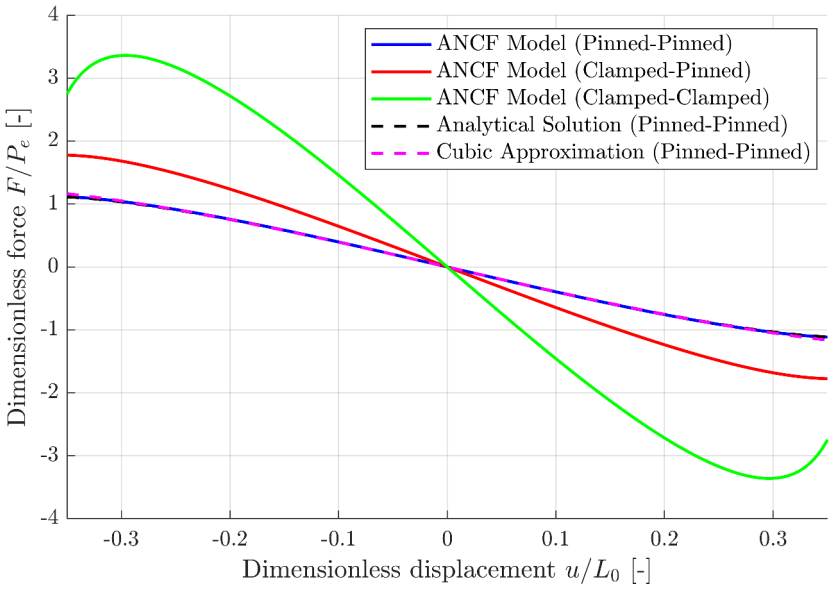

Figure 2: Comparison of dimensionless force-displacement ($F-u$) characteristics for a QZS mechanism under different boundary conditions. The numerical ANCF results for the Pinned-Pinned configuration are validated against the exact analytical solution and its cubic approximation derived in [2].

Parameter	*Symbol*	*Value*
Length of the undeformed beam	L_0	0.055 m
Beam width	b	0.02 m
Beam thickness	h	0.0007 m
Young's modulus	E	2.1×10^{11} Pa
Material density (steel)	ρ	7850 kg/m^3
Dimensionless initial imperfection	q_0/L_0	0.03
Compression ratio	L_{comp}/L	0.9
Load mass	m	17 kg
Linear spring stiffness	k	25 000 N/m

Table 1: Basic physical and geometrical parameters of the QZS mechanism.

Mode No.	*Pinned-Pinned Frequency [Hz]*	*Pinned-Clamped Frequency [Hz]*	*Clamped-Clamped Frequency [Hz]*
1	(-)2.32	(-)5.64	(-)10.94
2	1699.40	2009.76	2558.61
3	1717.57	2021.32	2568.43
4	4462.20	4583.60	4229.30
5	4471.14	4585.37	4229.90
6	8278.91	8471.39	8471.91
7	8283.79	8476.19	8474.02
8	13170.88	13660.89	12893.25
9	13174.03	13663.47	12897.90
10	19146.58	19727.26	20278.47

Table 2: Comparison of natural frequencies for different buckling boundary conditions. Mode 1 represents the isolated QZS mechanism (imaginary frequencies, represented here as negative values to indicate negative stiffness), while Modes 2–10 represent internal bending vibrations of the beams. The reference frequency of the linear system without the negative stiffness corrector is 6.10 Hz.

As shown in Figure 3, each type of leaf spring mounting exhibits a different force-displacement relationship. The pinned-pinned mounting is characterized by the lowest stiffness, and thus also by the lowest force as a function of position u.

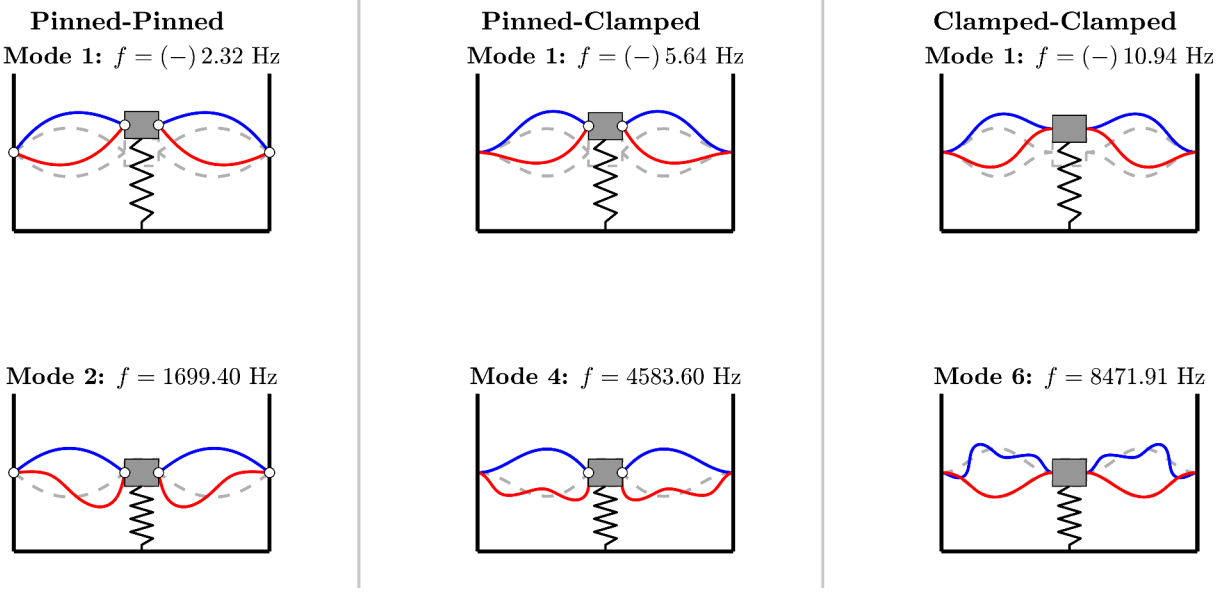

Figure 3: Comparison of selected vibration modes and their corresponding natural frequencies for three different boundary conditions of the buckled beams.

4 Conclusion

Three types of Euler buckled beam configurations were analyzed using a validated ANCF element model. These three variants were further analyzed to determine how the force acting on the central mass depends on its distance from the central equilibrium position. As shown in Table 2, the first eigen frequency of the systems corresponds to the oscillation of the central load mass and is very close to the eigen frequency of the mass-spring system. In Figure 3, it is clearly visible that the first mode shape corresponds to the vibrations of the central mass, while higher frequencies correspond to the vibrations of the leaf springs themselves. This achieves vibration isolation properties where higher frequencies do not interfere with the vibrations of the central mass.

Acknowledgement

The work has been supported by the Czech Science Foundation project 26-21353S “Vibration attenuation and stability enhancement of rotors with active high-static-low-dynamic stiffness supports”.

References

[1] BERZERI, M. and SHABANA, A. A. Development of simple models for the elastic forces in the absolute nodal co-ordinate formulation. *Journal of Sound and Vibration*. 2000, vol. 235, no. 4, pp. 539-565. Available from: https://doi.org/10.1006/jsvi.1999.2935.

[2] HUANG, Xiuchang; LIU, Xingtian; SUN, Jingya; ZHANG, Zhiyi and HUA, Hongxing. Vibration isolation characteristics of a nonlinear isolator using Euler buckled beam as negative stiffness corrector: A theoretical and experimental study. *Journal of Sound and Vibration*. 2014, vol. 333, no. 4, pp. 1132-1148. Available from: https://doi.org/10.1016/j.jsv.2013.10.026.

[3] TIMOSHENKO, Stephen P. and GERE, James M. *Theory of elastic stability*. 2nd Ed. Mineola: Courier Corporation, 2012. ISBN 978-0-486-47207-2.

APPLIED MECHANICS 2026
April 13 - 15, 2026, České Budějovice, Czech republic

FINITE ELEMENT MODEL UPDATING OF A COMPOSITE COMPONENT BASED ON EXPERIMENTAL MODAL ANALYSIS

Radek Zbončák[1]

Abstract: This paper presents finite element model updating of composite part of hybrid discs used in a carousel of an indexing gearbox based on experimental modal analysis. Two geometries, a full disc and a disc with a central opening for shaft insert, manufactured from short glass fibre reinforced epoxy, were investigated. Natural frequencies obtained experimentally were compared with idealized and modified FE models with material defined at the constituent level. By incorporating measured fibre volume fraction, porosity, and local fibre orientation, the modified model achieved an average deviation of approximately 5 %. The results confirm the suitability of the proposed approach for reliable prediction of dynamic behaviour.

Keywords: Composites, Natural frequency, FE model

1 Introduction

An indexing gearbox represents a specific type of cam mechanism whose purpose is to transform the uniform rotational motion of the input shaft into a unidirectional rotational motion of the output member with precisely defined dwell phases. It is a mechanical system consisting of at least one cam (radial or axial) and an output member connected to the cam through a general kinematic pair. The shape of the system's transmission function fundamentally influences the dynamic behaviour and mechanical properties of the entire mechanism.

A component of the indexing gearbox is the so-called carousel, which is a rotating body composed of a shaft and several discs forming the load-bearing part of the output mechanism referred to as the turret follower. The carousel is in contact with the cam via a roller and participates both in force transmission and in determining the overall dynamic behaviour of the mechanism. Its design, material composition, and stiffness have a direct impact on the service life, accuracy, and efficiency of the gearbox.

Traditionally, the carousel is manufactured from steel, which entails certain disadvantages (Figure 1). The high mass of steel components increases the moment of inertia about the rotational axis, negatively affecting the dynamic response of the system, increasing energy demands during acceleration and deceleration, and reducing the service life of components subjected to cyclic loading. Low natural frequencies may lead to resonance phenomena within the operating range, resulting in undesirable vibrations or failures.

For these reasons, replacing part of the carousel with lighter hybrid components based on fibre-reinforced polymers (FRP) with metallic inserts appears to be a promising solution. Weight reduction, decreased moment of inertia, and a simultaneous increase in natural frequencies significantly contribute to improving the overall dynamics of the mechanism, accelerating system response, increasing efficiency, and extending service life. At the same time, energy savings are achieved during cyclic operation of the gearbox, which is particularly important for high-frequency production lines.

[1] Ing. Radek Zbončák; VÚTS a. s.; Svárovská 619, 460 01 Liberec, Czechia, radek.zboncak@vuts.cz

The implementation of a hybrid design was enabled only by a change in the concept of the carousel assembly. The original rigid connection between the discs and the shaft (where the shaft and discs were manufactured as a single component) was replaced by a polygonal joint, allowing the discs to be produced separately and thus enabling the use of alternative materials.

This study deals with the finite element and experimental analysis of the dynamic properties of the composite part of a hybrid disc, with the aim of establishing an FE model capable of predicting the dynamic behaviour of the hybrid component.

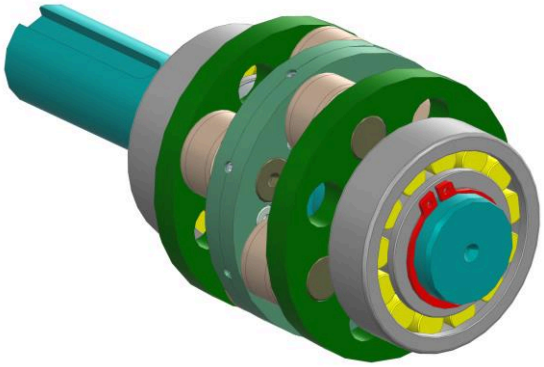

Figure 1: Original carousel of an indexing gearbox.

2 Dynamics of composites

Modal analysis represents a key tool of dynamic analysis for determining the natural frequencies and mode shapes of mechanical structures and their components. The main objective is the identification of potential resonance conditions and the assessment of dynamic stability within the operating speed range. [1] For a hybrid disc, the analysis demonstrates a strong dependence of natural frequencies on laminate stiffness, fibre volume fraction, and mass distribution. Increasing the specific stiffness of the composite leads to an increase in natural frequencies and their shift outside the operational frequency range, while the anisotropy of the composite material and its inherent damping significantly influence both the mode shapes and the vibration response amplitudes.

The discrepancies in the results may be attributed to the following factors:

- The idealized FE model assumes a homogenized material and idealized boundary conditions compared to the experimental setup.
- For FRP materials, it is common that quasi-static material constants do not correspond to the dynamic moduli in the measured frequency range.
- The density value directly influences the natural frequencies; therefore, determining it experimentally is more accurate than calculating it theoretically.
- Short fibres are not perfectly randomly oriented, and manufacturing may induce radial (circumferential) orientation, which can lead to incorrect estimation of the ratio between bending and shear stiffness (resulting in mode-dependent deviations).
- Skin–core effect: surface layers may exhibit different orientation or homogeneity compared to the core, causing thickness-dependent variations in mechanical properties.
- Fibre clustering, inhomogeneities, and local defects may occur, leading to local softening or stiffening; this can result in the splitting of degenerated modes into two closely spaced frequencies.
- Considering possible inhomogeneity, the measured results may also depend on the sensor location.

• Porosity reduces the composite moduli, increases damping, and consequently lowers the natural frequencies.
• Residual stresses after curing may influence the measured frequency values.

3 Experimental data

The composite body of the disc is manufactured from short glass fibres and epoxy resin using the cold press moulding technology. The mould consists of two parts and is made of artificial wood. The mixture of reinforcement and matrix is placed into the mould manually, which may lead to the formation of local inhomogeneities. The fibre orientation after demoulding is strongly influenced by the disc geometry, with fibres at the outer edge more frequently oriented tangentially to the circumferential boundary.

Based on measurements of the manufactured discs (Figure 2 and 3), the density of disc D1 is 1,830 kg/m³ and that of disc D2 is 1,839 kg/m³. The porosity of disc D1 is 3 % at a fibre volume fraction of 56 %, while disc D2 exhibits a porosity of 2 % at a fibre volume fraction of 55 %. Although the outer diameter of both manufactured discs is 80 mm, the thickness of D1 is 8.8 mm and that of D2 is 8 mm. The inner diameter of disc D2 is 40 mm.

Figure 2: Full composite disc - D1.

Figure 3: Composite disc with a shaft insert opening - D2.

The modal frequencies of the specimens are determined by experimental modal analysis. Primarily bending and torsional vibrations are measured, while the third dimension corresponding to the specimen thickness is neglected. Prior to testing, nodal points are marked and numbered on each specimen (Figure 4 and 5). An accelerometer is subsequently attached to the lower surface at position 10, which is identical for both specimens.

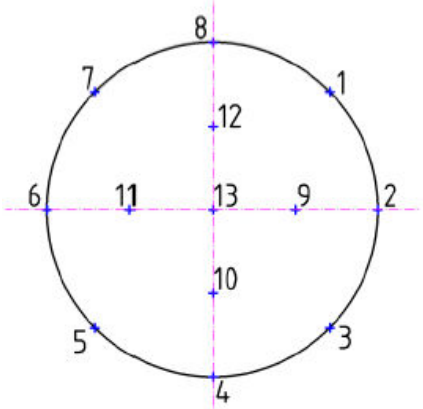

Figure 4: Scheme for full composite disc (D1) experiment.

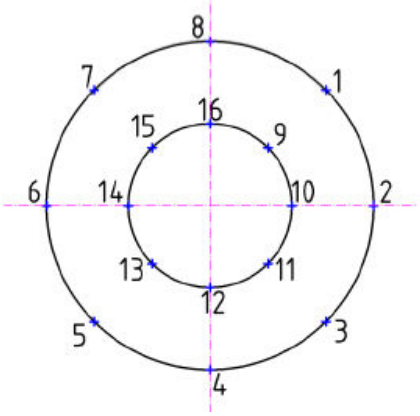

Figure 5: Scheme for measurement of composite disc with a shaft insert opening (D2).

The specimen is placed on a circular support with maximum compliance (nonwoven fabric with a layer of polyester wadding) with a diameter of 10 cm. The vibrations are excited by impacts from a modal hammer applied perpendicularly and sequentially at all marked nodal locations.

The measured values of the first five natural frequencies of discs D1 and D2 are summarized in Table 1.

	Full composite	Shaft opening
1st mode	4 134 Hz	3 047 Hz
2nd mode	4 406 Hz	3 178 Hz
3rd mode	6 980 Hz	6 030 Hz
4th mode	9 254 Hz	6 876 Hz
5th mode	9 316 Hz	8 270 Hz

Table 1. Values of natural frequencies obtained by experiment.

4 FEA

In addition to the experimental results (Table 1), the FE model updating process includes idealized, modified, and reference results (Table 2 and 3). For the assessment of FE model quality, the deviation between the experimental and modified results is decisive. The idealized results are primarily based on analytically determined material properties and a simplified composite structure. The modified results incorporate adjustments of the idealized properties based on experimental findings. The reference results predict the actual behaviour of a future prototype.

	1st mode	2nd mode	3rd mode	4th mode	5th mode
Experimental	4 134 Hz	4 406 Hz	6 980 Hz	9 254 Hz	9 316 Hz
Idealized – UD	3 921 Hz	3 953 Hz	6 458 Hz	8 093 Hz	8 096 Hz
deviation	*+5.4 %*	*+111.5 %*	*+8.1 %*	*+14.3 %*	*+15.1 %*
Idealized – Short	4 159 Hz	4 160 Hz	6 944 Hz	9 109 Hz	9 109 Hz
deviation	*-0.8 %*	*+5.9 %*	*+0.5 %*	*+1.6 %*	*+2.3 %*
Modified – Short	4 206 Hz	4 206 Hz	7 012 Hz	9 211 Hz	9 211 Hz
deviation	*-1.7 %*	*+4.7 %*	*-0.5 %*	*+0.5 %*	*+1.1 %*
Reference – Glass	3 899 Hz	3 901 Hz	6 495 Hz	8 600 Hz	8 605 Hz
Reference – Carbon	6 958 Hz	6 962 Hz	11 730 Hz	15 360 Hz	15 360 Hz

Table 2. Values of D1 natural frequencies obtained by simulation.

	1st mode	2nd mode	3rd mode	4th mode	5th mode
Experimental	3 047 Hz	3 178 Hz	6 030 Hz	6 876 Hz	8 270 Hz
Idealized – UD	2 769 Hz	2 788 Hz	6 110 Hz	6 863 Hz	6 867 Hz
deviation	*+10.1 %*	*+14.0 %*	*-1.3 %*	*+0.2 %*	*+20.4 %*
Idealized – Short	2 990 Hz	2 990 Hz	6 241 Hz	7 294 Hz	7 294 Hz
deviation	*+1.9 %*	*+6.3 %*	*-3.4 %*	*-5.7 %*	*+13.4 %*
Modified – Short	3 027 Hz	3 027 Hz	6 241 Hz	7 370 Hz	7 370 Hz
deviation	*+0.7 %*	*+5.0 %*	*-3.4 %*	*-6.7 %*	*+12.2 %*
Reference – Glass	3 027 Hz	3 027 Hz	6 241 Hz	7 370 Hz	7 370 Hz
Reference – Carbon	5 410 Hz	5 410 Hz	1 118 Hz	13 190 Hz	13 190 Hz

Table 3. Values of D2 natural frequencies obtained by simulation.

The idealized model is based on the actual geometry of the measured disc with a theoretical glass fibre volume fraction of 55 % and without voids in the epoxy resin. The laminate consists of 32 layers with uniform thickness and regular orientation. The stacking sequence is symmetric. The material is defined at the constituent level, with the reinforcement form (UD and short fibres) specified within the FEM software.

The modified model includes an adjusted fibre volume fraction and void content according to measured data. The fibre orientation in the edge region of the disc is also modified. The reference geometry of disc D1 has a diameter of 80 mm and a thickness of 8 mm. Disc D2 additionally contains a central opening with a diameter of 40 mm. The reference model further includes a comparison of two material variants, namely glass and carbon fibre reinforcement.

5 Discussion

The comparison of numerical and experimental results reveals a different sensitivity of the two geometries to the level of material model idealization. For the full disc D1, the idealized model with UD reinforcement shows significant deviations, for example +11.5 % for the 2nd mode and +15.1 % for the 5th mode. In contrast, the idealized model with short fibres exhibits substantially better agreement, with deviations ranging from −0.8 % to +5.9 %. After modification of the material parameters, further improvement is achieved and the deviations for D1 range between −1.7 % (1st mode) and +4.7 % (2nd mode), while for the higher modes they do not exceed ±1.1 %. This confirms that, for the full disc, the dynamic response is predominantly governed by global stiffness and mass, which can be captured with reasonable accuracy through appropriate model updating.

For disc D2 with a central opening, the situation differs. The idealized UD model shows pronounced discrepancies, particularly for the higher modes, for example +20.4 % for the 5th mode. Although the idealized short-fibre model improves the prediction of the 1st mode to +1.9 %, deviations of −5.7 % and +13.4 % remain for the 4th and 5th modes, respectively. The modified model, incorporating adjusted fibre volume fraction, density, and local fibre orientation, reduces the deviation of the 1st mode to +0.7 % and the 2nd mode to +5.0 %; however, for the higher modes the differences remain more pronounced (−6.7 % for the 4th mode and +12.2 % for the 5th mode). These results indicate a higher sensitivity of the geometry with a central opening to local stiffness distribution and material inhomogeneities, which cannot be fully captured within the applied material model.

Overall, the modified model achieves an average deviation of approximately 5 % for both discs, which can be considered very good agreement given the inherent variability of short-fibre FRP, the measured porosity (2–3 %), and manufacturing-related effects. The agreement in the character of the mode shapes between experiment and simulation further confirms that the constituent-based FE model is capable of reliably predicting the dynamic behaviour of both the full disc and the variant with a central opening, despite their different sensitivity to local stiffness variations.

6 Conclusion

Based on the work carried out, it can be concluded that the developed ply-based FE model, defined at the level of the individual composite constituents (matrix, reinforcement, and their volume fractions), is capable of accurately describing the dynamic behaviour of the composite discs of the hybrid carousel. A key step was the transition from an idealized approach to a modified material model reflecting the experimentally determined

fibre volume fraction, porosity, and local orientation of short fibres, particularly in the edge regions of the component.

The updated model achieves a deviation of natural frequencies of approximately 5 % compared to experimental measurements, which can be considered very good and fully acceptable from an engineering perspective, given the inherent inhomogeneity of short-fibre FRP materials and the simplifications related to manufacturing effects. The agreement of the mode shapes between simulation and experiment further confirms the suitability of the proposed FE model for predicting the dynamic behaviour of hybrid composite components and its applicability in the design of future lightweight carousel structures for indexing gearboxes.

Acknowledgement

This publication was supported by the Czech Ministry of Industry and Trade in the framework of the institutional support for long-term conceptual development of research organization - recipient VÚTS, a. s.

References

[1] VADIM V. SILBERSCHMIDT. Dynamic Deformation, Damage and Fracture in Composite Materials and Structures. Woodhead Publishing, 2016. ISBN 978-0-08-100870-6.

APPLIED MECHANICS 2026
April 13 - 15, 2026, České Budějovice, Czech republic

ON ACCELERATED CREEP TESTING OF 3D PRINTED ALSI7MG0.6 WITH DIC

Filip Zogata[1], Radim Halama[2], Petr Dymáček[3], Martin Mánek[4], Martin Zatloukal[5], Tomáš Leskovan[6]

Abstract: This contribution compares a conventional incremental step-load creep test with an accelerated, full-field creep testing methodology utilizing digital image correlation (DIC) on tubular specimens. The comparison demonstrates significant benefits of the DIC-enabled technique over the standard incremental approach, particularly in reducing measurement scatter and yielding more consistent creep parameters. All creep tests were conducted on vertically built, additively manufactured AlSi7Mg0.6 alloy specimens..

Keywords: Creep testing; Digital Image Correlation; AlSi7Mg0.6; Selective Laser Melting

1 Introduction

Conventional uniaxial creep testing is traditionally demanding, delivering only a single strain–time curve per specimen. This motivates the adoption of data-dense methodologies like Digital Image Correlation (DIC) [1],[2].

As a full-field optical technique, DIC enables the extraction of creep data from multiple locations on a single specimen under non-uniform stress fields, facilitating more efficient material screening and the validation of constitutive models where pointwise extensometers fails [2], [3]. Leveraging these advancements, this study applies these advancements to 3D-printed AlSi7Mg0.6 to resolve time-dependent deformation fields and identify creep responses under heterogeneous states.

2 Results

Figure 1 illustrates the strain–time response of 3D-printed AlSi7Mg0.6 obtained from the incremental creep test at 150 °C. The curve captures instantaneous strain jumps followed by periods of time-dependent deformation, ultimately culminating in accelerated tertiary creep and rupture. However, the short hold durations (~2000 s) prevent the material from fully exhausting transient mechanisms. Consequently, measured steady-state rates are heavily influenced by ongoing primary creep.

[1] Ing. Filip Zogata; Faculty of Mechanical Engineering, VŠB – Technical University of Ostrava; 17. listopadu 2172/15, 708 00 Ostrava, Czech Republic, filip.zogata@vsb.cz
[2] prof. Ing. Radim Halama, Ph.D.; Faculty of Mechanical Engineering, VŠB – Technical University of Ostrava; 17. listopadu 2172/15, 708 00 Ostrava, Czech Republic, radim.halama@vsb.cz
[3] Ing. Petr Dymáček, Ph.D.; Institute of Physics of Materials, Czech Academy of Sciences; Žižkova 22, 616 62 Brno, Czech Republic, pdymacek@ipm.cz
[4] Ing. Martin Mánek; Faculty of Mechanical Engineering, VŠB – Technical University of Ostrava; 17. listopadu 2172/15, 708 00 Ostrava, Czech Republic, martin.manek@vsb.cz
[5] Bc. Martin Zatloukal; Faculty of Mechanical Engineering, VŠB – Technical University of Ostrava; 17. listopadu 2172/15, 708 00 Ostrava, Czech Republic, martin.zatloukal.st@vsb.cz
[6] Bc. Tomáš Leskovan; Faculty of Mechanical Engineering, VŠB – Technical University of Ostrava; 17. listopadu 2172/15, 708 00 Ostrava, Czech Republic, tomas.leskovan.st@vsb.cz

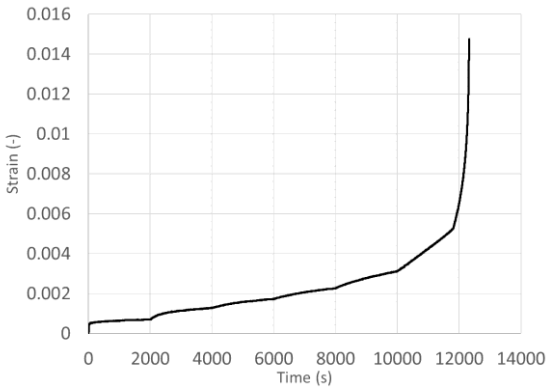

Figure 1: Creep time-strain curve from incremental test at 150°C

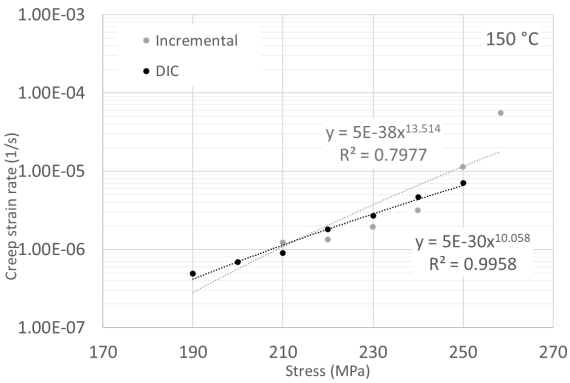

Figure 2: Comparison of apparent creep strain rates vs. stress extracted via the incremental method and the DIC-based full-field approach.

Despite this physical limitation of the accelerated timeline, Figure 2 demonstrates the substantial metrological advantage of the proposed DIC-based approach. While the incremental creep test yields highly scattered data ($R^2 = 0.7977$, $n \approx 13.5$), the full-field DIC methodology provides a remarkably consistent and reliable Norton power-law fit ($R^2=0.996$, $n \approx 10.1$) compared to the highly scattered incremental data, a critical limitation must be acknowledged. Due to the accelerated nature of the tests and relatively short hold times at each stress level, the material response likely does not reach a true secondary creep regime. As a result, the creep strain rates shown in Figure 2 for both measurement techniques inherently overestimate the true minimum creep rate (particularly visible in the DIC data at 190 and 200 MPa).

3 Conclusion

The implementation of DIC for accelerated creep testing of 3D-printed AlSi7Mg0.6 demonstrates superior precision and significantly reduced scatter compared to incremental methods. While the accelerated nature of the test means measured rates likely reflect unexhausted primary creep, DIC remains a robust tool for rapid comparative screening. For absolute calibration of long-term component behaviour, validation against conventional long-term data remains necessary.

Acknowledgement

The work on this paper was supported by the Czech Science Foundation grant 25-15579S and by the Specific Research Project SP2026/027.

References

[1] VAN ROOYEN, M.; FORSEY, A.N.; GUNGOR, S. and BECKER, T.H. Creep deformation measurement of ex-service 12% Cr steel over nonuniform stress fields using digital image correlation. *Strain*. 2021, vol. 58, no. 1, e12400. Available from: https://doi.org/10.1111/str.12400.

[2] PAŠKA, Z.; HALAMA, R.; DYMÁČEK, P., GOVINDARAJ, B. and ROJÍČEK, J. Comparison of Tensile and Creep Properties of SAC305 and SACX0807 at Room Temperature with DIC Application. *Applied Sciences*. 2024, vol. 14, 604. Available from: https://doi.org/10.3390/app14020604.

[3] NARAYANAN, A.; DUBEY, K.; DAVIES, C.M. and DEAR, J.P. The creep of alloy 617 at 700 °C: Material properties, measurement of strain and comparison between finite element analysis and digital image correlation. *International Journal of Solids and Structures*. 2017, vol. 129, pp. 195-203. Available from: https://doi.org/10.1016/j.ijsolstr.2017.08.021.